



Remotely sensed soil moisture proxies with application to modelling the spatial distribution of *Culicoides imicola*

Jasper Van doninck

Remotely sensed soil moisture proxies with application to modelling the spatial distribution of *Culicoides imicola*

Jasper Van doninck

2013



FACULTEIT BIO-INGENIEURSWETENSCHAPPEN



“It’s only a model”  
Patsy (Terry Gilliam) in  
*Monty Python and the Holy Grail*

**Promotors** **Prof. dr. ir. Niko E. C. Verhoest**  
Department of Forest and Water Management,  
Faculty of Bioscience Engineering, Ghent University

**Prof. dr. Bernard De Baets**  
Department of Mathematical Modelling, Statistics and Bio-  
informatics,  
Faculty of Bioscience Engineering, Ghent University

**Dean** **Prof. dr. ir. Guido Van Huylenbroeck**

**Rector** **Prof. dr. Paul Van Cauwenberge**

JASPER VAN DONINCK

REMOTELY SENSED SOIL MOISTURE PROXIES WITH  
APPLICATION TO MODELLING THE SPATIAL  
DISTRIBUTION OF *CULICOIDES IMICOLA*

Thesis submitted in fulfillment of the requirements for the degree of  
Doctor (PhD) of Applied Biological Sciences



Cover:

Photograph of a random tree in Calabria.

Reference:

J. Van doninck. *Remotely sensed soil moisture proxies with application to modelling the spatial distribution of Culicoides imicola*. PhD thesis, Ghent University, April 2013.

ISBN 978-90-5989-600-0

The author and the promotors give the authorization to consult and to copy parts of this work for personal use only. Every other use is subject to the copyright laws. Permission to reproduce any material contained in this work should be obtained from the author.





# Dankwoord

Ik kreeg ooit het verwijt dat ik nooit op een spontane, normale, vriendelijke manier ‘bedankt’ kan zeggen. Dat zou weleens kunnen kloppen. Maar daarom is het niet minder gemeend.

*Jasper*



# Table of contents

<b>Dankwoord</b>	<b>i</b>
<b>Table of contents</b>	<b>iii</b>
<b>List of figures</b>	<b>vii</b>
<b>List of tables</b>	<b>xiii</b>
<b>List of abbreviations and acronyms</b>	<b>xv</b>
<b>List of symbols and notations</b>	<b>xix</b>
<b>Samenvatting</b>	<b>xxv</b>
<b>Summary</b>	<b>xxvii</b>
<b>1 Introduction</b>	<b>1</b>
<b>Part I: Remotely sensed soil moisture proxies</b>	<b>5</b>
<b>2 Observation of soil moisture patterns through remote sensing</b>	<b>7</b>
2.1 Imaging the earth from space through electromagnetic radiation . . . . .	7
2.1.1 Properties of electromagnetic radiation . . . . .	7
2.1.2 Sources of electromagnetic radiation . . . . .	8
2.1.3 Interaction of electromagnetic radiation with objects . . . . .	10
2.1.4 Atmospheric attenuation . . . . .	12
2.1.4.1 Absorptance . . . . .	12
2.1.4.2 Reflectance . . . . .	12
2.1.5 Influence of surface properties . . . . .	13
2.1.5.1 Visible, near infrared, shortwave infrared . . . . .	13
2.1.5.2 Thermal infrared . . . . .	14
2.1.5.3 Microwaves . . . . .	15
2.2 Remote sensing systems . . . . .	16
2.2.1 Multispectral scanners . . . . .	16
2.2.1.1 Image acquisition principles . . . . .	17
2.2.1.2 Spectral characteristics . . . . .	18

2.2.1.3	Spatial and temporal resolution . . . . .	19
2.2.1.4	Past, present and future missions . . . . .	19
2.2.2	Radar . . . . .	20
2.2.2.1	Image acquisition principles . . . . .	20
2.2.2.2	Spectral characteristics . . . . .	21
2.2.2.3	Spatial and temporal resolution . . . . .	22
2.2.2.4	Past, present and future missions . . . . .	22
2.2.3	Radiometers . . . . .	24
2.2.3.1	Image acquisition principles . . . . .	24
2.2.3.2	Spectral characteristics . . . . .	24
2.2.3.3	Spatial and temporal resolution . . . . .	25
2.2.3.4	Past, present and future missions . . . . .	25
2.3	Soil moisture retrieval . . . . .	25
2.3.1	Multispectral scanners . . . . .	26
2.3.1.1	Empirical relationships and band ratioing . . . . .	26
2.3.1.2	Contextual surface temperature patterns . . . . .	28
2.3.1.3	Temporal surface temperature patterns . . . . .	30
2.3.2	Radar . . . . .	32
2.3.2.1	Physical and semi-empirical models . . . . .	32
2.3.2.2	Empirical and change detection models . . . . .	33
2.3.3	Radiometers . . . . .	35
<b>3</b>	<b>Study site and data collection</b>	<b>37</b>
3.1	Study site . . . . .	37
3.2	Elevation data . . . . .	39
3.3	In situ data . . . . .	39
3.3.1	Soil moisture data . . . . .	39
3.3.1.1	Continuous soil moisture measurements . . . . .	39
3.3.1.2	Field campaign . . . . .	40
3.3.2	Meteorological and pedological data . . . . .	42
3.4	A soil moisture model for Calabria . . . . .	42
3.4.1	Model structure . . . . .	42
3.4.2	Model inputs . . . . .	44
3.4.3	Model validation . . . . .	45
3.5	Remote sensing data . . . . .	50
3.5.1	Optical data . . . . .	50
3.5.2	SAR data . . . . .	50
3.5.3	Low resolution remote sensing soil moisture products . . . . .	50
<b>4</b>	<b>A soil moisture change detection algorithm for ASAR Wide Swath time series</b>	<b>53</b>
4.1	Introduction . . . . .	53
4.2	Study site and data . . . . .	54
4.3	Multitemporal soil moisture retrieval . . . . .	55
4.3.1	Change detection model . . . . .	55

4.3.2	Model parameters . . . . .	56
4.3.3	Vegetation and soil moisture dynamics . . . . .	57
4.4	Seasonality effects on model parameters . . . . .	60
4.4.1	Seasonality effects on $\beta$ . . . . .	60
4.4.2	Seasonality effects on $\sigma_{dry}^0(30^\circ)$ and $S$ . . . . .	63
4.5	Comparison with coarse resolution soil moisture products . . . . .	66
4.6	A further analysis of the influence of seasonality on the angular dependence of backscatter . . . . .	66
4.6.1	Linearity of ASAR angular dependence . . . . .	67
4.6.2	Monthly dynamics of ASAR and ASCAT angular dependence . . . . .	68
4.6.3	Towards high temporal resolution angular normalization of ASAR WS . . . . .	73
4.7	Conclusions . . . . .	76
<b>5</b>	<b>MODIS apparent thermal inertia as a soil moisture indicator</b>	<b>79</b>
5.1	Introduction . . . . .	79
5.2	Study area and datasets . . . . .	80
5.3	Sinusoidal approximation of the diurnal surface temperature cycle	81
5.3.1	Methodology . . . . .	81
5.3.2	Results and validation . . . . .	83
5.4	Apparent thermal inertia and soil moisture patterns over southern Africa . . . . .	85
5.4.1	Spatial <i>ATI</i> patterns . . . . .	86
5.4.2	Temporal <i>ATI</i> patterns . . . . .	88
5.5	Apparent thermal inertia and soil moisture patterns over Calabria .	91
5.6	Conclusions . . . . .	91
<b>6</b>	<b>Contextual surface temperature information as a soil moisture indicator</b>	<b>93</b>
6.1	Introduction . . . . .	93
6.2	Study area and datasets . . . . .	94
6.3	Normalization for terrain elevation . . . . .	95
6.3.1	Normalization approaches . . . . .	95
6.3.2	Results . . . . .	96
6.4	Normalization for terrain orientation . . . . .	100
6.4.1	Normalization approaches . . . . .	100
6.4.2	Results . . . . .	101
6.5	Influence of normalization on the $VI-T_S$ relationship . . . . .	103
6.6	Influence of normalization on soil dryness estimation . . . . .	105
6.6.1	Visual analysis . . . . .	106
6.6.2	In situ soil moisture . . . . .	106
6.7	Conclusions . . . . .	108
<b>7</b>	<b>Soil moisture proxies for species distribution modelling: conclusion</b>	<b>111</b>



---

<b>Part II: Spatial distribution modelling</b>	<b>113</b>
<b>8 Modelling the spatial distribution of <i>C. imicola</i> using climatic and remote sensing data</b>	<b>115</b>
8.1 Introduction . . . . .	115
8.1.1 History of bluetongue virus in the Mediterranean Basin . .	115
8.1.2 <i>Culicoides imicola</i> life cycle and habitat characteristics . .	116
8.1.2.1 Temperature . . . . .	117
8.1.2.2 Soil moisture . . . . .	117
8.1.2.3 Land use/land cover . . . . .	118
8.1.2.4 Topography . . . . .	118
8.1.2.5 Others . . . . .	118
8.1.3 <i>C. imicola</i> distribution modelling . . . . .	118
8.2 Study site and datasets . . . . .	121
8.2.1 <i>Culicoides</i> trapping data . . . . .	121
8.2.2 Climatic data . . . . .	122
8.2.3 Remote sensing data . . . . .	122
8.3 Description of modelling techniques . . . . .	123
8.4 Modelling of <i>C. imicola</i> in Calabria using climatic data . . . . .	124
8.5 Modelling of <i>C. imicola</i> in Calabria using remote sensing data . .	130
8.6 Conclusions . . . . .	132
<b>9 Conclusions and outlook</b>	<b>135</b>
9.1 Remotely sensed soil moisture proxies . . . . .	136
9.2 Spatial distribution modelling . . . . .	138
<b>Bibliography</b>	<b>141</b>
<b>A In situ soil moisture measurements</b>	<b>161</b>

# List of figures

1.1	Overview of the research structure. . . . .	3
2.1	The electromagnetic spectrum (after Lillesand <i>et al.</i> (2004)). . . . .	8
2.2	Spectral distribution of radiant exitance for blackbodies at 6000 K and 300 K. . . . .	9
2.3	Specular versus diffuse reflectance . . . . .	11
2.4	Basic principles of (a) optical sensors, (b) radars, (c) passive microwave sensors, with indication of wavelengths ( $\lambda$ ). . . . .	16
2.5	Across-track scanner characteristics. . . . .	17
2.6	Side-looking radar characteristics. . . . .	21
2.7	Conceptual representation of the trapezoidal VI- $T_S$ space. . . . .	29
3.1	Topography of the study site with indication of meteorological stations (left), land cover (from Corine land cover 2000 (European Environmental Agency, 2002), middle) and soil texture (right) of the Italian region of Calabria. . . . .	38
3.2	Location of in situ sites with sampling setup (inset), main cities and provinces of Vibo Valentia (green) and Crotona (red). . . . .	41
3.3	Processes incorporated in the hydrological model. . . . .	43
3.4	RMSE for interpolated values of temperature (crosses) and precipitation (diamonds) in function of IDW power parameter. . . . .	45
3.5	Validation of modelled soil moisture over 10 cm at 30 in situ sites (dots are site-averaged soil moisture, bars indicate standard deviations), based on meteorological input data of the day itself (a) and with one day time lag (b). . . . .	46
3.6	Validation of modelled soil moisture over 10 cm at in situ sites X1(top), X2 (middle) and X3 (bottom). . . . .	46
3.7	Validation of modelled soil moisture over 30 cm depth at (from top to bottom) Fitterizzi, Mongrassano, Torano, Chiaravalle and Satriano in situ stations. Left column: modelled (thick line) and in situ (blue line) volumetric soil moisture content for the years 2008–2009. Middle column: scatterplot of in situ and modelled soil moisture for the same period. Right column: modelled (thick line) and in situ (blue line) relative soil moisture during the same period. . . . .	49

4.1	Angular correction coefficient $\beta$ for each pixel in the study site (a); dry reference backscatter (b); sensitivity of the backscatter to soil moisture changes, derived as the difference between dry reference and wet reference backscatter (c). . . . .	57
4.2	Temporal behaviour of modelled soil moisture (black line), <i>NDVI</i> (thick green line) and ASAR soil moisture (crosses) for a pixel over arable land (a); scatterplot of modelled soil moisture, averaged over 16 days, and 16-day <i>NDVI</i> for the same pixel (b); scatterplot of modelled soil moisture and ASAR soil moisture for the same pixel (c). . . . .	58
4.3	Temporal behaviour of modelled soil moisture (black line), <i>NDVI</i> (thick green line) and ASAR soil moisture (crosses) for a pixel over deciduous forest (a); scatterplot of modelled soil moisture averaged over 16 days and 16-day <i>NDVI</i> for the same pixel (b); scatterplot of modelled soil moisture and ASAR soil moisture for the same pixel (c). . . . .	59
4.4	Correlation coefficients between modelled soil moisture averaged over 16 days and 16-day <i>NDVI</i> (a) and modelled soil moisture and ASAR soil moisture (b), for each pixel of the study site for the 3-year time series. . . . .	60
4.5	Angular correction coefficient for the summer months $\beta_{\text{summer}}$ (a), winter months $\beta_{\text{winter}}$ (b) and the difference between $\beta_{\text{summer}}$ and $\beta_{\text{winter}}$ (c). . . . .	61
4.6	Angular behaviour of ASAR backscatter for an arable land pixel. Crosses depict observations during summer months, triangles observations during winter months. Linear regression lines for summer and winter are in solid and dashed, respectively. . . . .	62
4.7	Increase in correlation coefficient ( $\Delta R$ ) for the change detection using a seasonal derivation of $\beta$ relative to the method using a fixed $\beta$ for the entire year. . . . .	63
4.8	Box plots of correlation coefficients between modelled soil moisture and ASAR soil moisture using a single angular correction (ASAR), ASAR soil moisture using a seasonal angular correction (ASAR*), TU Wien-EUMETSAT ASCAT surface soil moisture (ASCAT), AMSR-E soil moisture derived using the algorithm developed by Njoku <i>et al.</i> (2003) (AMSR-E NASA) and AMSR-E soil moisture derived using the LPRM of Owe <i>et al.</i> (2008) (AMSR-E LPRM), for all pixels of the respective products over the study site. Crosses indicate the arithmetic means. . . . .	64
4.9	Scatterplot of <i>NDVI</i> and ASAR WS backscatter for a pixel time series over arable land; the size of the dots represents $\Theta_{\text{model}}$ (large dots indicate high moisture levels). Dotted lines represent the average values of the 5% highest, respectively lowest, backscatter coefficients, the full line indicates the vegetation dependence of ASAR WS backscatter at low moisture levels. . . . .	65

4.10	Scatterplot of $\sigma^0(\theta)$ versus $\theta$ for three example pixels, crosses and boxes representing acquisitions during descending and ascending overpasses, respectively, full lines and dashed lines representing linear and quadratic fits, respectively (a). Difference in $R^2$ of quadratic and linear fit for each pixel of the study site (b). Frequency distribution of difference in $R^2$ of quadratic and linear fit (c). . . . .	68
4.11	Slope parameter ( $\beta_{\text{ASAR}}$ ) derived using all available data (a) and seasonal range of slopes derived on monthly basis ( $\Delta\beta_{\text{ASAR}}$ ) (b). Pixels characterized by non-linearity of the angular dependence have been masked. . . . .	70
4.12	Maximum error on normalized backscatter introduced by neglecting seasonal variability of $\beta_{\text{ASAR}}$ (a). Frequency distribution of this maximum error (b). Pixels characterized by non-linearity of the angular dependence have been masked. . . . .	71
4.13	Temporal behaviour of $\bar{\beta}_{\text{ASAR}}$ (full line) and $\hat{\beta}_{\text{ASCAT}}$ (dashed line) for three grid points dominated by (top to bottom) arable land, deciduous forest and mixed landcover (a). $R^2$ between monthly values of $\bar{\beta}_{\text{ASAR}}$ and $\hat{\beta}_{\text{ASCAT}}$ for all grid points of the DGG, blue and red indicating low and high values, respectively (b). Scatterplot of $\hat{\beta}_{\text{ASCAT}}$ and $\bar{\beta}_{\text{ASAR}}$ for all grid points pooled (c). . . . .	72
4.14	Validity of the assumption of temporal stability, expressed as coefficient of determination (a). Frequency distribution of the coefficient of determination (b). Pixels characterized by non-linearity of the angular dependence have been masked. . . . .	75
4.15	$\beta_{\text{ASCAT}}$ (full line), $\hat{\beta}_{\text{ASCAT}}$ (dashed line), $\beta_{\text{ASAR}}$ (dotted line) and $\beta_{\text{ASAR,d}}$ (dashdotted line) for an example ASAR WS pixel over cropland and the nearest ASCAT grid point. . . . .	76
5.1	Left: Two examples of harmonic analysis of phase angle ( $\psi$ ) time series, one with a strong seasonality (top) and one with a weak seasonality (bottom) of $\psi$ . Boxes are estimates of $\psi$ derived for days with four surface temperature observations. The resulting interpolation (full line) is calculated on the checked boxes only. Right: Map of the amplitude of the harmonic term. . . . .	83
5.2	Left: Average $RMSE$ for the year 2009, derived from days with four surface temperature observations. Right: Average $rRMSE$ , derived for the same period. . . . .	85
5.3	Left: MODIS apparent thermal inertia for March 26, 2009, with indication of locations of temporal profiles (Fig. 5.5). Right, top: Number of observations used to derive apparent thermal inertia on March 26, 2009. Right, bottom: VUA-NASA AMSR-E soil moisture for March 26, 2009, interpolated using a 7-day temporal average. . . . .	86

---

5.4	Scatterplot of AMSR-E soil moisture and apparent thermal inertia for March 26, 2009. . . . .	87
5.5	Temporal profiles of MODIS apparent thermal inertia (crosses) and VUA-NASA AMSR-E soil moisture (full line) for 2009. Right axis (AMSR-E soil moisture) has been scaled for each sub-figure separately for clarity. Sub-figures represent desert (a), savannah (b), cropland (c,d), wetland (e) and closed shrubland (f). . . . .	88
5.6	Correlation coefficients between modelled soil moisture and apparent thermal inertia for the entire 2-year time series (a) and for the months April–September in the 2-year time series (b). . . . .	91
6.1	Frequency distribution of $NDVI$ (shaded) and $F_c$ (bold) for the images acquired on July 8 (a), October 8 (b) and December 31 (c) 2009. . . . .	95
6.2	Scatterplots of elevation and land surface temperature on July 8 (a), October 8 (b) and December 31 (c) 2009. Full lines indicate linear regression over the unstratified images; dotted lines are regression lines calculated on fractional vegetation cover strata of 0.1 width. . . . .	97
6.3	Lapse rates derived using the unstratified regression method and the stratified regression method for the days of the year 2009 with sufficient (at least 5000) cloud-free pixels over Calabria. The standard lapse rate of 0.65 K per 100 m is displayed as a horizontal line. . . . .	99
6.4	Determination coefficient between observed surface temperature and surface temperature estimated using coefficients derived from unstratified and stratified regression and elevation (and vegetation index in the case of the stratified regression method) for the days of the year 2009 with sufficient (at least 5000) cloud-free pixels over Calabria. . . . .	100
6.5	Scatterplots of elevation and land surface temperature on July 8 (a), October 8 (b) and December 31 (c) 2009. Full lines indicate linear regression over the unstratified images; dotted lines are regression lines calculated on fractional vegetation cover strata of 0.1 width. . . . .	102
6.6	Scatterplots of $F_c$ and $T_S$ on July 8, derived using unnormalized surface temperature (a), and surface temperature normalized using the standard lapse rate (b), unstratified regression model (c) and stratified regression model (d). Full lines are empirical dry and wet edges. . . . .	103
6.7	Scatterplots of $F_c$ and $T_S$ on October 8, derived using unnormalized surface temperature (a), and surface temperature normalized using the standard lapse rate (b), unstratified regression model (c) and stratified regression model (d). Full lines are empirical dry and wet edges. . . . .	104

---

6.8	Scatterplots of $F_c$ and $T_S$ on December 31st, derived using unnormalized surface temperature (a), and surface temperature normalized using the standard lapse rate (b), unstratified regression model (c) and stratified regression model (d). Full lines are empirical dry and wet edges. . . . .	105
6.9	Temperature Vegetation Dryness Index for October 8, derived using unnormalized surface temperature (a), and surface temperature normalized using the standard lapse rate (b), unstratified regression (c) and stratified regression (d). Missing values indicate cloud cover. . . . .	107
6.10	Validation of the Temperature Vegetation Dryness Index for October 8, derived using unnormalized surface temperature (a), and surface temperature normalized using the standard lapse rate (b), unstratified regression (c) and stratified regression (d), with indication of regression lines and coefficients of determination (all significant at $p=0.05$ ). . . . .	108
8.1	Locations and abundances of <i>C. imicola</i> catches. . . . .	121
8.2	Relative importance of the different variables in the RF model based on climatic data. . . . .	127
8.3	Predicted probabilities of <i>C. imicola</i> and percentage of misclassifications at absence and presence sites, based on climatic data (left) and remotely sensed data (right). . . . .	128
8.4	Total precipitation for the month of May in the WorldClim (Hijmans <i>et al.</i> , 2005) dataset (a) and multiyear averaged MODIS <i>NDVI</i> for the month July(b). . . . .	129
8.5	Relative importance of the different variables in the RF model based on standard Aqua MODIS products. . . . .	131



# List of tables

2.1	Radar band designations (Lillesand <i>et al.</i> , 2004). . . . .	22
3.1	MODIS products used in this study ('MxD' stands for 'MOD' and MYD', indicating Terra and Aqua products, respectively, 'MCD' indicates combined products). . . . .	50
6.1	Slopes of regression lines between elevation and land surface temperature, given different fractional vegetation cover stratum widths. Missing values indicate strata with fewer than 500 pixels and are not included in further analysis. $F_c$ values larger than 1 are used for the unstratified image but not for the different stratum widths. . . . .	97
6.2	Slopes of regression lines between illumination ( $\cos(i)/\cos(z)$ ) and land surface temperature, given different fractional vegetation cover stratum widths. Missing values indicate strata with fewer than 500 pixels and are not included in further analysis. $F_c$ values larger than 1 are used for the unstratified image but not for the different stratum widths. . . . .	102
8.1	Accuracy measures of <i>C. imicola</i> distribution models (using random forests or linear discriminant analysis) for different input datasets. . . . .	125
8.2	Relative importance of the different variables ( $\times 100$ ) in the RF model based on climatic data. . . . .	127
8.3	Relative importance of the different variables ( $\times 100$ ) in the RF model based on standard Aqua MODIS products. . . . .	131





## List of abbreviations and acronyms

AMSR-E	Advanced Microwave Scanning Radiometer - Earth Observing System
AP	Alternating Polarization mode of ASAR
ARPACAL	Agenzia Regionale per la protezione dell' Ambiente della Calabria
ARSSA	Agenzia Regionale per lo Sviluppo e per i Servizi in Agricoltura
ASAR	Advanced Synthetic Aperture Radar
ASCAT	Advanced Scatterometer
AVHRR	Advanced Very High Resolution Radiometer
BTV	bluetongue virus
DEM	digital elevation model
DGG	discrete global grid
DORIS	Doppler Orbitography and Radiopositioning Integrated by Satellite
Envisat	Environmental Satellite
EROS	Earth Resources Observation and Science
ERS	European Remote Sensing
ESA	European Space Agency
EUMETSAT	European Organisation for the Exploitation of Meteorological Satellites
GM	Global Monitoring mode of ASAR
GMES	Global Monitoring for Environment and Security
GPS	Global Positioning System
H	horizontal polarization

HCMM	Heat Capacity Mapping Mission
IDW	inverse distance weighing
IEM	Integral Equation Model
IFOV	instantaneous field of view
IM	Image mode of ASAR
IR	infrared
JAXA	Japan Aerospace Exploration Agency
LDA	linear discriminant analysis
LP DAAC	Land Processes Distributed Active Archive Center
LPRM	Land Parameter Retrieval Model
MERIS	Medium Resolution Imaging Spectrometer
MetOp	Meteorological Operational satellite programme
MIRAS	Microwave Imaging Radiometer with Aperture Synthesis
MODIS	Moderate Resolution Imaging Spectroradiometer
NASA	National Aeronautics and Space Administration
NEST	Next ESA SAR Toolbox
NIR	near infrared
NOAA	National Oceanic and Atmospheric Administration
radar	radio detection and ranging
RF	random forests
RFI	radio frequency interference
ROC	Receiver Operating Characteristic
SAR	synthetic aperture radar
SLR	side looking radar
SMAP	Soil Moisture Active and Passive
SMOS	Soil Moisture and Ocean Salinity
SRTM	Shuttle Radar Topography Mission
SWIR	shortwave infrared
TDR	time-domain reflectometer

TI	thermal inertia
TIR	thermal infrared
TU Wien	Technische Universität Wien (Vienna University of Technology)
USDA	United States Department of Agriculture
UTC	Coordinated Universal Time
UV	ultraviolet
V	vertical polarization
VI	vegetation index
VUA	Vrije Universiteit Amsterdam
WS	Wide Swath mode of ASAR
WV	Wave mode of ASAR



# List of symbols and notations

$\cdot_i$	value at location or time $i$ of a parameter as defined in the text
$\cdot_{\max}$	maximum value over space or time of a parameter as defined in the text
$\cdot_{\min}$	minimum value over space or time of a parameter as defined in the text
$\alpha(\lambda)$	spectral absorptance [-]
$\alpha_0$	surface albedo [-]
$\beta$	angular correction coefficient [dB deg <sup>-1</sup> ]
$\bar{\beta}_{\text{ASAR}}$	spatial averaged angular correction coefficient for ASAR [dB deg <sup>-1</sup> ]
$\hat{\beta}_{\text{ASAR}}$	temporally averaged angular correction coefficient for ASCAT [dB deg <sup>-1</sup> ]
$\Gamma$	day angle [rad]
$\delta$	solar declination [rad]
$\partial$	partial derivative operator
$\Delta$	difference operator
$\varepsilon(\lambda)$	spectral emissivity [-]
$\varepsilon_0$	error term
$\theta$	incidence angle [rad]
$\Theta$	soil moisture content [m <sup>3</sup> m <sup>-3</sup> ]
$\Theta_{\text{dry}}$	soil moisture content at air dryness [m <sup>3</sup> m <sup>-3</sup> ]
$\Theta_{\text{fc}}$	soil moisture content at field capacity [m <sup>3</sup> m <sup>-3</sup> ]

$\Theta_{\text{sat}}$	soil moisture content at saturation [ $\text{m}^3 \text{m}^{-3}$ ]
$\Theta_{\text{ASAR}}$	ASAR-derived relative soil moisture content [-]
$\Theta_{\text{model}}$	modelled relative soil moisture content [-]
$\kappa$	Kappa index of agreement [-]
$\lambda$	wavelength [m]
$\nu$	frequency [Hz]
$\pi$	ratio of circle circumference to diameter ( $\approx 3.1415$ )
$\rho(\lambda)$	spectral reflectance [-]
$\rho_{\text{NIR}}$	reflectance in the near infrared part of the spectrum [-]
$\rho_{\text{red}}$	reflectance in the red part of the spectrum [-]
$\rho_{\text{SWIR}}$	reflectance in the shortwave infrared part of the spectrum [-]
$\sigma$	Stefan-Boltzmann constant ( $=5.670 \times 10^{-8} \text{W m}^{-2} \text{K}^{-4}$ )
$\sigma^0$	backscatter coefficient [dB]
$\sigma_{\text{dry}}^0$	dry reference backscatter [dB]
$\sigma_{\text{wet}}^0$	wet reference backscatter [dB]
$\sigma'$	first derivative of $\sigma^0$ with respect to $\theta$ [dB deg $^{-1}$ ]
$\sigma''$	second derivative of $\sigma^0$ with respect to $\theta$ [dB deg $^{-2}$ ]
$\tau(\lambda)$	spectral transmittance [-]
$\tau_{\text{atm}}$	atmospheric transmittance in the visible spectrum [-]
$\nu$	longitude [rad]
$\varphi$	latitude [rad]
$\chi$	drainage characteristic [-]
$\psi$	phase angle [rad]
$\omega$	angular velocity of rotation of the earth [rad s $^{-1}$ ]
$A$	diurnal surface temperature amplitude [K]
$A_1, A_2$	coefficients of Fourier series [-]
$ATI$	apparent thermal inertia [K $^{-1}$ ]

---

$AUC$	area under the ROC curve [-]
$c$	velocity of light ( $=3 \times 10^8 \text{ m s}^{-1}$ )
$C$	solar correction factor [-]
$D$	depth of soil moisture simulation [m]
$e$	Euler's number ( $\approx 2.7183$ )
$E_0$	amplitude of the electric field [ $\text{N C}^{-1}$ ]
$E_A$	absorbed energy [ $\text{W m}^{-2}$ ]
$E_I$	incident energy [ $\text{W m}^{-2}$ ]
$E_R$	reflected energy [ $\text{W m}^{-2}$ ]
$E_T$	transmitted energy [ $\text{W m}^{-2}$ ]
$ET$	evapotranspiration [ $\text{mm day}^{-1}$ ]
$ET_p$	potential evapotranspiration [ $\text{mm day}^{-1}$ ]
$F_c$	fractional vegetation cover [-]
$G$	ground heat flux [ $\text{W m}^{-2}$ ]
$h$	Planck constant ( $=6.626 \times 10^{-34} \text{ J s}$ )
$H$	elevation above sea level [m]
$i$	solar incidence angle [rad]
$I$	infiltration [ $\text{mm day}^{-1}$ ]
$J$	sensible heat flux [ $\text{W m}^{-2}$ ]
$k$	Boltzmann constant ( $=1.381 \times 10^{-23} \text{ J K}^{-1}$ )
$K_r$	reduction constant [-]
$K_{\text{sat}}$	saturated hydraulic conductivity [ $\text{mm day}^{-1}$ ]
$L$	day length [hours]
$LE$	latent heat flux [ $\text{W m}^{-2}$ ]
$M$	total radiant exitance [ $\text{W m}^{-2}$ ]
$M(\lambda)$	spectral radiant exitance [ $\text{W m}^{-2} \text{ m}^{-1}$ ]
$n$	number of data points [-]
$n_d$	day number [-]
$NDVI$	Normalized Difference Vegetation Index [-]



<i>NDWI</i>	Normalized Difference Water Index [-]
<i>O</i>	runoff [mm day <sup>-1</sup> ]
<i>p</i>	p-value in statistical significance testing [-]
<i>P</i>	precipitation intensity [mm day <sup>-1</sup> ]
<i>PCC</i>	percentage correctly classified [%]
<i>Q</i>	percolation to deeper soil layer [mm day <sup>-1</sup> ]
<i>R</i>	correlation coefficient [-]
<i>R<sup>2</sup></i>	determination coefficient [-]
<i>R<sub>n</sub></i>	net radiation [W m <sup>-2</sup> ]
<i>RMSE</i>	root mean square error
<i>rRMSE</i>	relative root mean square error [-]
<i>S</i>	sensitivity of backscatter to changes in soil moisture [dB]
<i>S<sub>0</sub></i>	solar constant (1367 W m <sup>-2</sup> )
<i>SEE</i>	standard error of estimate
<i>t</i>	time [s]
<i>T</i>	temperature [K]
$\overline{T_S}$	diurnal average surface temperature [K]
<i>T<sub>s</sub></i>	kinetic (remotely sensed) surface temperature [K]
<i>T<sub>s,dry</sub></i>	surface temperature at dry conditions [K]
<i>T<sub>s,wet</sub></i>	surface temperature at saturated conditions [K]
<i>TI</i>	thermal inertia [J m <sup>2</sup> s <sup>1/2</sup> K <sup>-1</sup> ]
<i>TVDI</i>	Temperature-Vegetation Dryness Index [-]
<i>W</i>	Wien's displacement constant (=2.898 × 10 <sup>-3</sup> mK)
<i>z</i>	solar zenith angle [rad]





# Samenvatting

Informatie over ruimtelijke of temporele bodemvochtpatronen is vereist als input in de modellering van processen of fenomenen in een ruime waaier van toepassingsdomeinen. Een van deze domeinen is het modelleren van de ruimtelijke verspreiding van *Culicoides imicola*, een insect dat als vector optreedt in de overdracht van verschillende pathogenen, waaronder het blauwtongvirus. Alle onvolwassen stadia van de levenscyclus van dit insect ontwikkelen zich in de bovenste paar centimeter van de bodem. Het bodemvochtgehalte in deze laag wordt dan ook verondersteld de ruimtelijke verspreiding van *C. imicola* te beïnvloeden. Ruimtelijke verschillen in bodemvocht worden, bijvoorbeeld, algemeen geacht het patroon van de verspreiding van *C. imicola* te bepalen in Calabrië, Italië. De soort komt hier voor aan de oostkust van het schiereiland, maar is afwezig aan de westelijke zijde. Tot op heden werd informatie omtrent bodemvocht echter niet rechtstreeks geïntegreerd in ruimtelijke verspreidingsmodellen voor deze soort. Een van de redenen hiervoor is dat het opmeten van bodemvocht door middel van veldwaarnemingen duur en tijdrovend is, en dus ongeschikt om te gebruiken op de schaal vereist voor verspreidingsmodellen. Teledetectie door satellieten laat wel toe om processen aan het aardoppervlak waar te nemen met geschikte ruimtelijke en temporele resolutie. Observatie van processen of toestandsvariabelen onder het aardoppervlak, zoals bodemvochtgehalte, is echter niet evident.

Verscheidene satellieten verzamelen data in het zichtbare, nabij-infrarode en thermisch infrarode deel van het elektromagnetisch spectrum. Analyse van ruimtelijke en/of temporele patronen in beelden genomen door deze satellieten leverde in eerder onderzoek reeds informatie op over evapotranspiratie of het daaraan gekoppelde bodemvochtgehalte. Twee technieken die gebruik maken van deze databronnen werden verder onderzocht in dit proefschrift. De eerste techniek bekomt informatie over het ruimtelijke patroon van evapotranspiratie of bodemvocht uit de analyse van contextuele informatie van een vegetatie-index en oppervlaktetemperatuur. De tweede relateert verschillen in de dagelijkse amplitude van de oppervlaktetemperatuur aan temporele variaties in thermische inertie of bodemvochtgehalte. Beide technieken slaagden erin bepaalde ruimtelijke of temporele verschillen in bodemvocht te detecteren. Hun toepasbaarheid bleek echter wel beperkt te zijn door een aantal factoren zoals het seizoen of de bedekking van de bodem door vegetatie. Bovendien zijn technieken die gebruik maken van data in het zichtbare en infrarode deel van het spectrum ongeschikt onder bewolkte omstandigheden.

Door gebruik te maken van informatie in het microgolfdomein van het elektromagnetisch spectrum kunnen mogelijk betere bodemvochtschattingen bekomen worden. Microgolven uitgezonden door een *synthetic aperture radar* (SAR) dringen doorheen eventuele wolken, alsook door de bovenste bodemlaag. De fractie van de uitgezonden straling die terugkaatst naar de sensor is indicatief voor het vochtgehalte van de bodem. De sterkte van het waargenomen signaal wordt echter ook beïnvloed door bodemruwheid en door vegetatie. De invloed van deze twee factoren kan deels uitgeschakeld worden door gebruik te maken van *change detection* technieken. Hierbij worden temporele verschillen in radar terugkaatsing gerelateerd aan verschillen in bodemvochtgehalte. Deze studie valideerde een dergelijk *change detection* algoritme voor een driejarige tijdsreeks van SAR beelden van Calabrië. De aldus verkregen bodemvochtschatting bleek gecorreleerd te zijn met gemodelleerd bodemvochtgehalte, doch eerder beperkt in gebieden met dichte vegetatie. Operationele SAR bodemvochtproducten gegenereerd door deze methodes kunnen de volgende jaren verwacht worden, eens de nodige datasets beschikbaar worden. Ondanks de goede resultaten behaald met deze *change detection* techniek bleken seizoensale verschillen in vegetatiebedekking de nauwkeurigheid van de bodemvochtschattingen te verminderen. Jaarlijkse variaties in vegetatie bleken de afhankelijkheid van de terugkaatsing op de invalshoek van het microgolfsignaal te beïnvloeden. In deze studie werd echter een multitemporele benadering voorgesteld die in staat bleek om deze seizoenaliteit te compenseren.

Het laatste deel van dit proefschrift behandelt de modellering van de ruimtelijke verspreiding van *C. imicola*. Verschillende modelleringstechnieken werden hiervoor reeds gebruikt, doch weinig studies vergeleken de prestaties van verschillende modellen. *Random forests*, een recente ensemble *machine learning* techniek, werd hier vergeleken met de vaak gebruikte lineaire discriminantanalyse. Verspreidingsmodellen gebaseerd op *random forests* bleken in staat om de aanwezigheid van het insect beter te voorspellen dan deze gebaseerd op lineaire discriminantanalyse. Als verklarende variabelen worden in *C. imicola* verspreidingsmodellen gebruikelijk ofwel klimatologische data ofwel data uit teledetectie gebruikt, of een combinatie van beide. Deze studie onderzoekt de nauwkeurigheid die bekomen wordt door klimatologische variabelen, dan wel vrij beschikbare teledetectievariabelen, te gebruiken. Er werd aangetoond dat klimatologische variabelen kunnen vervangen worden door data uit teledetectie, tegen de kost van een beperkt doch significant verlies in nauwkeurigheid. Dit biedt de mogelijkheid om deze ruimtelijke verspreidingsmodellen toe te passen over gebieden waar de kwaliteit van klimatologische data onbetrouwbaar is door de afwezigheid van meteorologische stations, of in regio's waar klimaatsverandering mogelijk verantwoordelijk is voor een uitbreiding van het leefgebied van *C. imicola*. Tot slot werd onderzocht of het toevoegen van de eerder berekende bodemvochtschattingen als verklarende variabelen de nauwkeurigheid van de ruimtelijke verspreidingsmodellen verbeterde.

## Summary

Information on the spatial or temporal pattern of soil moisture is required in modelling studies over a wide variety of domains. One of these domains is the modelling of the spatial distribution of *Culicoides imicola*, an insect vector of several pathogens, including the bluetongue virus. Since all the immature stages of this insect's life cycle occur in the top few centimetres of the soil, the moisture content in this soil layer is expected to constrain the spatial distribution of *C. imicola*. Spatial soil moisture differences are assumed to be responsible for the pattern of *C. imicola* occurrence in Calabria, Italy, where it is present at the eastern coast but absent at the western coast. Until now, however, information on soil moisture has not yet been integrated in spatial distribution models for this species. Acquisition of soil moisture through ground measurements is costly and time-consuming, and hence impractical for application at the spatial and temporal scales required in species distribution modelling. Satellite remote sensing does allow the observation of processes at the earth's surface at various spatial and temporal scales. Observation of sub-surface state variables such as soil moisture content is, however, not straightforward.

Several spaceborne sensors collect data in the visible, near infrared and thermal infrared part of the electromagnetic spectrum, with spatial and temporal resolutions allowing integration in *C. imicola* distribution models. Analysis of spatial and/or temporal patterns in images acquired at these wavelengths has previously yielded information on evapotranspiration or soil moisture content. Two techniques integrating these types of datasets were further investigated in this dissertation: one technique relating contextual patterns of surface temperature and a vegetation index to evapotranspiration or soil moisture content, the other relating the daily surface temperature amplitude to soil thermal inertia or soil moisture. Both techniques were able to detect certain spatial or temporal soil moisture changes, respectively. Their applicability was, however, found to be restricted by, amongst others, season and vegetation cover. Furthermore, satellite remote sensing in the visible and infrared wavelengths can be severely hampered by cloud cover.

Improved soil moisture retrieval can be expected when using information obtained in the microwave part of the electromagnetic spectrum. The microwave radiation emitted by a synthetic aperture radar (SAR) can penetrate cloud cover and even the top layer of the soil. The fraction of radiation reflected back to the sensor, called backscatter, is proportional to the surface soil moisture content. SAR

backscatter is, however, also influenced by vegetation cover and surface roughness. One way to eliminate these latter two influences is by employing a change detection approach, where temporal changes in surface backscatter are related to changes in soil moisture. This study validated a change detection soil moisture algorithm for a 3-year time series of SAR data over Calabria. The remotely sensed soil moisture product was found to be correlated to modelled soil moisture, although only moderately over densely vegetated terrain. Operational soil moisture products from SAR, generated by change detection approaches, are therefore within reach once large SAR datasets become available the following years. Despite the strong performance of the SAR change detection technique, seasonally changing vegetation was observed to influence the accuracy of soil moisture predictions. Vegetation phenology was found to influence the dependence of SAR backscatter on the incidence angle of the microwave signal. A multitemporal approach developed in this study was, however, able to account for this seasonal variability.

The final part of this dissertation focuses on the modelling of the spatial distribution of *C. imicola*. During the past decades, several modelling techniques have been used to this end, but few studies compared different techniques. Here, a novel ensemble machine learning technique called random forests is compared to the established linear discriminant analysis. Species distribution models based on random forests were found to be superior to those based on linear discriminant analysis. Species distribution modelling is usually performed using as predictive variables either climatic data, remotely sensed data or both. This study investigated the performance of models based on climatic variables versus those using remotely sensed variables. It was shown that climatic variables could be replaced by routinely produced and freely available remotely sensed data, with only a limited, though significant, decrease in prediction accuracies. This offers opportunities for the application of species distribution models in regions where climate data is unreliable due to the absence of meteorological stations, or in regions where climate change allows the range of *C. imicola* to expand. Finally, it was investigated whether the inclusion of remotely sensed soil moisture products as predictive variables increased the accuracy of the spatial distribution modelling.

# 1

## Introduction

Soil moisture is one of the key parameters in the global energy and water balance at the interface between the atmosphere and the land surface, through its control on evapotranspiration. Evapotranspiration, the sum of surface evaporation and plant transpiration, is the process through which water at the land surface is returned to the atmosphere. The solar energy used in this process can no longer be used for the heating of the land surface and the near-surface atmosphere. Spatially and temporally distributed soil moisture information is therefore required in many weather and climate models (Dirmeyer, 2000; Albergel *et al.*, 2010). Furthermore, information on soil moisture is used in a wide variety of domains, ranging from flood forecasting (e.g. Javelle *et al.*, 2010), over agricultural applications (e.g. Bolten *et al.*, 2010; McNairn *et al.*, 2012) to pest control (e.g. Liu *et al.*, 2008).

The most basic techniques for obtaining information on the spatiotemporal behaviour of soil moisture are in situ measurements, by ground sampling or electronic probing. Although these techniques allow an accurate derivation of the gravimetric or volumetric soil moisture content at the sampling point, their limitations are evident. In situ techniques only provide point measures, while operational applications mostly demand spatially distributed soil moisture information. The spatial variability of soil moisture can be large due to variations in topography or soil type. Representative area-wide estimates can thus only be obtained from many individual in situ observations. The cost associated with in situ observations makes that they are only useful in small scale applications. Alternatively, soil moisture can be modelled based on a conceptual framework (e.g.



Sheikh *et al.*, 2009) when sufficient meteorological, topographical, pedological and/or other datasets are available. The availability of these datasets, however, is the Achilles' heel of these models, rendering them useless in regions where one or more of them are unavailable.

Remote sensing from planes or satellites provides alternative means of repeatedly observing hydrological state variables over large areas. Today, several operational products provide global soil moisture estimates at near-daily frequency (Wagner *et al.*, 1999b; Njoku *et al.*, 2003; Owe *et al.*, 2008; Naeimi *et al.*, 2009). These products have in common that they are obtained from remote sensing data with a coarse spatial resolution, in the order of tens of kilometres, restricting their applicability to global or continental-scale applications. At the other end of spectrum, significant efforts have been made to obtain remotely sensed soil moisture at resolutions in the order of a metre (e.g. Lievens and Verhoest, 2011). Techniques developed for applications at these resolution, however, often demand controlled conditions, e.g. an absent or invariant vegetation cover of the terrain under investigation, and/or ancillary in situ datasets.

In between these extremes, many applications require information on soil moisture at intermediate spatial resolution (from tens of metres to a kilometre) over extents of several hundreds of kilometres. At this scale, landcover is often heterogeneous and the acquisition of ancillary in situ datasets is costly. The research presented here is situated in this context, and aims at deriving remotely sensed soil moisture-related information at approximately 1 km resolution, without requiring specific ancillary datasets. To this end, different sources of remote sensing products are used. This research aims at deriving soil moisture proxies, or indices that are related to spatial or temporal soil moisture patterns, rather than absolute gravimetric or volumetric soil moisture content. These soil moisture products are sufficient for many applications.

One field in which soil moisture proxies are expected to be useful is the distribution modelling of the *Culicoides imicola* biting midge. This species is the major vector of the bluetongue virus in Mediterranean Europe and Africa (Mellor *et al.*, 2000) and is a vector of several other viruses. A detailed knowledge of the spatial distribution of this species can thus assist in curtailing the spread of bluetongue. Soil moisture is one of the factors generally assumed to restrict the spatial distribution of *C. imicola*, since all immature stages of the species can be found in the top few centimetres of the soil. Until now, however, information on soil moisture has not yet been integrated in *C. imicola* distribution models, or only indirectly through variables assumed to be related to soil moisture. Part of this research therefore investigates whether the soil moisture proxies retrieved here can be used

to improve the species distribution modelling for the Italian region of Calabria.

This dissertation is divided into two main parts (Fig. 1.1). The first, and largest, part deals with the derivation of remotely sensed soil moisture proxies and starts with a general overview of the principles of spaceborne remote sensing and an introduction of soil moisture retrieval through remote sensing (Chapter 2). Chapter 3 introduces the study site and the remote sensing and ancillary datasets used in this study. A soil moisture model for Calabria is also discussed in this chapter. The following chapters, (4, 5 and 6) are parallel chapters discussing different techniques to derive soil moisture proxies from different types of remotely sensed imagery. Chapter 7 provides a brief discussion on the anticipated utility of these soil moisture proxies for species distribution modelling. The smaller second part of the document is dedicated to the species distribution modelling. This part consists of a single chapter (Chapter 8), in which different sources of information from which *C. imicola* distribution can be modelled are compared. Finally, Chapter 9 summarizes the conclusions of this research and discusses open issues and pathways for further research.

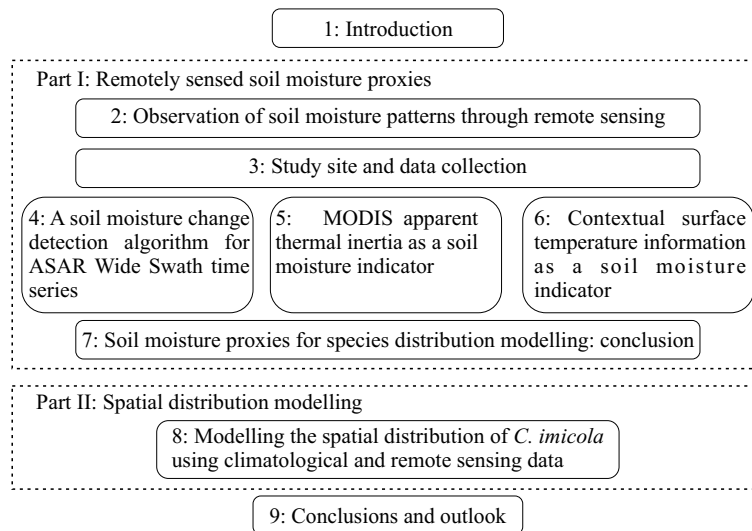


Figure 1.1: Overview of the research structure.

The research presented here was initiated in the framework of the EPIDE-MOIST (Improving epidemiological modelling using satellite derived soil moisture proxies) project (project number SR/02/124) funded by the STEREO II programme of the Belgian Science Policy (BELSPO). This 2-year project was a collaboration between different research groups of Ghent University and a private

partner (Avia-GIS), and its goal was twofold. The first aim was to investigate whether machine learning techniques could replace the popular and frequently used statistical methods in species distribution modelling. The second objective was to validate a number of operationally derivable remote sensing products that could act as a proxy for soil moisture. Additional funding allowing the completion of the doctoral research was granted by the Research Foundation Flanders (FWO) as part of the project G.0837.10, and by the Special Research Fund (BOF) of Ghent University.

Part I:

Remotely sensed soil moisture proxies



# 2

## Observation of soil moisture patterns through remote sensing

### 2.1 Imaging the earth from space through electromagnetic radiation

Remote sensing can be described as the technique of acquiring information on an object or phenomenon through a device without making any physical contact with the object or phenomenon under investigation. Probably the most familiar remote sensing device, though not always perceived that way, is the human eye. The eye allows humans to detect objects at a distance thanks to the visible light originating from the sun, a lamp or another light source that is reflected on the objects and directed towards the eye. Unlike the human eye, man-made remote sensing devices can be constructed to detect a much wider range of forms of radiation or energy than merely visible light. Some of these well-known forms of radiation are ultraviolet (UV) and infrared (IR) waves, heat, microwaves and radio waves. All these forms of energy are in essence very similar and have in common that they are all types of electromagnetic waves.

#### 2.1.1 Properties of electromagnetic radiation

In accordance with wave theory, electromagnetic energy can be described as a harmonic, sinusoidal electric field and a perpendicular magnetic field, propagating in a direction perpendicular to these two fields at the velocity of light ( $c = 3 \times 10^8 \text{ms}^{-1}$ ). The most common property to categorize electromagnetic waves, al-

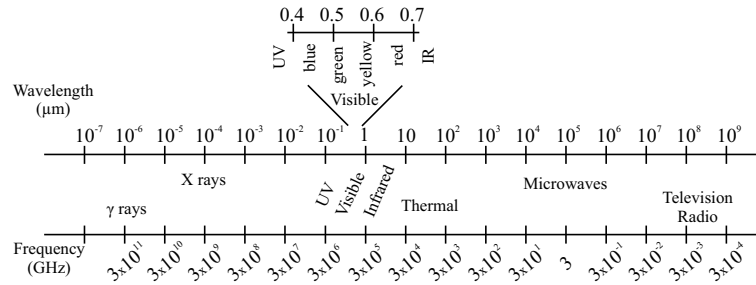


Figure 2.1: The electromagnetic spectrum (after Lillesand *et al.* (2004)).

lowing to situate the wave in the electromagnetic spectrum (Fig. 2.1), is the wavelength or frequency (Lillesand *et al.*, 2004). The wavelength  $\lambda$  is the distance between two successive peaks of the sinusoidal wave, and is typically expressed in units as a fraction of a metre (from nm over  $\mu\text{m}$  to cm and beyond). The frequency  $\nu$  is the number of sinusoidal wave cycles passing a fixed point per unit of time and is expressed in Hertz (Hz or, often, in GHz). Wavelength and frequency are related through the velocity of light as:

$$c = \nu\lambda . \quad (2.1)$$

A second property of an electromagnetic wave, or any sinusoidal function, is its amplitude. The amplitude is an indicator of the amount of energy contained in the wave. Although electromagnetic waves are composed of both an electric field and a magnetic field, it is common to consider only the amplitude of the electric field in remote sensing applications, since only this field is altered when electromagnetic waves interact with natural substances (Woodhouse, 2006).

A last property is the polarization of the electromagnetic wave. The polarization defines the plane, perpendicular to the direction of propagation, in which the wave oscillates (Woodhouse, 2006). As will be discussed later, polarization is mainly considered in radar applications. Two specific conditions of polarization can however be mentioned here: when the vibrations of the electric field are either in a plane horizontal to the earth's surface, or in a plane vertical to the surface. Not surprisingly, these specific conditions are termed horizontal polarization and vertical polarization, respectively.

## 2.1.2 Sources of electromagnetic radiation

As mentioned earlier, the sun or a lighting bulb are sources of electromagnetic energy. However, the surface of each object, or body, with a temperature above the absolute zero (0K or  $-273,15^\circ\text{C}$ ) radiates electromagnetic waves. The amount of energy that is radiated by a body, or the total radiant exitance  $M$  [ $\text{W m}^{-2}$ ], is

expressed by the Stefan-Boltzmann law:

$$M = \sigma T^4, \quad (2.2)$$

where  $\sigma$  is the Stefan-Boltzmann constant ( $5.670 \times 10^{-8} \text{ W m}^{-2} \text{ K}^{-4}$ ) and  $T$  is the temperature of the body [K]. Not only does the total energy emitted by an object change as a function of its temperature, so does the spectral distribution of the emitted energy. The total radiant exitance of a body in a specific wavelength  $M(\lambda)$  [ $\text{W m}^{-2} \text{ m}^{-1}$ ] is expressed by Planck's Law:

$$M(\lambda) = \frac{2hc^2}{\lambda^5} \frac{1}{e^{\frac{hc}{\lambda kT}} - 1}, \quad (2.3)$$

with  $h$  the Planck constant ( $6.626 \times 10^{-34} \text{ J s}$ ) and  $k$  the Boltzmann constant ( $1.381 \times 10^{-23} \text{ JK}^{-1}$ ).

It should be noted that Eqs. 2.2 and 2.3 are only valid for a blackbody, i.e. a theoretical, ideal radiator that absorbs and reemits all energy incident upon it. Real materials, however, only approach this ideal behaviour and emit only a fraction of the energy emitted by a blackbody of the same temperature. This fraction is function of the material, as well as wavelength specific, and called the material's emissivity ( $\epsilon(\lambda)$ , [-]):

$$\epsilon(\lambda) = \frac{\text{radiant exitance of an object at } T}{\text{radiant exitance of a blackbody at } T}. \quad (2.4)$$

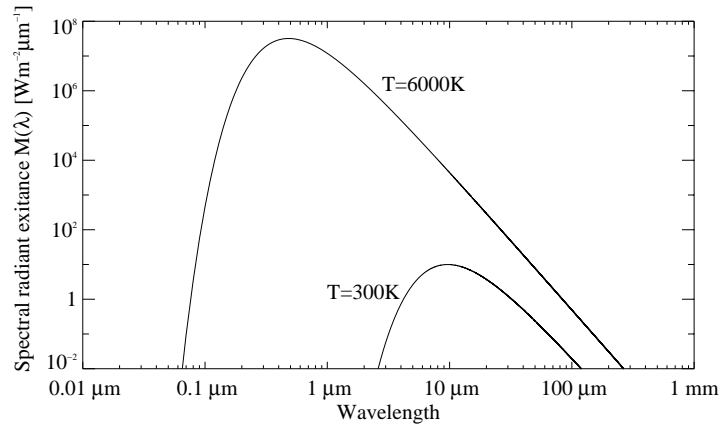


Figure 2.2: Spectral distribution of radiant exitance for blackbodies at 6000 K and 300 K.



The temperature of the sun is approximately 6000 K, that of the earth's surface approximately 300 K. The spectral radiant exitance  $M(\lambda)$  for blackbodies at these temperatures is given in Fig. 2.2. It is observed that the energy emitted by the sun is over all wavelengths higher than the earth's and that the peak of the solar radiant exitance is shifted towards the shorter wavelengths. For a given temperature, the spectral radiance as defined by Eq. 2.3 peaks at a wavelength  $\lambda_{\max}$  defined by Wien's displacement law:

$$\lambda_{\max}(T) = \frac{W}{T}, \quad (2.5)$$

where  $W$  is Wien's displacement constant ( $2.898 \times 10^{-3}$  mK). Given the peak of solar radiant exitance in the visible and adjacent wavelengths (around  $0.5 \mu\text{m}$ ), many remote sensing instruments capturing the solar energy reflected by the earth will be designed to operate in this part of the electromagnetic spectrum. Sensors aiming at recording radiation emitted by the earth itself can observe the highest amount of energy at wavelengths around  $10 \mu\text{m}$ .

### 2.1.3 Interaction of electromagnetic radiation with objects

When electromagnetic energy, emitted by the sun or another source, with a wavelength  $\lambda$  is incident on body, the incident energy ( $E_I(\lambda)$ , [ $\text{W m}^{-2}$ ]) is either absorbed, transmitted or reflected (also termed 'scattered'), where these three components sum up to the total incident energy (Lillesand *et al.*, 2004). The way in which incident energy is split into absorbed energy ( $E_A(\lambda)$ ), transmitted energy ( $E_T(\lambda)$ ) and reflected energy ( $E_R(\lambda)$ ), all in  $\text{W m}^{-2}$ , is determined both by the properties of the body and by the wavelength itself. When ratioing these three components into which incident energy is split, the spectral absorptance ( $\alpha(\lambda)$ , [-]), reflectance ( $\rho(\lambda)$ , [-]) and transmittance ( $\tau(\lambda)$ , [-]) are obtained (Lillesand *et al.*, 2004):

$$\alpha(\lambda) = \frac{E_A(\lambda)}{E_I(\lambda)} \quad \rho(\lambda) = \frac{E_R(\lambda)}{E_I(\lambda)} \quad \tau(\lambda) = \frac{E_T(\lambda)}{E_I(\lambda)}, \quad (2.6)$$

so that

$$\alpha(\lambda) + \rho(\lambda) + \tau(\lambda) = 1. \quad (2.7)$$

According to Kirchhoff's radiation law, a body's spectral absorptance equals its spectral emissivity:

$$\alpha(\lambda) = \varepsilon(\lambda). \quad (2.8)$$

For opaque bodies ( $\tau(\lambda) = 0$ ), such as the earth's land surface, combining Eqs. 2.7 and 2.8 defines the relationship between spectral reflectance and spectral emissivity:

$$\varepsilon(\lambda) + \rho(\lambda) = 1. \quad (2.9)$$

Apart from the amount of incident radiation that is reflected or scattered, the direction in which it is reflected is also of importance, since only the part of the radiation reflected towards the sensor can be captured. In this respect, a distinction is made between specular reflection and diffuse (or Lambertian) reflection, with gradations between these extremes (Fig. 2.3). Specular reflection is the mirrorlike behaviour that can be observed, in the visible spectrum, in the reflection of the sun on a flat water surface or polished piece of metal. The incoming radiation is here reflected under an angle equal to the angle of incidence. Conversely, diffuse reflectors reflect uniformly to all angles, as for example a dry soil, again in the visible wavelengths. In reality, however, most objects will display a behaviour somewhere in between specular and diffuse reflectance.

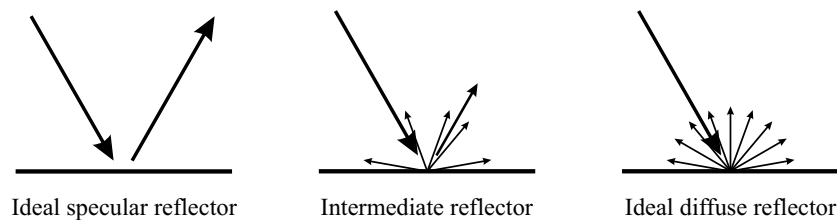


Figure 2.3: Specular versus diffuse reflectance

The geometric character of reflectance on a medium or surface is also described in terms of roughness, where rough surfaces exhibit a more diffuse reflection and smooth surfaces a specular reflection. It should be noted that roughness is dependent on the wavelength of the incident radiation, so that a surface can be rough with respect to shortwave visible or infrared radiation, but smooth with respect to microwave radiation.

A final remark concerning scattering is the distinction between surface scattering and volume scattering. Volume scattering will occur when the electromagnetic wave penetrates into the medium on which it is incident and scatters on the individual elements inside the medium (Woodhouse, 2006). In the case of surface scattering, on the other hand, the wave will not penetrate into the medium but reflects off its surface. Again, whether a medium will behave as a surface scatterer or as a volume scatterer depends on the wavelength. A single leaf, for example, will act as a volume scatterer for near infrared radiation, with the infrared wave reflecting at the interfaces of cell walls and intracellular spaces. An entire canopy can also act as a volume scatterer, but then for microwave radiation, with the different stems, branches and leaves making up the individual scatterers.

## 2.1.4 Atmospheric attenuation

In spaceborne remote sensing, it is evident that information contained in electromagnetic radiation reflected from, or emitted by, the earth's surface must penetrate the atmosphere surrounding the earth. Therefore, the atmosphere's transmittance ( $\tau(\lambda)$ ) must approach unity or, as a consequence, the absorptance ( $\alpha(\lambda)$ ) and reflectance ( $\rho(\lambda)$ ) along the path of the electromagnetic wave should be minimal.

### 2.1.4.1 Absorptance

A well-known type of atmospheric absorption is the blocking of ultraviolet radiation ( $0.1\ \mu\text{m}$ – $0.4\ \mu\text{m}$ ) by the ozone layer, protecting the human skin against skin cancer. Ozone is only one of the gases in the atmosphere that absorb electromagnetic radiation. Other efficient absorbers are water vapour, carbon dioxide and oxygen. Each of these block the electromagnetic radiation at specific wavelengths, making them useless for remote sensing applications. The wavelength ranges in which energy is not absorbed ( $\alpha(\lambda) \approx 0$ ), and thus allow remote sensing systems to 'see through' the atmosphere, are called atmospheric windows. Obviously, if one is interested in atmospheric composition or processes, the wavelengths in the absorption bands are to be employed.

### 2.1.4.2 Reflectance

Like all objects, atmospheric particles will reflect electromagnetic radiation in function of the wavelength. Reflection or scattering processes in the atmosphere are grouped based on the relative size of the scattering particles relative to the wavelength of the electromagnetic energy. As such, three processes are discerned: Rayleigh scattering, Mie scattering and nonselective scattering.

**Rayleigh scattering** A first type of scattering occurs when the size of the particles on which the electromagnetic radiation is incident is much smaller (about a factor 10) than the wavelength, and is called Rayleigh scattering. The effect of this type of scattering is inversely proportional to the fourth power of the wavelength, and thus drops quickly with increasing wavelength. Rayleigh scattering is responsible for the blue appearance of a clear sky, since in the visible part of the spectrum ( $0.4\ \mu\text{m}$ – $0.7\ \mu\text{m}$ ) the shorter blue wavelengths are reflected much stronger than others on the tiny atmospheric particles.

**Nonselective scattering** A different type of scattering occurs when the size of the particles on which the electromagnetic radiation is incident is much larger (about a factor 10) than the wavelength. In this case, the particle will appear as a surface to the electromagnetic wave and scatter all wavelengths about equally, hence the name nonselective scattering. This type of scattering can be observed when visible or infrared waves interact with water droplets, with diameters from  $5\ \mu\text{m}$  to  $100\ \mu\text{m}$ , formed in clouds. The equal scattering of all visible wavelengths

causes the white color of clouds, and prevents radiation in the shorter wavelengths to reach the earth's surface or the spaceborne sensor. Microwaves (1 mm–1 m), however, have a wavelength much longer than the diameter of these droplets, and will thus not be scattered nonselectively by clouds.

**Mie scattering** An intermediate type of scattering, when the wavelength is about the size of the particles, is called Mie scattering. This type of scattering can occur when visible light is incident on atmospheric dust particles, or shorter microwaves are incident on raindrops. The scattering behaviour is complex, and very sensitive to changes in particle size and wavelength (Woodhouse, 2006).

### 2.1.5 Influence of surface properties

This section discusses the influence of soil surfaces and vegetation canopy cover on electromagnetic radiation, with emphasis on the effects of (changes in) soil moisture. Interaction with artificial surfaces will not be discussed here since this goes beyond the scope of this research. Given the very different effect of surface properties on electromagnetic radiation with different wavelengths, a distinction is made between the effects on shortwave (visible (0.4  $\mu\text{m}$ –0.7  $\mu\text{m}$ ), near infrared (NIR, 0.7  $\mu\text{m}$ –1.4  $\mu\text{m}$ ) and shortwave infrared (SWIR, 1.4  $\mu\text{m}$ –3  $\mu\text{m}$ )), thermal infrared (TIR, 3  $\mu\text{m}$ –15  $\mu\text{m}$ ), and microwave (1 mm–1 m) radiation.

#### 2.1.5.1 Visible, near infrared, shortwave infrared

**Bare soil** The darkening of soils when water is added is a familiar phenomenon that can be observed by the human eye. A large number of laboratory studies investigated the moisture effect on a wide range of soils and all found a decrease of soil reflectance with increasing moisture content for the entire shortwave spectrum, although specific for each soil and each wavelength (Bowers and Hanks, 1965; Viscarra Rossel and McBratney, 1998; Muller and Décamps, 2000; Liu *et al.*, 2002; Lobell and Asner, 2002; Liu *et al.*, 2003; Whiting *et al.*, 2004; Demattê *et al.*, 2006; Haubrock *et al.*, 2008a; Liu *et al.*, 2009). When water is added to a dry soil, the first water is attracted to the soil particles. This change of the medium surrounding the particles from air to water changes the direction in which light is scattered, and increases the absorbance of the soil (Twomey *et al.*, 1986). Additional water that starts to fill the micro- and macropores in the soil has only limited effect on the visible reflectance. Strong absorption by water in the SWIR however causes  $\rho(\lambda)$  in these wavelengths to decrease even further. The high SWIR reflectance of dry soils enhances the contrast between dry and wet soils (Lobell and Asner, 2002). Two regions especially sensitive to soil water content are centered around 1.44  $\mu\text{m}$  and 1.99  $\mu\text{m}$  and form distinct water absorption features in the reflectance spectra of wet soils (Bowers and Hanks, 1965; Somers *et al.*, 2010).

**Vegetation canopy** Electromagnetic waves in the visible, NIR and SWIR wavelengths are largely reflected or absorbed by the top few millimetres of the surface.

Therefore, in the case of vegetated surfaces, the signal reaching the sensor will be dominated by the contribution of the canopy cover, and the soil signal will only contribute marginally. Direct observation of the soil and estimation of topsoil moisture content thus becomes impossible. However, spatial or temporal patterns in root zone soil moisture can, in some cases, be estimated indirectly from the influence of soil moisture on the vegetation canopy, since well-watered and water-stressed vegetation reflect the shortwave solar radiation differently. The low reflectance of green leaves in the visible part of the spectrum in general, and in the red wavelength in particular, is caused by the absorption of this light for photosynthesis (Gamon *et al.*, 1992). The large reflectance in the near infrared is caused by volume scattering in the leaves (Gausman, 1974). Low soil moisture levels over a period of time will cause plants to reduce water loss through transpiration and photosynthetic activity, while reducing the intercellular spaces in the leaves. This results in an increase in reflectance of red light and a reduced reflectance in the near infrared. Towards the longer wavelengths, the SWIR part of spectrum of vegetation is very sensitive to changes in moisture content through the strong absorption by leaf water (Gao, 1996).

### 2.1.5.2 Thermal infrared

**Bare soil** The temperature of a bare soil surface, which can be obtained from the total radiant exitance from the surface (Eq. 2.2), is determined by, amongst others, the moisture content in the top layer. Two moisture-related properties influencing surface temperature are thermal inertia and evaporation (Price, 1980). The thermal inertia of a material or surface determines its response to external temperature variations and is function of the material's bulk density, specific heat capacity and thermal conductivity, all of which are material specific. The thermal inertia of a material expresses itself in its diurnal temperature variation, with high thermal inertia resulting in small temperature variations, and vice versa. As a result of the high thermal inertia of water, the diurnal temperature variation of a water body is much lower than that of dry soil. Given all other soil properties constant over space and time, dry soils will therefore exhibit higher temperature variations than wet soils.

Evaporation over bare soil surfaces controls the surface temperature through the surface energy balance, which partitions the net radiation at a surface ( $R_n$ ) into a sensible heat flux ( $J$ ), latent heat flux ( $LE$ ) and ground heat flux ( $G$ ), all in  $\text{W m}^{-2}$ :

$$R_n = LE + J + G, \quad (2.10)$$

where the latent heat flux is the product of the amount of evaporated water and the latent heat of vaporization. An increase in evaporation, and hence the latent energy term in the energy balance, results in a decrease of energy available to heat the soil surface. Since evaporation requires the availability of moisture in the top layer of the soil, well-watered soil surfaces will therefore be cooler than dry surfaces.

**Vegetation canopy** Much like the shorter infrared and visible wavelengths, thermal infrared radiation is unable to penetrate a dense vegetation canopy cover. Surface temperature observed by satellites will therefore reflect the temperature of the top layer of the canopy in case the soil is covered by vegetation, and thus be influenced by the intensity of transpiration from the canopy (Lambin and Ehrlich, 1996). Canopy transpiration, soil evaporation and direct evaporation from plants combine into evapotranspiration. When plants can draw water from the root zone unlimitedly, evapotranspiration will allow the daytime canopy temperature to remain close to air temperature (Lambin and Ehrlich, 1996). When access to soil moisture is limited, however, the reduction of transpiration by stomatal closure will cause the canopy temperature to increase above air temperature.

### 2.1.5.3 Microwaves

**Bare soil** Soil moisture content is related to the surface reflectance and emissivity in the microwave part of the spectrum through the (relative) electric permittivity. The permittivity describes how a medium is influenced by a magnetic field, and is composed of a real part and an imaginary part. While the real part determines the propagation characteristics through the medium, the complex part determines the absorption as the electromagnetic wave travels through the medium. The real part of the electric permittivity of water is high as a result of the capability of water molecules to align with the electric field in the microwave region, a phenomenon also applied in microwave ovens. Dry soils, on the other hand, are characterized by a low real and imaginary component of the permittivity, which both rise when the moisture content increases (Woodhouse, 2006). The electric permittivity determines  $\epsilon(\lambda)$  of the bare soil surface and hence, following Eq. 2.8,  $\rho(\lambda)$ .

Surface emissivity and reflectance are also influenced by the geometric characteristics of the soil surface, or the roughness. The geometric characteristics will determine to which degree the surface will act as a specular or a diffuse reflector. This has as a result that  $\epsilon(\lambda)$  and  $\rho(\lambda)$  may be very different for a tilled and an untilled bare soil surface with the same moisture content.

**Vegetation canopy** A vegetation canopy can, in the microwave part of the spectrum, be seen as a volume of individual scattering elements of different sizes and orientation (Woodhouse, 2006). The degree in which microwave radiation will be able to penetrate the canopy cover is function of the wavelength. While the shorter wavelengths of a few millimetres will be scattered by elements as small as the leaves and twigs, wavelengths in the order of a metre will only interact with the larger elements such as tree trunks and will therefore more easily penetrate the canopy cover. As for dry soils, the moisture content in the vegetation canopy also influences the reflectance and emissivity.

## 2.2 Remote sensing systems

Since the launch of the first Sputnik satellite in 1957, numerous earth observation space missions have been undertaken. Data from several types of satellites have been used to infer information on spatial and/or temporal soil moisture patterns. Remote sensing systems can be classified based on the range of wavelengths of electromagnetic radiation that is observed. Additionally, a distinction can be made between passive and active systems. While passive systems observe the radiation emitted by an external energy source, i.e. the sun or earth, active systems provide their own source of electromagnetic radiation. As such, spaceborne remote sensing systems can be classified into three broad categories: multispectral optical systems, active microwave or radar systems and passive microwave systems (Fig. 2.4). It should be noted that other types of earth observing systems (such as lidar, an active system operating in the shortwave spectrum) exist, though these are not discussed here since they are seldomly used for the monitoring of soil moisture.

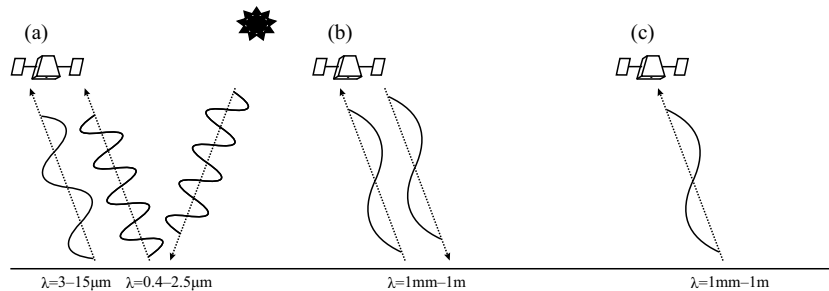


Figure 2.4: Basic principles of (a) optical sensors, (b) radars, (c) passive microwave sensors, with indication of wavelengths ( $\lambda$ ).

The following sections provide a brief overview of the main characteristics of these three groups of sensors. A number of past, present-day and future satellite missions, relevant to this research and/or mentioned throughout this document, are listed.

### 2.2.1 Multispectral scanners

Systems operating in wavelengths ranging from UV to TIR ( $0.3 \mu\text{m}-14 \mu\text{m}$ ) are also called optical sensors since in this range optical instruments such as lenses and mirrors can be used to reflect and refract electromagnetic radiation. These sensors are passive systems, capturing the amount of incident solar radiation reflected by the earth's surface or the amount of radiation emitted by the surface. This is typically done in a number of different spectral bands with a certain width, hence the name multispectral. When the number of spectral bands used is increased, and the width of the wavelength bands thus becomes smaller, the term hyperspectral is

used.

### 2.2.1.1 Image acquisition principles

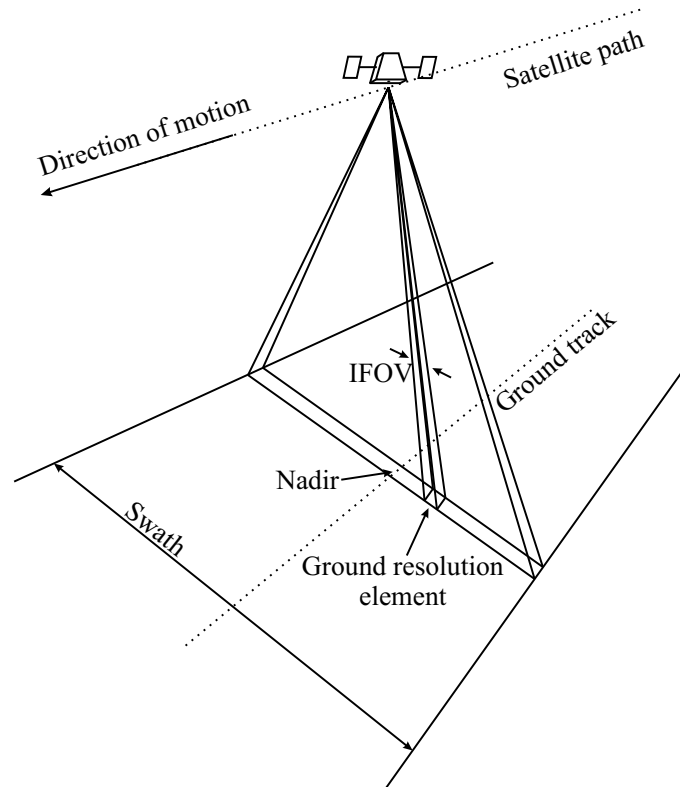


Figure 2.5: Across-track scanner characteristics.

A two-dimensional image acquired by a spaceborne sensor is formed by a line-by-line scanning of the earth's surface. The scanning of the different scan lines is done either by across-track scanning or by along-track scanning. In across-scanning (Fig. 2.5), a rotating mirror is used to successively scan along lines perpendicular to the direction of propagation of the sensor. The width of these scan lines is referred to as the swath. The second dimension is then added by the forward motion of the sensor. Along-track scanners also use the forward motion of the sensor to obtain the second dimension in an image. The different scan lines are in this case obtained by a linear array of detectors, rather than by a rotating mirror (Lillesand *et al.*, 2004).

It should be noted that scanning of the surface using the forward motion of the



spacecraft is not possible in the case that the sensor is at a fixed position in space relative to the surface, i.e. a geostationary sensor. These instruments are therefore designed to scan in two dimensions.

### 2.2.1.2 Spectral characteristics

**Surface reflectance** As seen in Fig. 2.2, solar exitance peaks in the visible part of the spectrum. Since this region corresponds to a wide atmospheric window, it is used in most multispectral sensors designed for land surface applications. Similarly, the near-infrared region is characterized by a high solar exitance and contains large atmospheric windows in between the atmospheric water vapour absorption regions at  $0.94\ \mu\text{m}$  and  $1.12\ \mu\text{m}$ . In the shortwave infrared, two atmospheric windows are roughly situated between  $1.5\ \mu\text{m}$  and  $1.8\ \mu\text{m}$  and between  $2.0\ \mu\text{m}$  and  $2.5\ \mu\text{m}$  (Vermote and Vermeulen, 1999).

The information that is electronically recorded by the sensor is the total radiance reaching the sensor. In order to transform this at-sensor radiance to surface reflectance, the total incoming radiation on the object or irradiance must be known, as well as the path radiance, or the radiance observed by the sensor that is reflected by the atmosphere itself (Lillesand *et al.*, 2004). Both irradiance and path radiance are function of the atmospheric conditions. Additionally, irradiance is function of the solar elevation and its distance to the earth.

**Surface temperature** Complementary to measuring the spectral reflectance of the earth's surface, some multispectral sensors include thermal scanners that measure the earth's surface temperature ( $T_s$ ). The derivation of surface temperature is based on the Stefan-Boltzmann law (Eq. 2.2), which defines the relation between blackbody temperature and total radiant exitance. From Fig. 2.2, we know that the earth's surface emits maximally in the thermal infrared region between  $3\ \mu\text{m}$  and  $15\ \mu\text{m}$ , with a peak at  $10\ \mu\text{m}$ . The atmospheric window between  $8\ \mu\text{m}$  and  $14\ \mu\text{m}$  is therefore the region of preference for determining surface temperature. Since the peak of radiant exitance shifts towards the shorter wavelengths with increasing temperature, the spectral window between  $3\ \mu\text{m}$  and  $5\ \mu\text{m}$  is sometimes included in multispectral sensors with the aim of monitoring of high-temperature phenomena such as forest fires or volcanoes.

The thermal radiation observed by a spaceborne sensor contains, in addition to the land surface signal, a contribution of the atmosphere. Furthermore, as mentioned in the previous section, the earth's surface emits only a certain fraction of the energy that a blackbody of the same temperature would emit, characterized by the emissivity  $\epsilon$ . These two aspects have to be accounted for in order to obtain reliable surface temperature estimates. Among the methods used to derive surface temperature from the observed infrared radiation are the split-window method (Wan and Dozier, 1996) and the day/night algorithm (Wan and Li, 1997). The split-window

method exploits the difference in atmospheric absorption of thermal infrared radiation in adjacent spectral bands, combined with emissivities estimated from land cover type (Snyder *et al.*, 1998) The day/night algorithm retrieves day- and nighttime surface temperature and emissivity simultaneously from pairs of daytime and nighttime data in seven TIR bands.

### 2.2.1.3 Spatial and temporal resolution

The spatial resolution of the sensor, defined by the size of the ground resolution element, is determined by the distance between the sensor and the surface and by the instantaneous field of view (IFOV) of the sensor (Lillesand *et al.*, 2004). The IFOV is the cone angle within which the incident energy is detected by the sensor. Since the IFOV of an across-track scanner remains constant, the spatial resolution at nadir will be higher (smaller ground resolution element) than towards the sides of the swath. Depending on the design of the sensor and the altitude at which it is flown, spatial resolutions in this group of sensors vary greatly, from as high as one metre to as low as a few kilometres.

Temporal resolution, or the time between two consecutive observations of the same place on earth, is generally restricted by the trade-off between spatial and temporal resolution, since higher spatial resolutions will usually result in smaller swaths. For geostationary satellites, the temporal resolution is only confined by the time of the sensor to scan the (half) earth disk. The temporal resolution for non-geostationary orbits is defined by the image swath and the orbit pattern. An important concept in this respect is the repeat cycle or the time for the satellite to return to the same ground track.

Since electromagnetic radiation in this part of the spectrum is scattered nonselectively by small water droplets, this type of remote sensing systems are rendered useless for land surface applications under conditions of cloud cover. The effect of cloud cover can be mitigated by image compositing. This process comprises the detection and filtering of cloud cover in a number of multitemporal images, and the assignment of a representative value based on the data collected under non-clouded conditions. Inevitably, this results in a decrease of the temporal resolution.

### 2.2.1.4 Past, present and future missions

An interesting category of multispectral scanners for application in species distribution modelling are the polar-orbiting medium resolution sensors, which provide spatial resolutions in the order of 1 km at revisit times of a few days.

**NOAA AVHRR** The family of Advanced Very High Resolution Radiometer (AVHRR) sensors is carried onboard the different National Oceanic and Atmospheric Administration (NOAA) satellites since 1978. The polar-orbiting satellites

operate at a heliosynchronous orbit, indicating that the ground path of the sensor crosses the equator at a fixed local solar time. The number of spectral bands in which the AVHRR sensor operates has increased over the years from four to six, with bands in the visible, NIR, SWIR and TIR part of the spectrum. Currently, five NOAA AVHRR sensors are operational. The AVHRR instrument is also carried onboard the MetOp (Meteorological Operational satellite programme) platforms operated by the European Organisation for the Exploitation of Meteorological Satellites (EUMETSAT).

**Aqua/Terra MODIS** The two Moderate Resolution Imaging Spectroradiometer (MODIS, NASA, 2013) instruments can be seen as a follow-on of the AVHRR sensors. MODIS is mounted on the Terra and Aqua spacecrafts, launched in 1999 and 2002, respectively. The daytime equatorial crossing time for these two heliosynchronous platforms, with a repeat cycle of 16 days, is 10:30 a.m. in descending orbit (north to south) for Terra, and 1:30 p.m. in ascending orbit for Aqua. Due to the large swath of the instrument (2330 km cross-track), each of the two sensors provides a near-global daily coverage day and night.

The MODIS instrument acquires information on reflected and emitted radiation in 36 narrow bands in the shortwave and thermal part of the spectrum. Spatial resolution ranges from 250 m for two bands in the red and near-infrared, over 500 m for 5 bands in the shortwave spectrum, to 1000 m for the remaining bands throughout the shortwave and thermal spectrum. Although designed for a lifetime of six years, both sensors are still operational.

**Envisat MERIS** The Medium Resolution Imaging Spectroradiometer (MERIS), carried by the European Space Agency's (ESA) Envisat platform, was designed to observe solar reflectance in fifteen spectral bands in the reflective part of the spectrum, programmable by ground control. MERIS can either operate in Full Resolution mode, with a spatial resolution of 300 m, or in Reduced Resolution mode of 1200 m. The sensor was operational until contact with Envisat was lost on April 8, 2012.

## 2.2.2 Radar

### 2.2.2.1 Image acquisition principles

Being an active system, a radar (radio detection and ranging) supplies its own source of electromagnetic radiation. Radar systems consist of an airborne or spaceborne antenna emitting short pulses of microwave energy sideways of the flight path (Fig. 2.6), hence the name side-looking radar (SLR). The radar image is formed, line by line using the forward motion of the platform, by measuring the strength of the returned signal together with the time required for the signal to travel towards the surface and back. The proportion of energy that is returned to-

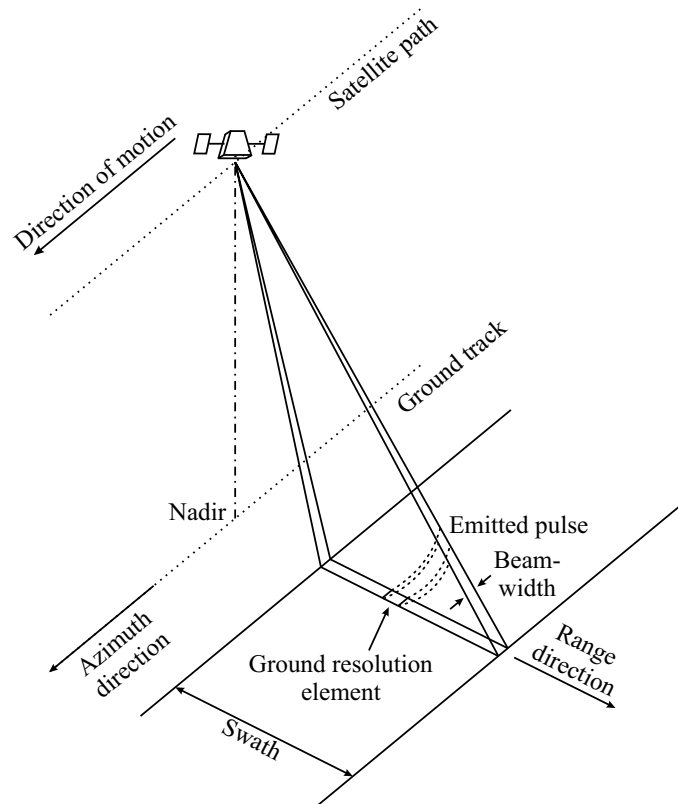


Figure 2.6: Side-looking radar characteristics.

wards the sensor is reflected in the backscatter coefficient ( $\sigma^0$ ) which is expressed in dB.

### 2.2.2.2 Spectral characteristics

Radars operate in the microwave part of the spectrum (1 mm to 1 m), which coincides with a large atmospheric window. These wavelengths are much longer than the diameter of water droplets in clouds, making them insensitive to nonselective scattering. In contrast to radiation in the visible, infrared and thermal wavelengths, microwaves can thus penetrate cloud cover. Since radar systems provide their own source of electromagnetic energy, they can also be operated day and night.

Contrary to multispectral optical systems, radar systems typically use only a single wavelength. The wavelength or frequency bands are referred to using a letter, originating from the military use of microwaves (Table. 2.1). While a main advantage of microwaves is that they can penetrate cloud cover, the shorter K and

X wavelengths can be severely attenuated by rainfall, when the drops become large with respect to wavelength.

Table 2.1: Radar band designations (Lillesand *et al.*, 2004).

Band	Wavelength $\lambda$ [cm]
$K_a$	0.75–1.1
K	1.1–1.67
$K_u$	1.67–2.4
X	2.4–3.75
C	3.75–7.5
S	7.5–15
L	15–30
P	30–100

Radars emit electromagnetic radiation with a certain polarization, typically in the vertical (V) or horizontal (H) plane with respect to the earth's surface. Similarly, the returning signal can be received in one of these planes. This results in four possible polarization schemes: two co-polarized (HH or VV) and two cross-polarized (HV or VH).

### 2.2.2.3 Spatial and temporal resolution

The spatial resolution of SLR is characterized by a range resolution, in the direction of the emitted wave, and an azimuth resolution, in the direction of the flight line. The range resolution is proportional to the duration of the emitted electromagnetic pulse. The azimuth resolution, defined by the beam width, is directly proportional to the wavelength and inversely proportional to the length of the antenna. This implies that large antenna lengths are required to obtain high spatial resolutions. This problem is circumvented by the use of synthetic aperture radar (SAR) systems. These systems, opposed to real aperture radars, simulate the effect of long physical antennas by using the motion of the antenna in space.

As for optical systems, the temporal resolution of radar imagery is generally related to radar swath, with a trade-off between temporal and spatial resolution. Given the all-weather capabilities of microwaves, the temporal resolution of surface observations is not restricted by cloud cover. However, the fact that these are active systems might in some cases limit the temporal resolution due to the high power demand.

### 2.2.2.4 Past, present and future missions

**ERS Scatterometer** The Wind Scatterometer (hereafter simply Scatterometer) was a real aperture radar system operating in C-band (5.6 cm, 5.3 GHz) in VV

polarization (European Space Agency, 2013). It was flown on the two European Remote Sensing (ERS) satellites ERS-1 (launched in 1991 and decommissioned in 2000) and ERS-2 (launched in 1995 and decommissioned in 2011). During a period of time, ERS-1 and ERS-2 flew in tandem, i.e. following the same path with exactly one day between the overpasses of the two satellites.

The Scatterometer emits and records sideways electromagnetic pulses in three beams (forward, transverse and backwards), allowing the observation of a single place on earth at three different incidence angles at virtually the same time. This design was initially developed to monitor wind speed and direction at the sea surface. The sensor covered a swath of approximately 500 km to the right of the satellite track, with a spatial resolution of approximately 50 km in the range and azimuth direction.

**MetOp ASCAT** The Advanced Scatterometer (ASCAT), the successor of the two ERS Scatterometers, functions much by the same principles and at the same frequency (Gelsthorpe *et al.*, 2000). Its 500 km twin swaths, to the left and right of the satellite's ground track, double the coverage, effectively doubling the temporal resolution. In addition to the nominal 50 km spatial resolution mode, the high-resolution mode offers 25 km spatial resolution, although at reduced radiometric resolution. The ASCAT instrument is flown as part of the payload on the polar-orbiting MetOp satellites.

**ERS SAR** Both ERS satellite were equipped with a C-band (5.6 cm, 5.3 GHz) SAR in VV polarization (European Space Agency, 2013). These sensors were designed to observe a swath of 100 km at the right of the track under a fixed look angle of 23° in the middle of the swath. The spatial resolution of ERS SAR data is approximately 30 m in the range and azimuth direction. Due to the high power usage, operation time was limited to maximum 12 minutes per orbit (of approximately 100 minutes).

**Envisat ASAR** The Advanced Synthetic Aperture Radar (ASAR) onboard Envisat is the successor of the ERS SAR missions, and possesses enhanced functionalities (European Space Agency, 2007). Unlike the ERS SAR instruments, the C-band ASAR can operate in different polarizations and in five programmable modes: Image (IM) mode, Wave (WV) mode, Alternating Polarization (AP) mode, Wide Swath (WS) mode and Global Monitoring (GM) mode. While the first three of these are high resolution (30 m) modes with narrow swaths (10 km–100 km), the latter two provide wider swaths (450 km) at reduced spatial resolution of 150 m (WS mode) or 1 km (GM mode). Both WS and GM mode can operate in VV polarization and HH polarization. Apart from their spatial resolution, the two modes differ in their radiometric accuracy, which is 0.65 dB in WS mode and approximately double of that in GM mode.

Data availability in a given mode is constricted by the mutual exclusivity of acquisition in the five different modes. Furthermore, the high data rate modes (IM, AP and WS) only allow operation time of 10 minutes per orbit. The low data rate modes (WV and GM) have an operational capability of 100 % of the orbit, and were therefore programmed as global background missions (the operation mode in absence of user demand) over ocean and land, respectively. The ASAR instrument was operational during the 10-year lifespan of Envisat, between 2002 and 2012.

**Radarsat SAR** The first Radarsat-1 was constructed by a consortium of Canadian and US public and private partners and was launched in 1995. It is equipped with a C-band radar operating in HH polarization, and is operational in different modes of varying swath and spatial resolution. Radarsat-2 was launched in 2007 and provides enhanced functionalities, including a full range of polarizations (Canadian Space Agency, 2011).

**Sentinel-1** In the framework of the European Union's and ESA's Global Monitoring for Environment and Security (GMES) programme, a series of Sentinel satellites is to be launched during the following decade. Sentinel-1 (Attema *et al.*, 2007; Berger *et al.*, 2012; Torres *et al.*, 2012), a constellation of two satellites of which the first is to be launched in 2013, carries a C-band (5.405 GHz) SAR operational in different modes. In Interferometric Wide Swath mode, global coverage at least once every twelve days for each of the satellites is expected, increasing to four to two days for high priority areas.

## 2.2.3 Radiometers

### 2.2.3.1 Image acquisition principles

Radiometers are passive scanners, operating in the microwave part of the electromagnetic spectrum. The image acquisition principles of a traditional imaging radiometer are very similar to those of scanners in the optical domain. While the forward motion of the sensor creates one dimension, a scanning transverse to this direction creates the second dimension. The main difference with optical sensors is that radiometers use antennas to detect the radiation emitted or reflected by the earth's surface. Some recent sensors employ different imaging techniques, which are briefly discussed later (in 2.2.3.4).

### 2.2.3.2 Spectral characteristics

Radiometers operate in the same spectral domain as radars, with the same band nomenclature. As seen in Fig. 2.2, the spectral exitance of the earth's surface in the microwave region is very low, although all object will still radiate faintly at these wavelengths. Since also the atmosphere has a temperature above 0 K, the signal received at the sensor will include contributions emitted by the earth's surface, emitted by the atmosphere and emitted by the sun and reflected by the surface

or the atmosphere.

An important source of noise in passive microwave observations are microwave emissions caused by human activity (Njoku *et al.*, 2005). Given the very low level of natural radiation emitted by the earth's surface, even small anthropogenic radar emissions can result in Radio Frequency Interference (RFI).

### 2.2.3.3 Spatial and temporal resolution

Since the earth's surface emits only faintly in the microwave part of the spectrum, large antenna beamwidths are required to obtain a detectable signal, resulting in a low spatial resolution. Typically, spatial resolutions of spaceborne microwave radiometers are in the order of several tens of kilometres. On the other hand, the low spatial resolution results in temporal resolutions of one to a few days.

### 2.2.3.4 Past, present and future missions

**AMSR-E** The Advanced Microwave Scanning Radiometer - Earth Observing System (AMSR-E), an instrument onboard the Aqua platform and operated by the Japan Aerospace Exploration Agency (JAXA), operates in six different spectral bands in the microwave part of the electromagnetic spectrum. The spatial resolution decreases with increasing wavelength, and ranges from approximately 5.4 km to 56 km. AMSR-E ceased operating in 2011.

**SMOS** The Soil Moisture and Ocean Salinity (SMOS) mission is the first mission dedicated specifically to the monitoring of soil moisture. In contrast to traditional radiometers, the Microwave Imaging Radiometer with Aperture Synthesis (MIRAS) instrument of the SMOS mission is a two-dimensional, Y-shaped, instrument containing an array of 69 L-band receivers (Kerr *et al.*, 2010). SMOS was launched as part of ESA's Living Planet programme in November 2009.

**SMAP** NASA's Soil Moisture Active and Passive (SMAP) mission, planned for launch in 2014, combines a radiometer and a SAR, both operating at L-band (Entekhabi *et al.*, 2010). In a specific design, radar and radiometer share a rotating 6 m diameter antenna system conically scanning the surface. The instrument is designed specifically to monitor soil moisture and freeze-thaw state.

## 2.3 Soil moisture retrieval

A plethora of techniques to infer information on spatial or temporal soil moisture values and/or patterns from information in the optical and microwave part of the spectrum have been suggested during the previous decades. This section reviews some of these methods, with focus on those most relevant for application in species distribution modelling. In this context, soil moisture proxies should preferably be



derived using only remote sensing data, and limit the necessity of ancillary in situ data.

### 2.3.1 Multispectral scanners

#### 2.3.1.1 Empirical relationships and band ratioing

Several laboratory studies empirically established non-linear, wavelength-specific and soil-specific relationships between soil moisture and soil reflectance (Lobell and Asner, 2002; Liu *et al.*, 2002; Whiting *et al.*, 2004). The longer wavelengths in the SWIR, and specifically around 1990nm, were found to be most suitable for determining soil moisture content (Lobell and Asner, 2002; Liu *et al.*, 2003). Notwithstanding the clear relationship between soil moisture and reflectance, operational applications of these empirical approaches using a single wavelength are limited, given the need for vast amounts of in situ soil moisture data, needed for calibration, and prior knowledge of soil type. Multiband approaches try to bypass this problem by combining information from different parts of the soil reflectance spectrum. Band differencing approaches are popular due to their simplicity and, in general, use two spectral bands of which one wavelength is more sensitive to changes in the feature of interest and the other is less sensitive. Indices can then be derived by applying a simple ratio or normalized difference of the two wavelengths. Haubrock *et al.* (2008a) developed a soil moisture proxy by pairwise computation of normalized differences of soil samples' reflectances in the visible, NIR and SWIR. The reflectance in the SWIR at 1800nm and 2119nm resulted in an optimal linear regression with soil moisture and was used to define the Normalized Difference Soil Moisture Index. Validation of this index (Haubrock *et al.*, 2008b) yielded promising results over terrain with sparse vegetation cover. Other multiband approaches include Gaussian models (Whiting *et al.*, 2004) or multiple regression models (Chang *et al.*, 2001; Demattê *et al.*, 2006; Hummel *et al.*, 2001). All of these techniques, however, remain of limited utility for operational estimation of soil moisture content over heterogeneous landscapes throughout the year, given the necessity for bare soil conditions. Additionally, many of these require spectral bands unavailable in present-day high temporal resolution sensors.

An alternative for soil moisture estimates based on the soil reflectance spectrum are vegetation indices which, in general, reflect the state of the vegetation cover. Vegetation indices are influenced by several factors, including landcover, climate, soil composition, but can also indicate vegetation water stress and can thus be used as a proxy for soil moisture. An important difference between estimates derived from reflectances of bare soils and those of vegetation canopies is the depth of the soil layer for which soil moisture is estimated. For bare soils this depth is only a few micrometers, while for a canopy this is the entire root zone, which in turn is vegetation specific. The most popular vegetation index is the Normalized Difference Vegetation Index (*NDVI*), derived from the reflectance in the

red ( $\rho_{\text{red}}$ ) and near-infrared ( $\rho_{\text{NIR}}$ ):

$$NDVI = \frac{\rho_{\text{NIR}} - \rho_{\text{red}}}{\rho_{\text{NIR}} + \rho_{\text{red}}}, \quad (2.11)$$

where the red and NIR bands are centered around approximately 650nm and 860nm, respectively. *NDVI* is usually used as an indicator of vegetation density, vegetation status or photosynthetic activity, its strength resulting from the large difference in reflectance for the two wavelengths over vegetation. Since high *NDVI* values will only occur at places where soil moisture allows vegetation to grow, the index can be used a soil moisture proxy in the widest sense. There is, however, another and more useful relation between soil moisture and *NDVI*. Low soil moisture levels over a certain period of time will cause plants to reduce water loss through transpiration and photosynthetic activity. This results in a slight increase of  $\rho_{\text{red}}$  and a drastic decrease of  $\rho_{\text{NIR}}$  caused by a reduced scattering in the intercellular spaces of the leaf, and thus a decrease in *NDVI*. Several studies have established a link —albeit sometimes weak— between remotely sensed *NDVI* and soil moisture content at different depths (Wang *et al.*, 2007; Gu *et al.*, 2008).

*NDVI* is possibly not the best indicator of plant water stress or soil moisture content since a certain period of drought stress is required before plants reduce their photosynthetic activity. Several authors (Gao, 1996; Ceccato *et al.*, 2001; Fensholt and Sandholt, 2003; Chen *et al.*, 2005; Yi *et al.*, 2007; Wang *et al.*, 2008) suggest the use of a normalized difference of SWIR wavelengths to assess foliage water content and associated root zone soil moisture. The Normalized Difference Water Index (*NDWI*) uses a SWIR wavelength ( $\rho_{\text{SWIR}}$ ) as water-sensitive band and the NIR as insensitive band, resulting in:

$$NDWI = \frac{\rho_{\text{NIR}} - \rho_{\text{SWIR}}}{\rho_{\text{NIR}} + \rho_{\text{SWIR}}}. \quad (2.12)$$

Different SWIR wavelengths have been suggested for use in Eq. 2.12, located either near the liquid water absorption feature of 1.2 $\mu\text{m}$  on the high reflectance plateau (Gao, 1996; Fensholt and Sandholt, 2003), or either around 1.6 $\mu\text{m}$  (Fensholt and Sandholt, 2003; Yi *et al.*, 2007) and 2.2 $\mu\text{m}$  (Yi *et al.*, 2007), in the atmospheric windows between the water-absorption features. Reflectance in all these wavelengths will rise significantly with decreasing leaf water content,  $\rho_{\text{NIR}}$  will remain relatively stable or drop slightly, resulting in an increasing *NDWI* with increasing moisture. Although most comparative studies found *NDWI* to be a better predictor of soil moisture (Jackson *et al.*, 2004; Chen *et al.*, 2005), other found no increased performance of *NDWI* compared to *NDVI* (Gu *et al.*, 2008). The superiority of *NDWI* is attributed to the early saturation of *NDVI* with increasing soil moisture (Jackson *et al.*, 2004). At a certain moisture level vegetation will no longer increase leaf water content or photosynthetic activity, thus stabilizing the vegetation indices.

Both *NDWI* and *NDVI* will be mainly influenced by the absence or presence and phenological phase of vegetation. Changes in a clear soil moisture signal could, however, be detected at the later stages in a winter wheat growing cycle (Yi *et al.*, 2007). A way to derive soil moisture proxies from vegetation indices over a changing phenology consists of subtracting a seasonal average derived from multi-year time series (Rulinda *et al.*, 2010). Adegoke and Carleton (2002) could relate a deseasoned *NDVI* with deseasoned soil moisture measurements, while Jackson *et al.* (2004) did the same using *NDWI*. The use of deseasoned time series is only applicable with stable seasonal patterns. In the case of, e.g., shifting crop rotation systems, deseasoned time series are rendered useless. Limitation of vegetation indices also clearly arise over bare soils, as vegetation indices are largely insensitive to changes in moisture content (Wang *et al.*, 2008).

### 2.3.1.2 Contextual surface temperature patterns

Several studies could empirically relate spatial changes in soil moisture to spatial changes in land surface temperature (Katra *et al.*, 2006; Boulet *et al.*, 2007; Giraldo *et al.*, 2009). While this offers opportunities of operational soil moisture mapping for certain applications, e.g. for precision agriculture, the use of  $T_S$  alone as a soil moisture proxy is limited to areas with homogeneous canopy cover. Over more heterogeneous landscapes, thermal data need to be combined with information from the reflected wavelengths in order to account for changes in canopy cover.

The complementary nature of information in the visible/near infrared and in the thermal infrared part of the electromagnetic spectrum has been studied intensively for the parameterization of evapotranspiration and soil moisture status during the past decades. A consistent negative relationship between remotely sensed vegetation indices (*VI*) and surface temperature ( $T_S$ ) was observed by several authors (Nemani and Running, 1989; Friedl and Davis, 1994; Moran *et al.*, 1994b; Prihodko and Goward, 1996; Goward *et al.*, 2002). The reasons for the decrease in surface temperature with increasing vegetation cover are manifold and an overview of these driving mechanisms is provided by Lambin and Ehrlich (1996), among others. In general, an increase in green biomass is associated with an increase in evapotranspiration, thus a decrease in surface temperature. The slope of the *VI*- $T_S$  relationship was found to be dependent on the general moisture conditions. While under arid conditions soils are capable of retaining a considerable part of the energy absorbed from sunlight and reach temperatures that exceed air temperature by several tens of degrees, the bulk temperature of a dense canopy remains close to air temperature, resulting in a strong decrease of surface temperature with increasing vegetation index. Under uniform wet conditions, on the other hand, both bare and fully vegetated surfaces will fully control surface temperature by evaporation and transpiration, resulting in only a weak decrease of surface temperature with increasing vegetation index. The slope of the *VI*- $T_S$  relationship has been related to regional surface resistance to evaporation or soil wetness or dryness, but was also

found to be controlled by land cover and local meteorological conditions (Nemani and Running, 1989; Nemani *et al.*, 1993; Friedl and Davis, 1994; Goward *et al.*, 2002; Higuruchi *et al.*, 2007).

The concept of the VI- $T_S$  relationship was further developed to accommodate for larger areas with wide ranges in moisture and land cover conditions (Moran *et al.*, 1994a; Carlson *et al.*, 1995). The hypothesis is that a triangular or trapezoidal shape appears when a scatterplot of vegetation index and surface temperature is derived for a remotely sensed image over an area covering a full range of soil moisture and vegetation cover conditions. This concept is illustrated in Fig. 2.7. Vertices A and B of the trapezoid represent entirely dry and wet soil, C and D represent water-stressed and well-watered vegetation, respectively. The line AC connects the pixels with the highest surface temperature —or driest conditions— for a given vegetation cover and is hence called the dry edge or hot edge. Similarly, the line BD is called the wet or cold edge, connecting fully evaporating or transpiring pixels.

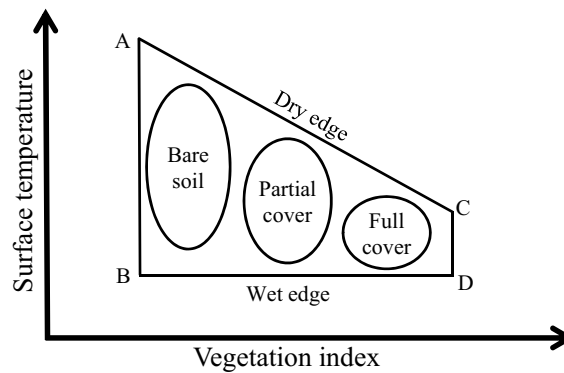


Figure 2.7: Conceptual representation of the trapezoidal VI- $T_S$  space.

The wet edge is often, as in Fig. 2.7, represented as a constant  $T_S$  value, equal to air temperature (Sandholt *et al.*, 2002; Vicente-Serrano *et al.*, 2004). A sloped wet edge is however probably more universally applicable (Moran *et al.*, 1994a). The range of  $T_S$  decreases with increasing VI due to the relative insensitivity of leaf temperature to soil water content.  $T_S$  will be close to air temperature at maximum VI, irrespective of soil moisture. The concept is therefore often simplified by combining C and D into a single vertex, thus producing a triangle and giving the concept its popular name "triangle method" (Carlson, 2007).

Estimates of soil moisture content can be made for each pixel from its position within the trapezoid or triangle, by linearly scaling its surface temperature between the corresponding values of the wet and dry edge for that pixel. The position of the dry and wet edge can be determined either empirically from the VI- $T_S$  scatter-

plot itself (Sandholt *et al.*, 2002; Patel *et al.*, 2009), or modelled using ancillary meteorological data (Carlson, 2007). As such, several indices have been presented that are based on the VI- $T_S$  relationship, including the Water Deficit Index (Moran *et al.*, 1994a), Temperature-Vegetation Dryness Index (Sandholt *et al.*, 2002), Vegetation Temperature Condition Index (Wan *et al.*, 2004; Sun *et al.*, 2008), Modified Temperature-Vegetation Dryness Index (Kimura, 2007), Temperature-Vegetation Wetness Index (Hassan *et al.*, 2007) and Soil Wetness Index (Mallick *et al.*, 2009). This multitude of indices reflects the large number of variations on the same concept (Petropoulos *et al.*, 2009), which may consist of differences in input data (e.g. Dupigny-Giroux and Lewis, 1999; Carlson, 2007), the method to derive the dry and wet edge (e.g. Verstraeten *et al.*, 2005; Tang *et al.*, 2010) or the amount of ancillary data used (e.g. Kimura, 2007).

### 2.3.1.3 Temporal surface temperature patterns

Several spaceborne sensors measure the surface temperature of a single location on earth at different moments throughout the day. This provides the opportunity to infer information on the surface's thermal inertia. As mentioned earlier, the thermal inertia of a material or surface determines its resistance to temperature variations and is function of the material's bulk density, specific heat capacity and thermal conductivity. Although neither of these three properties can be derived from remote sensing, related information can be derived from multitemporal surface temperature observations. As materials with higher thermal inertia will experience smaller temperature changes than materials with low thermal inertia, given identical external driving forces, the night/day or pre-sunrise/midday temperature differences in remote sensing images can be used to discriminate between materials (Hardgrove *et al.*, 2009) or soil moisture levels (Idso *et al.*, 1975). The first physically-based models to derive thermal inertia for geologic mapping of the earth's surface including remote sensing data originate from the early and mid 70s (Watson, 1973; Kahle *et al.*, 1976). More formulations for the computation of thermal inertia were suggested in the subsequent years (Idso *et al.*, 1976; Price, 1977, 1980; Pratt *et al.*, 1980; Abdellaoui *et al.*, 1986). However, these all assume the availability of meteorological and/or other ancillary data, and are thus of limited use.

In contrast to these earlier models, Xue and Cracknell (1995) developed a methodology that required only a single ground measurement, being the time of maximum surface temperature in the daytime. Applying a Fourier series solution on the temperature diffusion equation, respecting a set of boundary conditions, they obtained a second-order expression of surface temperature  $T_S$  in function of

the time of day  $t$  [s]:

$$T_S(t) = -\frac{A_c}{B_c} + (1 - \alpha_0)S_0\tau_{\text{atm}}A_1 \frac{\cos(\omega t - \psi_1)}{\sqrt{\omega TI^2 + \sqrt{2\omega}B_c TI + B_c^2}} + (1 - \alpha_0)S_0\tau_{\text{atm}}A_2 \frac{\cos(2\omega t - \psi_2)}{\sqrt{2\omega TI^2 + 2\sqrt{\omega}B_c TI + B_c^2}}, \quad (2.13)$$

where  $TI$  is thermal inertia [ $\text{J m}^{-2} \text{s}^{1/2} \text{K}^{-1}$ ],  $A_c$  and  $B_c$  are the linearization coefficients of the linearized boundary condition,  $\alpha_0$  is the surface albedo [-],  $S_0$  is the solar constant ( $1367 \text{ W m}^{-2}$ ),  $\tau_{\text{atm}}$  is the atmospheric transmittance in the visible spectrum [-],  $A_1$  and  $A_2$  coefficients of the Fourier series,  $\omega$  is the angular velocity of rotation of the earth [ $\text{rad s}^{-1}$ ], and  $\psi_1$  and  $\psi_2$  are phase angles [rad]. A further discussion of these factors is given by Xue and Cracknell (1995). When the difference in surface temperature at two overpasses ( $\Delta T_S$ ) is available, as well as the respective times of observation  $t_1$  and  $t_2$ , Eq. 2.13 can be solved for thermal inertia:

$$TI = \frac{(1 - \alpha_0)S_0\tau_{\text{atm}}}{\Delta T_S \sqrt{\omega}} \left\{ \frac{A_1 [\cos(\omega t_2 - \psi_1) - \cos(\omega t_1 - \psi_1)]}{\sqrt{1 + \frac{1}{b} + \frac{1}{2b^2}}} + \frac{A_2 [\cos(2\omega t_2 - \psi_2) - \cos(2\omega t_1 - \psi_2)]}{\sqrt{2 + \frac{\sqrt{2}}{b} + \frac{1}{2b^2}}} \right\}, \quad (2.14)$$

and

$$b = \frac{\tan(\omega t(T_{S,\text{max}}))}{1 - \tan(\omega t(T_{S,\text{max}}))}, \quad (2.15)$$

with  $t(T_{S,\text{max}})$  the time of maximum surface temperature [s]. For operational use, Xue and Cracknell (1995) suggest to replace this parameter by the time of maximum air temperature. This meteorological information may however not always be available. Furthermore, the time of maximum air temperature can differ from the time of maximum surface temperature. Sobrino and El Kharraz (1999a) therefore adapted this methodology by obtaining the time of maximum surface temperature from the remote sensing data itself. As such, a method to derive thermal inertia requiring only remotely sensed surface temperature and albedo was obtained.

A very basic approximation of thermal inertia, solely requiring surface albedo and a night-day surface temperature pair, was obtained by simplification of the Price (1977) model. This approximation was originally applied on Heat Capacity Mapping Mission (HCMM) data and named apparent thermal inertia ( $ATI$ ) (Short and Stuart, 1982):

$$ATI = C \frac{1 - \alpha_0}{\Delta T_S}, \quad (2.16)$$

where  $C$  is a solar correction factor dependent on latitude and solar declination. Apparent thermal inertia was initially found to be of limited use in areas with

strong evapotranspiration (Price, 1985). Wet surfaces allow considerable evaporation and/or transpiration during the daytime, thus reducing daytime surface temperatures through evaporative cooling and introducing errors in apparent thermal inertia. Nevertheless, apparent thermal inertia received renewed interest since the last decade for mapping of both geology (Mitra and Majumdar, 2004) and soil moisture (Tramutoli *et al.*, 2000; Verstraeten *et al.*, 2006; Veroustraete *et al.*, 2012) because of its simple formulation requiring remote sensing data only.

The coupling between apparent thermal inertia and soil moisture is not straightforward. True thermal inertia can be converted to soil moisture when soil properties are known (Lu *et al.*, 2009; Minacapilli *et al.*, 2009). Apparent thermal inertia might be directly related to soil moisture for areas with limited extent so that only a single soil and land cover type are present (e.g. individual fields). Over areas with varying geology or land use, however, soil moisture can only be extracted using a multitemporal approach (Tramutoli *et al.*, 2000; Verstraeten *et al.*, 2006). Since geology and soil composition in general change only over very long time scales, short-term changes in (apparent) thermal inertia can be linked to changes in soil moisture.

## 2.3.2 Radar

### 2.3.2.1 Physical and semi-empirical models

Physical models, of which the Integral Equation Model (IEM, Fung *et al.*, 1992; Fung, 1994; Fung and Chan, 2004) is one of the most widely applied, theoretically describe the radar backscattering coefficient for a given set of sensor characteristics (wavelength, polarization), surface characteristics (soil dielectric permittivity, roughness) and incidence angle. The dielectric permittivity, and consequently soil moisture, can then be derived by inverting this relationship. Evidently, this inversion requires that the set of sensor characteristics is known, as well as the soil roughness. The latter is generally expressed in terms of a root mean square height, a correlation length and an autocorrelation function. The in situ collection of this information is a tedious process, preventing the operational applicability of these physical models. Furthermore, roughness parameters are difficult to characterize, and different sets of roughness parameters can be obtained over the same terrain when different measurement techniques are applied (Verhoest *et al.*, 2008).

Semi-empirical models are still based on a theoretical description of the behaviour of radar backscatter, but model parameters are derived from large sets of experimental data. Two examples of this type of models are the model developed by Oh *et al.* (1992) and that by Dubois *et al.* (1995). The experimental derivation of the model parameter limits the model applicability to conditions similar to those for which the parameters were obtained.

The physical models and semi-empirical models mentioned here have in com-



mon that they are to be applied on bare soil fields in the absence of vegetation. Both physical (e.g. Lang and Sidhu, 1983) and semi-empirical (e.g. Attema and Ulaby, 1978) vegetation backscatter models have been suggested as additions to the soil backscatter models for vegetated conditions. These vegetation backscatter models are, however, affected by the same limitations as the physical and semi-empirical soil backscatter models.

### 2.3.2.2 Empirical and change detection models

When abundant soil moisture information is available, radar backscatter can empirically be linked to ground measurements using (linear) regression models. Several studies observed spatial and temporal correlations of varying strength between in situ soil moisture and radar backscatter over different environments across the globe. Paloscia *et al.* (2008) found (spatial)  $R^2$  values ranging from 0.45 to 0.65 for soil moisture content and backscatter values from Envisat ASAR in AP mode. Moisture and backscatter for 20 selected agricultural fields in northern Italy were averaged per field prior to the establishment of the linear regression. When data acquired on different dates was combined, an  $R^2$  of 0.82 was obtained. Medium to strong linear correlations ( $R = 0.48$  to  $R = 0.77$ ) were also found over sandy and rocky Sahelian sites in Mali (Baup *et al.*, 2007), using ASAR WS images. Over grassland and wetland sites at the Tibetan Plateau, van der Velde *et al.* (2008) observed determination coefficients between 0.43 and 0.50 for ASAR WS images, when backscatter values averaged over different areas were compared to in situ soil moisture values. In the Canadian arctic, a spatial correlation yielding  $R^2 = 0.431$  was found by Wall *et al.* (2010) for a late season Radarsat-1 C-band image. Saturated conditions earlier in the season, however, resulted in a poor correlation between backscatter and in situ soil moisture ( $R^2 = 0.038$ ). Other studies found determination coefficients ranging from 0.13 to 0.72 using a linear relationship (Baghdadi *et al.*, 2007), or from 0.81 to 0.92 using an exponential relationship (Loew *et al.*, 2006), for different land-use types in Europe. Lievens and Verhoest (2012) analysed a time series of Radarsat-2 images and observed different linear relationships for bare fields categorized in different roughness classes. Also, radar polarization influenced the relationship between soil moisture and backscatter. The use of multiple polarizations, however, was not found to improve soil moisture estimation accuracy (Baghdadi *et al.*, 2006).

Given the dependency of the relationship between backscatter coefficient and soil moisture on a variety of factors including land cover and roughness, empirical relationships derived from one site cannot be transferred to another site. This constrains the applicability of this type of empirical models. The consistently observed (linear) relationship between soil moisture and backscatter, however, offers perspectives for the operational monitoring of soil moisture patterns using multi-temporal change detection methods.

One of the key advantages of microwave remote sensing is its ability to cap-



ture information irrespective of weather conditions and both day and night, thus allowing the creation of long and regular time series. The multitemporal approach, which has received a lot of attention, starts from the assumption that the temporal variability of roughness and vegetation is in general at a much longer time scale than that of soil moisture, allowing to consider roughness and vegetation as constants while relating changes in backscatter coefficient to changes in soil moisture.

Shoshany *et al.* (2000) suggested the use of a simple ratio or a normalized difference of backscatter measurements at two different times. Both resulted in a strong linear correlation ( $R^2 > 0.85$ ) with relative soil moisture when applied on ERS-2 SAR over two bare study sites in Israel. Moran *et al.* (2000) used a similar technique but introduced a reference level by subtracting a dry season backscatter from the other VV polarized images of an ERS-2 SAR time series. While soil moisture and backscatter resulted in a poor correlation ( $R^2 = 0.27$ ), soil moisture change and backscatter change relative to the dry season values resulted in a strong correlation with  $R^2 = 0.93$ . The same differencing technique was applied on Evisat ASAR VV and HH dual-polarized data over a semi-arid site in Niger, resulting in  $R^2 = 0.70$  (Zribi *et al.*, 2007). This technique was further refined (Thoma *et al.*, 2006) by normalizing the difference with the dry reference image. All these studies were executed over a period of one to a few months, or in areas with little variations in natural vegetation, for which the assumption that soil roughness and vegetation cover can be considered as constant over time holds true. As this period extends to a year or several years it can be expected that changing roughness and/or vegetation will have an effect on the high resolution SAR backscatter.

An operational soil moisture change detection was developed for ERS Scatterometer data (Wagner *et al.*, 1999a,b). The Scatterometer measures the backscatter from three viewing directions by a fore-beam, a mid beam and an aft-beam, resulting in three backscattering coefficients  $\sigma^0(\theta, t)$  at approximately the same time  $t$  for the same place on earth, corresponding to three incidence angles  $\theta$  [rad]. The three backscatter values and their corresponding incidence angles are used to assess the incidence angle dependence of  $\sigma^0(\theta)$ . This is done by deriving the slope  $\sigma'(\theta, t)$  [dB deg<sup>-1</sup>] and the curvature  $\sigma''(t)$  [dB deg<sup>-2</sup>], being the first and second derivative of  $\sigma^0(\theta, t)$  with respect to  $\theta$ , respectively. The high temporal resolution of ERS Scatterometer allows to study the seasonal behaviour of the derivatives, which were found to be related to seasonal variations in vegetation canopy cover (Wagner *et al.*, 1999a). A backscatter coefficient normalized to a reference incidence angle set at 40°, can subsequently be obtained from  $\sigma^0(\theta, t)$  and the slope and curvature:

$$\sigma^0(40^\circ, t) = \sigma^0(\theta, t) - \sigma'(40^\circ, t)(\theta - 40^\circ) - \frac{1}{2}\sigma''(t)(\theta - 40^\circ)^2. \quad (2.17)$$

With long time series of normalized backscatter measurements,  $\sigma^0(40, t)$  can

be transformed to a relative soil moisture content  $m_S(t)$  [-]:

$$m_S(t) = \frac{\sigma^0(40^\circ, t) - \sigma_{dry}^0(40^\circ, t)}{\sigma_{wet}^0(40^\circ, t) - \sigma_{dry}^0(40^\circ, t)}, \quad (2.18)$$

where  $\sigma_{dry}^0(40^\circ, t)$  and  $\sigma_{wet}^0(40^\circ, t)$  are the backscatter corresponding to entirely dry and wet conditions, respectively. Since the backscatter at entirely dry and wet conditions varies throughout the year in response to vegetation phenology,  $\sigma_{dry}^0(40^\circ, t)$  and  $\sigma_{wet}^0(40^\circ, t)$  are also function of time (Wagner *et al.*, 1999a,c).

The ERS Scatterometer soil moisture product was validated using in situ data over various regions, including the Ukrainian plains (Wagner *et al.*, 1999a), the Canadian prairies (Wagner *et al.*, 1999b), a Western African vegetation transition zone (Wagner and Scipal, 2000) and the Duero Basin, Spain (Ceballos *et al.*, 2005). The soil moisture algorithm was also applied on the Scatterometer's successor ASCAT (Bartalis *et al.*, 2007), and several improvements in the derivation of the model parameters ( $\sigma'(40^\circ, t)$ ,  $\sigma''(t)$ ,  $\sigma_{wet}^0(40^\circ, t)$  and  $\sigma_{dry}^0(40^\circ, t)$ ) were implemented (Naeimi *et al.*, 2009).

The Scatterometer/ASCAT change detection method has been adapted to be applied on higher spatial resolution ASAR GM data (Pathe *et al.*, 2009; Mladenova *et al.*, 2010; Doubková *et al.*, 2012), ASAR WS data (Wagner *et al.*, 2008) and Radarsat-2 data (Lievens and Verhoest, 2012). A major problem in adapting the change detection method to SAR data is that these sensors lack the multi-angular capabilities of Scatterometer and ASCAT. As a consequence, the derivation of the model parameters at high temporal resolution is no longer possible. Soil moisture change detection methods for SAR data thus suffer from errors introduced by the neglect of vegetation phenology or other seasonal influences (Doubková *et al.*, 2012).

### 2.3.3 Radiometers

Until the launch of the SMOS mission in 2009, the passive microwave radiometer AMSR-E was, together with the Scatterometer and ASCAT, the main data source for global soil moisture products. Several soil moisture retrieval algorithms were developed based on radiative transfer functions, differing in their physical formulations, parameters and ancillary data used. Four of the most commonly used algorithms are those developed by NASA (Njoku *et al.*, 2003), by JAXA (Koike *et al.*, 2004), by the US Department of Agriculture (USDA), also called the single-channel algorithm (Jackson, 2003), and the algorithm developed by the Vrije Universiteit Amsterdam (VUA) in collaboration with NASA, also called the Land Parameter Retrieval Model (LPRM, Owe *et al.*, 2001, 2008). Several of these products can derive soil moisture from either AMSR-E's X-band or its C-band. Although C-band radiation is theoretically more suitable for the monitoring of soil moisture given the larger penetration depth, X-band soil moisture is, globally, less

influenced by RFI (Njoku *et al.*, 2005). The importance of X- and C-band RFI should be considered in function of the study site.

Several studies compared accuracies of the different AMSR-E soil moisture products, sometimes including the active microwave product (Wagner *et al.*, 2007; Draper *et al.*, 2009; Gruhier *et al.*, 2010; Jackson *et al.*, 2010; Brocca *et al.*, 2011). The accuracies of the different products varied strongly over the different study sites, with different accuracies for the nighttime and daytime overpasses. Overall, accuracies decrease with increasing vegetation cover.

Soil moisture retrieval from SMOS data is based on physical models, taking advantage of the multi-angular capabilities of the instrument (Kerr *et al.*, 2012). Further product development and initial validation (e.g. Al Bitar *et al.*, 2012; Pan *et al.*, 2012) are currently ongoing. RFI remains an issue in the SMOS soil moisture retrieval, even though the L-band is an internationally protected wavelength (Olivia *et al.*, 2012).

# 3

## Study site and data collection

### 3.1 Study site

The Italian region of Calabria is situated in the southwestern tip of mainland Italy (Fig. 3.1). The peninsula measures approximately 250 km in length and 30 km to 100 km from the Tyrrhenian coast in the west to the Ionian Sea in the east, and is dissected longitudinally by the Calabrian Apennines. Elevations of the highest peaks in this mountain range exceed 2000 m, thus creating strong altitudinal differences over relatively short horizontal distances.

The topography of Calabria is reflected in the general land use pattern, with agricultural land dominating the lower plains and deciduous and coniferous forests covering the hillsides and higher elevations (Fig. 3.1). Arable land consist mostly of cereal crops and is dominant in the Crotona province in the eastern part of the peninsula. Due to the Mediterranean climate, agriculture at the lower elevations is rainfall limited and crops exhibit a winter growing season. At the higher elevations, crops cultivated at the plateaus or in some wider valleys may be characterized by

---

Parts of this chapter have been published as: Van doninck J., Peters, J., Lievens, H., De Baets, B., Verhoest, N. (2012). Accounting for seasonality in a soil moisture change detection algorithm for ASAR Wide Swath time series. *Hydrology and Earth System Sciences*, **16**(3), 773-786, DOI: 10.5194/hess-16-773-2012.

Peters, J., Conte, A., Van doninck, J., Verhoest, N., De Clercq, E., Goffredo, M., De Baets, B., Hendrickx, G., Ducheyne, E. (2013). On the relation between spatio-temporal soil moisture dynamics and the geographical distribution of *Culicoides imicola*. *Ecology*, submitted.

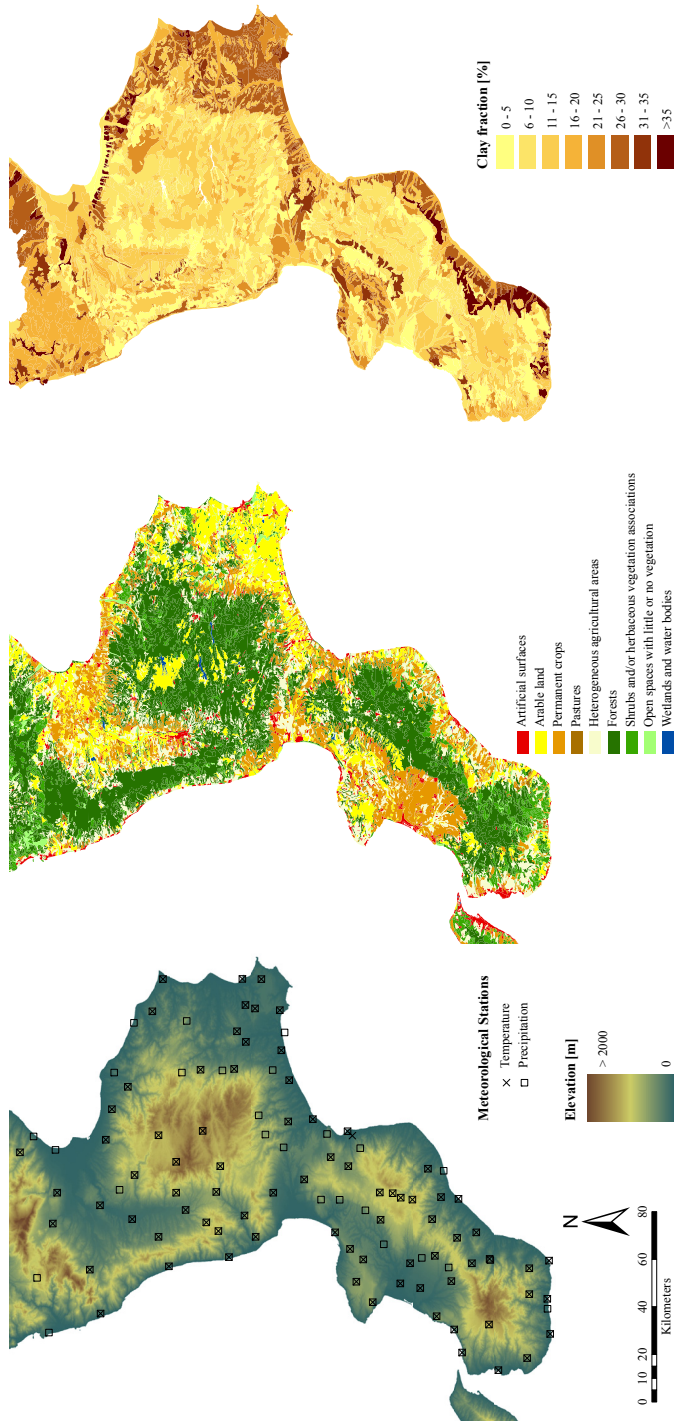


Figure 3.1: Topography of the study site with indication of meteorological stations (left), land cover (from Corine land cover 2000 (European Environmental Agency, 2002), middle) and soil texture (right) of the Italian region of Calabria.

different growing cycles as a result of lower temperatures and hence energy limited vegetation growth. Permanent crops are abundant around the city of Rosarno in the southeastern part of Calabria where these mainly consist of citrus and olive groves. Permanent crops in other parts of the region include, among others, vineyards.

Soil texture varies strongly over the peninsula (Fig. 3.1), with a clear east-west transition in texture. While sandy soils dominate the western coast and most higher elevations, higher silt and clay fractions are found in the plains and valleys along the eastern shoreline. Soil texture variability can be assumed to influence soil moisture content and its variability.

## 3.2 Elevation data

The digital elevation model (DEM) of Fig. 3.1 was created from Shuttle Radar Topography Mission (SRTM) data. This mission, flown onboard the space shuttle Endeavour in February 2000, collected elevation data for most part of earth's land surface using a C- and X-band radar (Farr *et al.*, 2007). The data used here is the 3 arcsec (approximately 90 m) DEM, version 4.1, obtained from the International Center for Tropical Agriculture - Consortium for Spatial Information website (<http://srtm.csi.cgiar.org/>).

In addition to SRTM, the 10 m resolution TINITALY/01 DEM (Tarquini *et al.*, 2012) was obtained for Calabria (<http://tinitaly.pi.ingv.it/>). This DEM, available for the entire Italian territory, was created from heterogeneous vector datasets and is freely available for scientific purposes.

## 3.3 In situ data

### 3.3.1 Soil moisture data

Two independent datasets of in situ soil moisture data were used in this study. A first dataset is obtained from permanent measurement stations. The second dataset was collected during a dedicated field campaign.

#### 3.3.1.1 Continuous soil moisture measurements

Five permanent in situ measurement stations, operated by the Centro Funzionale Multirischi della Calabria (<http://www.cfc Calabria.it>), are installed in Calabria (in Fitterizzi, Mongrassano, Torano, Chiaravalle and Satriano, labeled F, M, T, C and S in Fig. 3.2, respectively). At these stations, soil moisture measurements are recorded since 2001 at hourly intervals by Time Domain Reflectometers (TDR)

installed at 30, 60 and 90 cm depth (Brocca *et al.*, 2011). These data are provided to the scientific community through the International Soil Moisture Network (Dorigo *et al.*, 2011).

### 3.3.1.2 Field campaign

Additional soil moisture data was collected during a field campaign from September 16, 2009 until October 8, 2009. The initial goal of this field campaign was to obtain data that could be used as validation of remotely sensed soil moisture proxies. A major challenge in the validation of remotely sensed soil moisture using in situ measurements is bridging the scale gap between both (Brocca *et al.*, 2009). Since soil moisture can vary strongly over space due to variations in topography or soil composition, point-based in situ measurements are not necessarily representative for the area-averaged soil moisture content that is observed by remote sensing. A specific in situ measurement framework was set up to overcome this scale gap, where each in situ measurement site consists of a square grid of nine point measurements with a grid interspacing of 150 m (Fig. 3.2). As such, a spatial average and spatial variability of soil moisture can be assessed for each grid point, while maintaining a balance between accuracy and acquisition costs. Denser and/or larger in situ measurement grids would result in more reliable estimates of spatial averaged soil moisture and its variability, but would require more manpower. The consequence of this framework is that only a limited number of sites can be sampled each day and that, as a consequence, the temporal resolution of sampling is low. Therefore, a limited number of additional sites were selected that consisted of only a single measurement location but were sampled at higher temporal resolution. This would allow to obtain information on both spatial and temporal soil moisture patterns.

Between September 16 and September 29, 2009, 30 in situ measurement sites were selected, and coordinates of the grid points were recorded using a hand-held GPS (Garmin eTrex H). Sites were concentrated around the Crotona province in the eastern part of the peninsula and the Vibo Valentia province in the west, and labeled 1A to 1O (for Crotona) and 2A to 2O (for Vibo Valentia) in Fig. 3.2. A variety of land cover types were selected as sampling site, including croplands, forests, citrus and olive groves and grass- and shrubland. Often, a single site would contain various land cover types. Due to accessibility issues (mainly due to rugged terrain or fenced properties), some sites consist of fewer than nine grid points, with one site containing as few as four. Volumetric TDR measurements (TRIME-PICO64 probe, IMKO GmbH, Germany) and soil samples (converted to gravimetric soil moisture content) were acquired at all grid points during this first period, with exception of a few points where no TDR measurements could be made due to battery failure or dried-out soil. Both gravimetric and volumetric measurements were made over a depth of 10 cm.

All points were revisited during a second and third sampling period from 30/09



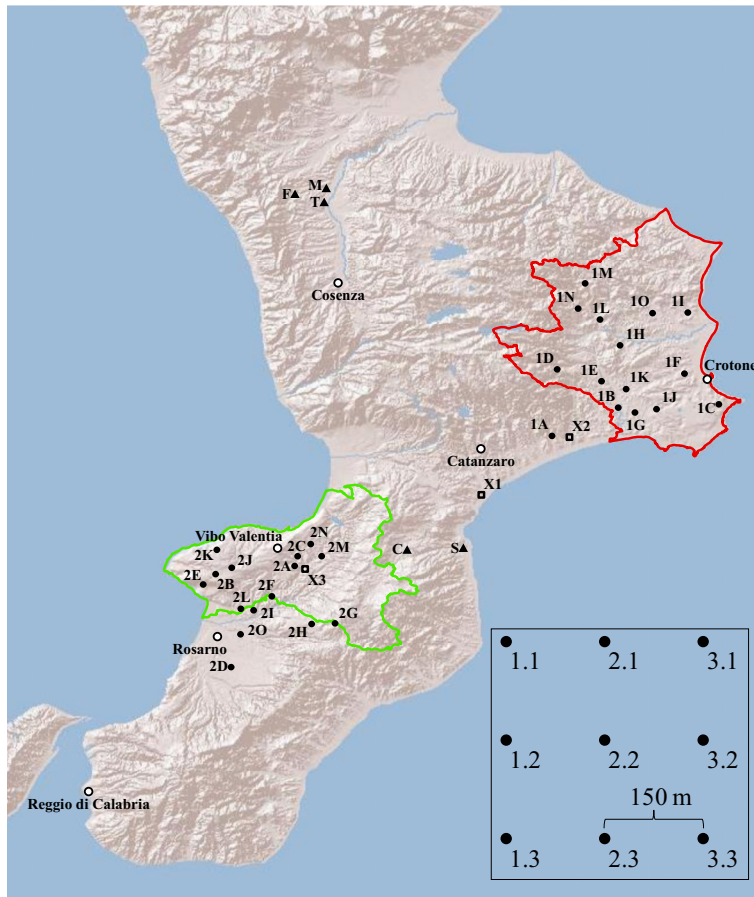


Figure 3.2: Location of in situ sites with sampling setup (inset), main cities and provinces of Vibo Valentia (green) and Crotona (red).

to 3/10/2009 and 7/10 to 8/10/2009, respectively. During the second period, only volumetric measurements were made, during the third period both volumetric and gravimetric soil moisture were collected. Soil moisture observations at the different grid points for all clusters, as well as their geographic coordinates, are given in Appendix A. The three additional individual points (labeled X1, X2 and X3 in Fig. 3.2) were selected in function of their accessibility and were sampled volumetrically and gravimetrically every one or two days, and occasionally multiple times per day.



### 3.3.2 Meteorological and pedological data

A dense network of meteorological stations is installed in Calabria by the Agenzia Regionale per la protezione dell'Ambiente della Calabria (ARPACAL). The stations record, at daily or higher resolution, several meteorological variables, including precipitation, temperature, wind velocity and direction and atmospheric pressure and humidity. From the online database ([www.arpacal.it](http://www.arpacal.it)), daily mean temperature and daily precipitation for the period 2000–2012 were obtained for 108 meteorological stations, of which 80 register temperature and all but one register precipitation (Fig. 3.1). It should be noted that not all of these stations were installed during the entire period 2000–2012 and that acquisitions may be missing for several days or months during which they were installed.

Soil mapping in the region of Calabria was performed by the Agenzia Regionale per lo Sviluppo e per i Servizi in Agricoltura (ARSSA). A digital soil map consisting of 2166 map polygons was developed based on more than 7000 soil samples (ARSSA, 2003). In addition to a general map of soil types, maps of several derived soil characteristics are provided. These include soil texture (sand, soil and silt fractions), fraction of soil organic matter, fraction of calcium carbonate and pH value.

## 3.4 A soil moisture model for Calabria

Although different sources of in situ soil moisture data were obtained in this study, these remain limited in both space and time. Therefore, a hydrological model was constructed to derive modelled soil moisture from meteorological and pedological data. Model outputs were validated using the different in situ soil moisture datasets, and can in turn be used as validation of remotely sensed soil moisture products. The validation of remotely sensed soil moisture using hydrological models is common practice to avoid the costly process of in situ data collection (Sandholt *et al.*, 2002; Pellarin *et al.*, 2006), and also helps to bypass the scale gap between in situ and remote sensing data.

### 3.4.1 Model structure

A spatially distributed soil moisture model, inspired by the hydrological BEACH model of Sheikh *et al.* (2009), was used here to estimate the soil moisture content of the topsoil. This particular model was selected because the soil moisture model needed to (1) run on a limited amount of readily available input data, (2) explicitly account for soil texture, (3) be spatially distributed, and (4) provide soil moisture estimates on a daily basis. The basic processes incorporated in the model are precipitation, infiltration, transpiration and evaporation (Fig. 3.3). The soil water

balance at location  $i$  is calculated as:

$$D \frac{\Delta\Theta_i}{\Delta t} = P_i - O_i - ET_i - Q_i, \quad (3.1)$$

where  $D$  is the depth of soil moisture simulation [mm],  $\Theta$  is the soil moisture content [ $\text{m}^3 \text{m}^{-3}$ ],  $P$  is precipitation [ $\text{mm day}^{-1}$ ],  $O$  is runoff [ $\text{mm day}^{-1}$ ],  $ET$  is evapotranspiration [ $\text{mm day}^{-1}$ ],  $Q$  is percolation to deeper soil layers [ $\text{mm day}^{-1}$ ], and  $\Delta t$  is the model time step [day].

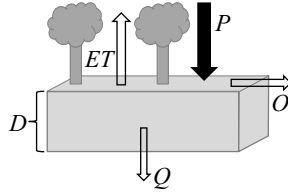


Figure 3.3: Processes incorporated in the hydrological model.

Runoff was estimated by a bucket model assuming that infiltration ( $I$ , [ $\text{mm day}^{-1}$ ]) proceeds until the infiltration capacity of the topsoil has been reached (Sheikh *et al.*, 2009):

$$O_i = P_i - I_i \text{ if } P_i > I_i, \quad (3.2)$$

where the infiltration during a time step of one day was defined as:

$$I_i \Delta t = \min [P_i \Delta t, (\Theta_{\text{sat}_i} - \Theta_i) D], \quad (3.3)$$

where the soil moisture content at saturation ( $\Theta_{\text{sat}}$ , soil water potential of  $-0.1$  kPa) was estimated through its empirical relationship with soil texture and soil organic matter content (Saxton and Rawls, 2006).

Daily evapotranspiration was estimated as a soil moisture dependent fraction of its potential rate ( $ET_{p,i}$ ); Hamon, 1963):

$$ET_{p,i} = 0.0138 L_i [\rho_{\text{sat}_i} T_i] \quad (3.4)$$

and

$$ET_i = K_r ET_{p,i},$$

with

$$K_r = \begin{cases} 0, & \text{if } \Theta_i < \Theta_{\text{dry}_i} \\ \frac{\Theta_i - \Theta_{\text{dry}_i}}{\Theta_{\text{fc}_i} - \Theta_{\text{dry}_i}}, & \text{if } \Theta_{\text{dry}_i} < \Theta_i < \Theta_{\text{fc}_i} \\ 1, & \text{if } \Theta_i > \Theta_{\text{fc}_i} \end{cases}, \quad (3.5)$$

where  $L$  is day length [hours],  $\rho_{\text{sat}}(T)$  [ $\text{g m}^{-3}$ ] the saturated absolute humidity at the mean daily air temperature  $T$ .  $\Theta_{\text{fc}}$  and  $\Theta_{\text{dry}}$  are the soil moisture content at field capacity (soil water potential of  $-33$  kPa) and air dryness (soil water potential of  $-22\,000$  kPa), respectively, and  $K_r$  is a dimensionless reduction constant, depending on the actual soil moisture content. If the actual soil moisture content is higher than the soil moisture content at field capacity, then evapotranspiration is at its potential rate. If the soil moisture content is lower, then the actual evapotranspiration is lower than its potential rate. This reflects the two evapotranspirative stages: an energy limiting stage ( $K_r = 1$ ) and a soil moisture limiting stage ( $K_r < 1$ ) (Sheikh *et al.*, 2009, and references therein).

The percolation during a time step of one day was estimated as (Raes, 2002):

$$Q_i \Delta t = D \chi_i (\Theta_{\text{sat}_i} - \Theta_{\text{fc}_i}) \frac{e^{\Theta_i - \Theta_{\text{fc}_i}} - 1}{e^{\Theta_{\text{sat}_i} - \Theta_{\text{fc}_i}} - 1}, \quad \text{if } \Theta_i > \Theta_{\text{fc}_i}, \quad (3.6)$$

where  $\chi$  is a dimensionless drainage characteristic that is related to the saturated hydraulic conductivity ( $K_{\text{sat}}$ , [ $\text{mm day}^{-1}$ ]) as:

$$\chi_i = 0.0866 e^{0.8063 \log K_{\text{sat}_i}}, \quad (3.7)$$

### 3.4.2 Model inputs

The digital soil map provided by ARSSA and gridded to a raster of 1 km resolution was used as a modelling basis. Soil texture and organic matter were transformed to maps of  $\Theta_{\text{sat}}$ ,  $\Theta_{\text{fc}}$ ,  $\Theta_{\text{dry}}$  and  $K_{\text{sat}}$ , following Saxton and Rawls (2006). Daily precipitation and mean air temperature observations obtained from all available meteorological stations were interpolated to this 1 km grid using inverse distance weighting (IDW). Because air temperature shows a strong negative linear correlation with elevation ( $R = -0.83$ , on average), this trend was removed using the SRTM DEM prior to interpolation. After interpolation, the trend was again added to the interpolated values.

In order to define the value of the power parameter required in IDW in an objective way, interpolation was executed using 15 values of the power parameter, ranging from 0.25 to 5. The accuracy of interpolation was assessed by means of the Root Mean Square Error (RMSE) for an independent validation set of 10 % of the meteorological stations, selected randomly for each day separately. The RMSE, averaged over all the days in the time series, in function of the power parameter is given in Fig. 3.4. It is observed that the RMSE reaches a minimum at a power parameter of 1.5 and 2 for temperature and precipitation, respectively.

The power parameters corresponding to the minimal RMSE were used for IDW of temperature and precipitation, now using all available meteorological stations. As such, time series of spatially interpolated daily precipitation and temperature for the period 2000–2012, at the 1 km grid of the pedological data, were obtained.

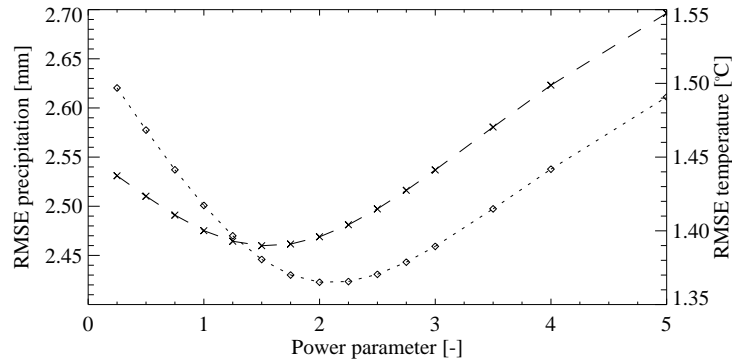


Figure 3.4: RMSE for interpolated values of temperature (crosses) and precipitation (diamonds) in function of IDW power parameter.

Precipitation and temperature could then, together with the fractions sand, silt, clay and soil organic matter, be used to solve the soil moisture balance (Eq. 3.1). The hydrological model was run for depths of the soil layer of 10 cm and 30 cm.

### 3.4.3 Model validation

Validation of the hydrological model, ran for a depth of 10 cm, was performed using the data obtained during the field campaign from September 16 until October 8, 2009. A first validation is based on the 30 sampling sites with clustered soil moisture observations. For each site, the different volumetric soil moisture observations were averaged to a representative value, and the standard deviation was computed. The scatterplot of the thus obtained in situ soil moisture versus the modelled 10 cm soil moisture of the corresponding days is given in Fig. 3.5(a). This validation results in a poor correlation ( $R^2 = 0.03$ ) between measured and modelled soil moisture. One reason for the poor correlation is the temporal gap between both. While most in situ observations were collected during the morning or early afternoon, the hydrological model provides daily soil moisture estimates based on the precipitation of the entire day. Rainfall during late afternoon or evening will thus introduce errors, as is the case for some of the low in situ soil moisture observations ( $< 0.1 \text{ m}^3 \text{ m}^{-3}$ ) which were acquired after a period without rainfall but abundant precipitation occurred later that day. To avoid these effects, modelled soil moisture was also validated with a time lag of one day (Fig. 3.5(b)). This drastically increased the coefficient of determination to 0.21. Nevertheless, the predictive capacity of the hydrological model remains low, especially for soil moisture levels around  $0.3 \text{ m}^3 \text{ m}^{-3}$ . This can be due to intra-day moisture fluctuation, simplifications in the model structure (e.g. the neglect of vegetation cover, which is different for all in situ sites) or uncertainties in the soil moisture map and the derivation of the soil water characteristics.

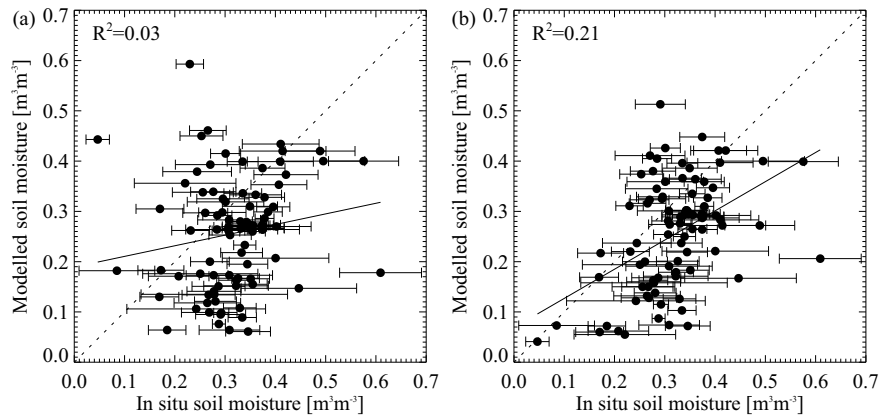


Figure 3.5: Validation of modelled soil moisture over 10 cm at 30 in situ sites (dots are site-averaged soil moisture, bars indicate standard deviations), based on meteorological input data of the day itself (a) and with one day time lag (b).

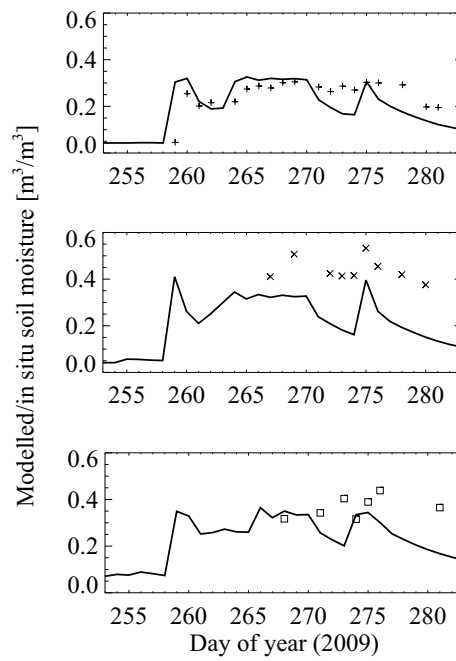
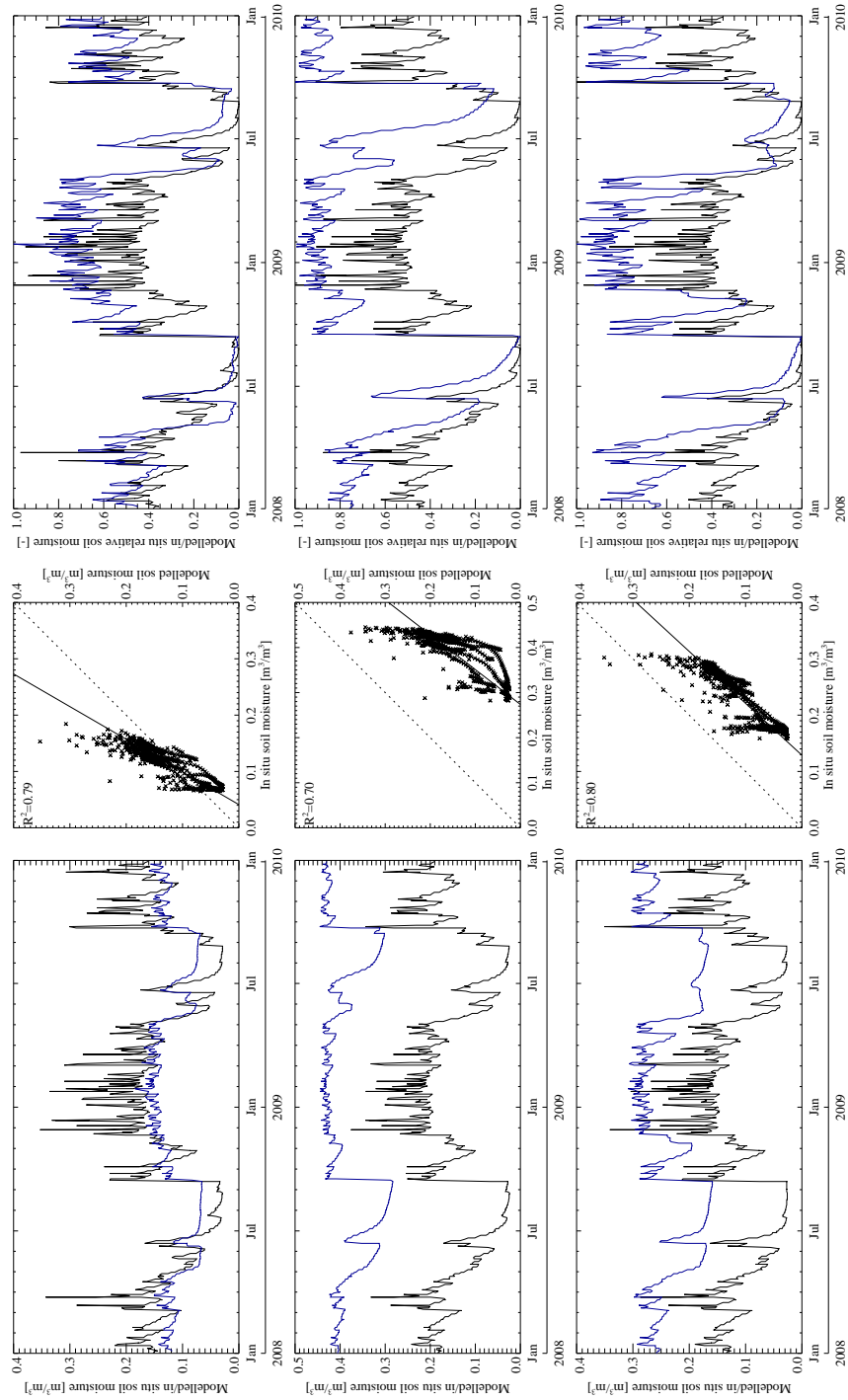


Figure 3.6: Validation of modelled soil moisture over 10 cm at in situ sites X1 (top), X2 (middle) and X3 (bottom).

A multitemporal validation for the three additional sampling points reveals the same problem of the time gap between in situ observations and model predictions (Fig. 3.6). Furthermore, systematic errors in absolute soil moisture content are observed, most notably for point X2. Some distinct increases and decreases in modelled soil moisture are, however, also observed in situ. The temporal behaviour of modelled soil moisture, however, corresponds to that of the in situ measurements.

The soil moisture generated for a surface layer of 30 cm depth was validated using the data provided by the International Soil Moisture Network. To this end, the hourly soil moisture measurements of the five in situ measurement stations were aggregated to daily averages. The temporal behaviour of modelled and in situ soil moisture for the years 2008 and 2009 is given in Fig. 3.7. It is observed that the hydrological model is unable to accurately reproduce the absolute soil moisture content of the in situ measurements. For all five stations, the dynamic range of soil moisture is overestimated. This is partly due to the fact that the hydrological model provides an average over the 30 cm top layer, while in situ measurements reflect the soil moisture content at a depth of 30 cm only. Additionally, soil moisture is systematically underestimated for the Mongrassano and Torano sites. This might be caused by local topography, which is not incorporated into the model, or by uncertainty on the soil map or on the conversion of soil texture and organic matter fractions to the soil water characteristics. Notwithstanding these discrepancies between modelled and in situ soil moisture, correlations between both are strong ( $R^2$  of 0.79, 0.70, 0.80, 0.85 and 0.78 for Fitterizzi, Mongrassano, Torano, Chiaravale and Satriano, respectively). When scaling both measured and modelled soil moisture between minimum and maximum values of the time series, a much stronger similarity between the two relative soil moisture contents is observed. Some gaps remain due to errors in the estimation of the soil water characteristics or as a result of incorrect interpolation of precipitation observations between meteorological stations.

Overall, it can be concluded that the basic hydrological model applied here is unable to correctly produce absolute soil moisture content for either the 10 cm or 30 cm top soil layer. The temporal dynamics of soil moisture, however, are well captured for both soil layer depths. It is therefore advisable to validate the remotely sensed soil moisture products temporally rather than spatially, and to use relative soil moisture content rather than absolute volumetric soil moisture content. A reference depth of 10 cm is chosen for the validation of remote sensing products, since modelled soil moisture over thinner layers could not be validated. Ideally, a soil moisture model with smaller time steps, e.g. hourly, would be used for validation in order to avoid errors introduced by varying meteorological conditions throughout the day. This would, however, drastically increase processing time.



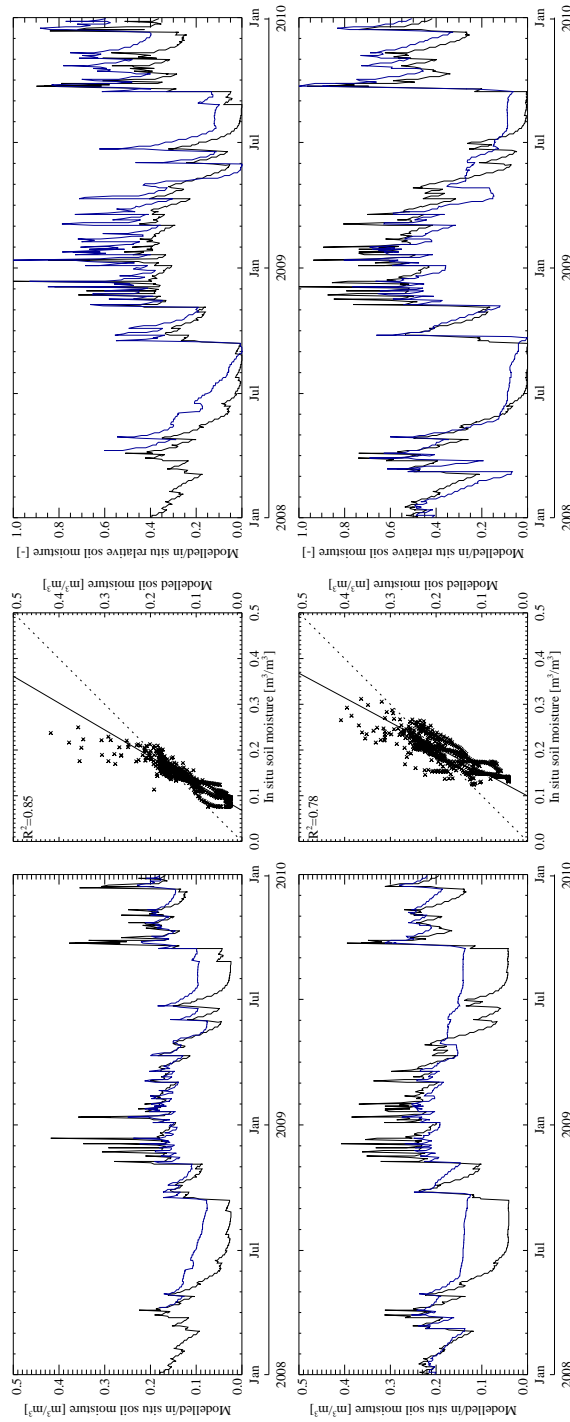


Figure 3.7: Validation of modelled soil moisture over 30 cm depth at (from top to bottom) Fitterizzi, Mongrassano, Torano, Chiaravalle and Satriano in situ stations. Left column: modelled (thick line) and in situ (blue line) volumetric soil moisture content for the years 2008–2009. Middle column: scatterplot of in situ and modelled soil moisture for the same period. Right column: modelled (thick line) and in situ (blue line) relative soil moisture during the same period.



## 3.5 Remote sensing data

### 3.5.1 Optical data

Standard preprocessed MODIS products for land applications are distributed through the Land Processes Distributed Active Archive Center (LP DAAC), located at the U.S. Geological Survey (USGS) Earth Resources Observation and Science (EROS) Center (<http://lpdaac.usgs.gov>). Products are either derived for Terra and Aqua separately or for both combined, and provided at different grid spacings and temporal compositing periods. Table 3.1 summarizes the products and datasets used in this study. For Calabria, these are all at 1 km resolution. Additionally, some global 0.05° (5600 m) products were acquired.

Table 3.1: MODIS products used in this study ('MxD' stands for 'MOD' and 'MYD', indicating Terra and Aqua products, respectively, 'MCD' indicates combined products).

Product name	Description	Spat. res.	Temp. res.
MCD43B3	albedo	1000 m	16 day
MCD43B3	albedo	0.05°	16 day
MxD11A1	land surface temperature and emissivity	1000 m	daily
MxD11A2	land surface temperature and emissivity	1000 m	8 day
MxD11C1	land surface temperature and emissivity	0.05°	daily
MxD13A2	vegetation indices	1000 m	16 day

### 3.5.2 SAR data

Although the Global Monitoring mode of ASAR was selected as the global background mission over land surfaces, only limited GM acquisitions over Europe are available due to different acquisition priorities over this continent. Wide Swath mode data over Calabria is more abundant. This study uses 130 WS images in VV polarization acquired during both ascending (42 images) and descending (88 images) overpasses between January 2008 and August 2011. This corresponds to, on average, 4 acquisitions per month. Descending mode images are acquired around 9:00 a.m., ascending mode images at 8:45 p.m. ASAR WS images are provided by ESA under a Category-1 proposal at level 1B preprocessing, which includes slant range to ground range corrections and resampling to a 75 m pixel spacing.

### 3.5.3 Low resolution remote sensing soil moisture products

Three operational coarse resolution soil moisture products are used as reference datasets. Two products are derived from AMSR-E data, each by applying a different algorithm. AMSR-E soil moisture products derived using the algorithm developed by NASA (Njoku *et al.*, 2003) are distributed by the National Snow

and Ice Data Center (Njoku, 2008). For this study, Level 3 descending mode soil moisture was acquired. The second AMSR-E product, the LPRM (Owe *et al.*, 2008) developed by VUA/NASA, is provided through the ADAGUC web portal ([http://geoservices.falw.vu.nl/adaguc\\_portal\\_dev/](http://geoservices.falw.vu.nl/adaguc_portal_dev/)). Both AMSR-E products are distributed in  $0.25^\circ$  pixel grids. Descending orbit soil moisture products were selected since these are assumed to provide more accurate estimates (Draper *et al.*, 2009; Jackson *et al.*, 2010), although this was contradicted in a recent comparative study (Brocca *et al.*, 2011). The third coarse resolution product used for comparison is the TU Wien-EUMETSAT ASCAT surface soil moisture product (Bartalis *et al.*, 2007; Naeimi *et al.*, 2009), based on a change detection algorithm. ASCAT data were provided by the TU Wien Institute of Photogrammetry and Remote Sensing (IPF) in a Discrete Global Grid with grid spacing of approximately 12.5 km.



# 4

## A soil moisture change detection algorithm for ASAR Wide Swath time series

### 4.1 Introduction

SAR systems can reach much higher spatial resolutions than the currently operational coarse resolution passive and active microwave soil moisture products, making them attractive for applications on watershed and field scale. Despite the large volume of research conducted on the derivation of soil moisture from SAR, routinely produced soil moisture maps are not yet available (Kerr, 2007). The difficulty of mapping soil moisture from SAR lies in the nature of the reflected signal, which is, apart from soil moisture, also influenced by terrain properties such as topography, vegetation cover and soil roughness. Separating the soil moisture contribution to the backscatter signal from the roughness and vegetation contribution has been attempted using physical backscatter models in combination with multiple-polarized and/or multi-angular data (Zribi *et al.*, 2005, 2007; Baghdadi *et al.*, 2006; Rahman *et al.*, 2008; Gherboudi *et al.*, 2011) or by using effective

---

This chapter is based on: Van doninck J., Peters, J., Lievens, H., De Baets, B., Verhoest, N.E.C. (2012). Accounting for seasonality in a soil moisture change detection algorithm for ASAR Wide Swath time series. *Hydrology and Earth System Sciences*, **16**(3), 773-786, DOI: 10.5194/hess-16-773-2012.

Van doninck, J., Wagner, W., Melzer, T., De Baets, B., Verhoest, N.E.C. (2013). Seasonality in the angular dependence of ASAR Wide Swath backscatter. *IEEE Geoscience and Remote Sensing Letters*, submitted.

roughness parameters (Su *et al.*, 1997; Baghdadi *et al.*, 2002; Rahman *et al.*, 2007; Lievens *et al.*, 2011; Lievens and Verhoest, 2011). However, the satellite and/or ancillary data required in these models are seldom readily available.

Alternatively, the modelling or description of vegetation and soil roughness has been circumvented using a multitemporal approach. When comparing two or more images over the same site, obtained over a time frame in which only minor vegetation or soil roughness variations occur, changes in backscatter can be attributed to changes in soil moisture (Narayan *et al.*, 2006). Shoshany *et al.* (2000), for example, suggested to use a normalized difference of SAR backscatter of two images as an indicator of soil moisture changes between the times of image acquisition. On a larger time series of 10 SAR images over one month time, Wickel *et al.* (2001) found high correlations between soil moisture change and backscatter change for wheat stubble fields. Pathe *et al.* (2009) presented a methodology, based on the ERS scatterometer and ASCAT soil moisture retrieval algorithm developed at the TU Wien (Wagner *et al.*, 1999b), to derive a 1 km soil moisture index from Envisat ASAR in GM mode and applied it to 697 ASAR GM images over Oklahoma. The same product was validated using in situ and airborne soil moisture data over an area in southeastern Australia (Mladenova *et al.*, 2010).

These kinds of multitemporal approaches offer opportunities for routinely mapping soil moisture at high spatial resolution with the upcoming Sentinel-1 mission (Attema *et al.*, 2007). Given the large data volume to be provided by Sentinel-1, soil moisture change detection techniques developed for ASAR are likely to be applicable and improved for Sentinel-1 data. One big challenge in a multitemporal soil moisture retrieval, however, remains the characterization of the influence of seasonally changing vegetation on the backscatter signal (Wagner *et al.*, 2009).

In this chapter, a change detection method is applied on a 3 year time series over Calabria, Italy, to infer a soil moisture index from ASAR Wide Swath data. The change detection is preceded by an angular correction to be able to compare images with different viewing geometries and validated using a hydrological model. Additionally, the influence of vegetation phenology in the different processing steps is assessed using a simple vegetation index from optical remote sensing.

## 4.2 Study site and data

This part of the research is performed on 80 descending mode ASAR Wide Swath images, completely or partially covering Calabria and acquired between January 2008 and December 2010. Preprocessed level 1B ASAR WS images were further preprocessed using Next ESA SAR Toolbox (NEST) software and included geometric correction by a Range-Doppler orthorectification (Small and Schubert, 2008), using the SRTM DEM and DORIS precise orbit files, and radiometric cal-

ibration. Because of the relatively low resolution of the SRTM DEM, ASAR WS images were resampled to 1 km resolution prior to incidence angle normalization. Downscaling to 1 km resolution was also performed to be able to compare the ASAR data with the coarser resolution MODIS *NDVI* data and the soil moisture data obtained from the hydrological model, even though this implies a reduction of the spatial resolution to that of ASAR in Global Monitoring mode.

MODIS *NDVI* images were used in order to obtain information on seasonal vegetation dynamics. Since *NDVI* changes only slowly over time (Fensholt and Sandholt, 2003), 16-day composite images at 1 km resolution were considered to be adequate to describe the yearly vegetation behaviour. The accuracy of the ASAR WS soil moisture index derived in this study is compared to accuracies of three operational coarse resolution soil moisture products: the AMSR-E NASA and AMSR-E LPRM products and the TU Wien-EUMETSAT ASCAT product.

### 4.3 Multitemporal soil moisture retrieval

#### 4.3.1 Change detection model

As a first step of the change detection model, effects on backscatter due to varying incidence angle were corrected by a pixel-wise multitemporal incidence angle normalization (Loew *et al.*, 2006; Zribi *et al.*, 2007; Wagner *et al.*, 2008; Pathe *et al.*, 2009). Using a linear model, which is sufficient for the range of incidence angles covered in Wide Swath mode, the angular dependence of backscatter is expressed as:

$$\sigma^0(\theta) = \gamma + \beta\theta, \quad (4.1)$$

where  $\sigma^0(\theta)$  is the backscatter coefficient [dB] at incidence angle  $\theta$  [deg], and  $\gamma$  [dB] and  $\beta$  [dB deg<sup>-1</sup>] are polynomial coefficients. These polynomial coefficients are found through linear regression between  $\theta$  and  $\sigma^0(\theta)$  for all the observations over an image pixel. The angular correction coefficient  $\beta$  can subsequently be used to normalize the backscatter observation to a common incidence angle of 30° ( $\sigma^0(30^\circ)$ ):

$$\sigma^0(30^\circ) = \sigma^0(\theta) - \beta(\theta - 30^\circ), \quad (4.2)$$

Since the linear model is not necessarily valid for the range of incidence angles found over sloped terrain, pixels with terrain slopes higher than 20° (27.69 % of all pixels) were masked and discarded for further analysis. Slopes higher than this threshold are also likely to be affected by radar layover.

The change detection model initially developed for ERS scatterometer and MetOp ASCAT (Wagner *et al.*, 1999b; Naeimi *et al.*, 2009), and subsequently applied on ASAR Global Monitoring (Pathe *et al.*, 2009; Mladenova *et al.*, 2010) and Wide Swath (Wagner *et al.*, 2008) data, was adopted in this chapter. In this multitemporal model, a relative surface soil moisture index ( $\Theta_{\text{ASAR}}$ ) is expressed

as:

$$\Theta_{\text{ASAR}} = \frac{\sigma^0(30^\circ) - \sigma_{\text{dry}}^0(30^\circ)}{S}, \quad (4.3)$$

where  $\sigma_{\text{dry}}^0(30^\circ)$  is the dry reference backscatter [dB], the pixel's backscatter coefficient at entirely dry conditions, and  $S$  is the sensitivity of the backscatter coefficient to soil moisture variations [dB]. The sensitivity is defined as the difference between  $\sigma_{\text{dry}}^0(30^\circ)$  and  $\sigma_{\text{wet}}^0(30^\circ)$ , the wet reference backscatter [dB], the pixel's backscatter at entirely wet conditions:

$$S = \sigma_{\text{wet}}^0(30^\circ) - \sigma_{\text{dry}}^0(30^\circ). \quad (4.4)$$

Dry and wet reference backscatter are extracted from  $\sigma^0(30^\circ)$  time series per pixel, where  $\sigma_{\text{dry}}^0(30^\circ)$  is defined as the average of the 5 % lowest backscatter coefficients in the time series and  $\sigma_{\text{wet}}^0(30^\circ)$  is the average of the 5 % highest backscatter coefficients. The 5 % averages are used to reduce possible noise effects. Although the dry reference and sensitivity can be expected to change seasonally as a result of vegetation phenology,  $\sigma_{\text{dry}}^0(30^\circ)$  and  $S$  are here initially treated as constants. Effects of neglecting the seasonal variations of vegetation are discussed later. Since  $\Theta_{\text{ASAR}}$  is a value between zero (under entirely dry conditions) and one (under fully saturated conditions), the modelled soil moisture is also rescaled to this range using the extreme values in the time series for each pixel. This way, both  $\Theta_{\text{ASAR}}$  and the rescaled modelled soil moisture ( $\Theta_{\text{model}}$ ) can be considered to represent the soil's degree of saturation and can be mutually compared. This also helps to reduce the effects of systematic errors in the hydrological model (Chapter 3).

### 4.3.2 Model parameters

The model parameters (angular correction coefficient  $\beta$ , dry reference backscatter  $\sigma_{\text{dry}}^0(30^\circ)$  and sensitivity  $S$ ) for the study site are displayed in Fig. 4.1. All three parameters reflect the general land cover pattern, with low  $\sigma_{\text{dry}}^0(30^\circ)$  and  $\beta$  and high  $S$  over arable land, and an inverse pattern for forested and urban areas. This has been observed in previous studies over different areas (Wagner *et al.*, 1999c, 2008; Pathe *et al.*, 2009).

Dry reference ranges from approximately -14 dB over arable land to -8 dB for forests, while the sensitivity varies between 1 dB and 6 dB for forests and arable land, respectively. Sensitivity values are notably smaller than those found by Wagner *et al.* (2008) for 73 ASAR WS images over the REMEDHUS soil moisture network in the Duero basin, Spain, where sensitivity ranged from 3 dB for forests and settlements to 12 dB over agricultural areas. In the latter study, dry and wet reference, and thus sensitivity, were obtained using the mean backscatter and standard deviation over a time series, assuming a normal distribution of backscatter

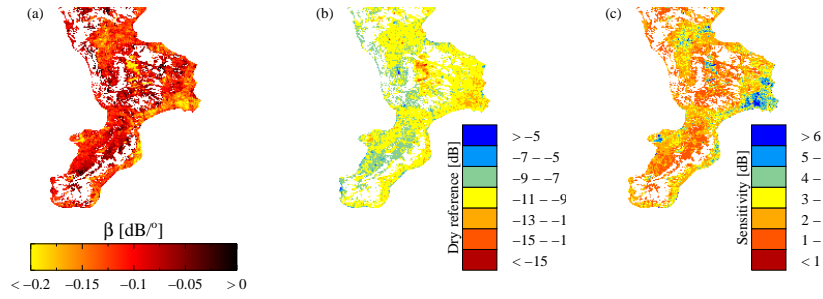


Figure 4.1: Angular correction coefficient  $\beta$  for each pixel in the study site (a); dry reference backscatter (b); sensitivity of the backscatter to soil moisture changes, derived as the difference between dry reference and wet reference backscatter (c).

values. This can explain the difference in the retrieved model parameters. Also, the number of images used in the present study might not be sufficient to correctly identify extreme dry and wet conditions, which will result in an underestimation of  $S$ . This is enhanced by the selection of dry and wet reference based on the 5 % lowest and highest backscatter coefficients. Longer and denser time series can be expected to result in more stable dry reference and sensitivity estimates.

High sensitivity values, relative to the sensor's radiometric accuracy, are a prerequisite to obtain reliable soil moisture estimates (Mladenova *et al.*, 2010). The low sensitivity values found over much of the study site thus might introduce high retrieval errors. The preprocessing step, however, included an averaging of the backscatter observations at 75 m pixel spacing to a 1 km grid. The noise reduction accompanying this averaging allows these low sensitivity pixels to be further processed.

### 4.3.3 Vegetation and soil moisture dynamics

Figures 4.2(a) and 4.3(a) show the temporal behaviour of  $\Theta_{\text{model}}$ ,  $\Theta_{\text{ASAR}}$  and  $NDVI$  for two 1 km pixels, one over arable land (cereal) at low elevation in the eastern part of the study site, the other over high elevation deciduous forests in the central southern part. The arable land pixel clearly exhibits a winter growing season, limited by the availability of soil moisture. The  $NDVI$  misses short-term changes in soil moisture and the seasonal cycle lags behind on the soil moisture cycle, which is typical for the conservative response of  $NDVI$  to soil moisture changes (Fensholt and Sandholt, 2003). The correlation of 16-day  $NDVI$  and  $\Theta_{\text{model}}$ , averaged over the 16-day compositing period (Fig. 4.2(b)), is therefore limited ( $R=0.55$ ). ASAR soil moisture shows a similar seasonal pattern for the arable land pixel, although the correlation with modelled soil moisture (Fig. 4.2(c)) is much stronger ( $R=0.80$ ).



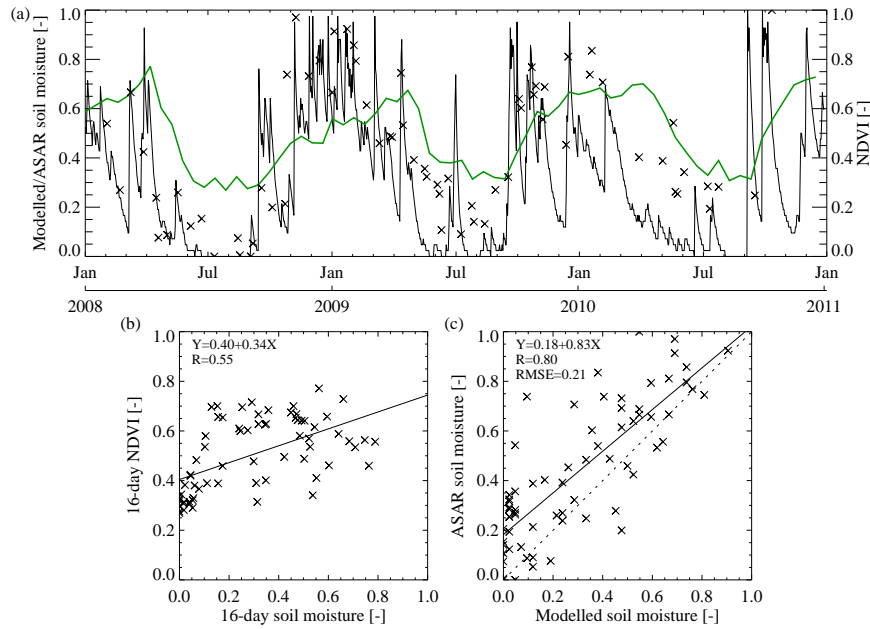


Figure 4.2: Temporal behaviour of modelled soil moisture (black line), *NDVI* (thick green line) and ASAR soil moisture (crosses) for a pixel over arable land (a); scatterplot of modelled soil moisture, averaged over 16 days, and 16-day *NDVI* for the same pixel (b); scatterplot of modelled soil moisture and ASAR soil moisture for the same pixel (c).

For the forest pixel, the *NDVI* cycle is in antiphase with the soil moisture cycle (Fig. 4.3(a)). This is because at this elevation, vegetation growth is energy limited rather than moisture limited, resulting in a summer growing season and a strong negative ( $R = -0.60$ ) correlation between *NDVI* and soil moisture (Fig. 4.3(b)). ASAR soil moisture for this pixel remains in phase with the modelled soil moisture, although the correlation (Fig. 4.3(c)) is much weaker ( $R = 0.50$ ) than for the arable land.

Figure 4.4 shows the correlation coefficient between  $\Theta_{\text{model}}$  and *NDVI* (Fig. 4.4(a)) and  $\Theta_{\text{model}}$  and  $\Theta_{\text{ASAR}}$  (Fig. 4.4(b)) for all pixels in the study site, and confirms what was observed in Figs. 4.2 and 4.3. *NDVI* shows a moderate to strong positive correlation with soil moisture for the lower elevations, both over arable land and over permanent crops (citrus and olive plantations), and a strong negative correlation over forest pixels at high elevations. For arable land at the higher elevations, the correlation coefficient for *NDVI* is close to zero. Correlation coefficients for ASAR soil moisture are in general much higher, with  $R$  values over 0.6 for most of the arable land areas. In regions with permanent crops,  $R$

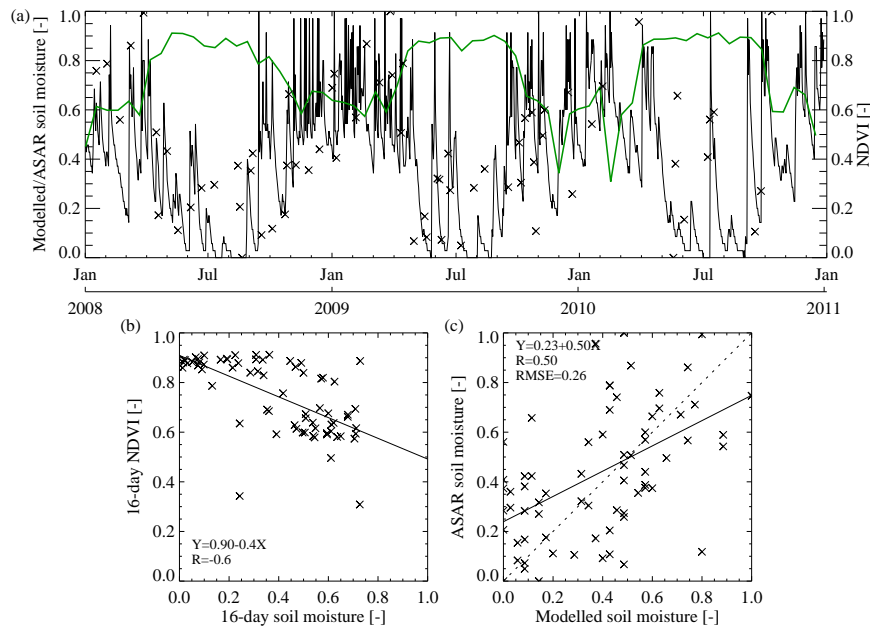


Figure 4.3: Temporal behaviour of modelled soil moisture (black line), *NDVI* (thick green line) and ASAR soil moisture (crosses) for a pixel over deciduous forest (a); scatterplot of modelled soil moisture averaged over 16 days and 16-day *NDVI* for the same pixel (b); scatterplot of modelled soil moisture and ASAR soil moisture for the same pixel (c).

values for  $\Theta_{ASAR}$  are lower and even slightly lower than those for *NDVI*. Over forests,  $\Theta_{ASAR}$  is weak to moderate positively correlated with  $\Theta_{model}$ .

Regions where *NDVI* is positively correlated with modelled soil moisture correspond to regions with a strong correlation between ASAR soil moisture and modelled soil moisture. This might suggest that the change detection algorithm, as applied on the ASAR Wide Swath data, does not as such reflect changes in surface soil moisture, but rather changes in vegetation phenology. However,  $\Theta_{ASAR}$  is in general correlated much stronger with  $\Theta_{model}$  than *NDVI* is, and even in many locations where *NDVI* is negatively correlated with soil moisture, the ASAR change detection method still results in moderate positive correlations. It can thus be assumed that soil moisture dynamics have a much stronger influence on SAR backscatter than vegetation dynamics, and the backscatter signal is influenced by soil moisture even under relatively dense canopies.

Figure 4.4(b) shows a strong correspondence with the spatial pattern of sensitivity to soil moisture (Fig. 4.1(c)), resulting in a correlation coefficient between

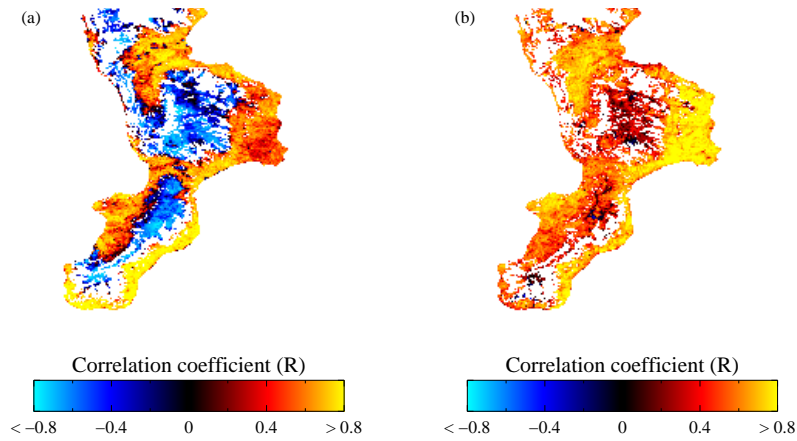


Figure 4.4: Correlation coefficients between modelled soil moisture averaged over 16 days and 16-day *NDVI* (a) and modelled soil moisture and ASAR soil moisture (b), for each pixel of the study site for the 3-year time series.

both images of 0.55. This confirms the presumption that a high  $S$  is required to obtain reliable soil moisture estimates. However, correlations of 0.5 and higher are observed for many pixels with sensitivities below 3 dB.

## 4.4 Seasonality effects on model parameters

In the preceding, changes in vegetation and surface roughness throughout the year have been ignored in defining the model parameters  $\beta$ ,  $\sigma_{\text{dry}}^0(30^\circ)$  and  $S$ , and in the derivation of the ASAR soil moisture index. Nevertheless, all three model parameters are possibly influenced by seasonality effects.

### 4.4.1 Seasonality effects on $\beta$

Influences of vegetation cover on the multitemporal incidence angle correction coefficient  $\beta$  can be observed in Fig. 4.1(a), where vegetated areas in general have a higher (less negative)  $\beta$ . This is caused by the lower angular dependence of the radar backscatter for vegetation compared to bare soils. The angular dependence can thus be expected to vary seasonally over vegetated surfaces. In the ERS and ASCAT retrieval algorithm, this seasonality was incorporated using the multi-angular capabilities of these sensors (Wagner *et al.*, 1999b). For SAR systems, Loew *et al.* (2006) derived the parameter  $\beta$  for the winter and summer season separately, and found higher values for the summer over a variety of landcover classes in a study area in Germany. This was consistent with the higher vegetation cover during the summer growing season.

Here, seasonality effects on  $\beta$  are assessed by performing the linear regression (Eq. 4.2) for the summer months (41 images between April and September) and the winter months (39 images between October and March) separately, corresponding to the months of minimum, respectively maximum, average rainfall, and roughly corresponding to the yearly vegetation patterns observed in Figs. 4.2a and 4.3a. This partitioning is somehow arbitrary since the seasonal vegetation cycle varies over the study site, depending on terrain altitude and land cover. Ideally, the partitioning should use smaller time intervals to fully capture vegetation phenology and/or include information on vegetation dynamics to define the endpoints of these intervals. This is, however, not feasible in this study due to the limited size of the image dataset.

The correction coefficient for each pixel in the study site for summer ( $\beta_{\text{summer}}$ ) and winter ( $\beta_{\text{winter}}$ ) months, and the difference between both, is given in Fig. 4.5. As expected, the largest differences are observed over arable land pixels. Contradictory, however,  $\beta$  is lower (more negative) over arable land in winter than in summer, while less negative values would be expected due to overall higher vegetation cover during the winter growing season.

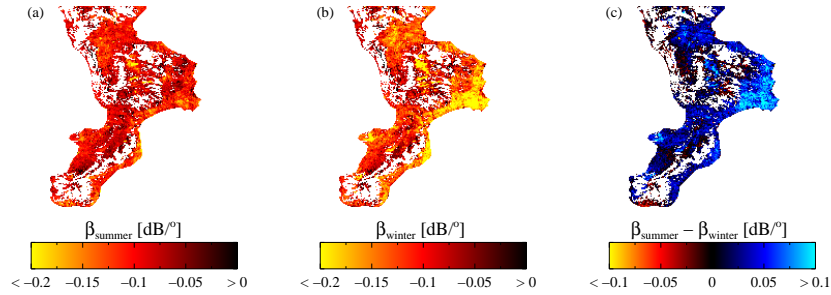


Figure 4.5: Angular correction coefficient for the summer months  $\beta_{\text{summer}}$  (a), winter months  $\beta_{\text{winter}}$  (b) and the difference between  $\beta_{\text{summer}}$  and  $\beta_{\text{winter}}$  (c).

When considering the incidence angle and backscatter coefficient scatterplot (Fig. 4.6) of the arable land pixel discussed earlier in Fig. 4.2, it is observed that, for a given incidence angle, backscatter coefficients are, as expected, generally higher during the wet winter than during the dry summer period. The range in  $\sigma^0(\theta)$  is small (approximately 3 dB) at high  $\theta$ , with small differences between summer and winter backscatter coefficients, and increases to approximately 5 dB at low incidence angles, causing the regression line of the winter images to be much steeper than the one of summer. A possible explanation for this apparent contradiction is that *NDVI* is not necessarily a good indicator of wet vegetation biomass, which is the physical property influencing radar backscatter. The time gap between the maxima of *NDVI* and the slope of the regression line has been

observed earlier for ERS scatterometer (Wagner *et al.*, 1999c) and was attributed to a later yearly peak of wet biomass in comparison to *NDVI*. An alternative explanation is that, apart from vegetation phenology, the seasonal variability of soil moisture also has an influence on  $\beta$ , although this contradicts previous findings and the basic assumptions of the change detection model (Wagner *et al.*, 1999b). Further research on the angular dependence of backscatter on soil moisture and vegetation cover and their interaction is required to clarify this.

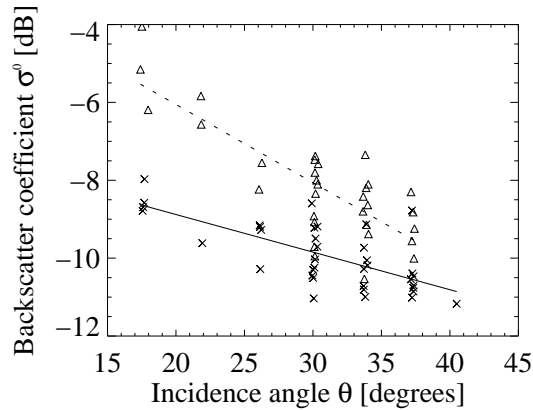


Figure 4.6: Angular behaviour of ASAR backscatter for an arable land pixel. Crosses depict observations during summer months, triangles observations during winter months. Linear regression lines for summer and winter are in solid and dashed, respectively.

Differences between  $\beta_{\text{summer}}$  and  $\beta_{\text{winter}}$  are up to 50 % of the correction coefficient derived using all data combined for several pixels in the study site. Incidence angle normalization was therefore performed for the two periods separately, after which  $\sigma_{\text{dry}}^0(30^\circ)$  and  $S$  and the soil moisture index were redefined. The temporal correlation with modelled soil moisture was then determined again for each pixel in the study site. The increase in  $R$ , relative to the method using a single incidence angle normalization, is given in Fig. 4.7. Although the average correlation coefficient increases only slightly (Fig. 4.8), local  $R$  increases up to 0.2 are observed at some places in the study site.

Pixels with a strong increase in correlation coefficient do not necessarily correspond to pixels with large differences between  $\beta_{\text{summer}}$  and  $\beta_{\text{winter}}$ . This results from the propagation of uncertainties, as presented by Pathe *et al.* (2009) and Mladenova *et al.* (2010), which is proportional to the ratio of the uncertainty on  $\beta$  to  $S$ . Consequently, small changes in  $\beta$  can result in significant soil moisture accuracy changes when  $S$  is low. For higher sensitivity values, even large changes

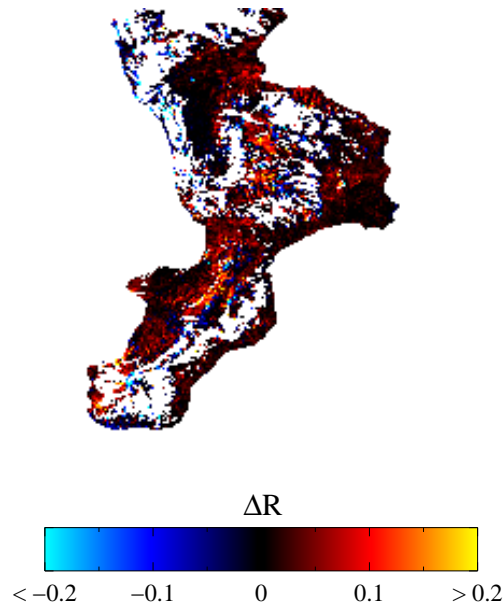


Figure 4.7: Increase in correlation coefficient ( $\Delta R$ ) for the change detection using a seasonal derivation of  $\beta$  relative to the method using a fixed  $\beta$  for the entire year.

do not manifestly influence model performance. A good description of the seasonal angular behaviour of SAR backscatter should therefore be incorporated in (future) multitemporal SAR soil moisture algorithms. Estimates of this behaviour at a monthly frequency can be derived when larger image databases become available.

#### 4.4.2 Seasonality effects on $\sigma_{dry}^0(30^\circ)$ and $S$

In addition to influences on the angular behaviour of SAR backscatter, seasonality can also be expected to influence the dry reference and sensitivity parameters. For a soil with a constant moisture content, backscatter will change in function of vegetation cover and soil roughness parameters. Both vegetation and roughness can be expected to change seasonally, the former through vegetation phenology and crop growth or harvest, the latter through agricultural practices such as ploughing. Both are likely to perturb the multitemporal soil moisture retrieval, especially over agricultural areas. An example of this can be seen in Fig. 4.2, where the ASAR soil moisture remains high towards the end of the growing season, during the same period in which the decrease in vegetation cover lags behind on the decrease in modelled soil moisture. Also, as a result of  $NDVI$  being in phase with arable land

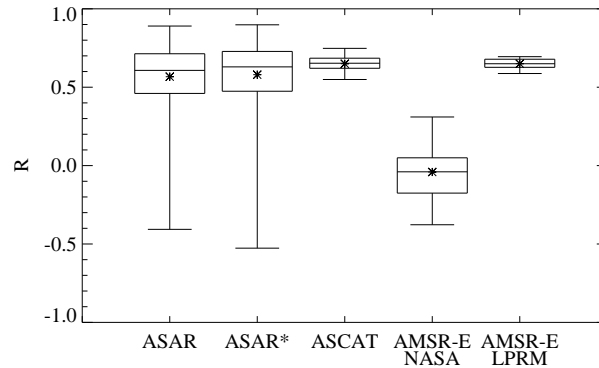


Figure 4.8: Box plots of correlation coefficients between modelled soil moisture and ASAR soil moisture using a single angular correction (ASAR), ASAR soil moisture using a seasonal angular correction (ASAR\*), TU Wien-EUMETSAT ASCAT surface soil moisture (ASCAT), AMSR-E soil moisture derived using the algorithm developed by Njoku *et al.* (2003) (AMSR-E NASA) and AMSR-E soil moisture derived using the LPRM of Owe *et al.* (2008) (AMSR-E LPRM), for all pixels of the respective products over the study site. Crosses indicate the arithmetic means.

over most low elevation arable land pixels, sensitivity values for these pixels might be expected to be overestimated. Conversely,  $S$  might be underestimated when the vegetation cycle is in antiphase with the soil moisture cycle, e.g. over the high elevation forest pixels.

While roughness changes are nearly impossible to assess without multi-angular and/or multi-polarized data or in situ measurements, vegetation dynamics can be easily incorporated using remotely sensed data. In the following, an approach is suggested to incorporate  $NDVI$  in the ASAR change detection algorithm. Vegetation phenology is here accounted for using a vegetation index rather than a seasonal description of dry reference and sensitivity, as by Wagner *et al.* (1999c), because the latter assumes a constant crop behaviour over different years. This might not always be valid, e.g. in the case of crop rotation or when the onset of the growing season varies with the time of rainfall.

In the scatterplot of  $\sigma^0(30^\circ)$  and the corresponding  $NDVI$  (Fig. 4.9) of the arable land pixel, a general positive relationship is observed which is consistent with both  $NDVI$  and ASAR backscatter being in phase with the seasonal soil moisture cycle. When considering the modelled soil moisture it is observed that, for low soil moisture levels, radar backscatter increases with increasing vegetation cover. A lower envelope line describing the backscatter behaviour in function of  $NDVI$ , by analogy with the concept applied by Moran *et al.* (2000), can thus be fitted to

the data. Instead of scaling  $\sigma^0(30^\circ)$  using a fixed  $\sigma_{\text{dry}}^0(30^\circ)$  and  $S$ , these can now be replaced by a dry reference and sensitivity changing in function of  $NDVI$ .

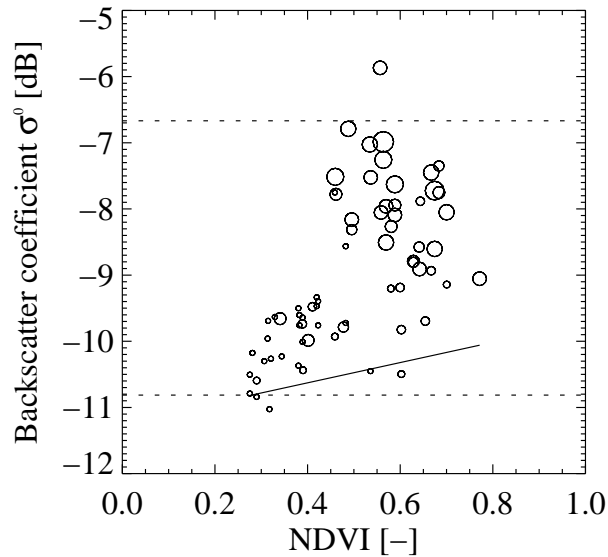


Figure 4.9: Scatterplot of  $NDVI$  and ASAR WS backscatter for a pixel time series over arable land; the size of the dots represents  $\Theta_{\text{model}}$  (large dots indicate high moisture levels). Dotted lines represent the average values of the 5% highest, respectively lowest, backscatter coefficients, the full line indicates the vegetation dependence of ASAR WS backscatter at low moisture levels.

When comparing the thus derived soil moisture index for this pixel with the index ignoring seasonality, only minor changes in performance are observed. In terms of correlation coefficient between  $\Theta_{\text{model}}$  and  $\Theta_{\text{ASAR}}$ , there is a deterioration from 0.80 to 0.78, while the  $RMSE$  improves slightly from 21% to 19%. This marginal change in accuracy might be due to a number of reasons. First, the hydrological model's accuracy is likely too low to evaluate small changes in the soil moisture index. Secondly, changes introduced by vegetation phenology might be too small compared to the total sensitivity to soil moisture to improve results, or  $NDVI$  might be a bad indicator for effects of vegetation change on backscatter. Finally, effects of soil roughness changes, which are not accounted for in this methodology, might be more important over arable land than changes in vegetation cover. Additionally, incorporating vegetation indices in the derivation of  $\sigma_{\text{dry}}^0(30^\circ)$  and  $S$ , as suggested here, is only possible when entirely dry conditions are present over the full range of vegetation phenology stages. This is only valid for few pixels in the study site, since this requires long time series at high temporal resolution in order to capture these extreme and possibly rare events.



## 4.5 Comparison with coarse resolution soil moisture products

The accuracy of the ASAR WS soil moisture was compared to accuracies obtained for coarse resolution soil moisture products (Fig. 4.8). Validation was performed using the 1 km hydrological model for the 2008–2010 period, averaged to the spatial resolution of the coarse resolution products. The AMSR-E NASA product, which produced estimates for 25 coarse resolution pixels, was not correlated with modelled soil moisture for this region ( $R = -0.18$  and  $R = -0.05$  for the lower and upper quartile, respectively), while AMSR-E LPRM soil moisture ( $R = 0.63$  and  $R = 0.68$  for the lower and upper quartile, respectively) and the TU Wien-EUMETSAT ASCAT surface soil moisture product ( $R = 0.62$  and  $R = 0.68$  for the lower and upper quartile, respectively) both produced equally strong correlations. It should however be noted that the VUA-NASA AMSR-E product provides soil moisture estimates for only 10 pixels, all lying in the northern, wider part of the Calabrian peninsula, whereas the ASCAT surface soil moisture provides estimates at 202 grid points distributed over the entire study area. These results are in agreement with the findings of Brocca *et al.* (2011), who reported superior results for AMSR-E LPRM and ASCAT in comparison to AMSR-E NASA over two in situ stations in Calabria. The change detection algorithm applied on ASAR WS data results in  $R$  values in the same range as those of the latter two coarse resolution products for most pixels in the study site ( $R = 0.47$  and  $R = 0.73$  for the lower and upper quartile, respectively, based on 9647 estimates using the method incorporating seasonality on  $\beta$ ).

## 4.6 A further analysis of the influence of seasonality on the angular dependence of backscatter

In the previous sections, it was shown that vegetation phenology can significantly alter the angular dependence of radar backscatter, and that ignoring this seasonality can hence degrade soil moisture retrieval accuracies by SAR systems. While in Section 4.4 a first attempt was made to circumvent influences of vegetation phenology on the the angular dependence of ASAR backscatter by dividing the year in a high-vegetation and a low-vegetation season, this section proposes a methodology to assess the effects of seasonality at monthly resolution and higher. This is achieved by combining ASAR WS data with low spatial resolution ASCAT data. This methodology assumes a linear dependence of ASAR WS backscatter on incidence angle, an assumption that is validated first.

### 4.6.1 Linearity of ASAR angular dependence

This part of the study is performed on the full time series of 130 ascending and descending mode ASAR WS images. In order to better exploit the high resolution of the Wide Swath mode, topographic correction (including masking of regions affected by radar shadow and/or layover) and radiometric calibration are performed using the 10 m resolution TINITALY/01 DEM, and the images are resampled to a grid of  $0.0025^\circ$  (approximately 300 m) resolution. The angular dependence of  $\sigma^0(\theta)$  on  $\theta$  can then again be assessed using Eq. 4.1, and normalization to a common incidence angle can be performed following Eq. 4.2. Equations 4.1 and 4.2 can obviously be easily adapted to account for possible non-linearity of the angular dependence of backscatter by adding a higher-order term in  $\theta$  (Baup *et al.*, 2007).

Several studies performed the angular normalization of ASAR backscatter assuming a linear relationship between  $\theta$  and  $\sigma^0(\theta)$  (Loew *et al.*, 2006; Wagner *et al.*, 2008; Pathe *et al.*, 2009). The rationale behind this is that although the relation between incidence angle and backscatter is typically not linear (Ulaby *et al.*, 1982), it can be considered as such for the limited incidence angle range in which the ASAR instrument operates. When using both ascending and descending mode images, however, the incidence angle range will extend beyond the typical range of  $20^\circ$ – $40^\circ$  for pixels over sloped terrain. For a slope of  $20^\circ$ , for example, the incidence angle range can increase to  $0^\circ$ – $60^\circ$ , a range for which the linear approximation of the angular dependence of backscatter is not necessarily valid.

The validity of the linear assumption is here investigated by fitting both a linear and a second order polynomial function to the multitemporal  $(\theta, \sigma^0(\theta))$  observations for each pixel individually. Figure 4.10(a) shows three examples of these linear and quadratic fits. For the top figure of Fig. 4.10(a), the incidence angle range is relatively small and the linear and quadratic fits result in a nearly identical coefficient of determination ( $R_{\text{lin}}^2$  and  $R_{\text{quad}}^2$ , respectively). With increasing incidence angle range (middle figure of Fig. 4.10(a)), it becomes apparent that the incidence angle-backscatter relationship is non-linear, although the difference between  $R_{\text{quad}}^2$  and  $R_{\text{lin}}^2$  remains small. The bottom figure of Fig. 4.10(a), however, shows that this relationship can become strongly non-linear when the incidence angle range becomes large. It is observed here that the typically negative relationship between  $\theta$  and  $\sigma^0(\theta)$  is inverted for low values of  $\theta$ .

The  $R^2$  of the second order polynomial fit will, by definition, be larger than that of the first order fit. The difference between both can be interpreted as a measure of the validity of the linear assumption of the angular dependence of backscatter. This difference in  $R^2$  is shown, for each pixel of the study site, in Fig. 4.10(b). Although non-linearity results in high differences in  $R^2$  for many pixels in the study site, the majority is characterized by differences below 0.1 (Fig. 4.10(c)). Strong non-linear relationships between  $\theta$  and  $\sigma^0(\theta)$  are dominantly found over sloped terrain covered by dense vegetation (Fig. 3.1).

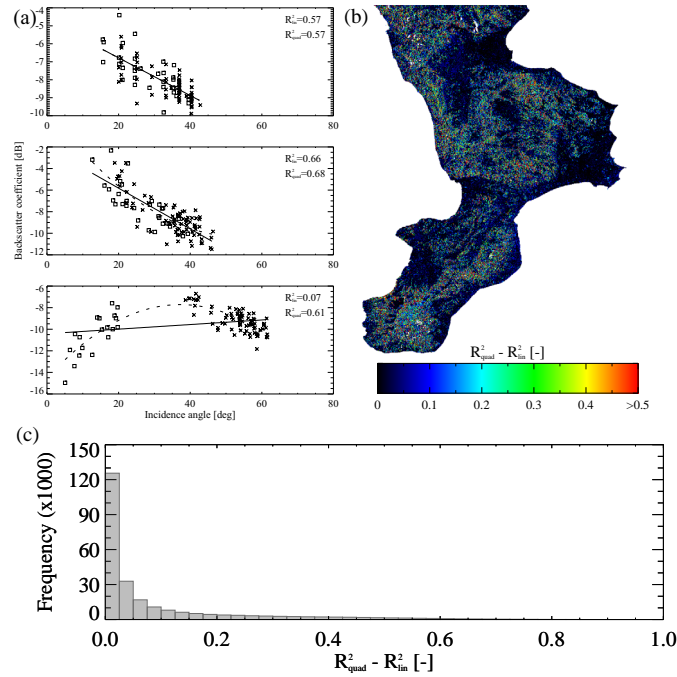


Figure 4.10: Scatterplot of  $\sigma^0(\theta)$  versus  $\theta$  for three example pixels, crosses and boxes representing acquisitions during descending and ascending overpasses, respectively, full lines and dashed lines representing linear and quadratic fits, respectively (a). Difference in  $R^2$  of quadratic and linear fit for each pixel of the study site (b). Frequency distribution of difference in  $R^2$  of quadratic and linear fit (c).

In the remainder of this section, only those pixels where the angular dependence of ASAR backscatter can be approximated by a linear relationship are retained. These are (subjectively) selected as those pixels where the difference in  $R^2$  is below 0.1, or 74.7% of the total number of pixels in the study site. For normalization of ASAR images over terrain with significant topography, however, the non-linear nature of the angular dependence should not be ignored.

#### 4.6.2 Monthly dynamics of ASAR and ASCAT angular dependence

As mentioned earlier, the derivation of  $\beta$  using images from all dates pooled ignores possible seasonal effects of vegetation. A possible solution to incorporate effects of seasonality on  $\beta$  is by applying Eq. 4.1 using a sliding time window. Here, the slope values (hereafter denoted as  $\beta_{ASAR}$ ) are derived on a monthly ba-

sis, fitting Eq. 4.1 to the  $(\theta, \sigma^0(\theta))$  couples of a 3-month window over all the years, i.e.  $\beta_{\text{ASAR}}$  for the month of January is derived using observations during December, January and February from 2008 to 2011. For larger datasets, the size of this temporal window could be reduced in order to increase the temporal resolution of the slope estimates.

The validity of the methodology is tested by comparing the monthly ASAR slopes to the slopes derived for ASCAT. Since both ASAR and ASCAT are C-band instruments operating at VV polarization, they can be assumed to be affected by the same seasonal vegetation patterns, and a correlation between the angular dependences of the two sensors is expected. To this end,  $\beta_{\text{ASAR}}$  values are re-sampled to the spatial resolution of ASCAT by averaging over a circular 12.5 km radius footprint centered at the ASCAT grid points:

$$\bar{\beta}_{\text{ASAR}} = \frac{1}{\text{area}(A)} \iint_A \beta_{\text{ASAR}}(x,y) dx dy, \quad (4.5)$$

where  $\bar{\beta}_{\text{ASAR}}$  represents the spatial average of  $\beta_{\text{ASAR}}$  at locations  $x,y$  over the area  $A$ .

As a by-product of the global soil moisture retrieved by the change detection algorithm for Scatterometer and ASCAT, slope and curvature values for the angular normalization are derived. The slope at  $40^\circ$  incidence angle and the curvature are generated for each day of the year (366 days), in the same discrete global grid (DGG) as the soil moisture product. Since the angular normalization technique for ASAR, discussed previously, produces only a slope and no curvature, the ASCAT curvature is used to convert, for each day, the ASCAT slope at  $40^\circ$  to an incidence angle of  $30^\circ$ , since this lies approximately halfway the range of ASAR WS incidence angles. The ASCAT slope at  $30^\circ$  is hereafter denoted as  $\beta_{\text{ASCAT}}$ . Additionally, in order to be able to compare ASCAT slopes to those derived for ASAR temporally, the temporal resolution of  $\beta_{\text{ASCAT}}$  is reduced to the temporal resolution of  $\bar{\beta}_{\text{ASAR}}$ . This is done by degrading  $\beta_{\text{ASCAT}}$  to monthly averages:

$$\hat{\beta}_{\text{ASCAT}} = \frac{1}{N} \sum_{d=1}^N \beta_{\text{ASCAT}}(d), \quad (4.6)$$

where  $\hat{\beta}_{\text{ASCAT}}$  represents the temporal average of  $\beta_{\text{ASCAT}}$  over  $N$  days.

The angular dependence of backscatter, expressed as the slope  $\beta_{\text{ASAR}}$  and derived using the entire multitemporal dataset of ASAR WS images, is given in Fig. 4.11(a). The general land cover pattern of Calabria is reflected, with strong negative values of  $\beta_{\text{ASAR}}$  over agricultural areas and values closer to zero over areas with a denser vegetation canopy cover. When including the effects of seasonal vegetation change by deriving the slope on a monthly basis, large seasonal differences in  $\beta_{\text{ASAR}}$  are observed. Differences between the second largest and the

second lowest monthly slope per pixel ( $\Delta\beta_{\text{ASAR}}$ , Fig. 4.11(b)) are approximately in the order of magnitude of the values of  $\beta_{\text{ASAR}}$  for the pooled data. The second highest and second lowest monthly values are selected here instead of the extreme values in order to reduce the effect of possible outliers in the monthly estimates of  $\beta_{\text{ASAR}}$ . These might be introduced through chance effects resulting from the smaller size of the datasets that are used to produce the monthly slopes. On average, 32.5 images are available for each 3-month sliding time window. When, by chance, all near-range (low incidence angle) or far-range (high incidence angle) acquisitions during a 3-month window are obtained during wet conditions (resulting in higher backscatter for these acquisitions), the resulting  $\beta_{\text{ASAR}}$  will be more negative or less negative, respectively, than would be expected. This source of errors can be reduced by including longer time series, e.g. the full 10-year ENVISAT ASAR archive instead of the current 3.5-year period.

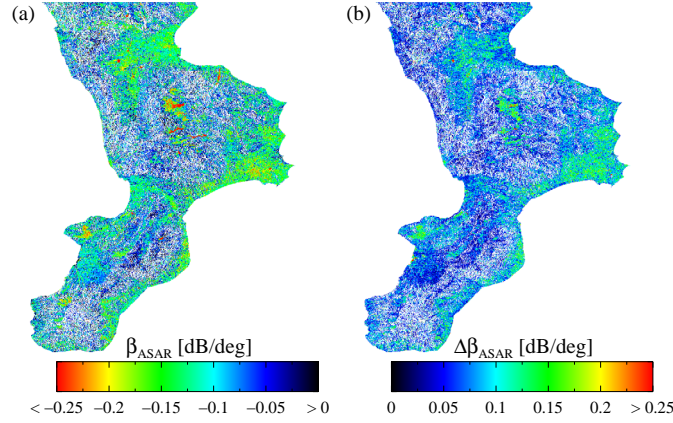


Figure 4.11: Slope parameter ( $\beta_{\text{ASAR}}$ ) derived using all available data (a) and seasonal range of slopes derived on monthly basis ( $\Delta\beta_{\text{ASAR}}$ ) (b). Pixels characterized by non-linearity of the angular dependence have been masked.

The large difference observed between  $\beta_{\text{ASAR}}$  obtained using the pooled data and  $\beta_{\text{ASAR}}$  for the individual months implies that errors will be introduced when this seasonality is ignored in an angular normalization. When backscatter is normalized to an incidence angle of  $30^\circ$  according to Eq. 4.2 and using the value of  $\beta_{\text{ASAR}}$  as displayed in Fig. 4.11(a), the maximum error on normalized backscatter  $\Delta\sigma^0(30^\circ)_{\text{max}}$  can be expressed as:

$$\Delta\sigma^0(30^\circ)_{\text{max}} = |\Delta\beta_{\text{max}}| |\Delta\theta_{\text{max}}|. \quad (4.7)$$

In Eq. 4.7,  $|\Delta\beta_{\text{max}}|$  is the maximum absolute difference between  $\beta_{\text{ASAR}}$  obtained for all multitemporal data pooled and  $\beta_{\text{ASAR}}$  obtained for monthly intervals. As before, the second largest and second lowest value of the slope are used here in order to avoid effects of outliers.  $|\Delta\theta_{\text{max}}|$  is the maximum incidence angle range

over which backscatter has to be normalized, and is thus function of the terrain's slope and orientation. The value of  $\Delta\sigma^0(30^\circ)_{\max}$  for each ASAR WS pixel is given in Fig. 4.12(a), its frequency distribution in Fig. 4.12(b). It is observed that  $\Delta\sigma^0(30^\circ)_{\max}$  is especially high over arable land, and lower over permanent crops and forests. For a large fraction of the (nonmasked) pixels over this study site,  $\Delta\sigma^0(30^\circ)_{\max}$  is in the order of, or higher than, 0.65 dB, the radiometric accuracy of the ASAR sensor in WS mode.

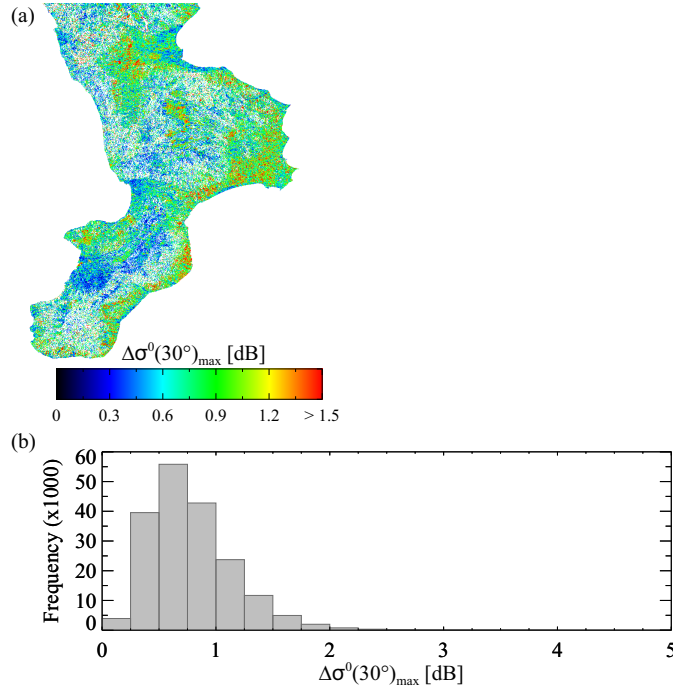


Figure 4.12: Maximum error on normalized backscatter introduced by neglecting seasonal variability of  $\beta_{\text{ASAR}}$  (a). Frequency distribution of this maximum error (b). Pixels characterized by non-linearity of the angular dependence have been masked.

When aggregating the ASAR WS slopes to the spatial resolution of ASCAT for each grid cell, and aggregating the ASCAT slopes to the monthly temporal resolution of the ASAR slopes, the correspondence between the temporal behaviour of  $\hat{\beta}_{\text{ASCAT}}$  and  $\bar{\beta}_{\text{ASAR}}$  can be investigated. This is done for three example points of the DGG in Fig. 4.13(a). The top profile of this figure represents a grid point dominated by arable land. This results in a strong seasonal signal, with  $\hat{\beta}_{\text{ASCAT}}$  and  $\bar{\beta}_{\text{ASAR}}$  during the summer months being much higher than during the winter months.  $\bar{\beta}_{\text{ASAR}}$  displays the same seasonal trend as  $\hat{\beta}_{\text{ASCAT}}$ , for this grid cell, resulting in a high  $R^2$  and relatively low root mean square error (RMSE). Unlike

for arable land, where aboveground biomass, and hence the angular dependence of backscatter, changes considerably throughout the year, the main scattering elements of a forest canopy (stems and branches) are present during the entire year.  $\hat{\beta}_{\text{ASCAT}}$  and  $\bar{\beta}_{\text{ASAR}}$  for a grid cell dominated by deciduous forest (middle figure of Fig. 4.13(a)) therefore exhibit much smaller seasonal fluctuations. The limited range of both  $\bar{\beta}_{\text{ASAR}}$  and  $\hat{\beta}_{\text{ASCAT}}$ , combined with even small retrieval errors in  $\bar{\beta}_{\text{ASAR}}$ , results in an intermediate  $R^2$ , even though the RMSE is low. The bottom figure of Fig. 4.13(a), finally, shows a grid cell over mixed landcover characterized by a low  $R^2$  and high RMSE. For this grid cell,  $\bar{\beta}_{\text{ASAR}}$  corresponds to  $\hat{\beta}_{\text{ASCAT}}$  for the period November–May, but they differ strongly for the period June–October. Possibly, the difference for these latter months is caused by the smaller size of the datasets on which the monthly values of  $\beta_{\text{ASAR}}$  were derived, as discussed earlier.

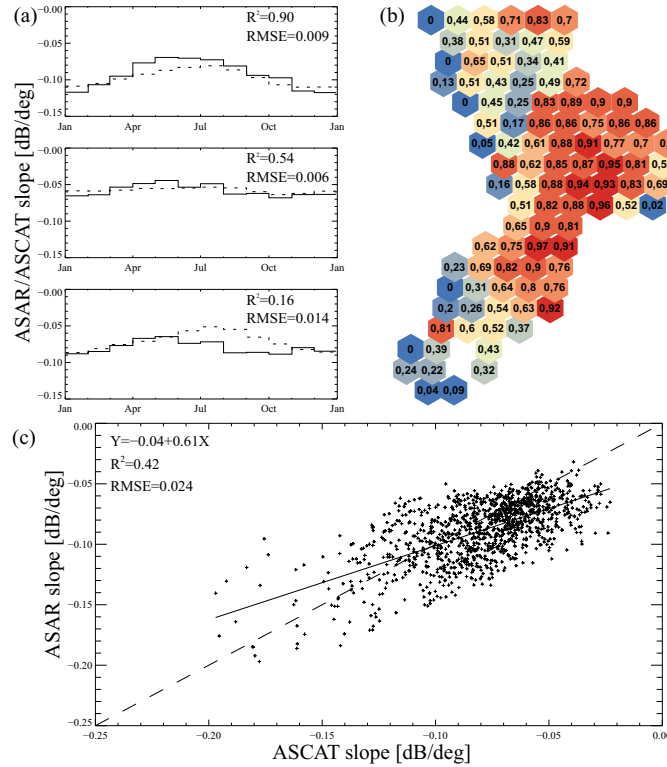


Figure 4.13: Temporal behaviour of  $\bar{\beta}_{\text{ASAR}}$  (full line) and  $\hat{\beta}_{\text{ASCAT}}$  (dashed line) for three grid points dominated by (top to bottom) arable land, deciduous forest and mixed landcover (a).  $R^2$  between monthly values of  $\bar{\beta}_{\text{ASAR}}$  and  $\hat{\beta}_{\text{ASCAT}}$  for all grid points of the DGG, blue and red indicating low and high values, respectively (b). Scatterplot of  $\hat{\beta}_{\text{ASCAT}}$  and  $\bar{\beta}_{\text{ASAR}}$  for all grid points pooled (c).



Figure 4.13(b) shows that, for most grid points of the DGG, the correlation between  $\bar{\beta}_{\text{ASAR}}$  and  $\hat{\beta}_{\text{ASCAT}}$  is intermediate to strong. Nevertheless, some low  $R^2$  values can be found for several grid points, especially in the western half of the study site. It should be noted that ASAR WS pixels masked due to non-linear behaviour of the angular dependence were not used to calculate  $\bar{\beta}_{\text{ASAR}}$ . Comparison of  $\bar{\beta}_{\text{ASAR}}$  and  $\hat{\beta}_{\text{ASCAT}}$  therefore implies that the masked ASAR WS pixels are representative for the general land cover within the ASCAT footprint, and not that, e.g., all forest pixels are masked while grassland pixels are unmasked. This might partly have caused some of the lower  $R^2$  values. Grid points for which more than half of the ASAR WS pixels were masked were not further processed. This was the case for two grid points in the south of the study site.

The scatterplot of  $\hat{\beta}_{\text{ASCAT}}$  and  $\bar{\beta}_{\text{ASAR}}$  for all grid points pooled (Fig. 4.13(c)) shows that the observations are scattered around the 1:1 relation that might be expected given the similar characteristics of both sensors. Strong deviations from this line, caused by processes discussed earlier, results in only an intermediate  $R^2$  and relatively high RMSE. The existence or non-existence of a universal 1:1 relation between  $\hat{\beta}_{\text{ASCAT}}$  and  $\bar{\beta}_{\text{ASAR}}$  could be clarified by further study over different sites. In general, however, it can be concluded that the linear regression of  $\sigma^0(\theta)$  versus  $\theta$  over monthly windows seems an adequate technique to capture the temporal dynamics of the angular dependence of ASAR WS backscatter over a variety of land cover types, and results are consistent with the angular dependence of ASCAT backscatter.

### 4.6.3 Towards high temporal resolution angular normalization of ASAR WS

Given the similar seasonal behaviour of the ASAR and ASCAT slope, a time-invariant or temporally stable (linear) relationship might exist between the high spatial resolution  $\beta_{\text{ASAR}}$  and the low spatial resolution  $\hat{\beta}_{\text{ASCAT}}$ :

$$\beta_{\text{ASAR}} = a_s + b_s \hat{\beta}_{\text{ASCAT}} . \quad (4.8)$$

The scaling coefficients  $a_s$  and  $b_s$  can easily be estimated for each ASAR pixel from the monthly slope  $\beta_{\text{ASAR}}$  and the ASCAT slope, aggregated to monthly resolution, of the nearest ASCAT grid point. The concept of temporal stability implies that regional scale temporal dynamics of surface properties are characteristic of local or point scale dynamics, and vice versa. One such surface property that is found to be characterized by temporal stability is soil moisture (Cosh *et al.*, 2008; Brocca *et al.*, 2009). Although soil moisture content can vary strongly within a few metres as a result of soil type or topography, the processes explaining its temporal dynamics, namely precipitation and evapotranspiration, are typically large scale processes. The temporal stability of surface soil moisture is reflected in the temporal stability of SAR backscatter (Wagner *et al.*, 2008), which in turn offers



prospects for the spatial disaggregation of coarse resolution remotely sensed soil moisture estimates.

In this study, the assumption of temporal stability between ASCAT and ASAR slope parameters in Eq. 4.8 implies that regional scale and local scale vegetation dynamics are similar. In other words, the assumption is valid when all land cover types within a low resolution ASCAT footprint exhibit a similar seasonal behaviour. Since in the Mediterranean climate of Calabria vegetation growth is strongly rainfall dependent, this would seem a realistic assumption. However, the heterogeneous land cover of the study site, combined with the strong topography and associated temperature regimes, might cause different regions within one ASCAT footprint to be characterized by different temporal vegetation dynamics. The validity of the linear temporal stability model can be expressed in terms of a coefficient of determination or a standard error of estimate. A strong correlation can be expected when the vegetation cover of the high resolution pixel footprint is similar to the overall coverage of the low resolution footprint. In that case, the scaling coefficients can be used, together with the daily ASCAT slope  $\beta_{\text{ASCAT}}$ , to interpolate the monthly  $\beta_{\text{ASAR}}$  to daily resolution.

Figure 4.14(a) indicates the validity of the assumption of linear temporal stability in terms of  $R^2$  for each ASAR WS pixel in relation to the nearest ASCAT grid point, Fig. 4.14(b) its frequency distribution. Although  $R^2$  is overall low, strong temporally stable relationships between  $\beta_{\text{ASAR}}$  and  $\hat{\beta}_{\text{ASCAT}}$  exist over many cropland pixels. Lower coefficients of determination over dense vegetation are due to the small dynamic range of  $\beta_{\text{ASAR}}$  at these pixels (Fig. 4.11(b)). Combined with even small errors on the monthly estimates  $\beta_{\text{ASAR}}$ , this results in a low  $R^2$ .

The differences in  $R^2$  magnitudes in Fig. 4.13 and Fig. 4.14 can be explained by the fact that the aggregated  $\bar{\beta}_{\text{ASAR}}$  and  $\hat{\beta}_{\text{ASCAT}}$  correspond to the same land surface footprint, while  $\beta_{\text{ASAR}}$  derived for a single pixel and  $\hat{\beta}_{\text{ASCAT}}$  might reflect the effects of entirely different land covers. For instance, the seasonal behaviour of angular backscatter dependence for a high resolution pixel dominated by forest will differ greatly from that of an ASCAT grid point if the greater region is dominated by cropland, or vice versa.

For those ASAR pixels with strong temporal stability between  $\beta_{\text{ASAR}}$  and  $\hat{\beta}_{\text{ASCAT}}$ , this linear relationship can be used, together with the high temporal resolution of  $\beta_{\text{ASCAT}}$ , to improve the temporal resolution of  $\beta_{\text{ASAR}}$ :

$$\beta_{\text{ASAR,d}} = a_s + b_s \beta_{\text{ASCAT}} , \quad (4.9)$$

where  $\beta_{\text{ASAR,d}}$  indicates the angular dependence of ASAR WS backscatter at daily resolution, and the scaling coefficients  $a_s$  and  $b_s$  are derived according to Eq. 4.8. This interpolation of the monthly  $\beta_{\text{ASAR}}$  estimates allows to avoid discontinuities between consecutive months in the angular normalization of ASAR WS images.

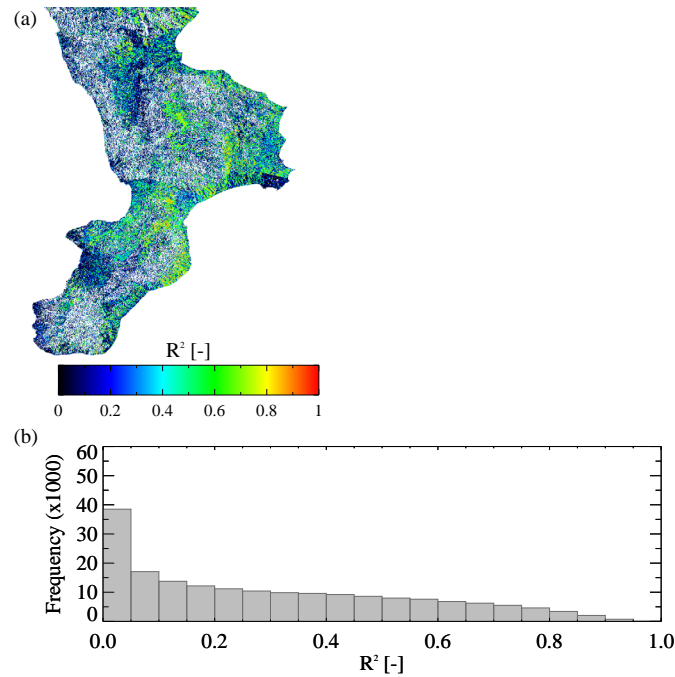


Figure 4.14: Validity of the assumption of temporal stability, expressed as coefficient of determination (a). Frequency distribution of the coefficient of determination (b). Pixels characterized by non-linearity of the angular dependence have been masked.

An example of this can be seen in Fig. 4.15 for an ASAR cropland pixel. It is observed in this example that the interpolated  $\beta_{\text{ASAR},d}$  deviates from the original  $\beta_{\text{ASAR}}$  during some months. The  $\beta_{\text{ASCAT}}$  product is, however, more stable than  $\beta_{\text{ASAR}}$ , given the multi-angular capabilities of ASCAT and the number of observations on which both are based. The interpolation algorithm based on temporal stability can therefore be assumed to filter out some of the errors introduced by the smaller number of images on the basis of which  $\beta_{\text{ASAR}}$  is computed.

Overall, the applicability of the interpolation based on temporal stability is somehow limited for this study site due to the strong fragmentation of land cover. Over more homogeneous terrain, however, this method is expected to be useful to increase the temporal resolution of monthly  $\beta_{\text{ASAR}}$ .

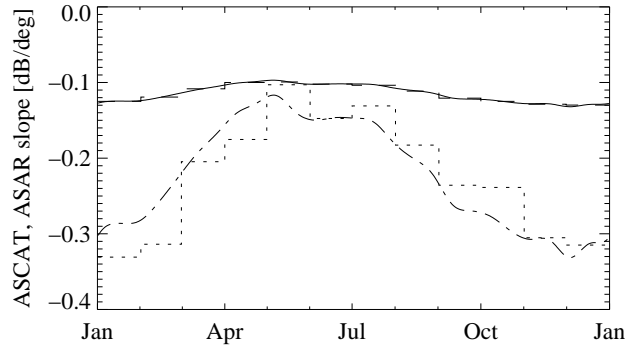


Figure 4.15:  $\beta_{\text{ASCAT}}$  (full line),  $\hat{\beta}_{\text{ASCAT}}$  (dashed line),  $\beta_{\text{ASAR}}$  (dotted line) and  $\beta_{\text{ASAR,d}}$  (dashdotted line) for an example ASAR WS pixel over cropland and the nearest ASCAT grid point.

## 4.7 Conclusions

In this chapter, a change detection technique was applied to infer a soil moisture index from a time series of 80 ASAR Wide Swath images over Calabria, Italy. Backscatter coefficients, normalized to an incidence angle of  $30^\circ$ , were scaled between the highest and lowest values in a time series of 3 years. Strong linear correlations with modelled soil moisture ( $R \approx 0.6$  to  $R \approx 0.8$ ) were found for most arable land pixels, while correlation coefficients for forests were moderate to low ( $R \approx 0.2$  to  $R \approx 0.5$ ).

Additionally, an effort was undertaken to account for seasonality effects in the derivation of the three change detection model parameters: angular correction coefficient, dry reference and sensitivity. In the multitemporal incidence angle correction, seasonality was incorporated by deriving the angular correction coefficient for the summer months and winter months separately. Especially for arable land, this resulted in large differences between the summer and winter correction coefficients. When applying the seasonal coefficients in the angular correction, validation with the modelled soil moisture resulted in increases in correlation coefficients between 10 and 20 % for many pixels in the study site, thus stressing the importance of an appropriate angular correction. In the derivation of dry reference and sensitivity, seasonality was integrated using MODIS Normalized Difference Vegetation Index. Unfortunately, no significant increase in soil moisture estimation accuracy was found. This is possibly because errors introduced by vegetation phenology in the derivation of dry reference and sensitivity are small relative to errors from other sources, such as soil roughness or sensor noise.

A further study of the angular correction coefficient, performed on the full time series of 130 ASAR images in ascending and descending mode showed that the assumption of a linear relationship between backscatter and incidence angle was not valid for a number of pixels, especially over sloped terrain. For those pixels where this assumption was true, the angular dependence of ASAR WS backscatter was found to vary strongly over cropland and moderately over terrain with permanent vegetation cover, consistent with the angular dependence obtained for ASCAT. The relationship between these can, applying the concept of temporal stability, be used to interpolate the monthly ASAR angular correction coefficients to daily estimates. When ignoring this seasonal variability in an angular normalization, errors in the order of the radiometric accuracy of ASAR WS and higher can be introduced.

Overall, change detection algorithms of high to medium spatial resolution and high temporal resolution SAR data, such as Envisat ASAR or the upcoming Sentinel-1 mission, offer promising approaches to routinely map surface soil moisture dynamics over a wide range of land cover types. These can be usable additions to low resolution soil moisture datasets from active and passive microwave sensors. Nevertheless, change detection algorithms should not neglect influences of seasonality in the derivation of the model parameters, especially the multitemporal angular correction coefficient.



# 5

## MODIS apparent thermal inertia as a soil moisture indicator

### 5.1 Introduction

Changes in apparent thermal inertia have already been related to changes in soil moisture content (Tramutoli *et al.*, 2000; Verstraeten *et al.*, 2006). Sensors on sun-synchronous polar orbiting satellites such as NOAA/AVHRR or Aqua and Terra MODIS provide day- and nighttime land surface temperature measurements on a near-daily basis at approximately 1 km resolution, which allows for the derivation of time series of daily apparent thermal inertia. However, these sensors suffer from the disadvantage, compared to lower resolution geostationary sensors, that the time of observation of a position on the ground may differ between two consecutive days. Aqua's equatorial crossing time, for example, is approximately 1:30 pm in ascending mode and 1:30 am in descending mode. Due to the wide swath width of the MODIS instrument (2330 km), however, the local solar time of observation at a particular point at the earth's surface can be considerably earlier or later than the time at nadir, resulting in possibly large differences in time of observation for two consecutive days. Additional heating or cooling will occur during this time span, hampering meaningful comparison of apparent thermal inertia images of different dates. A second limitation of most (apparent) thermal inertia methods up to present is that they use only two surface temperature observations as (ap-

---

This chapter is based on: Van doninck J., Peters, J., De Baets, B., De Clercq, E.M., Ducheyne, E., Verhoest, N.E.C. (2011). The potential of multitemporal Aqua and Terra MODIS apparent thermal inertia as a soil moisture indicator. *International Journal of Applied Earth Observation and Geoinformation*, **13**(6), 934-941, DOI: 10.1016/j.jag.2011.07.003.

proximations of) the diurnal temperature range, except for the method of Sobrino and El Kharraz (1999a) which requires four daily measurements. When one of these observations is lacking —due to cloud cover or because the area of interest lies between sensor swaths, which is common in regions near the equator— the (apparent) thermal inertia for that day can obviously not be derived.

In this chapter we propose a methodology to derive apparent thermal inertia by a multitemporal approach, using Aqua and Terra MODIS data of a full year. The method is based on a sinusoidal approximation of the diurnal surface temperature curve, where a sinusoid is fitted to either four, three or two MODIS land surface temperature observations, depending on the number of available observations. The methodology allows for a certain flexibility and exploits the full amount of information gathered by the MODIS instrument.

## 5.2 Study area and datasets

This part of the study is initially performed on the part of continental Africa south of the parallel of 15° South. This area comprises the countries of South Africa, Namibia, Botswana, Zimbabwe and parts of Mozambique. This study site is chosen to cover a variety of climate conditions, which vary significantly within the region from extremely arid along the Atlantic coast of Namibia to a Mediterranean climate around the Cape and humid at the eastern coast of Mozambique. A strong seasonality is present due to the proximity to the Tropic of Capricorn. In a second phase, the Calabria study site is included.

For the southern Africa study site, for reasons of data volume, the global 0.05° level 5 products MCD43B3 (Terra+Aqua 16-day albedo), MOD11C1 (Terra daily land surface temperature) and MYD11C1 (Aqua daily land surface temperature) were used in this study for the period January–December 2009. This way, the study area is covered by images of 600 by 400 pixels. Over the Calabria study site, the corresponding 1 km products are used, and this for the period 2008–2009. The 0.05° and 1 km surface temperature products differ from each other in the way the times of land surface temperature observations are provided. While for the 1 km product these are given in local solar time, they are in Coordinated Universal Time (UTC) for the M\*D11C1 products. Transformation to local solar time  $t_i$  [s] is done by:

$$t_i = t_i(\text{UTC}) + \frac{\upsilon}{\omega}, \quad (5.1)$$

where  $t_i(\text{UTC})$  is the Coordinated Universal Time [s] and  $\upsilon$  is the local longitude [rad].

Since no in situ or modelled soil moisture reference data were available for the entire southern Africa study site, AMSR-E soil moisture was used as a reference.

The (descending mode) soil moisture product at 0.25° resolution developed at the Vrije Universiteit Amsterdam (VUA) in collaboration with NASA (Owe *et al.*, 2008) was selected here over other products, given its superior retrieval capabilities in comparative studies (Draper *et al.*, 2009; Gruhier *et al.*, 2010; Wagner *et al.*, 2007). The region of southern Africa is only weakly influenced by radio frequency interference (Njoku *et al.*, 2005), which makes the AMSR-E soil moisture product for this region a reliable reference dataset. A 7-day running temporal average filter was applied on the soil moisture images of 2009 in order to fill data gaps and to reduce temporal noise. For Calabria, the modelled soil moisture was used as reference data.

## 5.3 Sinusoidal approximation of the diurnal surface temperature cycle

### 5.3.1 Methodology

The diurnal temperature cycle can be approximated as a sinusoid of the form:

$$T_S(t_i) = \bar{T}_S + \frac{A}{2} \cos(\omega t_i - \psi) , \quad (5.2)$$

where  $T_S(t_i)$  is the surface temperature [K] at time of day  $t_i$  [s],  $\bar{T}_S$  the diurnal average surface temperature [K],  $A$  the amplitude of the diurnal temperature cycle, [K],  $\omega$  the angular velocity of rotation of the Earth [ $\text{rad s}^{-1}$ ], and  $\psi$  is the phase angle [rad].

Considering the phase  $\psi$  known, e.g. from in situ measurements, then Eq. 5.2 contains two unknowns:  $\bar{T}_S$  and  $A$ . The amplitude and average temperature can thus be derived for each pixel for each day with two observations ( $t_i, T_S(t_i)$ ) or with more ( $n$ ) observations using a least squares approach. The solutions for  $A$  and  $\bar{T}$  then become, denoting  $T_i \equiv T_S(t_i)$ :

$$\frac{A}{2} = \frac{n \sum_{i=1}^n \cos(\omega t_i - \psi) T_i - \sum_{i=1}^n \cos(\omega t_i - \psi) \sum_{i=1}^n T_i}{n \sum_{i=1}^n \cos^2(\omega t_i - \psi) - (\sum_{i=1}^n \cos(\omega t_i - \psi))^2} \quad (5.3)$$

and

$$\bar{T}_S = \frac{\sum_{i=1}^n T_i - (A/2) \sum_{i=1}^n \cos(\omega t_i - \psi)}{n} . \quad (5.4)$$

With  $n = 2$ , the exact solution for the diurnal amplitude is:

$$\frac{A}{2} = \frac{T_1 - T_2}{\cos(\omega t_1 - \psi) - \cos(\omega t_2 - \psi)} . \quad (5.5)$$

The MODIS sensor onboard Aqua and Terra can provide up to four land surface temperature observations each day. A maximum number of observations can



be used to derive the diurnal temperature amplitude from Eqs. 5.3 or 5.5. In the case of only two temperature measurements, it is advisable to derive the diurnal amplitude using day-night pairs only, since two daytime or two nighttime observations would result in small differences in both numerator and denominator of Eq. 5.5.

In the derivation of Eqs. 5.3–5.5 we have assumed the phase  $\psi$ , corresponding to the time of maximum surface temperature, to be known. We suggest a variation on the method of Sobrino and El Kharraz (1999a) to derive this value. Starting from Eq. 5.2 and taking the difference between  $T_S(t_i)$  at two satellite overpass times and dividing this by the difference at two other overpass times, we obtain:

$$\psi = \arctan(\xi) + \pi \quad (5.6)$$

with

$$\xi = \frac{(T_1 - T_3)(\cos(\omega t_2) - \cos(\omega t_4)) - (T_2 - T_4)(\cos(\omega t_1) - \cos(\omega t_3))}{(T_2 - T_4)(\sin(\omega t_1) - \sin(\omega t_3)) - (T_1 - T_3)(\sin(\omega t_2) - \sin(\omega t_4))}. \quad (5.7)$$

While Sobrino and El Kharraz (1999b) used only three temperature observations with NOAA/AVHRR data, we use Eq. (5.7) with four MODIS observations in order to optimally approximate the sinusoidal fit on four data points and to minimize the probability that a phase angle is derived on days with cloud cover.  $\psi$  can thus be derived for a time series of MODIS images for all days with four surface temperature measurements. On the resulting time series of phase angle values we performed additional interpolation and smoothening. The reasons for this are twofold. The first is to eliminate day-to-day meteorological influences and influences of measurement errors. Second, the number of days with four daily MODIS ( $t_i, T_S(t_i)$ ) observations will be low on certain places on Earth. Interpolating  $\psi$  values allows for pixels on days with fewer than four observations to be further processed. The smoothening and interpolation are done by a harmonic analysis of time series (Verhoef, 1996). This algorithm basically calculates a Fourier series based on time series of  $\psi$  for each pixel in a scene. After selecting a limited number of frequencies, outliers in the original dataset relative to the modeled harmonic are discarded and a new Fourier series is calculated based on the remaining data points. This process is repeated iteratively until a predefined fit to the data is reached or until a predefined minimum number of  $\psi$  values remain. Given the potential seasonal variation of the time of maximum daytime temperature with solar declination or vegetation phenology, a single harmonic with a frequency of one year is likely to be sufficient. The interpolated value of  $\psi$  can then be retrieved for every pixel for every day of the year.

### 5.3.2 Results and validation

For each pixel in the study site, the phase angle  $\psi$  was computed according to Eqs. 5.6 and 5.7 for all calendar days of the year 2009 where four observations — i.e. a sequence of Aqua night, Terra day, Aqua day and Terra night images— were available. This was the case for on average 130 days, with a standard deviation of 30 days. These phase angle values were smoothed and interpolated for days with fewer than four observations by the harmonic analysis of time series using a single harmonic with a frequency of one year (Fig. 5.1). In general, the amplitude of the harmonic was found to be low, with an average of 0.81, indicating a difference in time of maximum surface temperature of 37 minutes over a full year. It should be noted that large gaps can occur in the original time series of  $\psi$ , which reduces the reliability of the constant and harmonic term estimates and causes a speckled effect on the maps of these terms (Fig. 5.1). This could possibly be mitigated by applying the harmonic analysis to a time series covering multiple years. In areas with multiple rainfall or growing seasons, e.g. in regions closer to the equator, the harmonic analysis using a single harmonic is likely to fall short. This can be solved by adding harmonic terms with higher frequencies.

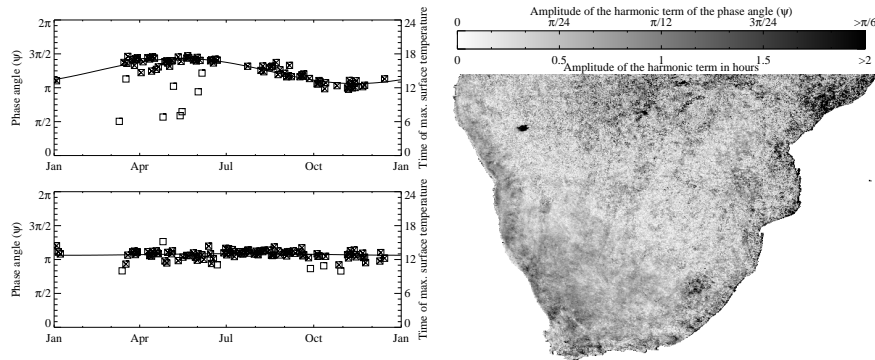


Figure 5.1: Left: Two examples of harmonic analysis of phase angle ( $\psi$ ) time series, one with a strong seasonality (top) and one with a weak seasonality (bottom) of  $\psi$ . Boxes are estimates of  $\psi$  derived for days with four surface temperature observations. The resulting interpolation (full line) is calculated on the checked boxes only. Right: Map of the amplitude of the harmonic term.

The derivation of the diurnal surface temperature amplitude, using the interpolated values of  $\psi$  and at least one daytime and one nighttime observation, assumes a sinusoidal behaviour of the surface temperature. To validate this assumption, the fit of the modelled temperature curve to the observations can be checked for pixels for the days where four observations are available. This results for each of these days in a root mean square error (*RMSE*). For a longer period of time, e.g. a full year, the average *RMSE* for each pixel in an image can thus be derived. The

performance of the sinusoidal model is compared to the advanced thermal inertia model of Xue and Cracknell (1995), further developed by Sobrino and El Kharraz (1999a), who used a second order approximation of the surface temperature (Eq. 2.13), and which can easily be rewritten in a way very similar to Eq. 5.2:

$$T_S(t_i) = a_0 + a_1 [C_1 \cos(\omega t_i - \psi) + C_2 \cos(2\omega t_i - f(\psi))] \quad (5.8)$$

with

$$C_1 = f_1(\delta, \phi, \psi) \quad \text{and} \quad C_2 = f_2(\delta, \phi, \psi) . \quad (5.9)$$

The coefficients  $a_0$  and  $a_1$  in Eq. 5.8 can be found similarly as in Eqs. 5.3 and 5.4, after which an average *RMSE* can be derived for days with four  $(t_i, T_S(t_i))$  observations in a similar way.

The validation of the sinusoidal approximation of the diurnal surface temperature behaviour (Eq. 5.2) is displayed in Fig. 5.2, which shows the spatial distribution of the average *RMSE* for the year 2009. This lies between 1 K and 2 K for most pixels in the study site (spatial average of 1.51 K and standard deviation of 0.22 K). Inland water bodies and wetlands show up clearly in Fig. 5.2 because of their low root mean square errors. These can be explained by the flat diurnal temperature behaviour of water, which makes them well described by a constant term only. Regions with high temperature amplitudes on the other hand will in general be characterized by larger errors on the temperature estimates. To eliminate these amplitude effects, a relative root mean square error (*rRMSE*) was derived by dividing the *RMSE* of each day by the amplitude of that day. The resulting map of the average *rRMSE* (Fig. 5.2), with most values between 5 percent and 15 percent of the diurnal temperature amplitude, indicates that the surface temperature behaviour of the more arid western part of the study site is relatively well described by the sinusoidal function. Large *rRMSE*'s at the more vegetated eastern coast however show that the sinusoidal approximation is not valid for these pixels, and that the apparent thermal inertia will there likely be of limited utility.

The validation of the advanced thermal inertia model of Xue and Cracknell (1995) (Eq. 5.8) resulted in a spatial average for the study site of 1.95 K with a standard deviation of 0.31 K. Notwithstanding its simplicity, the sinusoidal method thus seems to result in a better fit to the data than the more complex, physically-based model of Xue and Cracknell (1995). This could be due to a number of assumptions in the latter, including flat topography and a temperature range between 280 and 310 K, which are not imposed on the empirical sinusoidal approximation.

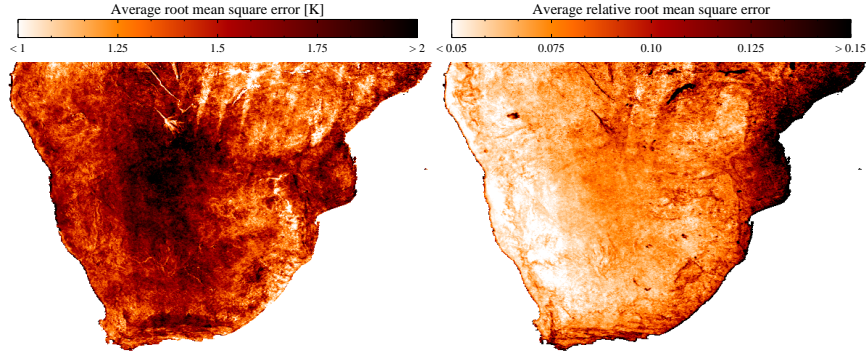


Figure 5.2: Left: Average *RMSE* for the year 2009, derived from days with four surface temperature observations. Right: Average *rRMSE*, derived for the same period.

#### 5.4 Apparent thermal inertia and soil moisture patterns over southern Africa

With the diurnal surface temperature amplitude derived from Eq. 5.3, apparent thermal inertia images are derived as (Short and Stuart, 1982):

$$ATI = C \frac{1 - \alpha_0}{A} \quad (5.10)$$

with

$$C = \sin \varphi \sin \delta (1 - \tan^2 \varphi \tan^2 \delta)^{1/2} + \cos \varphi \cos \delta \arccos(-\tan \varphi \tan \delta), \quad (5.11)$$

where *ATI* is apparent thermal inertia [ $\text{K}^{-1}$ ],  $\alpha_0$  the surface albedo [-], *C* the solar correction factor,  $\varphi$  the latitude [rad], and  $\delta$  is the solar declination [rad].

*ATI* thus is a measure of the temperature increase caused by the proportion of radiant energy that is absorbed by the Earth's surface. The solar correction factor *C* changes over space and time to normalize for solar flux variations with latitude and solar declination. The solar declination  $\delta$ , required for the calculation of *C*, is found using the method of Iqbal (1983):

$$\begin{aligned} \delta = & 0.006918 - 0.399912 \cos(\Gamma) + 0.070257 \sin(\Gamma) \\ & - 0.006758 \cos(2\Gamma) + 0.000907 \sin(2\Gamma) \\ & - 0.002697 \cos(3\Gamma) + 0.00148 \sin(3\Gamma) \end{aligned} \quad (5.12)$$

with

$$\Gamma = \frac{2\pi(n_d - 1)}{365.25}, \quad (5.13)$$

where  $\Gamma$  is the day angle [rad] and  $n_d$  is the day number [-].

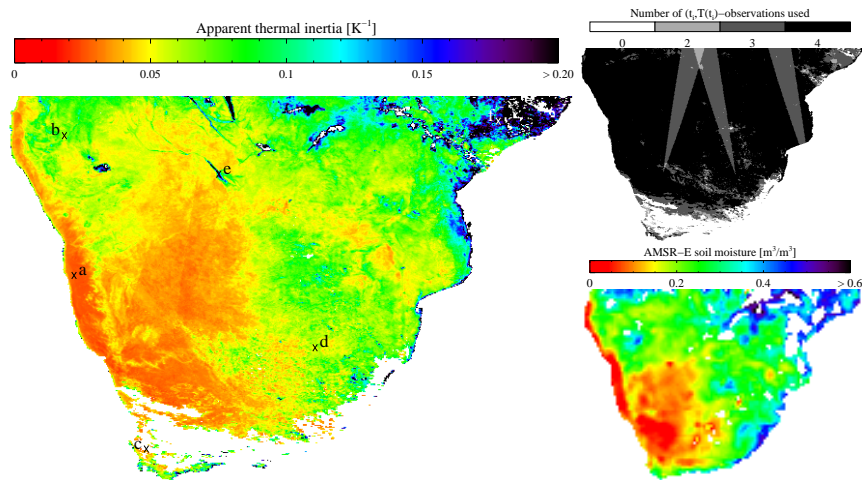


Figure 5.3: Left: MODIS apparent thermal inertia for March 26, 2009, with indication of locations of temporal profiles (Fig. 5.5). Right, top: Number of observations used to derive apparent thermal inertia on March 26, 2009. Right, bottom: VUA-NASA AMSR-E soil moisture for March 26, 2009, interpolated using a 7-day temporal average.

### 5.4.1 Spatial *ATI* patterns

Fig. 5.3 shows the *ATI* image at  $0.05^\circ$  resolution for March 26<sup>th</sup> and the corresponding AMSR-E soil moisture image at  $0.25^\circ$ . Comparison of both products shows that the apparent thermal inertia largely reflects the regional soil moisture pattern, with low values along the Atlantic coastline and higher values towards the East and North. Some specific dry or wet features can also be recognized in both images. The scatterplot of AMSR-E soil moisture versus MODIS apparent thermal inertia, downscaled by a 5 by 5 pixel averaging, for this date (Fig. 5.4) shows a clear, nearly linear, relation at the lower soil moisture ranges (below  $0.3 \text{ m}^3/\text{m}^3$ ). Above this level, a large amount of high-end noise is present with *ATI* values up to  $0.6 \text{ K}^{-1}$  (the ordinate in Fig. 5.4 has been limited to  $0.25 \text{ K}^{-1}$  for clarity), which limits the overall  $R^2$  for this date to 0.32.

Two possible reasons for this high end noise are unmasked water bodies and cloud cover in between surface temperature observations. These will both result in lower surface temperature amplitudes, hence unrealistically large *ATI* values. A third reason for the deviation of the best fit, especially in the higher soil moisture ranges, is the propagation of errors through the derivation of the apparent thermal inertia. Given a relationship of the type  $y = f(x_1, x_2, \dots, x_n)$ , the uncertainty on the dependent variable ( $\Delta y$ ) is expressed in a first order Taylor approximation as a

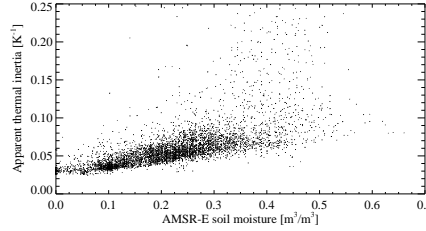


Figure 5.4: Scatterplot of AMSR-E soil moisture and apparent thermal inertia for March 26, 2009.

function of the uncertainties on the independent variables ( $\Delta x_1, \Delta x_2, \dots, \Delta x_n$ ):

$$\Delta y = \left| \frac{\partial y}{\partial x_1} \right| \Delta x_1 + \left| \frac{\partial y}{\partial x_2} \right| \Delta x_2 + \dots + \left| \frac{\partial y}{\partial x_n} \right| \Delta x_n . \quad (5.14)$$

The propagation of uncertainties on surface albedo and diurnal surface temperature amplitude through Eq. 5.10 is thus expressed as:

$$\Delta ATI = \left| \frac{C}{A} \right| \Delta \alpha_0 + \left| C \frac{1 - \alpha_0}{A^2} \right| \Delta A , \quad (5.15)$$

where  $\Delta ATI$  is the uncertainty on apparent thermal inertia [ $\text{K}^{-1}$ ],  $\Delta \alpha_0$  the uncertainty on surface albedo [-], and  $\Delta A$  is the uncertainty on amplitude [K].

The (squared) amplitude in the denominator of both terms of Eq. 5.15 indicates that in wet regions, hence with low temperature amplitudes,  $ATI$  will be very sensitive to errors on  $A$  and, to a lesser extent, on  $\alpha_0$ . This large sensitivity of thermal inertia to measurement errors at low day-night temperature differences was also acknowledged by other authors (Cai *et al.*, 2007; Verstraeten *et al.*, 2006) and is inherent to all formulations using temperature differences in the denominator.

Some sharp delineations appear in the  $ATI$  image (Fig. 5.3) which clearly do not correspond to sudden changes in soil moisture or land cover but are artefacts of the followed methodology. It can be observed that some of these (e.g. a triangular wedge running north northeast to south southwest in the western half of the study site) correspond to the different  $(t_i, T_S(t_i))$  combinations used (Fig. 5.3). This is clearly a trade-off for the flexibility of our method which allows for any number and combination of surface temperature observations to be fitted to the sinusoidal approximation. Forcing the method to use only a fixed set of observations would eliminate these artefacts, but would also result in a large amount of missing data in the regions between  $30^\circ$  north and south where consecutive MODIS swaths have no overlap. It can also be seen that some different input combinations result in seamless transitions in the  $ATI$  map. Other artefacts do not correspond to different  $(t_i, T_S(t_i))$  combinations used, but are already introduced in the derivation of  $\psi$

(Fig. 5.1) and can also be clearly discerned in Fig. 5.2. These originate from the 16-day repeat cycle of the Aqua and Terra spacecrafts and the associated fixed swath delineations at the one hand, and the limited thematic resolution of the time field of the M\*D11C1 products of 12 minutes at the other hand.

### 5.4.2 Temporal *ATI* patterns

As mentioned before, (apparent) thermal inertia is not only function of surface soil moisture, but also of surface geology and land cover. To eliminate these effects of geology it is useful to consider temporal *ATI* profiles on individual locations. By doing so, the signal can be considered to be mainly function of soil moisture, although changes in land cover, in particular vegetation phenology and agricultural practices, should not be ignored. Assuming a linear relationship between AMSR-E soil moisture and apparent thermal inertia, *ATI* can be converted to volumetric soil moisture estimates using the intercept and slope of linear regression between both. This way, the potential of *ATI* as a soil moisture indicator can be quantified in terms of a standard error of estimate (*SEE*).

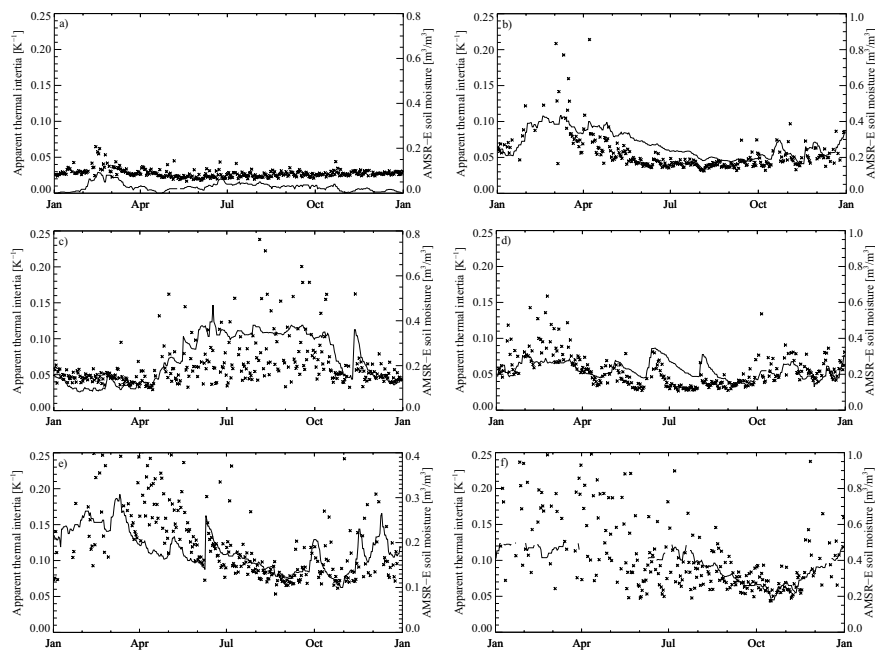


Figure 5.5: Temporal profiles of MODIS apparent thermal inertia (crosses) and VUA-NASA AMSR-E soil moisture (full line) for 2009. Right axis (AMSR-E soil moisture) has been scaled for each sub-figure separately for clarity. Sub-figures represent desert (a), savannah (b), cropland (c,d), wetland (e) and closed shrubland (f).



Fig. 5.5 displays a number of temporal *ATI* and AMSR-E soil moisture profiles of  $0.25^\circ$  resolution pixels at different locations in the study site (marked in Fig. 5.3), indicating the capabilities and limitations of the method used. A first time series for a pixel located in the Namib desert (a) shows a permanently low apparent thermal inertia, consistent with the passive microwave estimates ( $SEE=0.018\text{m}^3/\text{m}^3$ ). The lack of a seasonal *ATI* signal indicates that the solar correction factor *C* effectively corrects for differences in surface temperature amplitude induced by day length. Note that apparent thermal inertia will never become zero even at entirely dry soil, since that would require an infinite temperature amplitude. Low day-to-day noise may be caused by measurement uncertainty or different meteorological conditions (e.g. air temperature, wind velocity or air humidity).

A second profile (b) was taken over savannah pixels in the northwestern part of the study site where seasonal rains result in an increased soil moisture in the first part of the year. This increase is also visible in the *ATI*, although only few estimates are available between February and mid-March due to persistent cloud cover. *ATI* values are furthermore strongly scattered with spurious high outliers, likely caused by cloud cover in between surface temperature observations resulting in erroneous temperature amplitude estimates. An initial drying period in the second half of March is reflected in the *ATI*, as well as the gradual drying from May to October, including a dip in early August. For the remainder of the year the behaviour of *ATI* weakly reflects that of AMSR-E soil moisture, resulting in a *SEE* of  $0.059\text{m}^3/\text{m}^3$ .

The two following transects are taken over cropland, one in the vicinity of Cape Town (c,  $SEE=0.093\text{m}^3/\text{m}^3$ ), the other southwest of Johannesburg (d,  $SEE=0.043\text{m}^3/\text{m}^3$ ), with different wet seasons. In both transects, it can be seen that under wet (and vegetated) conditions, *ATI* only poorly reflects soil moisture conditions. During dryer and less clouded periods, however, some short-term wetting and drying events can be clearly discerned, including a drying, sudden wetting and consecutive drying sequence in October-November at site (c) and three wetting-drying events in May, June and August at site (d).

The next profile (e) is over the wetlands of the Okavango delta. Some striking correspondences to AMSR-E data here are a sudden increase in soil moisture early June, followed by a decrease in *ATI* until September. A drying sequence in the second half of March is also clearly reflected. For the remaining part of the year, correspondence is weak, especially between April and June. The overall *SEE* for the year 2009 is  $0.033\text{m}^3/\text{m}^3$ .

A last time series (f) is over a closed shrubland site at the northeastern part of the study site. Here the apparent thermal inertia method fails completely during the largest part of the year ( $SEE=0.106\text{m}^3/\text{m}^3$ ). Only during the dryer periods (October-November) a weak relationship between *ATI* and AMSR-E behaviour is



visible. It should be noted that the VUA-NASA algorithm produces no soil moisture estimates for a large part of the year for this pixel.

Most striking in the temporal profiles is that for relatively high soil moisture levels a large amount of noise is present in the *ATI* estimates, while this noise is absent at lower moisture levels. Also, *ATI* seems to perform poorly over vegetated surfaces, this in contrast to the findings of Verstraeten *et al.* (2006) who obtained good soil moisture estimates from apparent thermal inertia from Meteosat over European forests. This latter study, however, included the transformation of *ATI* to profile soil moisture over a depth of 1 m. The time lag and buffering associated with this conversion to profile soil moisture is likely to result in a filtering of noise on the original *ATI* estimates. The poor performance over vegetated terrain was already noticed in the poor fit of the surface temperature observation to the sinusoidal model (Fig. 5.2). Possibly a higher order model for the approximation of the surface temperature should be used over these areas, although the second order model of Xue and Cracknell (1995) provided a poorer fit to the data than the sinusoidal model. An alternative explanation is that persistent cloud cover or overpassing clouds between observations perturbate the expected temporal behaviour. A decisive answer to this can, however, not be provided without information with higher temporal resolution, e.g. from meteorological stations or geostationary sensors.

Over arid and semi-arid environments, apparent thermal inertia can clearly detect long-term and short-term soil moisture changes, although *ATI* declines at different rates than AMSR-E soil moisture in drying period. This can, amongst others, be observed in the drying period from May onwards in Fig. 5.5(b) and after the mid-June wetting event in Fig. 5.5(d). This is possibly caused by the depth of soil on which *ATI* and AMSR-E soil moisture depend. The microwave observations used to derive the AMSR-E soil moisture product is sensitive to moisture in approximately the top 1 cm of soil (Njoku *et al.*, 2003). The thermal infrared used in the derivation of land surface temperature and *ATI*, on the other hand, is only influenced by the first few millimetres of bare soil, which explains the faster decrease of *ATI*. Over vegetated soils, comparison of *ATI* and AMSR-E soil moisture becomes even more complex, since the algorithm to derive the latter separates influences of soil moisture and vegetation water content in the microwave signal. Apparent thermal inertia on the other hand does not discriminate between canopy cover and soil and will therefore be influenced by vegetation evapotranspiration. It will therefore also be influenced by the vegetation root zone moisture content, thus causing more discrepancies between *ATI* and AMSR-E soil moisture.

## 5.5 Apparent thermal inertia and soil moisture patterns over Calabria

*ATI* was derived for Calabria in a similar way, with the exception that only days on which four surface temperature observations were available were withheld. Since Calabria lies beyond the range of latitudes in which consecutive MODIS swaths do not overlap, the lack of  $(t_i, T_S(t_i))$  observations indicates cloud cover, and thus a disturbance of the anticipated sinusoidal temperature behaviour.

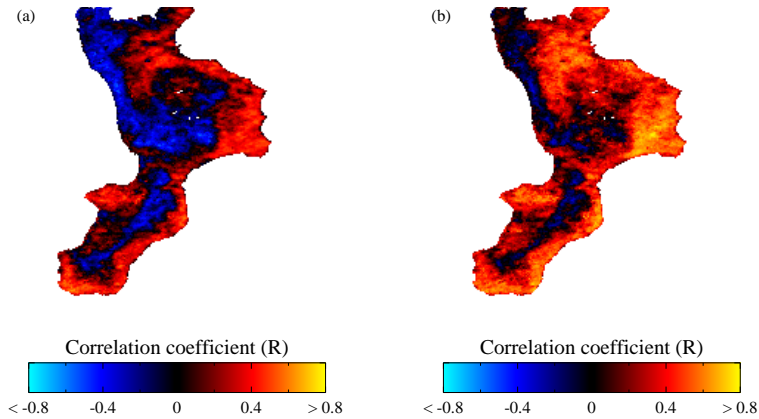


Figure 5.6: Correlation coefficients between modelled soil moisture and apparent thermal inertia for the entire 2-year time series (a) and for the months April–September in the 2-year time series (b).

Figure 5.6(a) shows the (temporal) correlation coefficient between modelled soil moisture and *ATI* for each pixel of the Calabria study site. It is observed that correlations are poor or, for many pixels, even negative. This could be expected based on the results for the southern African site, which indicated poor correlations over densely vegetated surfaces and during winter. When considering only the warmer and dryer months from April to September, it is observed that the correlation coefficient increases overall (Fig. 5.6(b)). Nevertheless, *R* values remain low when compared to those obtained using ASAR images and, for cropland pixels, even to those obtained for *NDVI* (Chapter 4).

## 5.6 Conclusions

A flexible method is presented for deriving apparent thermal inertia (*ATI*), and associated soil moisture related information, from Aqua and Terra MODIS optical and thermal data. In a first step, two, three or four daily temperature observations

are used to estimate the diurnal temperature amplitude in a sinusoidal approximation. The sinusoidal approximation provided a fit to the observations which approximates the estimated error on the MODIS land surface temperature measurements. The diurnal amplitude is then used in combination with surface albedo to produce daily *ATI* images. Temporal *ATI* profiles showed in general good correspondence with soil moisture derived from coarse resolution AMSR-E data over southern Africa, especially in arid and semi-arid environments. Over the more temperate study site of Calabria, correlations between *ATI* and soil moisture were found to be weak. Overall, apparent thermal inertia is a poor predictor of surface soil moisture over yearly time spans over vegetated areas. Short term changes of soil moisture are, however, well captured, especially under limited vegetation cover and during warmer periods.

The specific strength of the proposed methodology in comparison to other methods for deriving (apparent) thermal inertia is that there are no strict limitations on the number and time of day of land surface temperature observations. This considerably increases the number of *ATI* estimates that can be computed daily, especially in regions around the equator where swaths of medium spatial resolution sensors have in general no overlap.

An important limitation of the methodology is the vulnerability to noise introduced by meteorological conditions, which is inherent to the use of remote sensing data only. Spatial and/or temporal postprocessing algorithms could largely reduce this noise, e.g. by using the fact that meteorological influences will be strongly correlated spatially but only weakly correlated temporally. A second line of postprocessing is by coupling apparent thermal inertia to data from coarse resolution microwave radiometers (AMSR-E, SMOS) in data fusion models. This way the high spatial resolution information contained in *ATI* time series can be combined with relatively accurate low resolution soil moisture. Disaggregation of coarse resolution soil moisture with optical and thermal data has already been applied successfully (Chauhan *et al.*, 2003; Merlin *et al.*, 2009). The incorporation of thermal inertia into these kind of models seems a promising approach.

# 6

## Contextual surface temperature information as a soil moisture indicator

### 6.1 Introduction

Contextual information of remotely sensed surface temperature and vegetation indices have been used to infer information on spatial soil moisture patterns, usually through the so-called triangle method (Chapter 2). Remotely sensed soil moisture proxies generated by these methods have previously been applied successfully in species distribution modelling (Liu *et al.*, 2008; Berger *et al.*, 2013). A large number of variations on the triangle method have been suggested in literature. Notwithstanding these variations, almost all of these methods are based on a number of assumptions imposed on the study sites to which they are applied. First, these sites must be large enough to allow for a full range of vegetation cover and soil moisture conditions to be present, in order to be able to correctly define the dry and wet reference lines. On the other hand, they must be sufficiently small to avoid that surface temperature is influenced by other factors than fractional vegetation cover and soil moisture, such as latitude, elevation or spatially varying meteorological conditions. While it is debatable whether there are many places on earth where all these assumptions on the study site are valid, it is obvious that for a large number of places they are not. Until present, most authors deriving soil wetness status from the VI- $T_S$  space confined the method to relatively flat areas

---

This chapter is based on: Van doninck J., Peters, J., De Baets, B., De Clercq, E.M., Ducheyne, E., Verhoest, N.E.C. (2012). Influence of topographic normalization on the vegetation index-surface temperature relationship. *Journal of Applied Remote Sensing*, **6**, 063518, DOI: 10.1117/1.jrs.6.063518.

(e.g. Stisen *et al.*, 2008) or simply ignored topography (e.g. Han *et al.*, 2010). In a few studies, however, an attempt was made to incorporate topographic data into the VI- $T_S$  method (Vicente-Serrano *et al.*, 2004; Hassan *et al.*, 2007) using either an analytical or an empirical normalization approach. The performance of these normalization methods was, however, never validated.

Land surface temperature is the outcome of the equilibrium between incoming and outgoing energy balance components (Price, 1982). Topography influences the energy balance components in two fundamental ways. A first is through the orientation of the terrain, which controls the incoming solar radiation. Secondly, altitude differences affect the energy balance components that depend on air temperature, due to the general decrease of air temperature with elevation. A full topographic normalization thus needs to incorporate both terrain orientation and elevation above sea level.

This chapter therefore investigates the effects of terrain elevation and orientation on surface temperature, and more specifically on the VI- $T_S$  relationship for MODIS imagery over the region of Calabria. A new topographic normalization, a stratified linear regression approach, is presented and compared to two existing normalization methods. Additionally, the effect of the topographic normalization on a VI- $T_S$ -based soil dryness index is evaluated.

## 6.2 Study area and datasets

For this part of the research, performed on Calabria, 1 km Aqua daily land surface temperature products (MYD11A1) for the entire year 2009 were used, as well as the 16-day Normalized Difference Vegetation Index (*NDVI*) products covering the same period. The SRTM DEM was used as the source of elevation data. Three relatively unclouded days in the summer (July 8), autumn (October 8) and winter (December 31) of 2009 were selected to illustrate some of the discussed phenomena.

*NDVI* was converted to fractional vegetation cover ( $F_c$ ) following Carlson and Ripley (1997):

$$F_c = \left( \frac{NDVI - NDVI_{\min}}{NDVI_{\max} - NDVI_{\min}} \right)^2, \quad (6.1)$$

where  $NDVI_{\min}$  and  $NDVI_{\max}$  are the *NDVI* of bare soil and full vegetation cover, respectively.  $NDVI_{\min}$  and  $NDVI_{\max}$  are set to 0.25 and 0.90, corresponding respectively to the 1<sup>st</sup> and 99<sup>th</sup> percentile of the pooled *NDVI* values over a full year.  $F_c$  for an *NDVI* below  $NDVI_{\min}$  is set to 0, while an *NDVI* larger than  $NDVI_{\max}$  will result in a  $F_c$  larger than 1.

The choice for the fractional vegetation cover in the abscissa of the VI- $T_S$  space instead of the often used *NDVI* is slightly subjective. Despite the large body of re-

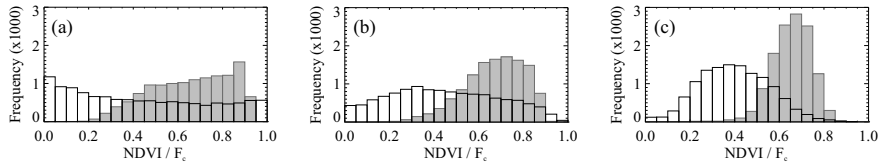


Figure 6.1: Frequency distribution of  $NDVI$  (shaded) and  $F_c$  (bold) for the images acquired on July 8 (a), October 8 (b) and December 31 (c) 2009.

search published on the topic, no comprehensive studies comparing both variables as input could be found. In this study, however,  $F_c$  is selected based on the frequency distribution of  $NDVI$  and  $F_c$  (Fig. 6.1). As can be seen in this figure,  $NDVI$  values are highly concentrated around 0.70, especially for the winter image. The empirical determination of the dry and wet edges requires a full range of moisture conditions over the complete range of the used vegetation index, which could be problematic in the case of a strongly peaked frequency distribution. The fractional vegetation cover is more evenly distributed throughout the  $[0,1]$  interval, allowing a better determination of the dry edge and wet edge.

The  $VI-T_S$ -based soil dryness index is validated for the autumn image of October 8, using data collected during the field survey on October 7 and 8 2009. Given the poor spatial consistency of the hydrological model (Chapter 3), this cannot be used in a spatial validation of the derived index. Since  $VI-T_S$ -based dryness estimates only provide values relative to other points of the same remotely sensed image of the same day, temporal validation of this method is irrelevant.

## 6.3 Normalization for terrain elevation

### 6.3.1 Normalization approaches

The influence of the air temperature lapse rate on the energy balance components has previously been simplified by applying a lapse rate of 0.65 K per 100 m on land surface temperature observations (Vicente-Serrano *et al.*, 2004). This number is based on the value of the idealized tropospheric lapse rate in a column of air (Brunt, 1933). This method has the disadvantage that the standard dry lapse rate of 0.65 K per 100 m is only an average value which may vary strongly in space and time (Stone and Carlson, 1979). Furthermore, this lapse rate refers to the decrease in air temperature in a vertical column of air which is heated from underneath by the land surface. In the topographic normalization problem, the near-surface air temperature is permanently influenced by heat exchange with the underlying land surface.

As an alternative, several authors have suggested a basic empirical approach, where the surface temperature gradient is estimated through linear regression be-

tween remotely sensed surface temperature and elevation ( $H$ ) (Warner and Chen, 2001; Jain *et al.*, 2008; Hais and Kučera, 2009). An empirical regression to estimate surface temperature lapse rates, which can subsequently be used in topographic normalization, has the advantage that it can account for changes in surface temperature lapse rates in time, while no in situ data are required. However, this method assumes that all factors influencing surface temperature, apart from elevation and orientation, can be treated as constant over the study site, or are independent of topography. Amongst these other factors affecting surface temperature are soil texture, soil moisture and vegetation cover, all of which might in some way be influenced by topography. Ideally, a topographic normalization should thus include information on these factors, in addition to a digital elevation model.

While it is difficult, if not impossible, to obtain soil moisture and texture in a heterogeneous terrain without in situ data, information on vegetation cover can be obtained easily through remote sensing. In the following, soil texture and moisture will thus be assumed to be independent of topography, while a new topographic normalization method will account for changes of vegetation cover with elevation. Changes in vegetation cover are customary in regions with strong topography, given the altitudinal zonation of vegetation and the suitability of different elevation ranges for different agricultural crops. The new normalization method introduced here bypasses the problem of altitudinal vegetation cover zonation by stratifying images over the study site into small intervals of fractional vegetation cover. Strata with a  $F_c$  width of 0.5, 0.2 and 0.1 are used in this study. Linear regressions between elevation and surface temperature are then performed on each stratum separately.

### 6.3.2 Results

Figure 6.2 shows the elevation-land surface temperature scatterplots for three relatively cloud-free days in summer (July 8), autumn (October 8) and winter (December 31), along with the regression lines for the unstratified images and for the images stratified in  $F_c$  intervals of width 0.1. A clear negative relation is apparent on all three dates, although temporal variations exist. The summer and autumn images consistently show lower temperatures with increasing fractional vegetation cover. This causes regression lines of the unstratified images for these dates to be much steeper than those of the small intervals.

Slopes of regression lines between elevation and surface temperature for the unstratified images and for the images stratified in 0.5, 0.2 and 0.1 intervals are given in Table 6.1. Again, summer and autumn show a similar behaviour, with in general decreasing (less negative) temperature gradients with decreasing stratum width. For the summer, the temperature gradient changes from -1.11 K per 100 m for the unstratified image, to an average of -0.73, -0.53 and -0.49 K per 100 m for the 0.5, 0.2 and 0.1 strata, respectively. In autumn, this decrease is less pronounced but still changes from -0.58 to -0.45, -0.39 and -0.38 K per 100 m for the unstrat-

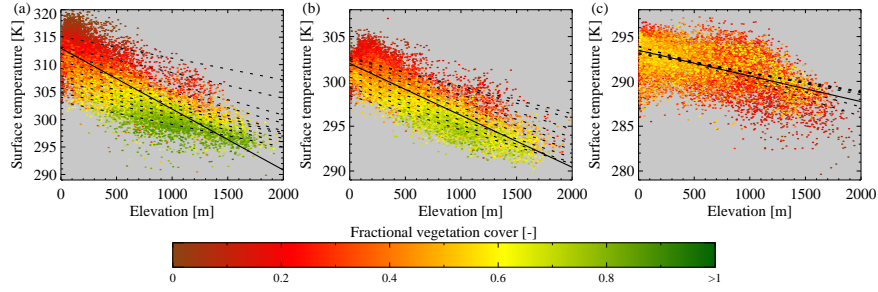


Figure 6.2: Scatterplots of elevation and land surface temperature on July 8 (a), October 8 (b) and December 31 (c) 2009. Full lines indicate linear regression over the unstratified images; dotted lines are regression lines calculated on fractional vegetation cover strata of 0.1 width.

Table 6.1: Slopes of regression lines between elevation and land surface temperature, given different fractional vegetation cover stratum widths. Missing values indicate strata with fewer than 500 pixels and are not included in further analysis.  $F_c$  values larger than 1 are used for the unstratified image but not for the different stratum widths.

Stratum		Slope [K/100m]		
Width	Endpoints	Jul. 8	Oct. 8	Dec. 31
Unstratified		-1.11	-0.58	-0.29
0.5	[0.0,0.5[	-0.86	-0.43	-0.31
	[0.5,1.0]	-0.61	-0.47	-0.21
0.2	[0.0,0.2[	-0.58	-0.32	-0.42
	[0.2,0.4[	-0.59	-0.40	-0.29
	[0.4,0.6[	-0.55	-0.42	-0.21
	[0.6,0.8[	-0.49	-0.43	-0.21
	[0.8,1.0]	-0.45	-0.38	/
0.1	[0.0,0.1[	-0.39	-0.30	/
	[0.1,0.2[	-0.47	-0.34	-0.39
	[0.2,0.3[	-0.56	-0.38	-0.34
	[0.3,0.4[	-0.56	-0.40	-0.25
	[0.4,0.5[	-0.57	-0.41	-0.22
	[0.5,0.6[	-0.52	-0.40	-0.21
	[0.6,0.7[	-0.48	-0.42	-0.22
	[0.7,0.8[	-0.46	-0.42	/
	[0.8,0.9[	-0.45	-0.38	/
	[0.9,1.0]	-0.41	/	/



ified image and the 0.5, 0.2 and 0.1 strata, respectively. For both the July 8 and October 8 images, variability of regression slopes within a given stratum width is small, and intercepts increase with decreasing  $F_c$ . This is apparent in the virtually parallel regression lines in Fig. 6.2. The winter image behaves differently, with very similar slopes for the unstratified image (-0.29 K per 100 m) and for the different stratum widths (averages of -0.26, -0.28 and -0.27 K per 100 m for 0.5, 0.2 and 0.1, respectively).

Stratification based on fractional vegetation cover manifestly influences the empirical topographic normalization, most obvious for the images acquired during the warmer months. For these two images, the large differences between the slope of regression lines for the unstratified datasets on the one hand and those for the different intervals on the other hand can be explained as the combined effect of the VI- $T_S$  relationship and the land cover pattern in Calabria. During the warmer post-harvest months, most fields at the lower elevations are barren, while the forest canopies at the higher elevations are fully developed. The general decrease of surface temperature with elevation is thus enhanced by the general increase in fractional vegetation cover with elevation and the decrease of surface temperature with increasing fractional vegetation cover. A simple empirical correction based solely on surface temperature and elevation would therefore overcompensate the decrease of surface temperature with elevation. This overcompensation is avoided by stratifying in increasingly smaller intervals of  $F_c$ , since this minimizes the effect of decreasing surface temperature with increasing vegetation cover, which is seen in the decreasing average slope with decreasing interval width. Given the limited decrease in slopes from the 0.2 to the 0.1 strata, further stratification in smaller intervals is considered inappropriate, since this may cause certain  $F_c$  strata to contain insufficient pixels or an insufficient range in elevation. Since the lapse rates —i.e. the negative of the slopes of linear regression— for the different  $F_c$  intervals for a given date are independent of the value of  $F_c$ , a representative stratified lapse rate can be derived by averaging the lapse rates of the individual strata of 0.1 width. This way, effects of possible outliers on the individual regressions are minimized.

As mentioned earlier, the stratified linear regression method assumes soil moisture and soil type to be independent of elevation. An elevation-dependence of these factors will introduce errors in the derivation of the surface temperature lapse rate. Under full canopy cover, however, the influence of soil type and topsoil moisture content on remotely sensed surface temperature and its lapse rate can be expected to be minimal. Since lapse rates for the bare soil strata and the full vegetation cover strata differ only slightly, the errors introduced by the assumptions of uniform soil properties are small compared to the differences in lapse rates between the three methods.

The lapse rates for all days of the year 2009 with sufficient cloud-free pixels, derived from the unstratified and the stratified linear regression models, are displayed in Fig. 6.3, together with the standard lapse rate of 0.65 K per 100 m. This

confirms the findings for the three selected days, with large differences between stratified and unstratified lapse rates during the summer months and very similar lapse rates during the winter months. Apart from a few exceptions, the stratified lapse rate is always lower than or equal to the unstratified lapse rate. Overall, a large day-to-day fluctuation of both the stratified and unstratified lapse rate is observed, while the stratified lapse rates are mostly below 0.65 K per 100 m and the unstratified lapse rates are in general above this number. Given the large day-to-day lapse rate variations, it should be advised against the use of a standard lapse rate of 0.65 K per 100 m in the normalization of land surface temperature.

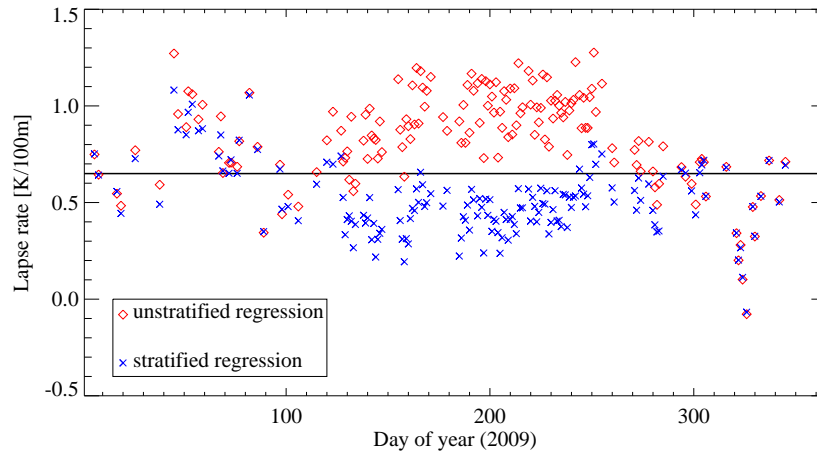


Figure 6.3: Lapse rates derived using the unstratified regression method and the stratified regression method for the days of the year 2009 with sufficient (at least 5000) cloud-free pixels over Calabria. The standard lapse rate of 0.65 K per 100 m is displayed as a horizontal line.

An assessment of the performance of different topographic normalization methods as such is difficult, since topographic normalization is never an objective in itself, but only a means to a higher goal. One way of evaluating these methods—at least those based on linear regression—is by comparing the observed surface temperatures with those obtained using the regression equation  $T_S = a + bH + \epsilon_0$ , where the coefficients  $a$  and  $b$  are derived using the two linear regression methods mentioned above, and  $\epsilon_0$  is an error term including systematic and random errors. In the case of stratified linear regression,  $a$  was found to be function of  $F_c$ , so that the equation becomes  $T_S = a_0 + a_1F_c + bH + \epsilon_0$ , where  $a_0$  and  $a_1$  are obtained using the nearly linear increase of intercepts with increasing fractional vegetation cover (Fig. 6.2). The coefficient of determination ( $R^2$ ) of both linear regression methods is a measure of the magnitude of the systematic errors and can thus be used as an indicator of the performance of the topographic normalization (Hais

and Kučera, 2009).

The  $R^2$  values for both methods for all cloud-free days of the year 2009 are shown in Fig. 6.4. Systematic errors for the unstratified regression method are notably higher than those for the stratified regression method during the summer months, resulting in much lower  $R^2$  values for the former. During winter, differences in  $R^2$  are much lower. The periods with large  $R^2$  differences correspond to the periods with large differences between the stratified and unstratified lapse rates (Fig. 6.3). The systematic errors are clearly reduced by incorporating information on fractional vegetation cover in the stratified regression method.

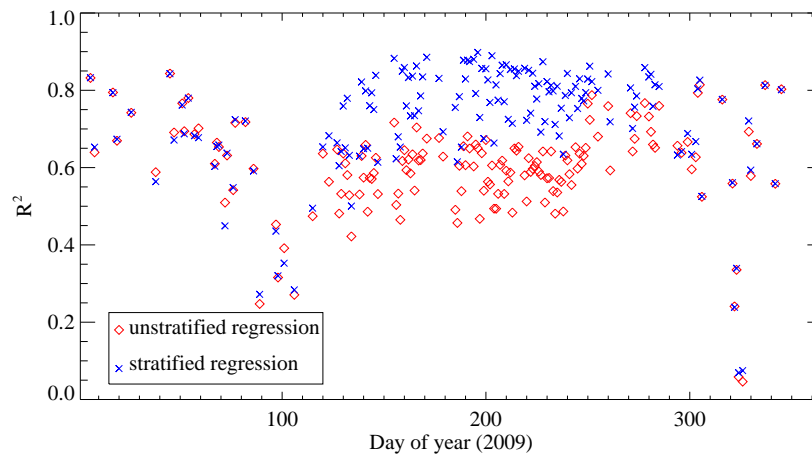


Figure 6.4: Determination coefficient between observed surface temperature and surface temperature estimated using coefficients derived from unstratified and stratified regression and elevation (and vegetation index in the case of the stratified regression method) for the days of the year 2009 with sufficient (at least 5000) cloud-free pixels over Calabria.

## 6.4 Normalization for terrain orientation

### 6.4.1 Normalization approaches

In the reflective part of the spectrum, normalization for terrain orientation is based on the solar incidence angle, which can be derived from the terrain slope and aspect on the one hand, and solar position at the time of image acquisition on the other. Several normalization methods using the solar incidence angle have been developed and studied intensively (Riaño *et al.*, 2003; Zhang *et al.*, 2011). A few studies (Warner and Chen, 2001; Vicente-Serrano *et al.*, 2004; Hais and Kučera, 2009)

tried to integrate illumination, or terrain orientation into an empirical topographic normalization. Here, the influence of terrain orientation is assessed through linear regression between  $T_s$  and the quotient of the cosine of the local solar incidence angle ( $i$ ) and the cosine of the solar zenith angle ( $z$ ), an approach previously followed by Vicente-Serrano *et al.* (2004).  $T_s$  used here is the surface temperature normalized for terrain elevation using the stratified regression, since this method provided the most realistic estimates. Normalization of the cosine of the incidence angle by the cosine of the zenith angle is done to obtain unity for horizontal terrain.

As for the elevation normalization, the empirical normalization for terrain orientation is performed using both the unstratified and the stratified approach. For the stratified linear regression, the same  $F_c$  of width 0.5, 0.2 and 0.1 are used.

## 6.4.2 Results

Figure 6.5 shows the  $(\cos(i)/\cos(z))$ -land surface temperature scatterplots for the three days mentioned earlier, along with the regression lines for the unstratified images and for the images stratified in  $F_c$  intervals of width 0.1. Slopes of regression lines for the unstratified images and for the images stratified in 0.5, 0.2 and 0.1 intervals are given in Table 6.2. Again, it is observed that stratification based on fractional vegetation cover influences the linear regression, most obvious for the July 8 and October 8 images. Again, this can be attributed to the biased land use, where croplands are concentrated in flat or slightly sloping areas and strong slopes are in general heavily vegetated.

It is observed for the autumn image that the slope is no longer constant for the different strata within a given width, but that the dependency of surface temperature on illumination decreases with increasing vegetation cover. This is due to the ability of a full canopy cover to maintain a skin temperature close to air temperature, irrespective of the amount of incident solar radiation (Lambin and Ehrlich, 1996). Surface temperature in the July 8 image is hardly related to illumination, as indicated by the regression coefficients being close to zero for the 0.1 strata. This is partly due to the high elevation of the sun at the time of image acquisition, resulting in a small range of  $\cos(i)/\cos(z)$ . Secondly, using the incidence angle as a proxy for the integrated solar heating ignores the antecedent heating during the day, which can be important during summer. Alternatively, Aqua MODIS data could be replaced by Terra data. The late-morning acquisition of the Terra satellite will result in a smaller perturbation by antecedent heating than the early-afternoon acquisition of Aqua (Warner and Chen, 2001). However, early-afternoon images will enhance the contrast between the surface temperature of dry soils and moist soils, making them more suitable for this specific application. Because of the complexity introduced by antecedent heating, topographic normalization will in the following be restricted to the influence of elevation of the terrain above sea level, ignoring terrain orientation.

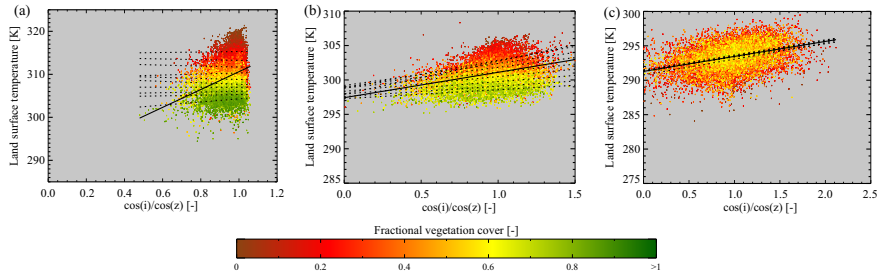


Figure 6.5: Scatterplots of elevation and land surface temperature on July 8 (a), October 8 (b) and December 31 (c) 2009. Full lines indicate linear regression over the unstratified images; dotted lines are regression lines calculated on fractional vegetation cover strata of 0.1 width.

Table 6.2: Slopes of regression lines between illumination ( $\cos(i)/\cos(z)$ ) and land surface temperature, given different fractional vegetation cover stratum widths. Missing values indicate strata with fewer than 500 pixels and are not included in further analysis.  $F_C$  values larger than 1 are used for the unstratified image but not for the different stratum widths.

Stratum		Slope [K]		
Width	Endpoints	Jul. 8	Oct. 8	Dec. 31
Unstratified		20.74	3.69	2.18
0.5	[0.0,0.5[	11.18	3.39	2.24
	[0.5,1.0]	1.84	1.87	1.99
0.2	[0.0,0.2[	4.95	4.24	2.34
	[0.2,0.4[	0.60	3.08	2.23
	[0.4,0.6[	-0.74	2.34	2.07
	[0.6,0.8[	0.66	1.60	2.14
	[0.8,1.0]	2.17	1.31	/
0.1	[0.0,0.1[	0.56	4.78	/
	[0.1,0.2[	-0.85	4.04	2.29
	[0.2,0.3[	-1.11	3.20	2.30
	[0.3,0.4[	1.22	2.84	2.17
	[0.4,0.5[	-1.20	2.31	2.17
	[0.5,0.6[	-1.68	2.13	1.94
	[0.6,0.7[	-0.07	1.81	2.12
	[0.7,0.8[	0.78	1.51	/
	[0.8,0.9[	0.74	1.30	/
	[0.9,1.0]	3.66	/	/

## 6.5 Influence of normalization on the VI- $T_S$ relationship

Effects of topography and the different topographic normalization methods on the VI- $T_S$  relationship are shown in Figs. 6.6 to 6.8 for the three aforementioned dates. The scatterplot of fractional vegetation cover and uncorrected land surface temperature exhibits a clear negative relationship for the summer and autumn images, while this is absent in the winter image. The absence of a negative relationship during the winter months supports the findings of Sun and Kefalos (2007) and Karnieli *et al.* (2010) that a negative correlation only exists in areas and seasons when moisture, and not energy, is the limiting factor for evaporation and vegetation growth (e.g. in arid and semi-arid regions and in temperate regions during the warmer months).

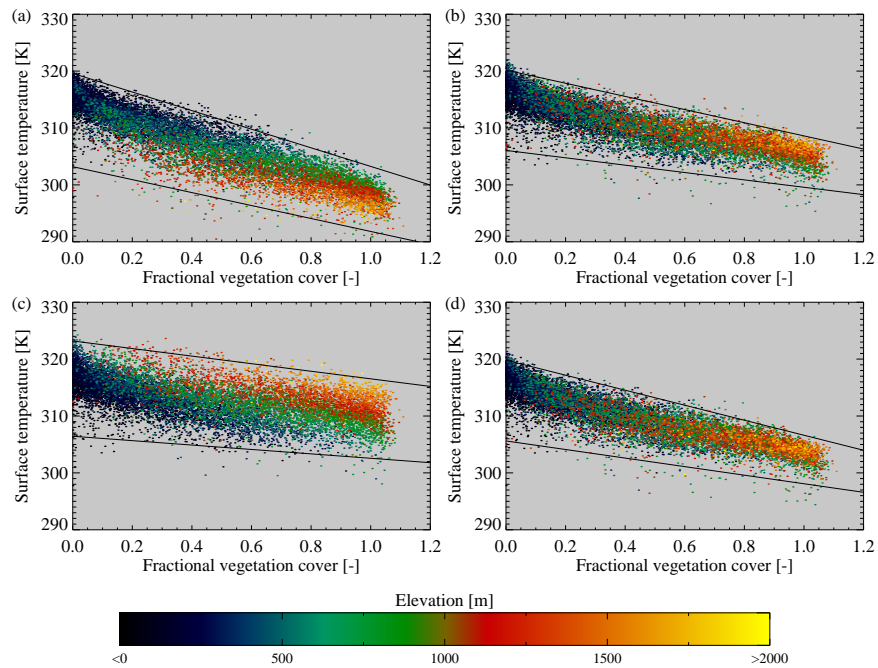


Figure 6.6: Scatterplots of  $F_c$  and  $T_S$  on July 8, derived using unnormalized surface temperature (a), and surface temperature normalized using the standard lapse rate (b), unstratified regression model (c) and stratified regression model (d). Full lines are empirical dry and wet edges.

Visual inspection of the scatterplots using land surface temperature normalized with the standard lapse rate and the unstratified regression shows that, for the

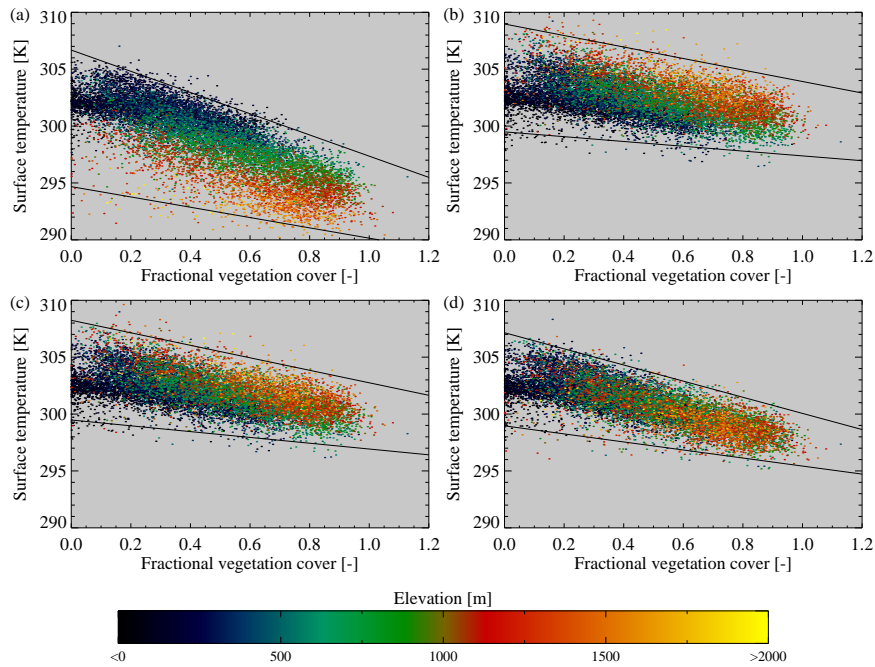


Figure 6.7: Scatterplots of  $F_c$  and  $T_S$  on October 8, derived using unnormalized surface temperature (a), and surface temperature normalized using the standard lapse rate (b), unstratified regression model (c) and stratified regression model (d). Full lines are empirical dry and wet edges.

summer and autumn images, these normalization methods seem to overcorrect the influence of elevation. This results in systematically higher temperatures at higher elevations and a decrease of the slope of the  $VI-T_S$  relationship. For the winter image, unstratified regression seems to provide a correct normalization, while the standard lapse rate seriously overcorrects elevation. The topographic normalization based on stratified linear regression visually results in the clearest  $VI-T_S$  relationship for the summer and autumn images. A nearly identical scatterplot as for unstratified regression is found for the winter image, which could be expected from the very similar lapse rates for these methods (0.29 K and 0.27 K per 100 m for unstratified and stratified regression, respectively). The visual interpretation of the  $VI-T_S$  scatterplots corresponds to the findings of Fig. 6.4 that the stratified linear regression method yields better results for the warmer months, while stratified and unstratified regression produce similar results during the colder months. The standard lapse rate of 0.65 K per 100 m is inferior to the stratified regression method for all three dates.

The overcorrection observed during the warmer months for the unstratified

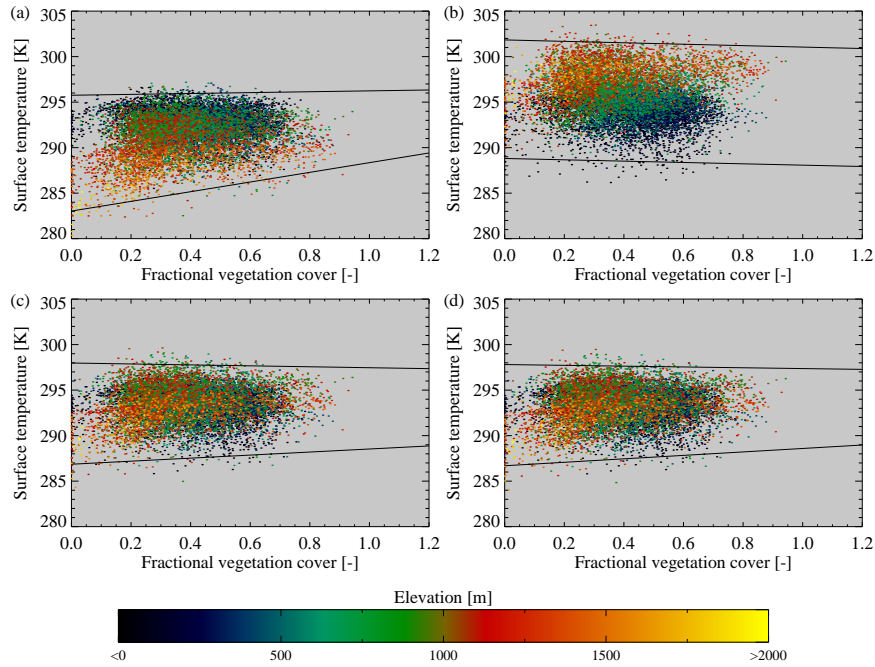


Figure 6.8: Scatterplots of  $F_c$  and  $T_S$  on December 31st, derived using unnormalized surface temperature (a), and surface temperature normalized using the standard lapse rate (b), unstratified regression model (c) and stratified regression model (d). Full lines are empirical dry and wet edges.

regression method (Figs. 6.6(c) and 6.7(c)) can clearly be attributed to the overestimation of the unstratified lapse rate, which in turn is caused by the negative VI- $T_S$  relationship and the increase of vegetation cover with elevation during this period. The stratified regression method does incorporate possible effects of the VI- $T_S$  relationship, resulting in an overall much lower lapse rate (Fig. 6.3) and a visually realistic topographic normalization (Figs. 6.6 to 6.8). During the winter months, the stratified regression method loses its advantage over the unstratified one due to the absence of a negative VI- $T_S$  relationship.

## 6.6 Influence of normalization on soil dryness estimation

The different topographic correction methods can also be validated by studying their influence on the derivation of a Temperature-Vegetation Dryness Index



(*TVDI*). *TVDI* is derived as (Sandholt *et al.*, 2002; Wang *et al.*, 2004):

$$TVDI = \frac{T_S - T_{S,wet}(F_c)}{T_{S,dry}(F_c) - T_{S,wet}(F_c)} \quad (6.2)$$

where  $T_{S,dry}(F_c)$  and  $T_{S,wet}(F_c)$  are the maximum and minimum (normalized) surface temperature, respectively, given the pixel's  $F_c$  and thus correspond to the dry and wet edges. The sloped wet and dry edges are derived through linear regression on the minimum, respectively maximum,  $T_S$  values within  $F_c$  intervals of 0.01 width (Patel *et al.*, 2009). The different normalization methods are validated by comparing the *TVDI* they generate with in situ soil moisture measurements.

### 6.6.1 Visual analysis

The Temperature-Vegetation Dryness Index was derived for the October 8 image, since this date coincides with in situ soil moisture measurements. Given the limited amount of in situ soil moisture data in the study area, and the limited amount of in situ data in regions with strong topography in general, this part of the validation is more illustrative. Topographic normalization clearly changes the shape of the fraction vegetation cover-land surface temperature scatterplot, as well as the position of the empirically derived dry and wet edges (Figs. 6.6 to 6.8). It is therefore not surprising that the resulting *TVDI* is also strongly affected by the type of topographic normalization (Fig. 6.9). The *TVDI* image derived using the uncorrected land surface temperature (Fig. 6.9(a)) strongly reflects the topography of Calabria, with low *TVDI* values at high elevations and vice versa. These patterns are no longer present in the *TVDI* images derived using the standard lapse rate and unstratified regression (Fig. 6.9(b)–(c)), although the overcorrection of elevation that was visible in the scatterplots (Fig. 6.7) is also apparent in some extreme low values at high elevations. This overcompensation is not observed in the *TVDI* image based on stratified regression (Fig. 6.9(d)).

### 6.6.2 In situ soil moisture

Validation of the Temperature Vegetation Dryness Index with in situ volumetric soil moisture content (Fig. 6.10) shows a clear negative relation for all three topographic normalization methods. The relation between uncorrected *TVDI* and soil moisture is much weaker. Although stratified regression, out of the three normalization methods, results in the largest  $R^2$  (0.32 versus 0.25 and 0.28 for the standard lapse rate and the unstratified regression method, respectively), the differences between the  $R^2$  values are not significant (at  $p = 0.05$ ). These absolute values and relative differences should be treated with the necessary reservation because of a number of reasons. First, there is the discrepancy between the moment of image acquisition (October 8) and the in situ soil moisture collection (October 7 and 8). A second point of caution is that the depth of in situ soil moisture collection (0–10 cm) does not correspond to the depth of the soil in which moisture influences

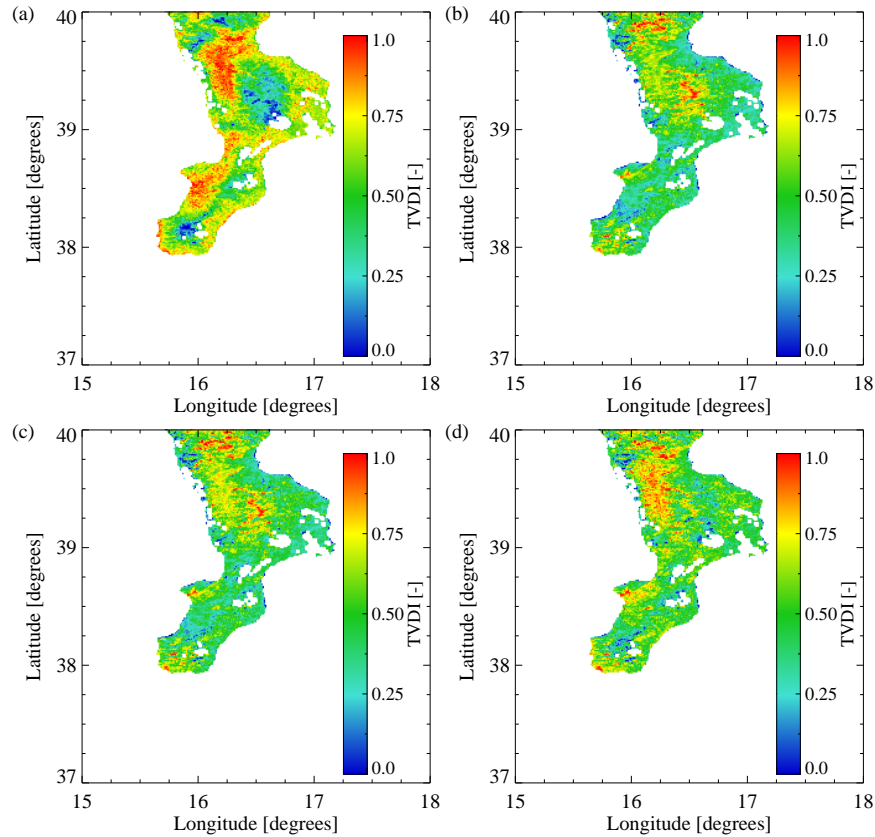


Figure 6.9: Temperature Vegetation Dryness Index for October 8, derived using unnormalized surface temperature (a), and surface temperature normalized using the standard lapse rate (b), unstratified regression (c) and stratified regression (d). Missing values indicate cloud cover.

surface temperature through evaporative or transpirative control. This depth ranges from a few millimetres to centimetres over bare soil to the root zone under fully developed vegetation. Finally, validation is hampered by the limited range of in situ soil moisture content (mostly between  $0.25$  and  $0.40 \text{ cm}^3/\text{cm}^3$ ). Nevertheless, it appears that the topographic normalization based on stratified regression is a suitable method to allow  $VI-T_S$ -based methods to be applied in regions with variations in elevations, and is superior to applying a standard lapse rate of  $0.65 \text{ K per } 100 \text{ m}$  or a lapse rate derived through simple linear regression.

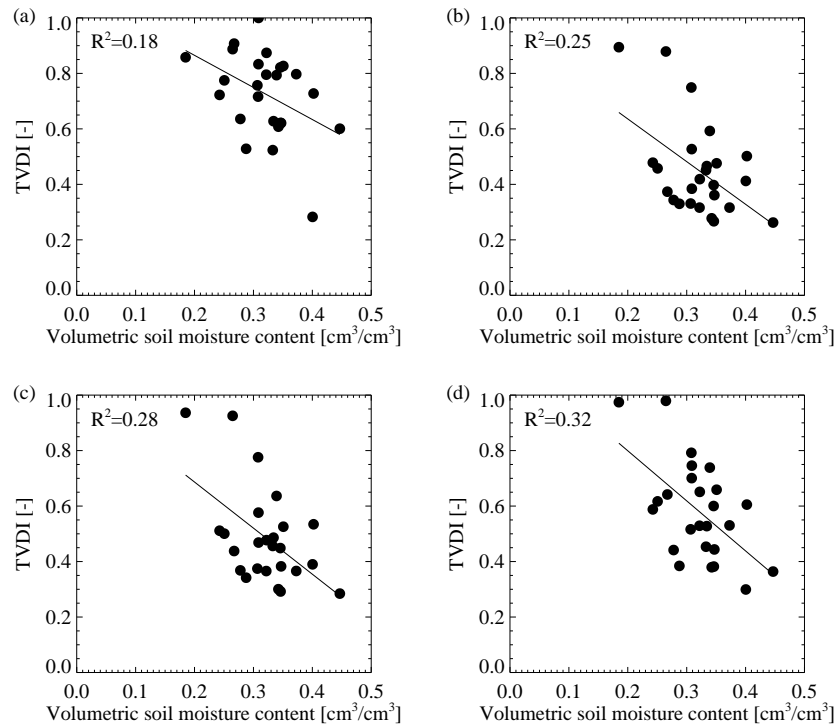


Figure 6.10: Validation of the Temperature Vegetation Dryness Index for October 8, derived using unnormalized surface temperature (a), and surface temperature normalized using the standard lapse rate (b), unstratified regression (c) and stratified regression (d), with indication of regression lines and coefficients of determination (all significant at  $p=0.05$ ).

## 6.7 Conclusions

The utility of the vegetation index-surface temperature space for the derivation of evapotranspiration and soil wetness status is severely restricted in areas with strong topography. This is because surface temperature is influenced by terrain elevation and orientation, as well as by soil moisture. Existing strategies to account for altitudinal effects include topographic normalization of remotely sensed land surface temperature based on a standard lapse rate of 0.65 K per 100 m or on a lapse rate derived through linear regression of elevation and surface temperature. In this study, it was shown that lapse rates of Aqua MODIS land surface temperature vary strongly between consecutive days. Using a fixed standard lapse rate in topographic normalization ignores this variability and will therefore result in a sub-optimal correction. While applying a lapse rate based on linear regression is useful

in case of homogeneous landcover or under conditions where spatial differences in evaporative cooling are negligible, it becomes problematic when vegetation cover changes with elevation. The latter is the case in regions like Calabria where lower elevations are occupied by croplands and forests are found at higher elevations, combined with different periods of the growing season over the different elevation ranges. Simple linear regression between elevation and land surface temperature is here affected by the negative VI- $T_S$  relationship, and causes strong overestimations of the surface temperature lapse rate.

A new topographic normalization was proposed in this chapter, based on stratified linear regression. In this approach, the study site is first stratified in small vegetation fraction intervals. A separate linear regression between elevation and surface temperature is then performed for each interval. It was found that, for a given date, the slopes of regression lines were approximately equal for all vegetation fraction intervals. The average value of these slopes can thus be used in the topographic normalization. Although the new topographic normalization method is here only tested for Calabria, similar behaviour may be expected when applied to other regions where vegetation type shifts with elevation.

Visual interpretation of VI- $T_S$  scatterplots derived using the different normalization techniques showed a clearer and less elevation-dependent VI- $T_S$  relationship for the stratified regression normalization for different periods throughout the year. The dryness index derived using this normalization method resulted, for a limited reference dataset, in a slightly stronger negative correlation with in situ soil moisture than the other methods.

In addition to the decrease of temperature with elevation, topography also influences  $T_S$  through the terrain orientation relative to the sun. A normalization based on the solar incidence angle showed that, under some conditions, the relationship between solar incidence angle and surface temperature is function of vegetation cover. A stratified regression therefore also seems a promising approach for this type of normalization. However, antecedent heating of the surface limits the use of the solar incidence angle as the independent variable in the regression. Further study of the effect of antecedent heating on the normalization for terrain orientation is therefore required.

It can be concluded that the choice of a topographic normalization method can strongly alter the vegetation index-surface temperature relationship. Using an appropriate normalization widens the applicability of the VI- $T_S$  relation for the derivation of soil wetness or dryness status in mountainous terrains, although other influences on surface temperature, such as atmospheric forcing, terrain orientation or soil texture, still impose restrictions on the methodology. The topographic normalization and soil dryness status estimation are not restricted by the availability of any sort of ancillary data, except for a (remotely sensed) digital elevation model. The validation of the influence of topographic normalization on the soil dryness

index in this study used only a limited amount of reference data. Future validation should include a larger amount of in situ data. Unfortunately, in this respect, most extensive in situ soil moisture networks are, to our knowledge, located over flat or gentle topographies. Additionally, spatial validation of medium resolution remotely sensed soil moisture products using in situ data remains difficult due to the scale gap between both data sources.

# 7

## Soil moisture proxies for species distribution modelling: conclusion

In this first part, three selected remotely sensed soil moisture proxies were studied and further developed, and their temporal or spatial correlation with in situ or modelled soil moisture was assessed. This chapter discusses the anticipated utility of these soil moisture proxies when integrated in species distribution models.

Two proxies were derived from MODIS visible, near infrared and thermal infrared data. The popular contextual surface temperature methods (Chapter 6) have the advantage that they provide relative spatial differences in soil moisture. In other words, they identify which regions are, at a given moment in time or over a given range of time, wetter or dryer than other regions in the satellite image. While Chapter 6 derived a soil dryness index for daily surface temperature observations, there is no reason why temporally averaged surface temperature should not be used. In theory, proxies obtained through this method could thus be useful for species distribution modelling, and indeed have been integrated in the modelling of desert locust (Liu *et al.*, 2008) and blacklegged tick (Berger *et al.*, 2013) habitat. However, these contextual 'triangle' methods are often applied without much consideration of the specific circumstances under which they are to be applied, e.g. by ignoring the effect of elevation on surface temperature, which can be severe in regions like Calabria. Nevertheless, it was shown in Chapter 6 that the limitations imposed by topography can be easily circumvented by a topographic normalizing. A second issue is that this method is only to be used under conditions

when evapotranspiration is energy limited. During winter, indices derived through this methods can thus be assumed to be poorly correlated to surface soil moisture.

Apparent thermal inertia, a second proxy using MODIS shortwave and thermal data, was also found to be correlated to soil moisture content spatially and temporally (Chapter 5). This correlation might partly be induced by a vegetation signal, since also *NDVI* was found to be correlated to soil moisture (Chapter 4). Nevertheless, *ATI* showed to be able to detect short-term wetting and drying events. As for the contextual surface temperature methods, *ATI* can be assumed to be of limited utility during winter months and over dense canopy cover. Given these restrains, the utility of this proxy in species distribution modelling is questionable.

By far the best temporal correlation with modelled soil moisture was found for the ASAR WS soil moisture index (Chapter 4), and this for a variety of cover types and without restriction with regard to the season. An important issue for applicability of this proxy in species distribution models is that it only reflects a degree of saturation. One pixel can have a higher degree of saturation than another while having a lower volumetric soil moisture content. Nevertheless, this proxy allows to detect which pixels remain relatively wet, or dry, during certain periods, and at which speed surface wetness decreases after a precipitation event. The main restriction of this ASAR product, like for all SAR systems up to date, is the limited temporal resolution. This can be expected to improve with the launch of the first Sentinel satellite.

The aim of the previous chapters was to derive soil moisture proxies without requiring abundant ancillary datasets. This was important for the proxies to be applicable in distribution models over a variety of regions. The only ancillary dataset used was the remotely sensed SRTM digital elevation model. This DEM is available for all land surfaces between 60° N and 56° S and should thus not pose restrictions for most applications. For operational applications, different postprocessing methods could be applied on the soil moisture proxies investigated in the previous chapters. These include the identification and filtering of outliers and the spatial and/or temporal interpolation of missing data. These postprocessing steps are, however, outside the scope of this dissertation.

Part II:  
Spatial distribution modelling





# 8

## Modelling the spatial distribution of *C. imicola* using climatic and remote sensing data

### 8.1 Introduction

#### 8.1.1 History of bluetongue virus in the Mediterranean Basin

Bluetongue is a disease, listed by the World Organisation for Animal Health, caused by the bluetongue virus (BTV), a species of the *Orbivirus* genus (Wilson and Mellor, 2009). BTV is capable of infecting any type of ruminant, including cattle, deer, goats and camelids, but mainly affects populations of sheep. Although most infected animals develop no detectable signs, symptoms of bluetongue are manifold, including the death of the animal. The blue tongue giving the disease its name is only seldomly developed.

Until halfway the twentieth century, BTV was only observed in parts of Africa and Cyprus (Wilson and Mellor, 2009). From the 1950s onwards, outbreaks of bluetongue were observed in Israel (1951), the USA (1952), Spain and Portugal (1956–1960), Asia (1961) and Australia (1975). By the end of the century, BTV had spread to roughly all the land masses from approximately 35° S to 40° N, with

---

This chapter is based on: Van doninck, J., De Baets, B., Peters, J., Hendrickx, G., Ducheyne, E., Verhoest, N.E.C. (2013). Modelling the spatial distribution of *Culicoides imicola*: climatic versus remote sensing data. *International Journal of Applied Earth Observation and Geoinformation*, submitted.

different serotypes of the virus occurring in different locations. On the old continent, BTV started to spread rapidly from 1998 onwards, first being detected on several Greek islands and reaching mainland Greece and Kosovo in 2001. Meanwhile, at the other side of the Mediterranean, another BTV serotype spread from Tunisia, Algeria and Morocco to the Balearic islands, Corsica, Sardinia, Sicily and southern Italy by the end of the year 2000. In August 2006, an outbreak of bluetongue was reported in the Netherlands and rapidly spread to Belgium, France, Luxembourg and, the following years, Denmark, Switzerland, the Czech Republic and the UK (Saegerman *et al.*, 2008).

The bluetongue virus has sporadically been observed to be transmitted orally between animals, or transplacental between mother and offspring (De Clercq *et al.*, 2008). Overall, however, BTV is a vector-borne disease, spread by female adults of several species of biting midges of the genus *Culicoides*.

### 8.1.2 *Culicoides imicola* life cycle and habitat characteristics

*Culicoides* (Diptera: Ceratopogonidae) is a genus within which more than 1400 species have been identified worldwide (Mellor *et al.*, 2000), all measuring from 1 mm to 3 mm in size. The life cycle of *Culicoides* includes three immature stages, egg, larva and pupa, and a mature or imago stage. Breeding sites of the immature stages vary greatly for the different species, ranging from rotting vegetation and animal dung over different types of soil to tree holes.

The vast majority of *Culicoides* species are blood sucking, attacking mammals and birds. Blood feeding by adult females is required for the maturation of the eggs. Since most *Culicoides* species are crepuscular, the peak activity of blood feeding is around sunset and sunrise. It is during these blood meals that viruses can be transmitted from *Culicoides* to host animal and vice versa. Apart from BTV, several other viruses affecting non-human mammals can be transmitted, the most important being African horse sickness virus, epizootic hemorrhagic disease virus, equine encephalosis virus, Akabane virus, bovine ephemeral virus and the Palyam virus. The only significant virus affecting humans transmitted by *Culicoides* is the Oropauche virus (Mellor *et al.*, 2000). Each of these viruses is transmitted by only a fraction of the 1400 different *Culicoides* species.

In the Mediterranean Basin, a single species, *C. imicola*, is considered as the main vector of BTV. The recent northward spread of bluetongue indicates that species other than *C. imicola* also act as vectors, since the spatial distribution of this species is confined to Africa and Mediterranean Europe. Climate change may, however, be responsible for an expansion of the territory of *C. imicola* in the fringe of the Mediterranean Basin, although Conte *et al.* (2009) found no geographic expansion of this species in Italy.

Given the economic consequences of diseases transmitted by *Culicoides* spp. in general, and *C. imicola* in particular, several laboratory and field studies have been

conducted in order to determine the habitat characteristics of the different species. Additionally, modelling studies tried to derive these habitat characteristics using data from of in situ *Culicoides* trapping sites and meteorological, remote sensing and other datasets. The main environmental factors identified to constrain the distribution of *Culicoides* spp., and more specifically *C. imicola*, are listed here.

### 8.1.2.1 Temperature

Air temperature is considered as one of the major limiting factors of *C. imicola* distribution on a continental scale, although the precise biological basis of this dependency is unclear. For several *Culicoides* species, correlations between air temperature and species activity, larval survivorship and adult mortality were observed in trapping or laboratory studies (Mellor *et al.*, 2000). In a laboratory study, Veronesi *et al.* (2009) observed that the period required for blood-feeding *C. imicola* females to produce adult progeny occupied 34–56 days at 20°C, 15–21 days at 25°C and 11–16 days at 28°C. Additionally, freezing temperatures are known to kill adult midges, thus reducing catch abundances at sites affected by frost (Venter *et al.*, 1997).

This dependency on air temperature was confirmed in several *C. imicola* modelling studies using climatic data. Purse *et al.* (2007) found *C. imicola* in the Mediterranean Basin to occur in warm (annual mean 12–20°C) regions with low seasonal variations. A model developed by Wittmann *et al.* (2001) identified three temperature variables (minimum of the monthly minimum temperatures, maximum of the monthly maximum temperatures and number of months per year with a mean temperature above 12.5°C) as significant determinants for the Iberian peninsula.

### 8.1.2.2 Soil moisture

A second important variable is soil moisture, since a large part of the life cycle of *Culicoides* species (the development from egg to larva and pupa) is completed in the upper soil layer, with highest concentrations of immature *Culicoides* in the first 5 cm (Blackwell and King, 1997; Uslu and Dik, 2006). *C. imicola* has been observed to prefer semi-moist breeding sites, and has been found in drainage canals and puddles created by leakage from water pipes (Braverman *et al.*, 1974; Mellor and Pizolis, 1979). Foxi and Delrio (2010) state that *C. imicola* was found to breed preferentially in mud 20 cm above the pond shoreline, where soils are not subject to flooding. While Delrio *et al.* (2002) (cited in Foxi and Delrio (2010)) observed *C. imicola* larvae in saturated soils, its pupae drown on immersion in water (Nevill, 1967, cited in Veronesi *et al.* (2009)).

### 8.1.2.3 Land use/land cover

Land use and vegetation cover conditions under which *C. imicola* preferably live and breed are poorly understood. From modelling studies, Conte *et al.* (2007a) state that *C. imicola* can be classified as heliophilic, favouring less vegetated shrub and grassland. This is in accordance with a number of observations of breeding sites in moist grasslands (Braverman *et al.*, 1974; Mellor and Pizolis, 1979). The preferred land use or land cover for adults is, however, less documented.

### 8.1.2.4 Topography

Topography as such is not a limiting factor in the distribution of *C. imicola*, but clearly affects the three above factors. It is therefore not surprising that terrain elevation, slope and/or orientation were found as determining factors in distribution models (Conte *et al.*, 2007a). While elevation mainly controls air temperature, the slope will influence drainage of the soil and thus the soil moisture level. Terrain slope, combined with orientation, will also influence the amount of sunlight received. All three topographic factors will furthermore affect natural and cultural land use and land cover.

### 8.1.2.5 Others

Other factors found to determine the species' distribution include wind, soil properties (soil organic matter, soil texture) and the availability of hosts. Where wind speed affects adult *Culicoides* activity, by suppressing activity above certain thresholds (Mellor *et al.*, 2000), soil properties determine the suitability of breeding sites. The importance of soil texture can be related to the soil moisture factor, where clayey soils can retain water for longer periods than more sandy soils. Differences in soil texture are assumed to be responsible for the peculiar pattern of *C. imicola* occurrence in Calabria, Italy (Conte *et al.*, 2007b; Peters *et al.*, 2013), where it is present at the eastern, Ionian, seaboard and absent at the western, Tyrrhenian, coastline. Soil organic matter is essential for larval growth Kettle (1977), and ruminant hosts are required for the blood-feeding of adult females and the production of progeny (Mellor *et al.*, 2000).

## 8.1.3 *C. imicola* distribution modelling

Numerous studies tried to model the spatial distribution of the occurrence and/or abundance of *C. imicola* or *Culicoides* spp. at different study sites and over different spatial scales. In an early study, Baylis *et al.* (1998) compared *C. imicola* abundances at 28 trapping sites in Morocco with data from meteorological stations installed at the trapping sites (wind speed, humidity, air temperature and soil temperature) and remotely sensed data (*NDVI*). Linear correlations between the different climatic variables and abundance yielded the highest correlations for wind speed and for average annual minimum *NDVI*. It was, however, noted that the correlation between *C. imicola* abundance and wind velocity is problematic in

the application in predictive models, given the difficulty to interpolate this property between meteorological stations. A model operationally applicable was developed by Wittmann *et al.* (2001), where *C. imicola* of 30 trapping sites in the Iberian peninsula were used to train a logistic regression model based on 10 climatic variables for the period 1931–1960 and altitude. The trained model resulted in a percentage of correctly classified trapping sites of 85 % in an internal validation, meaning that the validation dataset was the same as the training dataset. The trained model parameters were then used to extrapolate the results over the entire Mediterranean Basin. Calistri *et al.* (2003), however, validated these parameters for Italy, and Calabria in particular, and found that the trained model was unable to classify *C. imicola* presence and absence sites.

An alternative method was introduced by Baylis *et al.* (2001), who used a combination of 40 remote sensing variables derived from temporal Fourier processing of AVHRR data, topographic data and vapour pressure deficit in a model based on discriminant analysis. The model, trained on 44 *C. imicola* trapping sites in Portugal, Spain and Morocco resulted in 93.2 % correctly classified sites in an internal validation. Similar models, but based on remote sensing data only, were applied to 87 trapping sites in Portugal (Tatem *et al.*, 2003) and 248 sites in Sicily (Purse *et al.*, 2004), resulting in, respectively, 95.4 % and 87 % correctly classified pixel, again in an internal validation.

Most *C. imicola* distribution models are based on either logistic regression or discriminant analysis, although the used data sources may vary strongly. Guis *et al.* (2007), for example, included landcover variables, as well as landscape metrics derived from high resolution imagery in a logistic regression model for Corsica. Conte *et al.* (2003) included the amount of running water to meteorological and topographic data for a model for Italy based on 546 trapping sites, resulting in 75 % correctly classified sites in an internal validation. Acevedo *et al.* (2010) included the availability of host species, as well as landcover, climatic and pedological variables, for a model based on trappings during the period 2005–2008 in Spain.

Few studies investigated the difference in performance between different modelling techniques. In a study by Peters *et al.* (2011), discriminant analysis and logistic regression were compared to a novel ensemble learning technique called random forests. In a study over the Iberian peninsula using trapping data from 2004 until 2006 and both climate and remote sensing data, the random forests model was found to be superior to the other models when no preprocessing of the trapping data was performed. This preprocessing consisted of the reduction of the entomological data records, in order to reduce uncertainty associated with the field data. After an appropriate data reduction, accuracies of predictions based on discriminant analysis and logistic regression were found to increase significantly.

While the studies mentioned in this section employ either climatic data, re-

remote sensing data or both, no studies compared the accuracies of the predicted distributions based on climatic versus remote sensing data. Yet, the use of remote sensing data can be assumed to offer some advantages over climatic data. First of all, spaceborne remote sensing offers global coverage at a fixed spatial resolution, while area-covering climatic data must be interpolated between meteorological stations. The accuracy of the interpolated values is therefore dependent on the density of the meteorological network. Furthermore, climatic datasets, e.g. those developed by Hijmans *et al.* (2005), provide monthly values based on averaging over long time spans of up to 50 years. This prevents to assess the influence of climate change during this period, rendering meteorological observations from dynamic into static variables. The long records of remote sensing products allow assessing changing climate and landcover conditions, while providing temporal resolutions higher than the monthly resolutions of climatic datasets. It should be noted, however, that many studies undo the advantages of remote sensing by using multi-year averages. Calvete *et al.* (2008), for example, tried to model the distribution of *Culicoides* from trapping data from 2004 to 2006, while using monthly averaged *NDVI* data from 1981 to 2003. Similarly, Baylis *et al.* (2001) used remote sensing data acquired between 1982 and 1994 in combination with trapping data between 1993 and 1995, and Tatem *et al.* (2003) used trapping data from 2000 and 2001 with remote sensing data from 1992 to 1996.

Clearly, the use of solely remote sensing entails some disadvantages. Some environmental variables, such as air temperature, air humidity or precipitation, are much easier to measure from in situ stations than from remote sensing, if measurable at all. This part of the study therefore aims at comparing the accuracies of *C. imicola* distribution modelling based on solely climatic data records versus solely some routinely produced remote sensing products. The random forest modelling technique is used to this end, and is compared to results obtained from the more commonly used linear discriminant analysis.

Notwithstanding the assumed influence of soil moisture on the suitability of *Culicoides* spp. breeding sites, information on soil moisture has, as yet, not been used in distribution models. This is due to the absence of routinely produced high to medium spatial resolution remotely sensed soil moisture products, and due to the difficulty of interpolation soil moisture point measurements over large areas. Some authors (e.g. Baylis *et al.*, 2001) argue that remotely sensed variables, such as *NDVI*, can be interpreted as soil moisture proxies and therefore allow the identification of *C. imicola* presence and absence sites. Others (Conte *et al.*, 2007b) linked the distance of trapping sites from fine textured soil to the water holding capacity of the soil, and thus the suitability for breeding sites. This chapter therefore additionally investigates whether the soil moisture proxies discussed in the previous part can improve accuracies when adding them to models based on the routinely produced remote sensing products.

## 8.2 Study site and datasets

This part of the study is performed over the peninsula of Calabria (Fig. 3.1), and uses some of the remotely sensed datasets employed and derived in the previous part, which are again briefly discussed here. Additionally, climatic and *C. imicola* trapping data over the site were acquired.

### 8.2.1 *Culicoides* trapping data

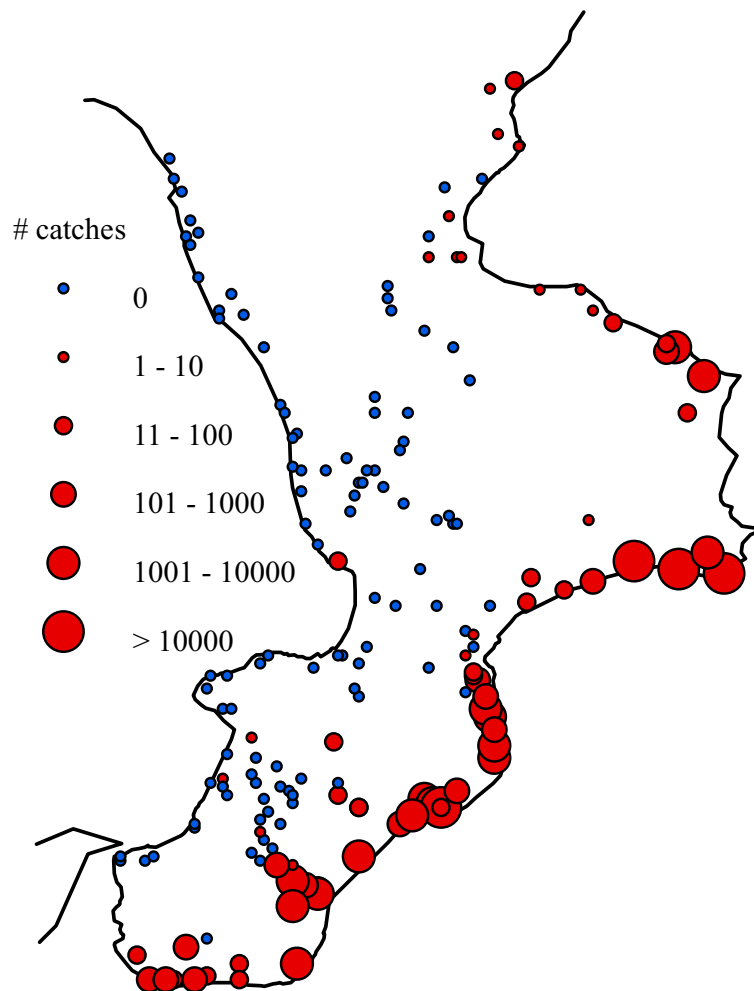


Figure 8.1: Locations and abundances of *C. imicola* catches.

Since 2000, the Entomological National Surveillance Programme monitors the spatial and temporal dynamics of the *C. imicola* population in Italy using Onder-



steep-type blacklight traps in accordance with standardized surveillance procedures (Goffredo and Meiswinkel, 2004). Captures are examined to determine the total number of insects, the total number of *Culicoides* and the total number of *C. imicola*. For this study, the dataset consists of the total number of *C. imicola* collected during the months of highest abundance (August–October) of the years 2000 and 2001, at 169 trapping sites throughout Calabria (Fig. 8.1). *C. imicola* abundances were transformed to absences (zero catches) and presences (non-zero catches), resulting in 102 absence records and 68 presence records. Data from two trapping sites were omitted since these sites were situated outside the region for which climatic and remote sensing datasets were obtained.

### 8.2.2 Climatic data

The WorldClim dataset (Hijmans *et al.*, 2005) is a set of raster layers of climatic variables at 30'' (approximately 1 km) resolution, covering all land masses except Antarctica. The available layers contain monthly values of minimum, maximum and mean temperature and total precipitation, representative for the period 1950–2000, derived from interpolation of monthly values recorded at meteorological stations. Data accuracy is restricted by the density of the meteorological stations, which is especially low in parts of Asia, Africa and South-America (Hijmans *et al.*, 2005). For Europe, a relatively dense network of stations is used to produce the climatic variables.

The 48 climatic data layers for Calabria are freely available for academic and other non-commercial use, and downloadable through the WorldClim website ([www.worldclim.org](http://www.worldclim.org)). No further preprocessing on the climatic variables was performed.

### 8.2.3 Remote sensing data

Routinely generated remote sensing products used in this part of the study are the Aqua MODIS 8-day daytime and nighttime land surface temperature (MYD11A2) and the monthly *NDVI* (MYD13A3) at 1 km resolution. Images from 2002 until 2010 were acquired and combined into representative monthly averages for this period of daytime and nighttime surface temperature and *NDVI*, resulting in a total of 36 data layers. Remotely sensed data representative for the period 2002–2010 can, for Calabria, be used in combination with *C. imicola* trapping data from 2000 and 2001, since no expansion of the geographical range of *C. imicola* was detected during the first decade of this century (Conte *et al.*, 2009). MODIS Aqua datasets were preferred over those of Terra, since Aqua's equatorial crossing times are at 1:30 a.m. and 1:30 p.m., while Terra's are at 10:30 a.m. and 10:30 p.m. Daytime and nighttime surface temperatures observed by Aqua will thus be closer to maximum and minimum temperatures, respectively, which are relevant in the *C. imicola*

life cycle.

The three remotely sensed soil moisture proxies discussed in the previous part of this dissertation are, in an adapted form, included in the species distribution modelling. ASAR Wide Swath relative soil moisture (Chapter 4), resampled to 1 km resolution, was produced for the entire time series of 130 images. Since it was observed that the assumption of a linear angular dependence of backscatter is not necessarily valid when both ascending and descending mode ASAR WS images were used, angular correction was performed here following a second order polynomial fit. The soil moisture retrieval model ignoring seasonality of the different model parameters (angular correction coefficients, dry reference and sensitivity) is used here. In contrast to the product validated in Chapter 4, areas with strong topography are not masked, since the species distribution modelling requires full coverage of the study site by all variables. Nevertheless, it can be expected that soil moisture retrieval at these pixels performs poorly. The relative soil moisture estimates at the dates of image acquisition are combined to multiyear monthly averages.

In contrast to the apparent thermal inertia product at daily resolution developed in Chapter 5, the *ATI* used here is based on 8-day composite surface temperature data from 2002 until 2010. The reason for this is twofold. First, the use of 8-day composites allows the amount of data to be processed for a period of 9 years to remain manageable. Second, 8-day composites reduce the amount of noise that can be present due to insufficiently masked cloud cover. The temperature amplitude required in the derivation of *ATI* (Eq. 5.10) is therefore replaced by the difference between the 8-day daytime and nighttime surface temperature, rather than using a sinusoidal approximation. Subsequently, 8-day *ATI* values are combined into twelve monthly multiyear averages.

Twelve Temperature-Vegetation Dryness Index images (Chapter 6) are derived using the monthly multiyear surface temperature and *NDVI* images discussed earlier in this section. Monthly daytime  $T_S$  images were normalized for influences of elevation using the stratified normalization technique introduced in Chapter 6. The monthly *TVDI* can then be interpreted as representing the long-term availability (or shortage) of soil moisture for evapotranspiration, relative to other places in the study site.

### 8.3 Description of modelling techniques

Random forests (RF, Breiman, 2001) is a data-driven modelling technique, assigning observations with unknown class membership based on a model trained using observations with known class membership. This machine learning technique generates many classification trees, each of which is grown using a randomly drawn

subset of the original dataset. The nodes of the different classification trees are grown using the best split variable selected out of a randomly selected subset of predictive variables (Liaw and Wiener, 2002). The number of trees grown and the number of predictive variables used to split the nodes are two user-defined parameters, here set to 300 and 3, respectively, following Peters *et al.* (2011). Once all classification trees of the random forest are trained, the predictive variables of observations with unknown class membership are classified by each classification tree, resulting in a unique class label (absence or presence) for each tree. The proportion of trees assigning a presence label is interpreted as the probability of occurrence. Random forests have been applied successfully in ecological distribution modelling (Peters *et al.*, 2007, 2011; Sehgal *et al.*, 2011).

An additional feature of random forests is the assessment of the predictive variable's importance, where the effect of a random permutation of a variable on the classifier performance is investigated. The decrease in classifier performance can be interpreted as a measure of the variable's importance. The permutation of informative variables will thus result in a strong decrease in the classifier's performance, while non-informative variables will cause a minor change in performance when permuted.

The random forests classifier is compared to the more traditional linear discriminant analysis (LDA, Venables and Ripley, 2002). LDA aims at finding a discriminant function, or a linear combination of the predictive variables, by assigning coefficients to the predictive variables in such a way that the resulting function optimally discriminates between absence and presence classes. As for random forests, linear discriminant analysis requires training observations with known membership to compute the discriminant function. A threshold set on the discriminant function then allows to classify observations with unknown class membership. In contrast to RF, the statistical LDA makes some simplifying assumptions, such as normality of the predictive variables. Both RF and LDA classifiers are implemented in the statistical software environment R.

## 8.4 Modelling of *C. imicola* in Calabria using climatic data

The 48 climatic variables were, together with the *C. imicola* presence/absence information, used to train and validate the species distribution models based on RF and LDA. Model performance was assessed by a threefold cross validation. In this validation, the dataset is split randomly in three disjoint subsets of equal size, and each subset is used to validate the model trained on the remaining two subsets. As a result, each record in the original dataset will be assigned a predicted probability of *C. imicola* occurrence, which can be classified into an absence or presence

using a certain threshold. Additionally, the three trained models are applied on the area-covering dataset of climatic variables to produce habitat suitability maps for Calabria.

Three different accuracy measures are used in this study to mutually validate the different modelling techniques: the percentage correctly classified sites (*PCC*), the kappa index of agreement ( $\kappa$ ) and the area under the Receiver Operating Characteristic (ROC) curve (*AUC*). *PCC* is the most basic accuracy measure defined as:

$$PCC = 100 \frac{n_{\text{correct}}}{n_{\text{total}}}, \tag{8.1}$$

where  $n_{\text{correct}}$  is the number of correctly classified sites and  $n_{\text{total}}$  is the total number of classified sites. The  $\kappa$  statistic (Cohen, 1960) includes an adjustment for the percentage correctly classified sites by chance agreement ( $PCC_e$ ):

$$\kappa = \frac{PCC - PCC_e}{100 - PCC_e}. \tag{8.2}$$

Both *PCC* and  $\kappa$  require the predicted probabilities to be transformed into a presence or absence using some threshold. This threshold is here set to 0.5. A threshold-independent accuracy measure is the area under the ROC curve (Fawcett, 2006). In ROC graphs, the true positive rate (fraction of observations that are predicted correctly) is plotted versus the false positive rate (fraction of observed absences that are predicted incorrectly), for all possible threshold values between zero and one. The *AUC*, which ranges between zero and one, thus describes the likelihood that a presence site is assigned a higher modelled probability than an absence site, with a value higher than 0.5 when the model performs better than random guessing.

Table 8.1: Accuracy measures of *C. imicola* distribution models (using random forests or linear discriminant analysis) for different input datasets.

	<i>PCC</i> (st. dev.) [%]		$\kappa$ (st. dev.) [%]		<i>AUC</i> (st. dev.) [%]	
	RF	LDA	RF	LDA	RF	LDA
WorldClim	87.7 (1.4)	84.3 (2.2)	76.0 (2.9)	67.1 (4.5)	92.5 (1.2)	89.2 (1.8)
MODIS	85.9 (1.6)	86.3 (1.8)	70.4 (3.3)	71.3 (3.7)	91.2 (1.4)	89.9 (1.3)
+ $\Theta_{\text{ASAR}}$	85.3 (1.4)	84.1 (2.1)	69.2 (3.0)	66.7 (4.3)	90.7 (1.3)	87.7 (1.7)
+ <i>ATI</i>	85.7 (1.4)	84.0 (2.1)	69.9 (3.0)	66.6 (4.3)	90.9 (1.3)	88.5 (1.6)
+ <i>TVDI</i>	84.7 (1.5)	85.1 (2.0)	68.1 (3.1)	68.7 (4.3)	90.8 (1.5)	89.4 (1.8)

The 3-fold cross validation, and computation of the accuracy statistics, is performed for 100 runs, each with a random selection of the training and validation folds, in order to minimize chance effects introduced by this random selection. This results in 100 values of *PCC*,  $\kappa$  and *AUC*, for both the RF and LDA technique. The average value and standard deviation for the three accuracy measures

are given in Table 8.1. Additionally, since each trapping site will be assigned a predicted absence of presence during each run, the spatial distribution and number of misclassifications can be displayed. This is done for the random forests technique in Fig. 8.3. Besides the predictions at the trapping sites, this figure also displays the probability of *C. imicola* occurrence for the entire Calabrian peninsula, derived from averaging the RF outputs over the different runs and different folds.

Random forests performs significantly better ( $p < 0.0001$ ) than linear discriminant analysis for all three performance measures when modelling *C. imicola* based on the WorldClim dataset. Nearly 88 % of the sites are correctly classified using RF, compared to 84 % with LDA. These accuracies are close to the 87.5 % obtained by Conte *et al.* (2007a) over the same study site with an LDA model trained using meteorological data, topography, landcover, *NDVI* and aridity and *Culicoides* trapping data from 2000 until 2004. Fig. 8.3 shows that the climatic data allow to capture the general east-west distribution of *C. imicola*, with probabilities close to 100 % along the eastern coast and low values at the western coastline and the central mountain ranges. Misclassification of absence and presence sites are located in regions with intermediate probabilities and often in regions where presence and absence locations are found over short distances, e.g. near the city of Rosarno at the western coast.

When comparing the misclassifications in Fig. 8.3 with the catch abundances in Fig. 8.1, it is observed that many of the misclassified presence sites are characterized by low ( $< 10$ ) *C. imicola* catch abundances, with sometimes as few as a single catch over the two-year period. This can either indicate a very small population of *C. imicola* in these regions, and might result in the failure of trapping the species at neighbouring sites, even though it might also be present there. In this case, the absence sites can represent false absences. Alternatively, these presence sites might represent false presences, where the trapped individual was transported to this region by the wind, but was unable to establish a population. Finally, the possibility of a misclassification of a different species of *Culicoides* as *C. imicola* cannot be excluded.

The importance of the different climatic variables, as identified by the RF model, is given in Table 8.2 and Fig. 8.2. The variable importance of the different precipitation variables is much higher than the temperature variables. These numbers should, however, be treated with caution, since the different temperature variables can be expected to be strongly correlated, both between  $T_{\min}$ ,  $T_{\text{mean}}$  and  $T_{\max}$  mutually as between the different months. Strongly correlated variables are known to result in lower variable importances (Genuer *et al.*, 2010). Nevertheless, the total amount of precipitation in the months of May and April seems to influence the distribution of *C. imicola*. When considering the spatial pattern of total precipitation for the month of May (Fig. 8.4(a)), it is observed that this pattern corresponds strongly to the predicted probability of *C. imicola* presence (Fig. 8.3). Absence sites correspond to regions with high precipitation amounts, while pres-

Table 8.2: Relative importance of the different variables ( $\times 100$ ) in the RF model based on climatic data.

	$T_{\min}$	$T_{\text{mean}}$	$T_{\max}$	$P$
Jan	0.34	0.27	0.40	0.37
Feb	0.30	0.33	0.55	2.87
Mar	0.31	0.32	0.54	0.24
Apr	0.24	0.25	0.42	5.17
May	0.28	0.25	0.54	7.52
Jun	0.28	0.59	1.84	3.37
Jul	0.27	0.48	1.35	0.83
Aug	0.28	0.42	1.35	3.79
Sep	0.26	0.40	1.08	2.54
Oct	0.23	0.34	0.47	1.28
Nov	0.27	0.36	0.58	0.56
Dec	0.39	0.31	0.48	0.35

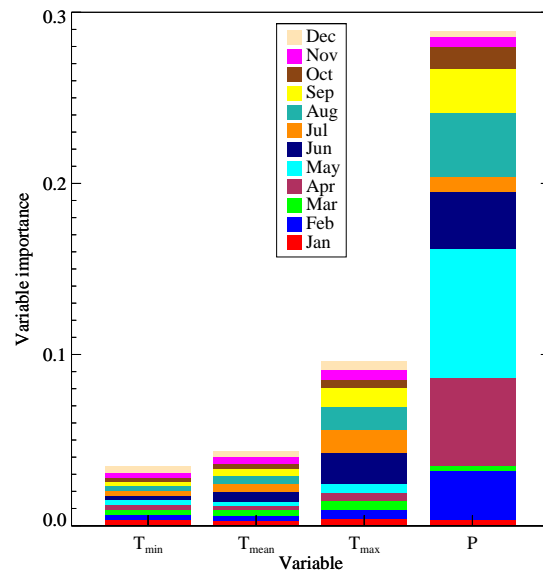


Figure 8.2: Relative importance of the different variables in the RF model based on climatic data.

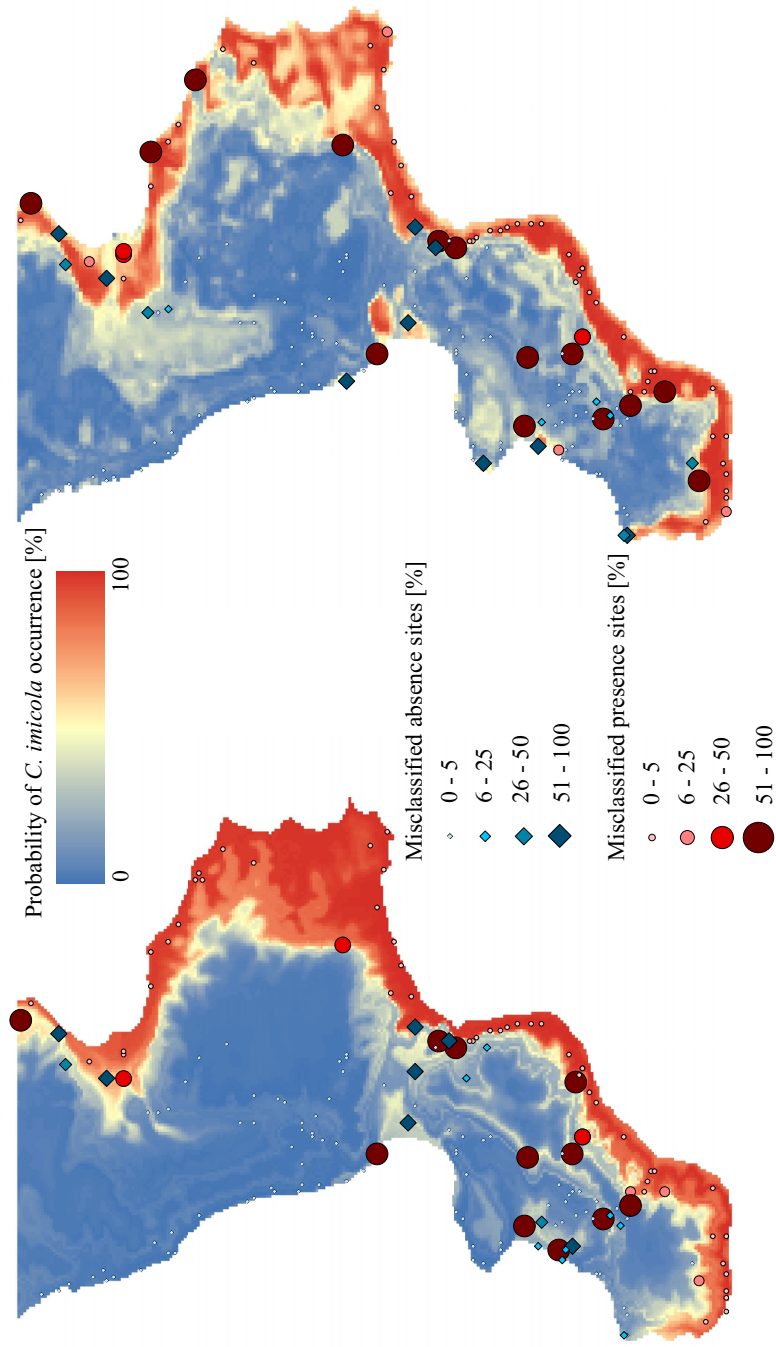


Figure 8.3: Predicted probabilities of *C. imicola* and percentage of misclassifications at absence and presence sites, based on climatic data (left) and remotely sensed data (right).



ence sites receive much less rainfall. A similar pattern is found for the month of April, albeit with much higher absolute precipitation totals. The east-west gradient of rainfall can be explained by the predominant westerly winds in this part of the Mediterranean (Abulafia, 2012), which causes precipitation to fall at the western side of the mountain range dissecting the peninsula.

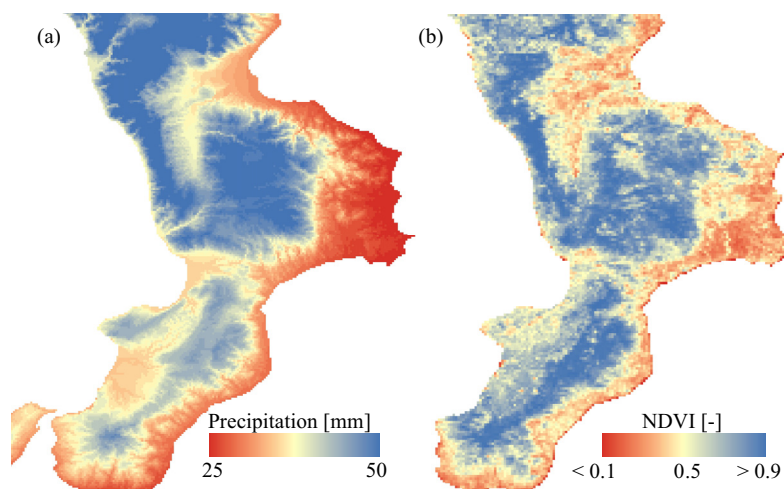


Figure 8.4: Total precipitation for the month of May in the WorldClim (Hijmans *et al.*, 2005) dataset (a) and multiyear averaged MODIS *NDVI* for the month July(b).

The high amount of precipitation at *C. imicola* absence sites might support the hypothesis that these sites are unsuitable because the species' pupae will drown due to the high rainfall, thus interrupting the species' life cycle. At the eastern coast, *C. imicola* might survive due to dryer conditions in spring. This would be an alternative, or complement, to previous assumptions (Conte *et al.*, 2007b) that *C. imicola* survives where fine-textured soils are capable of retaining sufficient moisture during summer. The rainfall-based assumption, however, can explain the absence of the species in the northwestern part of the study site where fine-textured soils can be found (Fig. 3.1) which should support populations of *C. imicola* according to the texture-based assumption.

The overall importance of the 36 temperature variables is low, even though temperature is known to restrict *C. imicola* distribution at global scale and is in Calabria probably largely responsible for its absence at higher elevations. As mentioned earlier, these low importances are partly due to the strong correlations between the different variables. A reduction or transformation of the variables (e.g. through a temporal Fourier analyses as performed by Baylis *et al.* (2001))



will possibly result in an entirely different view.

## 8.5 Modelling of *C. imicola* in Calabria using remote sensing data

In a first instance, the distribution model was trained solely on the standard MODIS products (daytime and nighttime surface temperature and *NDVI*), averaged over multiple years to representative monthly values. The accuracy measures (Table 8.1) indicate no significant difference between performance of the RF and LDA models in terms of *PCC* and  $\kappa$ . In terms of *AUC*, RF performs significantly ( $p < 0.0001$ ) better than LDA. When comparing accuracies of the models based on remotely sensed input data versus those using climatic data, it is observed that the RF predictions using climatic data are significantly better ( $p < 0.0001$  for all accuracy measures) than these using remote sensing data. The percentage correctly classified sites decreased by approximately two percent when replacing climatic variables by remotely sensed variables. The opposite is observed for the LDA models, with the *PCC* increasing by two percent when using remotely sensed data. Both threshold-dependent measures differ significantly ( $p < 0.0001$ ) for the LDA models using different input data, as does the threshold-independent *AUC* ( $p = 0.0019$ ).

The predicted *C. imicola* distribution map (Fig. 8.3) obtained from the RF model using remotely sensed data strongly resembles the one obtained from the WorldClim dataset. The misclassified trapping sites also occur in the same regions. Climatic datasets can thus be replaced by remotely sensed datasets for *C. imicola* distribution modelling without compromising prediction accuracies. Furthermore, remotely sensed data might be preferred for modelling studies in other regions than Calabria, where the meteorological stations between which the climatic data is interpolated are sparse, or where the spatial distribution of *C. imicola* is expected to expand due to climate change. Finally, a different preprocessing of the higher temporal resolution remotely sensed datasets might reveal information that is lost when using monthly averaged variables.

A study of the variable importance (Table 8.3 and Fig. 8.5) reveals that the most important remotely sensed variables are the daytime surface temperature during the months of June, July and August. This is in agreement with the variable importances obtained for the climatic variables, where the maximum temperature during these three months were identified as the most important temperature variables. The months of June, July and August also yield the highest importances among the different *NDVI* variables. The multiyear averaged *NDVI* for the month of July (Fig. 8.4(b)) partly reflects the general landcover and topography of Calabria (Fig. 3.1). The *NDVI* during summer, however, also shows a clear corre-

Table 8.3: Relative importance of the different variables ( $\times 100$ ) in the RF model based on standard Aqua MODIS products.

	$T_{S,day}$	$T_{S,night}$	$NDVI$
Jan	2.29	0.68	0.33
Feb	1.10	0.86	0.39
Mar	0.36	0.58	0.47
Apr	0.09	0.65	0.16
May	1.20	0.65	0.56
Jun	3.67	1.06	2.90
Jul	4.39	1.31	3.01
Aug	2.71	0.63	2.04
Sep	1.01	0.89	1.29
Oct	0.56	0.82	0.60
Nov	0.87	0.79	0.03
Dec	0.87	0.75	0.14

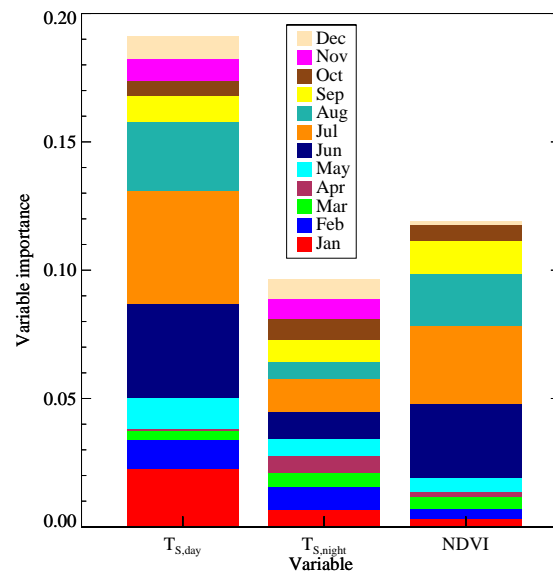


Figure 8.5: Relative importance of the different variables in the RF model based on standard Aqua MODIS products.

spondence to the total rainfall during the month of May (Fig. 8.4(a)). This is not surprising, since abundant rainfall during late spring and early summer allows vegetation to grow throughout the dryer summer season. High *NDVI* values here correspond to *C. imicola* absence sites. This contradicts the findings of Baylis *et al.* (1998), who linked the species' abundance in Morocco to soil moisture through *NDVI* proposing that "areas in Morocco with high levels of soil moisture in late summer or autumn provide more, larger and/or more enduring breeding sites for *C. imicola*, as well as supporting more photosynthetically active vegetation and hence having higher *NDVI*'t'. This link has subsequently been used to extrapolate trained models to Mediterranean-wide predictions (Baylis *et al.*, 2001). The present study, however, demonstrates that conclusions drawn for one region of the Mediterranean Basin cannot simply be extrapolated to others.

The final part of this study aimed at improving the *C. imicola* distribution models by integrating the three remotely sensed soil moisture proxies. From Table 8.1, however, it is observed that none of the proxies improves the modelling accuracies when adding them to the standard MODIS products, for any of the three accuracy measures or the two modelling techniques. This does not mean that soil moisture content has no influence on the spatial distribution of *C. imicola*. Rather, this could indicate that soil moisture is already accounted for in the distribution model indirectly through the standard MODIS products. The relationship between the total rainfall during spring and *NDVI* during summer was already discussed in this section. In fact, *NDVI* observed at a certain place and time is function of a number of factors such as vegetative cover, climate, and soil properties including moisture content. The links between remotely sensed surface temperature and evapotranspiration, and hence soil moisture, were discussed in the first part of this dissertation. It is therefore not surprising that remotely sensed soil moisture proxies derived using MODIS  $T_S$  and/or *NDVI* (in casu *ATI* and *TVDI*) provide no additional information beneficial for the species distribution modelling. The ASAR-derived soil moisture product adds an entirely different source of information and could be expected to improve modelling results, given the stronger correlation to soil moisture over a variety of cover types than the MODIS products. The low temporal resolution, however, apparently restricts the utility of this product.

## 8.6 Conclusions

This chapter aimed at comparing *C. imicola* distribution modelling accuracies using climatological data versus standard remote sensing data. Additionally, the influence of including remotely sensed soil moisture proxies, discussed in the previous part of this dissertation, was investigated. Two modelling techniques were employed: the established linear discriminant analysis and random forests, a novel ensemble learning technique. The importance of the different input variables was assessed using the random forests technique.

For the models based on climatic data, RF outperformed LDA for all investigated accuracy measures. Analysis of the variable importance revealed that the *C. imicola* distribution is largely determined by the amount of precipitation during spring. It is unclear whether this dependence is causal, where intense rainfall might interrupt the species' life cycle by drowning one of its immature stages, or merely coincidental or linked through other processes.

Replacing the climatic variables by standard MODIS products resulted in a significant, although limited, reduction of the predictive capability of the RF model, while slightly increasing the accuracies of the LDA model. The most important remotely sensed variables could be linked to meteorological variables. Given the restrictions of climatic data with respect to temporal and spatial resolution, the use of remotely sensed datasets in species distribution modelling is advisable.

The addition of remotely sensed soil moisture to the standard MODIS products did not result in improved modelling accuracies. Possibly, spatial soil moisture patterns are already accounted for indirectly through the surface temperature and vegetation index variables. Alternatively, the accuracy and/or temporal resolution of the soil moisture proxies produced in this study might be insufficient.



# 9

## Conclusions and outlook

The aim of this research was to derive surface soil moisture from remotely sensed imagery, in order to integrate this into species distribution models. In function of this specific application domain, a number of prerequisites were imposed on the soil moisture product. Firstly, its spatial resolution should be in the order of 100 m to 1 km, covering areas in the order of 100 km to 1000 km. Secondly, it should provide information on soil moisture content over a variety of landcover types and throughout the entire year. Finally, the soil moisture should be derived without requiring the integration of ancillary in situ or meteorological datasets, in order to be globally applicable. Apart from these restrictions, the species distribution models do not require actual gravimetric or volumetric moisture content, but rather an index, or proxy, that is correlated temporally or spatially to soil moisture.

The study was performed on the peninsula of Calabria, a region in the southwestern tip of mainland Italy characterized by a pronounced topography and a variety of landcover conditions. Different sources of reference data were collected in order to validate the remotely sensed soil moisture products (Chapter 3). A dedicated field survey was set up to collect repeated in situ soil moisture measurements at thirty sites. Additionally, soil moisture collected at five permanent measuring stations was obtained. Given the large extent of the study site, the in situ measurements were deemed insufficient as a reference dataset. A soil moisture model was therefore constructed, using a soil texture map of Calabria in combination with daily temperature and precipitation observations at a large number of meteorological stations in Calabria. The soil moisture generated by this model was found to be poorly correlated with the in situ measurements spatially, but strongly correlated temporally. Since soil moisture products are generally validated temporally rather

than spatially, it was concluded that the modelled soil moisture could be used as a reference validation dataset.

Notwithstanding its adequate performance, some improvements might be made to the hydrological model. First of all, the simple model based on the model of Sheikh *et al.* (2009) was constructed to produce soil moisture at daily time steps. However, precipitation at the meteorological stations was available at hourly time steps. A conversion of the model to hourly time steps would allow to compare remotely sensed soil moisture to modelled soil moisture at the time of satellite overpass. Secondly, the evapotranspiration in the model is derived using a very basic formulation, including only the mean daily temperature. The meteorological dataset, however, supplies both daily minimum temperature and daily maximum temperature, as well as the wind velocity and direction and the atmospheric humidity and pressure. This would, together with information on land cover from, e.g., Corine Land Cover or *NDVI* products, allow to produce more reliable estimates of evapotranspiration.

## 9.1 Remotely sensed soil moisture proxies

Two data sources, meeting the required spatial resolution and coverage, were used to infer soil moisture proxies. The first is an active microwave sensor, Envisat's Advanced Synthetic Aperture Radar, operated in Wide Swath mode. Radar backscatter is linked directly to soil moisture content through the dielectric constant of water molecules, which is much higher than that of dry soil. Apart from soil moisture, radar backscatter is also influenced by surface roughness and vegetation cover, which hampers the retrieval of soil moisture through physical backscatter models. This problem was circumvented using a change detection technique, based on the method developed by Wagner *et al.* (1999b) for the low resolution ERS Scatterometer, where changes in soil moisture are assumed to take place at much shorter timescales than changes in roughness and vegetation cover. This technique has previously been applied successfully on higher resolution ASAR data (Wagner *et al.*, 2007; Pathe *et al.*, 2009). Until now, however, the influence of seasonally changing vegetation cover on the change detection model parameters for high resolution imagery has been ignored. The research in Chapter 4 therefore focuses on the influence of vegetation phenology on the model parameters, in particular on the angular correction coefficient. It was found that temporal variations in the angular dependence of ASAR backscatter could be in the order of magnitude of the value of the parameter itself, and should therefore not be ignored in soil moisture change detection algorithms. Relative soil moisture content derived using this change detection was found to be strongly correlated to modelled soil moisture over areas with limited vegetation cover, and moderately correlated over densely vegetated regions.

The results obtained in this chapter are encouraging with respect to soil moisture retrieval from Sentinel-1, a constellation of two SAR sensors of which the first is to be launched shortly. In comparison to ASAR, Sentinel-1 will be characterized by acquisitions at a low number of fixed incidence angles, thus eliminating the issue of incidence angle normalization (Hornáček *et al.*, 2012) and its seasonal variability. Nevertheless, seasonality will continue to affect the other model parameters: dry reference backscatter and sensitivity. For Scatterometer data, Wagner *et al.* (1999c) observed that the seasonal variation of the dry reference can be linked to the seasonal variation of the angular dependence. Given the fixed acquisition angles of Sentinel-1, soil moisture retrieval algorithms for this sensor will be unable to employ this link. Further study of the 10-year archive of Envisat ASAR images can, in preparation of Sentinel-1 data processing, provide an insight into the influence of vegetation phenology on change detection model parameters.

The second type of remotely sensed data in this research is imagery in the optical domain (visible, near-infrared and thermal infrared part of the spectrum) obtained by the MODIS sensor. Unlike for the microwave part of the spectrum, there is no direct relationship between reflectance in the shorter wavelengths and the soil's dielectric constant or moisture level. Instead, soil moisture content is linked to surface temperature observed in the thermal wavelengths, through its link with evaporative cooling and thermal inertia. Chapter 5 discusses the utility of apparent thermal inertia as a soil moisture indicator. Apparent thermal inertia is derived from the difference between maximum daytime and nighttime temperature, its temporal behaviour is generally considered to be correlated to temporal changes in soil moisture. One prerequisite for a multitemporal analysis of apparent thermal inertia, however, is that the different nighttime and daytime surface temperature observations are made at a fixed time. This is not the case for most sun-synchronous sensors such as MODIS. As an alternative, the diurnal temperature behaviour was here approximated as a sinusoidal function fitted to up to four surface temperature observations. The amplitude of the sinusoidal was subsequently used as the day-night temperature difference to derive apparent thermal inertia. Apparent thermal inertia was found to be a good indicator of surface soil moisture content for semi-arid conditions and sparse canopy cover. Under dense canopy cover or wet conditions, however, apparent thermal inertia was found to be of limited use.

One of the main weaknesses of the apparent thermal inertia as estimated here is that clear-sky conditions are assumed in between the different surface temperature observations. Clearly, this is not necessarily so, and cloud cover may severely add noise to the thermal inertia estimates. One way to avoid this is by integrating data from geostationary satellites, which have temporal resolutions up to a few minutes and could therefore easily detect temporal cloud dynamics. Furthermore, their high temporal resolution could allow a better characterization of the diurnal surface temperature behaviour than the simple sinusoidal approximation.



A final soil moisture proxy (Chapter 6) was derived from contextual information in the thermal infrared, combined with a vegetation index. This is a popular method to infer information on spatial differences in evapotranspiration or soil moisture content, although it is subject to a number of preconditions. One of these preconditions is that the area under investigation is flat, so that surface temperature will only be influenced by differences in fractional vegetation cover and availability of soil moisture for evapotranspiration, and not by topography. Topography in Calabria severely influences surface temperature. This chapter therefore concentrates on the topographic normalization of surface temperature. A new empirical topographic normalization was suggested, containing a correction for the terrain elevation and a correction for terrain orientation. Both of these corrections consisted of a stratification of the study site based on fractional vegetation cover. The dependence of surface temperature on elevation was found to be independent of fractional vegetation cover, while the dependence on orientation was found to be dependent on vegetation cover. A soil dryness index obtained from normalized surface temperature resulted in a better correlation than indices using the original surface temperature or surface temperature normalized using different approaches.

The empirical normalization of surface temperature for terrain orientation employed the solar incidence angle at time of image acquisition as the independent variable. This, however, ignores the effect of antecedent heating, which is dependent of the solar incidence angle during a number of minutes or hours prior to image acquisition. The effect of antecedent heating was found to be important during summer. Further research on topographic normalization of remotely sensed surface temperature should focus on this issue.

All three soil moisture proxies were able to, to a certain extent, reflect spatial and/or temporal soil moisture patterns. This offers opportunities for the use of these proxies in spatial disaggregation models. These models aim at retrieving high spatial resolution soil moisture from coarse resolution soil moisture obtained from active or passive microwave sensors and moisture-related variable at high resolution (e.g. Chauhan *et al.*, 2003; Merlin *et al.*, 2008; Piles *et al.*, 2011).

## 9.2 Spatial distribution modelling

The second part of this research investigated the use of remote sensing products, and in particular remotely sensed soil moisture proxies, in *C. imicola* distribution modelling. *C. imicola* is the main vector of the bluetongue virus in the Mediterranean Basin. Two modelling techniques were compared, and species distribution models based on random forests were superior to those based on linear discriminant analysis. Also, it was shown that remotely sensed data could be used as predictive variables instead of climatic data, with only a limited decrease in pre-

diction accuracies. This offers opportunities for the application of species distribution models in regions where climatic data is unreliable due to the absence of meteorological stations, or in regions where climate change allows the range of *C. imicola* to expand. The inclusion of remotely sensed soil moisture proxies as predictive variables did not increase model performance. This might be because soil moisture is already, indirectly, integrated in the standard remote sensing products.

The region of Calabria is characterized by a peculiar spatial distribution of *C. imicola* biting midges. In the central mountain range, the absence of the species can be attributed to the overall lower temperatures. The temperature regime of the eastern and western shorelines are, however, similar, while the species can be found at the former, but is absent at the latter. This difference is usually attributed to the difference in soil texture, and hence water holding capacity and soil moisture, where high soil moisture content allows the immature stages of *C. imicola* to survive through summer. This study points at the importance of rainfall during spring, with *C. imicola* presence sites being characterized by low rainfall. It is unclear whether the relation between these variables and the occurrence of the midge is coincidental or causal.

Further study of *C. imicola* could focus on the type of remote sensing data to be included, and in particular the preprocessing of remote sensing products. In this study, multiyear monthly averages are used, which can be strongly correlated mutually. The input variables thus contain redundant information, while other information is lost through this averaging. This loss of information is reduced when using techniques like temporal Fourier transforms. The effect of predictive variable preprocessing on prediction accuracy deserves further investigation.



## Bibliography

- Abdellaoui, A., Becker, F., and Olory-Hechinger, E. (1986). Use of Meteosat for mapping thermal inertia and evapotranspiration over a limited region in Mali. *Journal of Climate and Applied Meteorology*, **25**(11), 1489–1506.
- Abulafia, D. (2012). *The Great Sea*. Penguin Books.
- Acevedo, P., Ruiz-Fons, F., Estrada, R., Márques, A. L., Miranda, M. A., Gortázar, C., and Lucientes, J. (2010). A broad assessment of factors determining *Culicoides imicola* abundance: modelling the present and forecasting its future in climate change scenarios. *Plos ONE*, **5**(12), e14236.
- Adegoke, J. O. and Carleton, A. M. (2002). Relations between soil moisture and satellite vegetation indices in the U.S. Corn Belt. *Journal of Hydrometeorology*, **3**(4), 395–405.
- Al Bitar, A., Leroux, D., Kerr, Y. H., Merlin, O., Richaume, P., Sahoo, A., and Wood, E. F. (2012). Evaluation of SMOS soil moisture product over continental U.S. using the SCAN/SNOTEL network. *IEEE Transactions on Geoscience and Remote Sensing*, **50**(5), 1572–1586.
- Albergel, C., Calvet, J. C., Mahfouf, J. F., Rüdiger, C., Barbu, A. L., Lafont, S., Roujean, J. L., Walker, J. P., Crapeau, M., and Wigneron, J. P. (2010). Monitoring of water and carbon fluxes using a land data assimilation system: a case for southwestern France. *Hydrology and Earth System Sciences*, **14**, 1109–1124.
- ARSSA (2003). I suoli della Calabria: Carta dei suoli in scala 1:250.000. Agenzia Regionale per lo Sviluppo e per i Servizi in Agricoltura, Servizio Agropedologia.
- Attema, E., Bargellini, P., Edwards, P., Levrini, G., Lokas, S., Moeller, L., Rosich-Tell, B., Secchi, P., Torres, R., Davidson, M., and Snoeij, P. (2007). Sentinel-1: The radar mission for GMES operational land and sea services. *ESA Bulletin*, **131**, 10–17.
- Attema, E. P. W. and Ulaby, F. T. (1978). Vegetation modeled as a water cloud. *Radio Science*, **13**(2), 357–364.
- Baghdadi, N., King, C., Chanzy, A., and Wigneron, J. (2002). An empirical calibration of the integral equation model based on SAR data, soil moisture and

- surface roughness measurement over bare soils. *International Journal of Remote Sensing*, **23**(20), 4325–4340.
- Baghdadi, N., Holah, N., and Zribi, M. (2006). Soil moisture estimation using multi-incidence and multi-polarization ASAR data. *International Journal of Remote Sensing*, **27**(10), 1907–1920.
- Baghdadi, N., Aubert, M., Cerdan, O., Franchistéguy, L., Viel, C., Martin, E., Zribi, M., and Desprats, J. F. (2007). Operational mapping of soil moisture using Synthetic Aperture Radar data: application to the Touch Basin (France). *Sensors*, **7**, 2458–2483.
- Bartalis, Z., Wagner, W., Naeimi, V., Hasenauer, S., Scipal, K., Bonekamp, H., Figa, J., and Anderson, C. (2007). Initial soil moisture retrieval from the METOP-A Advanced Scatterometer (ASCAT). *Geophysical Research Letters*, **34**(20), L20401.
- Baup, F., Mougin, E., de Rosnay, P., Timouk, F., and Chênerie, I. (2007). Surface soil moisture estimation over the AMMA Sahelian site in Mali using ENVISAT/ASAR data. *Remote Sensing of Environment*, **109**, 473–481.
- Baylis, M., Bouayoune, H., Touti, J., and El Hasnaoui, H. (1998). Use of climate data and satellite imagery to model the abundance of *Culicoides imicola*, the vector of African horse sickness virus, in Morocco. *Medical and Veterinary Entomology*, **12**, 255–266.
- Baylis, M., Mellor, P. S., Wittmann, E. J., and Rogers, D. J. (2001). Prediction of areas around the Mediterranean at risk of bluetongue by modelling the distribution of its vector using satellite imaging. *Veterinary Record*, **149**(21), 639–643.
- Berger, K. A., Wang, Y., and Mather, T. N. (2013). MODIS-derived land surface moisture conditions for monitoring blacklegged tick habitat in southern New England. *International Journal of Remote Sensing*, **34**(1), 73–85.
- Berger, M., Moreno, J., Johannessen, J. A., Levelt, P. F., and Hanssen, R. F. (2012). ESA's sentinel mission in support of Earth system science. *Remote Sensing of Environment*, **120**(SI), 84–90.
- Blackwell, A. and King, F. C. (1997). The vertical distribution of *Culicoides impunctatus* larvae. *Medical and Veterinary Entomology*, **11**(1), 46–48.
- Bolten, J. D., Crow, W. T., Jackson, T. J., Zhan, X., and Reynolds, C. A. (2010). Evaluating the utility of remotely-sensed soil moisture retrieval for operational agricultural drought monitoring. *IEEE Journal of Selected Topics in Applied Earth Observation and Remote Sensing*, **3**, 57–66.
- Boulet, G., Chehbouni, A., Gentine, P., Duchemin, B., Ezzahar, J., and Hadria, R. (2007). Monitoring water stress using time series of observed to unstressed surface temperature difference. *Agricultural and Forest Meteorology*, **146**, 159–172.

- Bowers, S. A. and Hanks, R. J. (1965). Reflection of radiant energy from soils. *Soil Science*, **100**(2), 130–138.
- Braverman, Y., Galun, R., and Ziv, M. (1974). Breeding sites of some *Culicoides* spp. (Diptera: Ceratopogonidae) in Israel. *Mosquito News*, **34**(3), 303–308.
- Breiman, L. (2001). Random forests. *Machine Learning*, **45**, 5–32.
- Brocca, L., Melone, F., Moramarco, T., and Morbidelli, R. (2009). Soil moisture temporal stability over experimental areas in Central Italy. *Geoderma*, **148**(3-4), 364–374.
- Brocca, L., Hasenauer, S., Lacava, T., Melone, F., Moramarco, T., Wagner, W., Dorigo, W., Matgen, P., Martínez-Fernández, J., Llorens, P., Latron, J., Martin, C., and Bitelli, M. (2011). Soil moisture estimation through ASCAT and AMSR-E sensors: an intercomparison and validation study across Europe. *Remote Sensing of Environment*, **115**, 3390–3408.
- Brunt, D. (1933). The adiabatic lapse-rate for dry and saturated air. *Quarterly Journal of the Royal Meteorological Society*, **59**(252), 351–360.
- Cai, G., Xue, Y., Hu, Y., Wang, Y., Guo, J., Luo, Y., Wu, C., Zhong, S., and Qi, S. (2007). Soil moisture retrieval from MODIS data in Northern China Plain using thermal inertia model. *International Journal of Remote Sensing*, **28**(16), 3567–3581.
- Calistri, P., Goffredo, M., Caporale, V., and Meiswinkel, R. (2003). The distribution of *Culicoides imicola* in Italy: application and evaluation of current mediterranean models based on climate. *Journal of Veterinary Medicine*, **B 50**, 132–138.
- Calvete, C., Estrada, R., Miranda, M. A., Borrás, D., Calvo, J. H., and Lucientes, J. (2008). Modelling the distributions and spatial coincidence of bluetongue vectors *Culicoides imicola* and the *Culicoides obsoletus* group throughout the Iberian peninsula. *Medical and Veterinary Entomology*, **22**, 124–134.
- Canadian Space Agency (2011). <http://www.asc-csa.gc.ca/eng/satellites/>.
- Carlson, T. (2007). An overview of the “triangle” method for estimating surface evapotranspiration and soil moisture from satellite imagery. *Sensors*, **7**, 1612–1629.
- Carlson, T. N. and Ripley, D. A. (1997). On the relation between NDVI, fractional vegetation cover, and leaf area index. *Remote Sensing of Environment*, **62**(3), 241–252.
- Carlson, T. N., Gillies, R. R., and Schmugge, T. J. (1995). An interpretation of methodologies for indirect measurement of soil water content. *Agricultural and Forest Meteorology*, **7**(3-4), 191–205.

- Ceballos, A., Scipal, K., Wagner, W., and Martínez-Fernández, J. (2005). Validation of ERS scatterometer-derived soil moisture data in the central part of the Duero Basin, Spain. *Hydrological Processes*, **19**, 1549–1556.
- Ceccato, P., Flasse, S., Tarantola, S., Jacquemoud, S., and Grégoire, J.-M. (2001). Detecting vegetation leaf water content using reflectance in the optical domain. *Remote Sensing of Environment*, **77**, 22–33.
- Chang, C.-W., Laird, D. A., Mausbach, M. J., and Hurburgh, Jr., C. R. (2001). Near-infrared reflectance spectroscopy-principal components regression analysis of soil properties. *Soil Science Society of America Journal*, **65**, 480–490.
- Chauhan, N., Miller, S., and Ardanuy, P. (2003). Spaceborne soil moisture estimation at high resolution: a microwave-optical/IR synergistic approach. *International Journal of Remote Sensing*, **24**(22), 4599–4622.
- Chen, D., Huang, J., and Jackson, T. J. (2005). Vegetation water content estimation for corn and soybeans using spectral indices derived from MODIS near- and short-wave infrared bands. *Remote Sensing of Environment*, **98**, 225–236.
- Cohen, J. (1960). A coefficient of agreement for nominal scales. *Educational and Psychological Measurement*, **20**, 37–46.
- Conte, A., Giovannini, A., Savini, L., Goffredo, M., Calistri, P., and Meiswinkel, R. (2003). The effect of climate on the presence of *Culicoides imicola* in Italy. *Journal of Veterinary Medicine*, **B 50**, 139–147.
- Conte, A., Goffredo, M., Ippoliti, C., and Meiswinkel, R. (2007a). Influence of biotic and abiotic factors on the distribution and abundance of *Culicoides imicola* and the *Obsoletus Complex* in Italy. *Veterinary Parasitology*, **150**(4), 333–344.
- Conte, A., Ippoliti, C., Savini, L., Goffredo, M., and Meiswinkel, R. (2007b). Novel environmental factors influencing the distribution and abundance of *Culicoides imicola* and the *Obsoletus Complex* in Italy. *Veterinaria Italiana*, **43**(3), 571–580.
- Conte, A., Gilbert, M., and Goffredo, M. (2009). Eight years of entomological surveillance in Italy show no evidence of *Culicoides imicola* geographical range expansion. *Journal of Applied Ecology*, **46**, 1332–1339.
- Cosh, M. H., Jackson, T. J., Moran, S., and Bindlish, R. (2008). Temporal persistence and stability of surface soil moisture in a semi-arid watershed. *Remote Sensing of Environment*, **112**(2), 304–313.
- De Clercq, K., Vandenbussche, F., Vandemeulebroucke, E., Vanbinst, T., De Leeuw, I., Verheyden, B., Goris, N., Mintiens, K., Méroc, E., Herr, C., Hooybergs, J., Houdart, P., Sustronck, B., De Deken, R., Maquet, G., Bughin, J., Saulmont, M., Lebrun, M., Bertels, G., and Miry, C. (2008). Transplacental bluetongue infection in cattle. *Veterinary Records*, **162**(17), 564–564.

- Delrio, G., Deliperi, S., Foxi, S., Pantaleoni, R. A., and Piras, S. (2002). Osservazioni in Sardegna sulla dinamica di popolazione di *Culicoides imicola* Kieffer vettore della bluetongue. In *Atti XIX Congresso Nazionale Italiano di Entomologia*, pages 1089–1094, Catania, 10-15 June 2002.
- Demattê, J. A. M., Sousa, A. A., Alves, M. C., Nanni, M. R., Fiorio, P. R., and Costa Campo, R. (2006). Determining soil water status and other soil characteristics by spectral proximal sensing. *Geoderma*, **135**, 179–195.
- Dirmeyer, P. A. (2000). Using a global soil wetness dataset to improve seasonal climate simulations. *Journal of Climate*, **13**, 2900–2922.
- Dorigo, W. A., Wagner, W., Hohinsinn, R., Hahn, S., Paulik, C., Xaver, A., Gruber, A., Drusch, M., Mecklenburg, S., van Oevelen, P., Robock, A., and Jackson, T. (2011). The International Soil Moisture Network: a data hosting facility for global in situ soil moisture measurements. *Hydrology and Earth System Sciences*, **15**, 1675–1698.
- Doubková, M., Van Dijk, A. I. J. M., Sabel, D., Wagner, W., and Blöschl, G. (2012). Evaluation of the predicted error of the soil moisture retrieval from C-band SAR by comparison against modelled soil moisture estimates over Australia. *Remote Sensing of Environment*, **120**, 188–196.
- Draper, C. S., Walker, J. P., Steinle, P. J., de Jeu, R. A. M., and Holmes, T. R. H. (2009). An evaluation of AMSR-E derived soil moisture over Australia. *Remote Sensing of Environment*, **113**, 703–710.
- Dubois, P. C., van Zyl, J., and Engman, E. T. (1995). Measuring soil moisture with imaging radars. *IEEE Transactions on Geoscience and Remote Sensing*, **33**, 915–926.
- Dupigny-Giroux, L.-A. and Lewis, J. E. (1999). A moisture index for surface characterization over a semiarid area. *Photogrammetric Engineering & Remote Sensing*, **65**(8), 937–945.
- Entekhabi, D., Njoku, E. G., O'Neill, P., Kellogg, K., Crow, W. T., Edelstein, W. N., Entik, J. K., Goodman, S. D., Jackson, T. J., Johnson, J., Kimball, J., Piepmeier, J. R., Koster, R., Martin, N., McDonald, K. C., Moghaddam, M., Moran, M. S., Reichle, R., Shi, J. C., Spencer, M. W., Thurman, S. W., Tsang, L., and Van Zyl, J. (2010). The soil moisture active passive (SMAP) mission. *Proceedings of the IEEE*, **98**(5), 704–716.
- European Environmental Agency (2002). Corine land cover 2000 (clc2000) seamless vector database. <http://www.eea.europa.eu/data-and-maps/data/corine-land-cover-2000-clc2000-seamless-vector-database>.
- European Space Agency (2007). ASAR product handbook. <http://envisat.esa.int/handbooks/asar/>.



- European Space Agency (2013). Earthnet Online. <https://earth.esa.int/web/guest/home/>.
- Farr, T. G., Rosen, P. A., Caro, E., Crippen, R., Duren, R., Hensley, S., Kobrick, M., Paller, M., Rodriguez, E., Roth, L., Seal, D., Shaffer, S., Shimada, J., Umland, J., Werner, M., Oskin, M., Burbank, D., and Alsdorf, D. (2007). The Shuttle Radar Topography Mission. *Review of Geophysics*, **45**, RG2004.
- Fawcett, T. (2006). An introduction to ROC analysis. *Pattern Recognition Letters*, **27**, 861–874.
- Fensholt, R. and Sandholt, I. (2003). Derivation of a shortwave infrared water stress index from MODIS near- and shortwave infrared data in a semiarid environment. *Remote Sensing of Environment*, **87**, 111–121.
- Foxi, C. and Delrio, G. (2010). Larval habitats and seasonal abundance of *Culicoides* biting midges found in association with sheep in northern Sardinia, Italy. *Medical and Veterinary Entomology*, **24**(2), 199–209.
- Friedl, M. A. and Davis, F. W. (1994). Sources of variation in radiometric surface temperature over a tallgrass prairie. *Remote Sensing of Environment*, **48**(1), 1–17.
- Fung, A. K. (1994). *Microwave Scattering and Emission Models and Their Applications*. Artech House, Boston, UK.
- Fung, A. K. and Chan, K. S. (2004). An update on the IEM surface backscattering model. *IEEE Geoscience and Remote Sensing Letters*, **1**(2), 75–77.
- Fung, A. K., Li, Z. Q., and Chan, K. S. (1992). Backscatter from a randomly rough dielectric surface. *IEEE Transactions on Geoscience and Remote Sensing*, **30**(2), 356–369.
- Gamon, J. A., Peñuelas, J., and Field, C. B. (1992). A narrow-waveband spectral index that tracks diurnal changes in photosynthetic efficiency. *Remote Sensing of Environment*, **41**, 35–44.
- Gao, B. (1996). NDWI - a Normalized Difference Water Index for remote sensing of vegetation liquid water from space. *Remote Sensing of Environment*, **58**, 257–266.
- Gausman, H. W. (1974). Leaf reflectance of near-infrared. *Photogrammetric Engineering*, pages 183–191.
- Gelsthorpe, R. V., Schied, E., and Wilson, J. J. W. (2000). ASCAT - Metop's Advanced Scatterometer. *ESA Bulletin*, **102**, 19–27.
- Genuer, R., Poggi, J., and Tuleau-Malot, C. (2010). Variable selection using Random Forests. *Pattern Recognition Letters*, **31**(14), 2225–2236.

- Gherboudi, I., Magagi, R., Berg, A. A., and Toth, B. (2011). Soil moisture retrieval over agricultural fields from multi-polarized and multi-angular RADARSAT-2 SAR data. *Remote Sensing of Environment*, **115**(1), 33–43.
- Giraldo, M. A., Bosch, D., Madden, M., Usery, L., and Finn, M. (2009). Ground and surface temperature variability for remote sensing of soil moisture in a heterogeneous landscape. *Journal of Hydrology*, **368**(1-4), 214–223.
- Goffredo, M. and Meiswinkel, R. (2004). Entomological surveillance of blue-tongue in Italy: methods of capture, catch analysis and identification of *Culicoides* biting midges. *Veterinaria Italiana*, **40**, 260–265.
- Goward, S. N., Xue, Y., and Czajkowski, K. P. (2002). Evaluating land surface moisture conditions from the remotely sensed temperature/vegetation index measurements. An exploration with the simplified simple biosphere model. *Remote Sensing of Environment*, **79**(2-3), 225–242.
- Gruhler, C., de Rosnay, P., Hasenauer, S., Holmes, T., de Jeu, R., Kerr, Y., Mougin, E., Njoku, E., Timouk, F., Wagner, W., and Zribi, M. (2010). Soil moisture active and passive microwave products: intercomparison and evaluation over a Sahelian site. *Hydrology and Earth System Sciences*, **14**, 141–156.
- Gu, Y., Hunt, E., Wardlow, B., Basara, J. B., Brown, J. F., and Verdin, J. P. (2008). Evaluation of MODIS NDVI and NDWI for vegetation drought monitoring using Oklahoma Mesonet soil moisture data. *Geophysical Research Letters*, **35**, L22401.
- Guis, H., Tran, A., De La Rocque, S., Baldet, T., Gerbier, G., Barragué, B., Biteau-Coroller, F., Roger, F., Viel, J.-F., and Mauny, F. (2007). Use of high spatial resolution satellite imagery to characterize landscapes at risk for bluetongue. *Veterinary Research*, **38**(5), 669–683.
- Hais, M. and Kučera, T. (2009). The influence of topography on the forest surface temperature retrieved from Landsat TM and ASTER thermal channels. *ISPRS Journal of Photogrammetry and Remote Sensing*, **64**(6), 585–591.
- Hamon, R. W. (1963). Computation of direct runoff amounts from storm rainfall. In *International Association of Scientific Hydrology*, volume 63, pages 52–62. Wallingford, Oxon, U.K.
- Han, Y., Wang, Y., and Zhao, Y. (2010). Estimating soil moisture conditions of the greater Changbai Mountains by land surface temperature and NDVI. *IEEE Transactions on Geoscience and Remote Sensing*, **48**(6), 2509–2515.
- Hardgrove, C., Moersch, J., and Whisner, S. (2009). Thermal imaging of alluvial fans: a new technique for remote classification of sedimentary features. *Earth and Planetary Science Letters*, **285**, 124–130.

- Hassan, Q. K., Bourque, C. P.-A., Meng, F.-R., and Cox, R. M. (2007). A wetness index using terrain-corrected surface temperature and normalized difference vegetation index derived from standard MODIS products: an evaluation of its use in a humid forest-dominated region of eastern Canada. *Sensors*, **7**(10), 2028–2048.
- Haubrock, S.-N., Chabrillat, S., Kuhnert, M., Hostert, P., and Kaufmann, H. (2008a). Surface soil moisture quantification and validation based on hyperspectral data and field measurements. *Journal of Applied Remote Sensing*, **2**, 023552.
- Haubrock, S.-N., Chabrillat, S., Lemmnitz, C., and Kaufmann, H. (2008b). Surface soil moisture quantification models from reflectance data under field conditions. *International Journal of Remote Sensing*, **29**(1), 3–29.
- Higuchi, A., Hiyama, T., Fukuta, Y., Suzuki, R., and Fukushima, Y. (2007). The behaviour of a surface temperature/vegetation index (TVX) matrix derived from 10-day composite AVHRR images over monsoon Asia. *Hydrological Processes*, **21**(9), 1157–1166.
- Hijmans, R. J., Cameron, S. E., Parra, J. L., Jones, P. G., and Jarvis, A. (2005). Very high resolution interpolated climate surfaces for global land areas. *International Journal of Climatology*, **25**(15), 1965–1978.
- Hornáček, M., Wagner, W., Sabel, D., Truong, H., Snoeij, P., Hahmann, T., Diedrich, E., and Doubková, M. (2012). Potential for high resolution systematic global surface soil moisture retrieval via change detection using Sentinel-1. *IEEE Transactions on Geoscience and Remote Sensing*, **5**(4), 1303–1311.
- Hummel, J. W., Sudduth, K. A., and Hollinger, S. E. (2001). Soil moisture and organic matter prediction of subsurface soils using an NIR sensor. *Computers and Electronics in Agriculture*, **32**(2), 149–165.
- Idso, S., Jackson, R., and Reginato, R. (1976). Compensating for environmental variability in the thermal inertia approach to remote sensing of soil moisture. *Journal of Applied Meteorology*, **15**(8), 811–817.
- Idso, S. B., Jackson, R. D., Reginato, R. J., Kimball, B. A., and Nakayama, F. S. (1975). The dependence of bare soil albedo on soil water content. *Journal of Applied Meteorology*, **14**(1), 109–113.
- Iqbal, M. (1983). *Introduction to Solar Radiation*. Academic Press, Toronto.
- Jackson, T. J. (2003). Measuring surface soil moisture using passive microwave remote sensing. *Hydrological Processes*, **7**(2), 139–152.
- Jackson, T. J., Chen, D., Cosh, M., Li, F., Anderson, M., Walthall, C., Doriaswamy, P., and Hunt, E. R. (2004). Vegetation water content mapping using Landsat data derived normalized difference water index for corn and soybean. *Remote Sensing of Environment*, **92**(4), 475–482.

- Jackson, T. J., Cosh, M. H., Bindlish, R., Starks, P. J., Bosch, D. D., Seyfried, M., Goodrich, D. C., Moran, M. S., and Du, J. (2010). Validation of Advanced Microwave Scanning Radiometer soil moisture products. *IEEE Transactions on Geoscience and Remote Sensing*, **48**(12), 4256–4272.
- Jain, S. K., Goswami, A., and Saraf, A. K. (2008). Determination of land surface temperature and its lapse rate in the Satluj River basin using NOAA data. *International Journal of Remote Sensing*, **29**(11), 3091–3103.
- Javelle, P., Fouchier, C., Arnaud, P., and Lavabre, J. (2010). Flash flood warning at ungauged locations using radar rainfall and antecedent soil moisture estimations. *Journal of Hydrology*, **394**(1-2), 267–274.
- Kahle, A., Gillespie, A., and Goetz, A. (1976). Thermal inertia: a new geologic mapping tool. *Geophysical Research Letters*, **3**(1), 26–28.
- Karnieli, A., Agam, N., Pinker, R. T., Anderson, M., Imhoff, M. L., Gutman, G. G., Panov, N., and Goldberg, A. (2010). Use of NDVI and land surface temperature for drought assessment: merits and limitations. *Journal of Climate*, **23**(3), 618–633.
- Katra, I., Blumberg, D. G., Lavee, H., and Sarah, P. (2006). A method for estimating the spatial distribution of soil moisture of arid microenvironments by close range thermal infrared imaging. *International Journal of Remote Sensing*, **27**(12), 2599–2611.
- Kerr, Y. H. (2007). Soil moisture from space: Where are we? *Hydrogeology Journal*, **15**, 117–120.
- Kerr, Y. H., Waldteufel, P., Wigneron, J. P., Delwart, S., Cabot, F., Boutin, J., Escorihuela, M.-J., Font, J., Reul, N., Gruhier, C., Juglea, S. E., Drinkwater, M. R., Hahne, A., Martin-Neira, M., and Mecklenburg, S. (2010). The SMOS mission: new tool for monitoring key elements of the global water cycle. *Proceedings of the IEEE*, **98**(5), 666–687.
- Kerr, Y. H., Waldteufel, P. R., Wigneron, J. P., Ferrazzoli, P., Mahmoodi, A., Al Bitar, A., Cabot, F., Gruhier, C., Juglea, S. E., Leroux, D., Mialon, A., and Delwart, S. (2012). The SMOS soil moisture retrieval algorithm. *IEEE Transactions on Geoscience and Remote Sensing*, **50**(5), 1384–1403.
- Kettle, D. S. (1977). Biology and bionomics of bloodsucking Ceratopogonids. *Annual Review of Entomology*, **22**, 33–51.
- Kimura, R. (2007). Estimation of moisture availability over the Liudaogou river basin of the Loess Plateau using new indices with surface temperature. *Journal of Arid Environments*, **70**(2), 237–252.

- Koike, T., Nakamura, Y., Kaihotsu, I., Dawa, G., Matsuura, N., Tamagawa, K., and Fuji, H. (2004). Development of an advanced microwave scanning radiometer (AMSR-E) algorithm of soil moisture and vegetation water content. *Annual Journal of Hydraulic Engineering*, **48**(2), 217–222.
- Lambin, E. F. and Ehrlich, D. (1996). The surface temperature - vegetation index space for land cover change analysis. *International Journal of Remote Sensing*, **17**(3), 463–487.
- Lang, R. H. and Sidhu, J. S. (1983). Electromagnetic backscattering from a layer of vegetation: a discrete approach. *IEEE Transactions on Geoscience and Remote Sensing*, **21**, 62–71.
- Liaw, A. and Wiener, M. (2002). Classification and regression by random forest. *R News*, **2**(3), 18–22.
- Lievens, H. and Verhoest, N. E. C. (2011). On the retrieval of soil moisture in wheat fields from L-band SAR based on water cloud modeling, the IEM and effective roughness parameters. *IEEE Geoscience and Remote Sensing Letters*, **8**(4), 740–744.
- Lievens, H. and Verhoest, N. E. C. (2012). Spatial and temporal soil moisture estimation from RADARSAT-2 imagery over Flevoland, The Netherlands. *Journal of Hydrology*, **456**, 44–56.
- Lievens, H., Verhoest, N. E. C., De Keyser, E., Vernieuwe, H., Matgen, P., Álvarez-Mozos, J., and De Baets, B. (2011). Effective roughness modelling as a tool for soil moisture retrieval from C- and L-band SAR. *Hydrology and Earth System Sciences*, **15**(1), 151–162.
- Lillesand, T. M., Kiefer, R., and Chipman, J. W. (2004). *Remote sensing and image interpretation*. John Wiley & Sons, fifth edition edition.
- Liu, H.-J., Zhang, Y.-Z., Zhang, X.-L., Zhang, B., Song, K.-S., Wang, Z.-M., and Tang, N. (2009). Quantitative analysis of moisture effect on black soil reflectance. *Pedosphere*, **19**(4), 532–540.
- Liu, W., Baret, F., Gu, X., Tong, Q., Zheng, L., and Zhang, B. (2002). Relating soil moisture to reflectance. *Remote Sensing of Environment*, **81**, 238–246.
- Liu, W., Baret, F., Gu, X., Zhang, B., Tong, Q., and Zeng, L. (2003). Evaluation of methods for soil surface moisture estimation from reflectance data. *International Journal of Remote Sensing*, **24**(10), 2069–2083.
- Liu, Z., Shi, X., Warner, E., Ge, Y., Yu, D., Ni, S., and Wang, H. (2008). Relationship between oriental migratory locust plague and soil moisture extracted from MODIS data. *International Journal of Applied Earth Observation and Geoinformation*, **10**, 84–91.

- Lobell, D. A. and Asner, P. A. (2002). Moisture effects on soil reflectance. *Soil Science Society of America Journal*, **66**, 722–727.
- Loew, A., Ludwig, R., and Mauser, W. (2006). Derivation of surface soil moisture from ENVISAT ASAR wide swath and image mode data in agricultural areas. *IEEE Transactions on Geoscience and Remote Sensing*, **44**(4), 889–899.
- Lu, S., Ju, Z., Ren, T., and Horton, R. (2009). A general approach to estimate soil water content from thermal inertia. *Agricultural and Forest Meteorology*, **149**(10), 1693–1698.
- Mallick, K., Bhattacharya, B. K., and Patel, N. K. (2009). Estimating volumetric surface moisture content for cropped soils using a soil wetness index based on surface temperature and NDVI. *Agricultural and Forest Meteorology*, **149**(4), 1327–1342.
- McNairn, H., Merzouki, A., Pacheco, A., and Fitzmaurice, J. (2012). Monitoring soil moisture to support risk reduction for the agriculture sector using RADARSAT-2. *IEEE Journal of Selected Topics in Applied Earth Observation and Remote Sensing*, **5**(3), 824–834.
- Mellor, P. S. and Pizolis, G. (1979). Observations on breeding sites and light-trap collections of *Culicoides* during an outbreak of bluetongue in Cyprus. *Bulletin of Entomological Research*, **69**(2), 229–234.
- Mellor, P. S., Boorman, J., and Baylis, M. (2000). *Culicoides* biting midges: their role as arbovirus vectors. *Annual Review of Entomology*, **45**, 307–340.
- Merlin, O., Walker, J. P., Chehbouni, A., and Kerr, Y. (2008). Towards deterministic downscaling of SMOS soil moisture using MODIS derived soil evaporative efficiency. *Remote Sensing of Environment*, **112**, 3935–3946.
- Merlin, O., Al Bitar, A., Walker, J., and Kerr, Y. (2009). A sequential model for disaggregating near-surface soil moisture observations using multi-resolution thermal sensors. *Remote Sensing of Environment*, **113**, 2275–2284.
- Minacapilli, M., Iovino, M., and Blanda, F. (2009). High resolution remote estimation of soil surface water content by a thermal inertia approach. *Journal of Hydrology*, **379**(3-4), 229–238.
- Mitra, D. and Majumdar, T. (2004). Thermal inertia mapping over the Brahmaputra basin, India using NOAA-AVHRR data and its possible geological applications. *International Journal of Remote Sensing*, **25**(16), 3245–3260.
- Mladenova, I., Lakshmi, V., Walker, J. P., Panciera, R., Wagner, W., and Doubkova, M. (2010). Validation of the ASAR Global Monitoring Mode soil moisture product using the NAFE'05 data set. *IEEE Transactions on Geoscience and Remote Sensing*, **48**(6), 2498–2508.

- Moran, M. S., Clarke, T. R., Inoue, Y., and Vidal, A. (1994a). Estimating crop water deficit using the relation between surface-air temperature and spectral vegetation index. *Remote Sensing of Environment*, **49**(3), 246–263.
- Moran, M. S., Clarke, T. R., Kustas, W. P., Wetz, M., and Amer, S. A. (1994b). Evaluation of hydrologic parameters in a semiarid rangeland using remotely sensed spectral data. *Water Resources Research*, **30**(5), 1287–1297.
- Moran, M. S., Hymer, D. C., Qi, J., and Sano, E. E. (2000). Soil moisture evaluation using multi-temporal synthetic aperture radar (SAR) in semiarid rangeland. *Agricultural and Forest Meteorology*, **105**, 69–80.
- Muller, E. and Décamps, H. (2000). Modeling soil moisture-reflectance. *Remote Sensing of Environment*, **76**, 173–180.
- Naemi, V., Scipal, K., Bartalis, Z., Hasenauer, S., and Wagner, W. (2009). An improved soil moisture retrieval algorithm for ERS and METOP scatterometer observations. *IEEE Transactions on Geoscience and Remote Sensing*, **47**(7), 1999–2013.
- Narayan, U., Lakshmi, V., and Jackson, T. J. (2006). High-resolution change estimation of soil moisture using L-band radiometer and radar observations made during the SMEX02 experiments. *IEEE Transactions on Geoscience and Remote Sensing*, **44**(6), 1545–1554.
- NASA (2013). Modis website. [modis.gsfc.nasa.gov](http://modis.gsfc.nasa.gov).
- Nemani, R., Pierce, L., Running, S., and Goward, S. (1993). Developing satellite-derived estimates of surface moisture status. *Journal of Applied Meteorology*, **32**(3), 548–557.
- Nemani, R. R. and Running, S. W. (1989). Estimation of regional surface resistance to evapotranspiration from NDVI and thermal-IR AVHRR data. *Journal of Applied Meteorology*, **28**(4), 276–284.
- Nevill, E. M. (1967). *Biological studies on some South African Culicoides species (Diptera: Ceratopogonidae) and the morphology of their immature stages*. Master's thesis, University of Pretoria, Pretoria.
- Njoku, E. (2008). AMSR-E/Aqua Daily L3 Surface Soil Moisture, Interpretive Parameters, & QC EASE-Grids V002, [01/01/2008-31/12/2010]. Boulder, Colorado USA: National Snow and Ice Data Center. Digital media. Updated daily.
- Njoku, E., Ashcroft, P., Chan, T., and Li, L. (2005). Global survey and statistics of radio-frequency interference in AMSR-E land observations. *IEEE Transactions on Geoscience and Remote Sensing*, **43**(5), 938–947.
- Njoku, E. G., Jackson, T. J., Lakshmi, V., Chan, T. K., and Nghiem, S. V. (2003). Soil moisture retrieval from AMSR-E. *IEEE Transactions on Geoscience and Remote Sensing*, **41**(2), 215–229.



- Oh, Y., Sarabindi, K., and Ulaby, F. T. (1992). An empirical model and an inversion technique for scattering from bare soil surfaces. *IEEE Transactions on Geoscience and Remote Sensing*, **30**(2), 370–381.
- Olivia, R., Daganzo-Eusebio, E., Kerr, Y. H., Mecklenburg, S., Nieto, S., Richaume, P., and Gruhier, C. (2012). SMOS radio frequency interference scenario: status and actions taken to improve the RFI environment in the 1400–1427-MHz passive band. *IEEE Transactions on Geoscience and Remote Sensing*, **50**(5), 1427–1439.
- Owe, M., de Jeu, R. A. M., and Walker, J. (2001). A methodology for surface soil moisture and vegetation optical depth retrieval using the microwave polarization difference index. *IEEE Transactions on Geoscience and Remote Sensing*, **39**(8), 1643–1654.
- Owe, M., de Jeu, R. A. M., and Holmes, T. R. H. (2008). Multisensor historical climatology of satellite-derived global land surface moisture. *Journal of Geophysical Research*, **113**(F1), F01002.
- Paloscia, S., Pampaloni, P., Pettinato, S., and Santi, E. (2008). A comparison of algorithms for retrieving soil moisture from ENVISAT/ASAR images. *IEEE Transactions on Geoscience and Remote Sensing*, **46**(10), 3274–3284.
- Pan, M., Sahoo, A. K., Wood, E. F., Al Bitar, A., Leroux, D., and Kerr, Y. (2012). An initial assessment of SMOS derived soil moisture over the continental United States. *IEEE Transactions on Geoscience and Remote Sensing*, **5**(5), 1448–1457.
- Patel, N. R., Anapashsha, R., Kumar, S., Saha, S., and Dadhwal, V. K. (2009). Assessing potential of MODIS derived temperature/vegetation condition index (TVDI) to infer soil moisture status. *International Journal of Remote Sensing*, **30**(1), 23–39.
- Pathe, C., Wagner, W., Sabel, D., Doubkova, M., and Basara, J. B. (2009). Using ENVISAT ASAR Global Mode data for surface soil moisture retrieval over Oklahoma, USA. *IEEE Transactions on Geoscience and Remote Sensing*, **47**(2), 468–480.
- Pellarin, T., Calvet, J.-C., and Wagner, W. (2006). Evaluation of ERS scatterometer soil moisture products over a half-degree region in southwestern France. *Geophysical Research Letters*, **33**, L17401.
- Peters, J., De Baets, B., Verhoest, N. E. C., Samson, R., Degroeve, S., De Becker, P., and Huybrechts, W. (2007). Random forests as a tool for ecohydrological distribution modelling. *Ecological Modelling*, **207**(2-4), 304–318.
- Peters, J., De Baets, B., Van doninck, J., Calvete, C., Lucientes, J., De Clercq, E. M., Ducheyne, E., and Verhoest, N. E. C. (2011). Absence reduction in



- entomological surveillance data to improve niche-based distribution models for *Culicoides imicola*. *Preventive Veterinary Medicine*, **100**(1), 15–28.
- Peters, J., Conte, A., Van doninck, J., Verhoest, N., De Clercq, E., Goffredo, M., De Baets, B., Hendrickx, G., and Ducheyne, E. (2013). On the relation between spatio-temporal soil moisture dynamics and the geographical distribution of *Culicoides imicola*. *Ecohydrology*. In review.
- Petropoulos, G., Carlson, T. N., Wooster, M. J., and Islam, S. (2009). A review of Ts/VI remote sensing based methods for the retrieval of land surface energy fluxes and soil surface moisture. *Progress in Physical Geography*, **33**(2), 224–250.
- Piles, M., Camps, A., Vall-llossera, M., Corbella, I., Panciera, R., Rüdiger, C., Keer, Y. H., and Walker, J. (2011). Downscaling SMOS-derived soil moisture using MODIS visible/infrared data. *IEEE Transactions on Geoscience and Remote Sensing*, **49**(9), 3156–3166.
- Pratt, D., Forster, S., and Ellyett, C. (1980). A calibration procedure for Fourier series thermal inertia models. *Photogrammetric Engineering & Remote Sensing*, **46**(4), 529–538.
- Price, J. (1977). Thermal inertia: a new view of the earth. *Journal of Geophysical Research*, **82**(18), 2582–2590.
- Price, J. (1980). The potential of remotely sensed thermal infrared data to infer surface soil moisture and evaporation. *Water Resources Research*, **16**(4), 787–795.
- Price, J. (1985). On the analysis of thermal infrared imagery: the limited utility of apparent thermal inertia. *Remote Sensing of Environment*, **18**(1), 59–73.
- Price, J. C. (1982). On the use of satellite data to infer surface fluxes at meteorological scales. *Journal of Applied Meteorology*, **21**(8), 1111–1122.
- Prihodko, L. and Goward, S. N. (1996). Estimation of air temperature from remotely sensed surface observations. *Remote Sensing of Environment*, **60**(3), 335–346.
- Purse, B. V., Tatem, A. J., Caracappa, S., Rogers, D. J., Mellor, P. S., Baylis, M., and Torina, A. (2004). Modelling the distribution of *Culicoides* bluetongue virus vectors in Sicily in relation to satellite-derived climate variables. *Medical and Veterinary Entomology*, **18**(2), 90–101.
- Purse, B. V., McCormick, B. J. J., Mellor, P. S., Baylis, M., Boorman, J. P. T., Borrás, D., Burgu, I., Capela, R., Caracappa, S., Collantes, F., De Liberato, C., Delgado, J. A., Denison, E., Georgiev, G., El Harak, M., De La Rocque, S., Lhor, Y., Lucientes, J., Mangana, O., Miranda, M. A., Nedelchev, N., Nomikou, K., Ozkul, A., Patakakis, M., Pena, I., Scaramozzino, P., Torina, A., and Rogers,

- D. J. (2007). Incriminating bluetongue virus vectors with climate envelope models. *Journal of Applied Ecology*, **44**(6), 1231–1242.
- Raes, D. (2002). Budget: a soil water and salt balance model. Reference manual, Version 5.0., Katholieke Universiteit Leuven.
- Rahman, M. M., Moran, M. S., Thoma, D. P., Bryant, R., Sano, E., Holifield Collins, C., Skirvin, S., Kershner, C., and Orr, B. (2007). A derivation of roughness correlation length for parameterizing radar backscatter models. *International Journal of Remote Sensing*, **28**(18), 3995–4012.
- Rahman, M. M., Moran, M. S., Thoma, D. P., Bryant, R., Holifield Collins, C. D., Jackson, T., Orr, B. J., and Tischler, M. (2008). Mapping surface roughness and soil moisture using multi-angle radar imagery without ancillary data. *Remote Sensing of Environment*, **112**, 391–402.
- Riaño, D., Chuvieco, E., Salas, J., and Aguado, I. (2003). Assessment of different topographic corrections in Landsat-TM data for mapping vegetation types (2003). *IEEE Transactions on Geoscience and Remote Sensing*, **41**(5), 1056–1061.
- Rulinda, C. M., Bijker, W., and Stein, A. (2010). Image mining for drought monitoring in eastern Africa using Meteosat SEVIRI data. *International Journal of Applied Earth Observation and Geoinformation*, **12**(S1), S63–S68.
- Saegerman, C., Berkvens, D., and Mellor, P. S. (2008). Bleutongue epidemiology in the European Union. *Emerging Infectious Diseases*, **14**(4), 539–544.
- Sandholt, I., Rasmussen, K., and Andersen, J. (2002). A simple interpretation of the surface temperature/vegetation index space for assessment of surface moisture status. *Remote Sensing of Environment*, **79**(2-3), 213–224.
- Saxton, K. E. and Rawls, W. J. (2006). Soil water characteristic estimates by texture and organic matter for hydrologic solutions. *Soil Science Society of America Journal*, **70**, 1569–1578.
- Sehgal, R. N. M., Buermann, W., Harrigan, R. J., Bonneaud, C., Loiseau, C., Chasar, A., Sepil, I., Valkiūnas, G., Iezhova, T., Saatchi, S., and Smith, T. B. (2011). Spatially explicit predictions of blood parasites in a widely distributed African rainforest bird. *Proceedings of the Royal Society B*, **278**, 1025–1033.
- Sheikh, V., Visser, S., and Stroosnijder, L. (2009). A simple model to predict soil moisture: Bridging event and continuous hydrological (BEACH) modelling. *Environmental Modelling & Software*, **24**, 542–556.
- Short, N. and Stuart, Jr., L. (1982). The Heat Capacity Mapping Mission (HCMM) anthology. Technical report, NASA.

- Shoshany, M., Svoray, T., Curran, P. J., Foody, G. M., and Perevolotsky, A. (2000). The relationship between ERS-2 SAR backscatter and soil moisture; generalization from a humid to semi-arid transect. *International Journal of Remote Sensing*, **21**(11), 2337–2343.
- Small, D. and Schubert, A. (2008). Guide to ASAR geocoding. RSL-ASAR-GC-AD.
- Snyder, W. C., Wan, Z., Zhang, Y., and Feng, Y. Z. (1998). Classification-based emissivity for land surface temperature measured from space. *International Journal of Remote Sensing*, **19**(14), 2753–2774.
- Sobrino, J. and El Kharraz, M. (1999a). Combining afternoon and morning NOAA satellites for thermal inertia estimation 1. algorithm and its testing with Hydrologic Atmospheric Pilot Experiment-Sahel data. *Journal of Geophysical Research*, **104**(B8), 9446–9453.
- Sobrino, J. and El Kharraz, M. (1999b). Combining afternoon and morning NOAA satellites for thermal inertia estimation 2. methodology and application. *Journal of Geophysical Research*, **104**(B8), 9455–9465.
- Somers, B., Gysels, V., Verstraeten, W. W., Delalieux, S., and Coppin, P. (2010). Modelling moisture-induced soil reflectance changes in cultivated sandy soils: a case study in citrus orchards. *European Journal of Soil Science*, **61**(6), 1091–1105.
- Stisen, S., Sandholt, I., Nørgaard, A., Fensholt, R., and Høgh Jensen, K. (2008). Combining the triangle method with thermal inertia to estimate regional evapotranspiration - applied to MSG-SEVERI data in the Senegal River basin. *Remote Sensing of Environment*, **112**(3), 1242–1255.
- Stone, P. H. and Carlson, J. H. (1979). Atmospheric lapse rate regimes and their parameterization. *Journal of the Atmospheric Sciences*, **36**(3), 415–423.
- Su, Z., Troch, P., and De Troch, F. (1997). Remote sensing of bare surface soil moisture using EMAC/ESAR data. *International Journal of Remote Sensing*, **18**(10), 2105–2124.
- Sun, D. and Kefalos, M. (2007). Note on the NDVI-LST relationship and the use of temperature-related drought indices over North America. *Geophysical Research Letters*, **34**(24), L24406.
- Sun, W., Wang, P.-X., Zhang, S.-Y., Zhu, D.-H., Liu, J.-M., Chen, J.-H., and Yang, H.-S. (2008). Using the vegetation temperature condition index for time series drought occurrence monitoring in the Guanzhong Plain, PR China. *International Journal of Remote Sensing*, **29**(17-18), 5133–5144.

- Tang, R., Li, Z.-L., and Tang, B. (2010). An application of the Ts-VI triangle method with enhanced edges determination for evapotranspiration estimates from MODIS data in arid and semi-arid regions: implementation and validation. *Remote Sensing of Environment*, **114**(3), 540–551.
- Tarquini, S., Vinci, S., Favalli, M., Doumaz, F., Fornaciai, A., and Nannipieri, L. (2012). Release of a 10-m-resolution DEM for the Italian territory: Comparison with global-coverage DEMs and anaglyph-mode exploration via the web. *Computers & Geosciences*, **38**, 168–170.
- Tatem, A. J., Baylis, M., Mellor, P. S., Purse, B. V., Capela, R., Pena, I., and Rogers, D. J. (2003). Prediction of bluetongue vector distribution in Europe and north Africa using satellite imagery. *Veterinary Microbiology*, **97**(1-2), 13–29.
- Thoma, D. P., Moran, M. S., Bryant, R., Rahman, M., Holifield-Collins, C. D., Skirvin, S., Sano, E. E., and Slocum, K. (2006). Comparison of four models to determine surface soil moisture from C-band radar imagery in a sparsely vegetated semiarid landscape. *Water Resources Research*, **42**, W01418.
- Torres, R., Snoeij, P., Geudtner, D., Bibby, D., Davidson, M., Attema, E., Potin, P., Rommen, B., Floury, N., Brown, M., Navas Traver, I., Deghaye, P., Duesmann, B., Rosich, B., Miranda, N., Bruna, C., L'Abbate, M., Croci, R., Pietropaolo, A., Huchler, M., and Rostan, F. (2012). GMES Sentinel-1 mission. *Remote Sensing of Environment*, **120**(SI), 9–24.
- Tramutoli, V., Claps, P., Marella, M., Pergola, N., and Sileo, C. (2000). Feasibility of hydrological application of thermal inertia from remote sensing. In *Proc. of 2nd Plinius Conference on Mediterranean Storms, Siena, Italy, 16-18 October 2000*.
- Twomey, S. A., Bohren, C. F., and Mergenthaler, J. L. (1986). Reflectance and albedo differences between wet and dry surfaces. *Applied Optics*, **25**(3), 431–437.
- Ulaby, F. T., Moore, R. K., and Fung, A. K. (1982). *Microwave Remote Sensing: Active and Passive, volume II: Radar Remote Sensing and Surface Scattering and Emission Theory*. Artech House, Boston.
- Uslu, U. and Dik, B. (2006). Vertical distribution of Culicoides larvae and pupae. *Medical and Veterinary Entomology*, **20**(3), 350–352.
- van der Velde, R., Su, Z., and Ma, Y. (2008). Impact of soil moisture dynamics on ASAR  $\sigma^0$  signatures and its spatial variability observed over the Tibetan Plateau. *Sensors*, **8**, 5479–5491.
- Venables, W. N. and Ripley, B. D. (2002). *Modern Applied Statistics with S*. Springer, fourth edition edition.

- Venter, G. J., Nevil, E. M., and Van der Linde, T. C. D. (1997). Seasonal abundance and parity of stock-associated *Culicoides* species (Diptera : Ceratopogonidae) in different climatic regions in southern africa in relation to their viral vector potential. *Onderstepoort Journal Of Veterinary Research*, **64**(4), 25–271.
- Verhoef, W. (1996). Application of harmonic analysis of NDVI time series (HANTS). In S. Azzali and M. Menenti, editors, *Fourier Analysis of Temporal NDVI in the Southern African and American Continents*, pages 19–24. DLO Winand Staring Centre, Wageningen, The Netherlands.
- Verhoest, N., Lievens, H., Wagner, W., Álvarez-Mozos, J., Moran, M., and Mattia, F. (2008). On the soil roughness parameterization problem in soil moisture retrieval of bare surfaces from synthetic aperture radar. *Sensors*, **8**, 4213–4248.
- Vermote, E. F. and Vermeulen, A. (1999). Atmospheric correction algorithm: spectral reflectances (MOD09). ATBD version 4.0.
- Veronesi, E., Venter, G. J., Labuschagne, K., Mellor, P. S., and Carpenter, S. (2009). Life history of *Culicoides (Avaritia) imicola* Kieffer in the laboratory at different rearing temperatures. *Veterinary Parasitology*, **163**(4), 370–373.
- Veroustraete, F., Li, Q., Verstraeten, W. W., Chen, X., Bao, A., Dong, Q., Liu, T., and Willems, P. (2012). Soil moisture content retrieval based on apparent thermal inertia for Xinjiang province in China. *International Journal of Remote Sensing*, **33**(12), 3870–3885.
- Verstraeten, W. W., Veroustraete, F., and Feyen, J. (2005). Estimating evapotranspiration of European forests from NOAA-imagery at satellite overpass time: towards an operational processing chain for integrated optical and thermal sensor data products. *Remote Sensing of Environment*, **96**(2), 256–276.
- Verstraeten, W. W., Veroustraete, F., van der Sande, C. J., Grootaers, I., and Feyen, J. (2006). Soil moisture retrieval using thermal inertia, determined with visible and thermal spaceborne data, validated for European forest. *Remote Sensing of Environment*, **101**, 299–314.
- Vicente-Serrano, S. M., Pons-Fernández, X., and Cuadrat-Prats, J. M. (2004). Mapping soil moisture in the central Ebro river valley (northeast Spain) with Landsat and NOAA satellite imagery: a comparison with meteorological data. *International Journal of Remote Sensing*, **25**(20), 4325–4350.
- Viscarra Rossel, R. A. and McBratney, A. B. (1998). Laboratory evaluation of a proximal sensing technique for simultaneous measurement of soil clay and water content. *Geoderma*, **85**, 19–39.
- Wagner, W. and Scipal, K. (2000). Large-scale soil moisture mapping in western Africa using the ERS Scatterometer. *IEEE Transactions on Geoscience and Remote Sensing*, **38**(4), 1777–1782.

- Wagner, W., Lemoine, G., and Rott, H. (1999a). A method for estimating soil moisture from ERS Scatterometer and soil data. *Remote Sensing of Environment*, **70**, 197–207.
- Wagner, W., Noll, J., Borgeaud, M., and Rott, H. (1999b). Monitoring soil moisture over the Canadian Prairies with the ERS Scatterometer. *IEEE Transactions on Geoscience and Remote Sensing*, **37**(1), 206–216.
- Wagner, W., Lemoine, G., Borgeaud, M., and Rott, H. (1999c). A study of vegetation cover effects on ERS Scatterometer data. *IEEE Transactions on Geoscience and Remote Sensing*, **37**(2), 938–948.
- Wagner, W., Naeimi, V., Scipal, K., de Jeu, R., and Martínez-Fernández, J. (2007). Soil moisture from operational meteorological satellites. *Hydrogeology Journal*, **15**, 121–131.
- Wagner, W., Pathe, C., Doubkova, M., Sabel, D., Bartsch, A., Hasenauer, S., Blöschl, G., Scipal, K., Martínez-Fernández, J., and Löw, A. (2008). Temporal stability of soil moisture and radar backscatter observed by the Advanced Synthetic Aperture Radar (ASAR). *Sensors*, **8**, 1174–1197.
- Wagner, W., Sabel, D., Doubkova, M., Bartsch, A., and Pathe, C. (2009). The potential of Sentinel-1 for monitoring soil moisture with high spatial resolution at global scale. In *Symposium of Earth Observation and Water Cycle Science*.
- Wall, J., Collingwood, A., and Treitz, P. (2010). Monitoring surface moisture state in the Canadian High Arctic using synthetic aperture radar (SAR). *Canadian Journal of Remote Sensing*, **36**(S1), S124–S134.
- Wan, Z. and Dozier, J. (1996). A generalized split-window algorithm for retrieving land-surface temperature from space. *IEEE Transactions on Geoscience and Remote Sensing*, **34**(4), 892–905.
- Wan, Z. and Li, Z. (1997). A physics-based algorithm for retrieving land-surface emissivity and temperature from EOS/MODIS data. *IEEE Transactions on Geoscience and Remote Sensing*, **35**(4), 980–996.
- Wan, Z., Wang, P., and Li, X. (2004). Using MODIS land surface temperature and normalized difference vegetation index products for monitoring drought in the southern Great Plains, USA. *International Journal of Remote Sensing*, **25**(1), 61–72.
- Wang, C., Qi, S., Niu, Z., and Wang, J. (2004). Evaluating soil moisture status in China using the temperature-vegetation dryness index (TVDI). *Canadian Journal of Remote Sensing*, **30**(5), 671–679.
- Wang, L., Qu, J. J., Hao, X., and Zhu, Q. (2008). Sensitivity studies of the moisture effects on MODIS SWIR reflectance and vegetation water indices. *International Journal of Remote Sensing*, **29**(24), 70.

- Wang, X., Xie, H., Guan, H., and Zhou, X. (2007). Different responses of MODIS-derived NDVI to root-zone soil moisture in semi-arid and humid regions. *Journal of Hydrology*, **340**, 12–24.
- Warner, T. A. and Chen, X. (2001). Normalization of Landsat thermal imagery for the effects of solar heating and topography. *International Journal of Remote Sensing*, **22**(5), 773–788.
- Watson, K. (1973). Periodic heating of a layer over a semi-infinite solid. *Journal of Geophysical Research*, **78**(26), 5904–5910.
- Whiting, M. L., Li, L., and Ustin, S. L. (2004). Predicting water content using Gaussian model on soil spectra. *Remote Sensing of Environment*, **89**, 535–552.
- Wickel, A. J., Jackson, T. J., and Wood, E. F. (2001). Multitemporal monitoring of soil moisture with RADARSAT SAR during the 1997 Southern Great Plains hydrology experiment. *International Journal of Remote Sensing*, **22**(8), 1571–1583.
- Wilson, A. J. and Mellor, P. S. (2009). Bluetongue in Europe: past, present and future. *Philosophical Transactions of the Royal Society B*, **364**, 2669–2681.
- Wittmann, E. J., Mellor, P. S., and Baylis, M. (2001). Using climate data to map the potential distribution of *Culicoides imicola* (diptera: Ceratopogonidae) in europe. *Revue Scientifique et Technique de l'Office International des Epizooties*, **20**(3), 731–740.
- Woodhouse, I. H. (2006). *Introduction to microwave remote sensing*. CRC Press, Taylor & Francis Group, Boca Raton, FL.
- Xue, Y. and Cracknell, A. (1995). Advanced thermal inertia modelling. *International Journal of Remote Sensing*, **16**(3), 431–446.
- Yi, Y., Yang, D., Chen, D., and Huang, J. (2007). Retrieving crop physiological parameters and assessing water deficiency using MODIS data during the winter wheat growing period. *Canadian Journal of Remote Sensing*, **33**(3), 189–202.
- Zhang, Z., De Wulf, R. R., Van Coillie, F. M. B., Verbeke, L. P. C., De Clercq, E. M., and Ou, X. (2011). Influence of different topographic correction strategies on mountain vegetation classification accuracy in the Lancang Watershed, China. *Journal of Applied Remote Sensing*, **5**, 053512.
- Zribi, M., Baghdadi, N., Holah, N., and Fafin, O. (2005). New methodology for soil surface moisture estimation and its application to ENVISAT-ASAR multi-incidence data inversion. *Remote Sensing of Environment*, **96**(3-4), 485–496.
- Zribi, M., Saux-Picart, S., André, C., Descroix, L., Otlé, C., and Kallel, A. (2007). Soil moisture mapping based on ASAR/ENVISAT radar data over a Sahelian region. *International Journal of Remote Sensing*, **28**(16), 3547–3565.

# A

## In situ soil moisture measurements

The following tables provide the geographic coordinates of the in situ measurement locations in Calabria that were visited during the field campaign. In general, each point was visited three times, and gravimetric (g/g) and/or volumetric ( $\text{cm}^3/\text{cm}^3$ ) soil moisture measurements were made using an auger and TDR, respectively.



Site 1A								
ID	Latitude	Longitude	16/09/2009		30/09/2009		7/10/2009	
			g/g	cm <sup>3</sup> /cm <sup>3</sup>	g/g	cm <sup>3</sup> /cm <sup>3</sup>	g/g	cm <sup>3</sup> /cm <sup>3</sup>
1.1	38°56'31.7"	16°45'08.6"	0.0770	0.0310	0.2975	0.4167	0.4467	
1.2	38°56'27.7"	16°45'11.9"	0.0725		0.2446	0.3527	0.3337	
1.3	38°56'23.3"	16°45'14.6"	0.0120	0.0373	0.0613	0.0913	0.0793	
2.1	38°56'35.8"	16°45'11.8"	0.0279	0.0643	0.1170	0.1937	0.1660	
2.2	38°56'30.8"	16°45'15.1"	0.0544	0.0657	0.2188	0.4040	0.2993	
2.3	38°56'26.8"	16°45'18.9"	0.0097	0.0383	0.2762	0.4567	0.3010	
3.1	38°56'37.9"	16°45'15.3"	0.0285	0.0210	0.1010	0.1217	0.1187	
3.2	38°56'34.2"	16°45'19.5"	0.0780	0.0273	0.0877	0.1183	0.0660	
3.3	38°56'30.4"	16°45'23.4"	0.0785	0.0877	0.2571	0.3517	0.3720	

Site 1B								
ID	Latitude	Longitude	16/09/2009		30/09/2009		07/10/2009	
			g/g	cm <sup>3</sup> /cm <sup>3</sup>	g/g	cm <sup>3</sup> /cm <sup>3</sup>	g/g	cm <sup>3</sup> /cm <sup>3</sup>
1.1	39°0'37.6"	16°54'40.6"	0.2323	0.3337	0.5430	0.6080	0.5880	
1.2	39°0'35.1"	16°54'46"	0.2103	0.3093			0.4587	
1.3	39°0'32.8"	16°54'51.5"	0.2077	0.3287			0.3273	
2.1	39°0'29.9"	16°54'37"	0.0979	0.0813	0.4238	0.5283	0.6473	
2.2	39°0'29.1"	16°54'43.2"	0.0662	0.1703			0.4633	
2.3	39°0'28.2"	16°54'49.4"	0.0379	0.0747			0.3233	
3.1	39°0'42"	16°54'42.8"	0.1165	0.1660			0.4050	
3.2	39°0'39.5"	16°54'48.2"	0.1336	0.2580	0.5405	0.6913	0.4747	
3.3	39°0'37.1"	16°54'53.7"	0.0704	0.2627			0.3323	

Site 1C								
ID	Latitude	Longitude	16/09/2009		01/10/2009		07/10/2009	
			g/g	cm <sup>3</sup> /cm <sup>3</sup>	g/g	cm <sup>3</sup> /cm <sup>3</sup>	g/g	cm <sup>3</sup> /cm <sup>3</sup>
1.1	39°1'7.5"	17°9'5.1"	0.0646	0.0387	0.3750		0.2931	0.3837
1.2	39°1'2.6"	17°9'5.1"	0.0516	0.0333	0.3743		0.2583	0.3317
1.3	39°0'57.7"	17°9'4.9"	0.0541	0.0500	0.3656		0.2854	0.3870
2.1	39°1'7.1"	17°9'11.3"	0.0559		0.3487		0.2560	0.3517
2.2	39°1'2"	17°9'10"	0.0660	0.0540	0.3727		0.3123	0.3877
2.3	39°0'57.2"	17°9'11.2"	0.0632	0.0537	0.3808		0.3385	0.4317
3.1	39°1'6.7"	17°9'14.8"	0.0691	0.0740	0.3760		0.2051	0.3343
3.2	39°1'2.1"	17°9'16.7"	0.1576	0.2603	0.4009		0.2946	0.5440
3.3	39°0'57.4"	17°9'17.4"	0.0687	0.1147	0.4129		0.3354	0.4670

Site 1D								
ID	Latitude	Longitude	18/09/2009		30/09/2009		07/10/2009	
			g/g	cm <sup>3</sup> /cm <sup>3</sup>	g/g	cm <sup>3</sup> /cm <sup>3</sup>	g/g	cm <sup>3</sup> /cm <sup>3</sup>
1.1	39°6'2.9"	16°46'2"	0.2337	0.1203	0.2720		0.5736	0.2760
1.2	39°6'1.7"	16°46'0.9"	0.1429	0.1623	0.3013		0.4396	0.2913
2.1	39°6'2"	16°46'4.1"	0.2209	0.2023	0.3137		0.2078	0.3063
2.2	39°6'1.1"	16°46'2.2"	0.1620	0.1670	0.2793		0.1552	0.2847
2.3	39°6'0.2"	16°46'0.3"	0.1301	0.2243	0.2920		0.2004	0.2717
3.1	39°6'3.2"	16°46'0.1"	0.2311	0.1390	0.2960		0.5086	0.2957

Site 1E

ID	Latitude	Longitude	18/09/2009		30/09/2009		07/10/2009	
			g/g	cm <sup>3</sup> /cm <sup>3</sup>	g/g	cm <sup>3</sup> /cm <sup>3</sup>	g/g	cm <sup>3</sup> /cm <sup>3</sup>
1.1	39°4'25"	16°52'23.8"	0.1817	0.3160		0.3890	0.3142	0.3657
1.2	39°4'22.6"	16°52'18.4"	0.1943	0.2390		0.3783	0.2076	0.3240
1.3	39°4'19.7"	16°52'13.4"	0.2150	0.2667		0.3267	0.2328	0.2927
2.1	39°4'21.6"	16°52'28.2"	0.2475	0.2880		0.3710	0.2149	0.3820
2.2	39°4'19.8"	16°52'20.7"	0.1255	0.3243		0.3983	0.2161	0.3357
2.3	39°4'15.8"	16°52'17.2"	0.1616	0.1967		0.3787	0.2034	0.3090
3.1	39°4'20"	16°52'31.7"	0.1959	0.3030		0.4213	0.2010	0.3420
3.2	39°4'17.5"	16°52'24"	0.1282	0.2350		0.4207	0.2569	0.4337
3.3	39°4'13.5"	16°52'20.5"	0.2323	0.3200		0.3850	0.2435	0.3383

Site 1F

ID	Latitude	Longitude	18/09/2009		01/10/2009		07/10/2009	
			g/g	cm <sup>3</sup> /cm <sup>3</sup>	g/g	cm <sup>3</sup> /cm <sup>3</sup>	g/g	cm <sup>3</sup> /cm <sup>3</sup>
1.1	39°5'20.1"	17°4'11.4"	0.0997	0.2017		0.3300	0.1685	0.3087
1.2	39°5'20.3"	17°4'17.7"	0.0728	0.1407		0.2305	0.0819	0.1777
1.3	39°5'21.5"	17°4'23.8"	0.1729	0.1633		0.3377	0.2146	0.3333
2.1	39°5'23.6"	17°4'9.6"	0.1199			0.3619	0.2194	0.3360
2.2	39°5'25.4"	17°4'15.8"	0.0764			0.2365	0.1090	0.2420
2.3	39°5'26.2"	17°4'22"	0.1082	0.1217		0.2903	0.1488	0.3223
3.1	39°5'27.4"	17°4'8.4"	0.1126			0.3143	0.1946	0.2817
3.2	39°5'29.9"	17°4'13.9"	0.0685			0.2140	0.1181	0.2320
3.3	39°5'30.8"	17°4'20"	0.1121	0.2343		0.2672	0.1590	0.2667

Site 1G

ID	Latitude	Longitude	21/09/2009		01/10/2009		07/10/2009	
			g/g	cm <sup>3</sup> /cm <sup>3</sup>	g/g	cm <sup>3</sup> /cm <sup>3</sup>	g/g	cm <sup>3</sup> /cm <sup>3</sup>
1.1	38°59'57.4"	16°57'2.5"	0.2470	0.2893		0.3113		0.4367
1.2	38°59'52.6"	16°57'2.5"	0.2124	0.3783		0.4264		0.5193
1.3	38°59'48.6"	16°57'4.7"	0.2251	0.2653		0.3562		0.3250
2.1	38°59'57.6"	16°57'8.7"	0.2047	0.3007		0.2899		0.3180
2.2	38°59'53"	16°57'9.9"	0.2033	0.2420		0.3483		0.3500
2.3	38°59'48.4"	16°57'11"	0.2154	0.3343		0.3898		0.3550
3.1	38°59'58.4"	16°57'14.9"	0.2112	0.2757		0.3449		0.3273
3.2	38°59'53.6"	16°57'16"	0.1442	0.1393		0.3583		0.4380
3.3	38°59'48.8"	16°57'17.2"	0.2220	0.2103		0.3749		0.3017

Site 1H

ID	Latitude	Longitude	21/09/2009		01/10/2009		07/10/2009	
			g/g	cm <sup>3</sup> /cm <sup>3</sup>	g/g	cm <sup>3</sup> /cm <sup>3</sup>	g/g	cm <sup>3</sup> /cm <sup>3</sup>
1.1	39°9'25"	16°55'8.4"	0.2344	0.3593		0.3459	0.2500	0.3443
1.2	39°9'30.5"	16°55'6.6"	0.1645	0.2953		0.4048	0.1652	0.3197
1.3	39°9'35.1"	16°55'4.7"	0.1977	0.2997		0.4081	0.3079	0.4160
2.1	39°9'23.1"	16°55'2.9"	0.2451	0.3507		0.3828	0.2402	0.3467
2.2	39°9'28.2"	16°55'1"	0.2696	0.3383		0.3335	0.2938	0.3800
2.3	39°9'34.5"	16°54'58.4"	0.2095	0.3477		0.3399	0.2453	0.3670
3.1	39°9'21.5"	16°54'56.8"	0.1894	0.3080		0.3621	0.1970	0.3317
3.2	39°9'26.3"	16°54'55.3"	0.2576	0.3800		0.4379	0.3212	0.4613
3.3	39°9'30.8"	16°54'53.5"				0.3519	0.2712	0.3877

Site II

ID	Latitude	Longitude	24/09/2009		02/10/2009		07/10/2009	
			g/g	cm <sup>3</sup> /cm <sup>3</sup>	g/g	cm <sup>3</sup> /cm <sup>3</sup>	g/g	cm <sup>3</sup> /cm <sup>3</sup>
1.1	39°14'4.4"	17°4'47"	0.2529	0.4107		0.3553	0.2049	0.3528
1.2	39°14'7.9"	17°4'50.6"	0.2680	0.5613		0.5413	0.1747	0.3886
1.3	39°14'11.6"	17°4'54.7"	0.2446	0.3587		0.3567	0.1677	0.2664
2.1	39°14'7"	17°4'39.9"	0.2772	0.3507		0.5437	0.1553	0.3394
2.2	39°14'9.9"	17°4'43.8"	0.3216	0.4060		0.3113	0.2171	0.3226
2.3	39°14'15.4"	17°4'50.8"	0.2201	0.3597		0.3760	0.1403	0.2911
3.1	39°14'12.7"	17°4'35.9"	0.3169	0.3870		0.3540	0.2127	0.3281
3.2	39°14'15.6"	17°4'41.2"	0.2997	0.4570		0.4120	0.1980	0.3258
3.3	39°14'18.7"	17°4'46"	0.2248	0.3970		0.4793	0.1886	0.3651

Site IJ

ID	Latitude	Longitude	26/09/2009		03/10/2009		07/10/2009	
			g/g	cm <sup>3</sup> /cm <sup>3</sup>	g/g	cm <sup>3</sup> /cm <sup>3</sup>	g/g	cm <sup>3</sup> /cm <sup>3</sup>
1.1	39°0'25.2"	17°0'8"	0.2548	0.4197		0.4400		0.3743
1.2	39°0'20.3"	17°0'8.1"	0.3090	0.3900		0.3340		0.3347
1.3	39°0'15.5"	17°0'8.2"	0.3040	0.4843		0.4537		0.3620
2.1	39°0'25.2"	17°0'14.2"	0.3201	0.5590		0.4857		0.3277
2.2	39°0'20.3"	17°0'14.4"	0.2837	0.4673		0.4273		0.3587
2.3	39°0'15.5"	17°0'14.5"	0.2729	0.3977		0.3663		0.3470
3.1	39°0'25"	17°0'20.4"	0.3507	0.6070		0.5097		0.3710
3.2	39°0'20.1"	17°0'20.6"	0.3027	0.5497		0.4420		0.3427
3.3	39°0'15.3"	17°0'20.7"	0.3462	0.5830		0.3313		0.2287

Site IK

ID	Latitude	Longitude	26/09/2009		02/10/2009		07/10/2009	
			g/g	cm <sup>3</sup> /cm <sup>3</sup>	g/g	cm <sup>3</sup> /cm <sup>3</sup>	g/g	cm <sup>3</sup> /cm <sup>3</sup>
1.1	39°3'20.9"	16°55'50.7"	0.2997	0.4643		0.4953	0.2391	0.3470
1.2	39°3'18.5"	16°55'56.1"	0.3358	0.5670		0.4193	0.2698	0.3640
1.3	39°3'15.7"	16°56'1.2"	0.3212	0.5803		0.5380	0.3064	0.4323
2.1	39°3'16.7"	16°55'47.5"	0.3177	0.5525		0.5430	0.2920	0.3870
2.2	39°3'14.3"	16°55'52.9"	0.3279			0.6033	0.2271	0.3457
2.3	39°3'11.5"	16°55'58.1"	0.3113			0.5283	0.2805	0.4593
3.1	39°3'12.4"	16°55'44.7"	0.2949			0.4427	0.2240	0.3423
3.2	39°3'10.3"	16°55'49.5"	0.3312	0.6143		0.4343	0.2519	0.3473
3.3	39°3'7.5"	16°55'54.6"	0.3888	0.6743		0.3960	0.2201	0.3397

Site IL

ID	Latitude	Longitude	29/09/2009		03/10/2009		07/10/2009	
			g/g	cm <sup>3</sup> /cm <sup>3</sup>	g/g	cm <sup>3</sup> /cm <sup>3</sup>	g/g	cm <sup>3</sup> /cm <sup>3</sup>
1.1	39°13'7.6"	16°52'1.8"	0.2114	0.3157		0.3646	0.1531	0.3148
1.2	39°13'11.5"	16°52'2.1"	0.2254	0.4063		0.3688	0.1856	0.3759
1.3	39°13'15.7"	16°52'0.4"	0.3021	0.3960		0.4110	0.2495	0.3851
2.1	39°13'7.5"	16°52'9.3"	0.1462	0.2997		0.3199		0.3233
2.2	39°13'12.2"	16°52'8"	0.1691	0.3117		0.3415		0.3156
2.3	39°13'16.9"	16°52'6.9"	0.2652	0.4147		0.4424		0.3685
3.1	39°13'8.2"	16°52'15.5"	0.1581	0.3190		0.3148		0.2890
3.2	39°13'13"	16°52'14.6"	0.2299	0.3520		0.3848	0.1840	0.3544
3.3	39°13'17.7"	16°52'12.9"	0.2477	0.4317		0.4214	0.2451	0.3885

Site 1M

ID	Latitude	Longitude	29/09/2009		03/10/2009		07/10/2009	
			g/g	cm <sup>3</sup> /cm <sup>3</sup>	g/g	cm <sup>3</sup> /cm <sup>3</sup>	g/g	cm <sup>3</sup> /cm <sup>3</sup>
1.1	39°18'22"	16°49'52.8"	0.2011	0.2827	0.3978	0.1816	0.2448	
1.2	39°18'24.8"	16°49'57.9"	0.2138	0.3450	0.3499	0.2055	0.3289	
1.3	39°18'26.9"	16°50'3.6"	0.2279	0.3397	0.3626	0.1764	0.3313	
2.1	39°18'18.2"	16°49'56.7"	0.1710	0.3203	0.3619	0.1794	0.3346	
2.2	39°18'20.4"	16°50'1.9"	0.2742	0.4073	0.3759	0.3176	0.3988	
2.3	39°18'22.8"	16°50'7"	0.1686	0.2963	0.2126	0.1418	0.3071	
3.1	39°18'14"	16°49'59.8"	0.2219	0.3410	0.3834	0.2283	0.3608	
3.2	39°18'16.3"	16°50'5.3"	0.2395	0.4023	0.3304	0.1756	0.3439	
3.3	39°18'18.6"	16°50'10"	0.2074	0.3590	0.3700	0.1770	0.3452	

Site 1N

ID	Latitude	Longitude	29/09/2009		03/10/2009		07/10/2009	
			g/g	cm <sup>3</sup> /cm <sup>3</sup>	g/g	cm <sup>3</sup> /cm <sup>3</sup>	g/g	cm <sup>3</sup> /cm <sup>3</sup>
1.1	39°14'50.1"	16°48'56.3"	0.2017	0.3397	0.3772	0.2275	0.3562	
1.2	39°14'50.2"	16°49'2.5"	0.2388	0.3417	0.3792	0.2317	0.3487	
1.3	39°14'49.2"	16°49'8.6"	0.1809	0.2967	0.3428	0.1674	0.3138	
2.1	39°14'45.2"	16°48'56"	0.3287	0.3293	0.3715	0.2687	0.3318	
2.2	39°14'45.5"	16°49'1.2"	0.2074	0.3560	0.3645	0.2182	0.3189	
2.3	39°14'44.4"	16°49'7.3"	0.2455	0.3247	0.3252	0.1921	0.3213	
3.1	39°14'40.7"	16°48'53.4"	0.2008	0.2750	0.3219	0.1727	0.3059	
3.2	39°14'40.8"	16°48'59.8"	0.2270	0.3147	0.3169	0.2500	0.3152	
3.3	39°14'39.7"	16°49'6"	0.2553	0.3860	0.3952	0.2270	0.3950	

Site 1O

ID	Latitude	Longitude	29/09/2009		02/10/2009		07/10/2009	
			g/g	cm <sup>3</sup> /cm <sup>3</sup>	g/g	cm <sup>3</sup> /cm <sup>3</sup>	g/g	cm <sup>3</sup> /cm <sup>3</sup>
1.1	39°14'0"	16°59'41"	0.2640	0.3627	0.4340	0.2815	0.3432	
1.2	39°14'3.2"	16°59'36.3"	0.2446	0.3440	0.4053	0.3041	0.3686	
1.3	39°14'6.8"	16°59'32.1"	0.3230	0.3880	0.5507	0.2463	0.3227	
2.1	39°14'3.3"	16°59'45.6"	0.2604	0.3307	0.4077	0.1705	0.3101	
2.2	39°14'6.6"	16°59'40.7"	0.2090	0.2560	0.3030	0.3199	0.3199	
2.3	39°14'10.1"	16°59'36.7"	0.2481	0.3643	0.3913	0.2416	0.3643	
3.1	39°14'6.6"	16°59'50.2"	0.2551	0.3320	0.4980	0.1841	0.2967	
3.2	39°14'9.7"	16°59'45.4"	0.2406	0.3143	0.3603	0.2486	0.3838	
3.3	39°14'13.3"	16°59'41.3"	0.2706	0.3247	0.3447			

Site 2A

ID	Latitude	Longitude	17/09/2009		30/09/2009		08/10/2009	
			g/g	cm <sup>3</sup> /cm <sup>3</sup>	g/g	cm <sup>3</sup> /cm <sup>3</sup>	g/g	cm <sup>3</sup> /cm <sup>3</sup>
1.1	38°37'49.2"	16°8'21.7"	0.2996	0.2967		0.3883	0.2760	0.3370
1.2	38°37'51.1"	16°8'27.6"	0.2525	0.2833		0.2783	0.2545	0.3500
1.3	38°37'52.5"	16°8'33.8"	0.2876	0.3387		0.2533	0.3016	0.2823
2.1	38°37'53.8"	16°8'19.9"	0.2164	0.3193		0.2910	0.2212	0.3070
2.2	38°37'55"	16°8'26.4"	0.2791	0.3077		0.3224	0.2814	0.3103
2.3	38°37'57.1"	16°8'31.9"	0.2925	0.3143		0.2216	0.2574	0.3287
3.1	38°37'58.4"	16°8'18.5"	0.2828	0.3277		0.2917	0.2614	0.2910
3.2	38°37'59.4"	16°8'24.5"	0.2305	0.2393		0.2831	0.1783	0.2413
3.3	38°38'1.7"	16°8'29.8"	0.2610	0.2823		0.3204	0.2906	0.3123

Site 2B

ID	Latitude	Longitude	17/09/2009		30/09/2009		08/10/2009	
			g/g	cm <sup>3</sup> /cm <sup>3</sup>	g/g	cm <sup>3</sup> /cm <sup>3</sup>	g/g	cm <sup>3</sup> /cm <sup>3</sup>
1.1	38°36'50.6"	15°57'2.7"	0.2500	0.2977		0.3008	0.1904	0.3247
1.2	38°36'46.1"	15°57'0.4"	0.2648	0.3497		0.3533	0.2738	0.3343
1.3	38°36'41.2"	15°56'59.6"	0.3450	0.2427		0.3060	0.2448	0.2350
2.1	38°36'48.6"	15°57'8.4"	0.2597	0.3253		0.3169	0.2489	0.1627
2.2	38°36'44"	15°57'6.5"	0.3266	0.3740		0.2672	0.2391	0.3187
2.3	38°36'39.3"	15°57'4.9"	0.3687	0.2460		0.2740	0.2178	0.1607
3.1	38°36'48.3"	15°57'14.7"	0.4222	0.2837		0.2272	0.4006	0.2980
3.2	38°36'43.8"	15°57'12.5"	0.4562	0.2653		0.2380	0.3881	0.2633
3.3	38°36'39.2"	15°57'10.5"	0.5224	0.2353		0.2439	0.4498	0.2853

Site 2C

ID	Latitude	Longitude	17/09/2009		30/09/2009		08/10/2009	
			g/g	cm <sup>3</sup> /cm <sup>3</sup>	g/g	cm <sup>3</sup> /cm <sup>3</sup>	g/g	cm <sup>3</sup> /cm <sup>3</sup>
1.1	38°39'9.5"	16°8'54.6"	0.2188	0.2690		0.3700	0.2715	0.3380
1.2	38°39'13.5"	16°8'58"	0.2525	0.3173		0.3878	0.2545	0.3633
1.3	38°39'17.9"	16°9'0.9"	0.2799	0.2787		0.3686	0.2486	0.3547
2.1	38°39'11.7"	16°8'48.9"	0.2488	0.2907		0.3528	0.3566	0.3780
2.2	38°39'16.2"	16°8'51.2"	0.2204	0.3147		0.3622	0.3039	0.4283
2.3	38°39'21.5"	16°8'56.6"	0.2072	0.2887		0.2947	0.2766	0.3027
3.1	38°39'15.6"	16°8'44.8"	0.2532	0.2650		0.3008	0.3149	0.3433
3.2	38°39'22.5"	16°8'47.5"	0.3035	0.2270		0.2815	0.3100	0.3097
3.3	38°39'25.2"	16°8'52.7"	0.2101	0.3103		0.3806	0.2440	0.3393

Site 2D

ID	Latitude	Longitude	19/09/2009		01/10/2009		08/10/2009	
			g/g	cm <sup>3</sup> /cm <sup>3</sup>	g/g	cm <sup>3</sup> /cm <sup>3</sup>	g/g	cm <sup>3</sup> /cm <sup>3</sup>
1.1	38°23'21.1"	15°59'22.9"	0.2684	0.1887		0.3190	0.3458	0.3172
1.2	38°23'24.8"	15°59'23.2"	0.2942	0.2113		0.2153	0.3149	0.2613
2.1	38°23'21.6"	15°59'20.5"	0.2615	0.2590		0.2947	0.3428	0.4117
2.2	38°23'25.1"	15°59'20.9"	0.2823	0.2670		0.1937	0.3233	0.2971

Site 2E

ID	Latitude	Longitude	19/09/2009		01/10/2009		08/10/2009	
			g/g	cm <sup>3</sup> /cm <sup>3</sup>	g/g	cm <sup>3</sup> /cm <sup>3</sup>	g/g	cm <sup>3</sup> /cm <sup>3</sup>
1.1	38°35'7.9"	15°55'19"	0.1117	0.2173		0.1977	0.1362	0.2387
1.2	38°35'9.2"	15°55'25"	0.2270	0.2407		0.2110	0.0947	0.2227
1.3	38°35'12.6"	15°55'9.6"	0.1360	0.2580		0.1267	0.1023	0.1713
2.1	38°35'14.6"	15°55'18.4"	0.3759	0.3130		0.2290	0.1212	0.1657
2.2	38°35'13.9"	15°55'25.5"	0.1189	0.1923		0.1643	0.1996	0.2317
2.3	38°35'17.3"	15°55'12"	0.1182	0.1173		0.1440	0.0981	0.1660
3.1	38°35'19.5"	15°55'20.3"	0.1479	0.2193		0.1857	0.1063	0.1833
3.2	38°35'18.8"	15°55'26.4"	0.1483	0.1650		0.0773	0.1336	0.1403
3.3	38°35'21.7"	15°55'14.6"	0.1415	0.1460		0.1977	0.1203	0.1437

Site 2F

ID	Latitude	Longitude	19/09/2009		02/10/2009		08/10/2009	
			g/g	cm <sup>3</sup> /cm <sup>3</sup>	g/g	cm <sup>3</sup> /cm <sup>3</sup>	g/g	cm <sup>3</sup> /cm <sup>3</sup>
1.1	38°33'33.1"	16°5'1.5"	0.1614	0.3367		0.4111	0.2228	0.3393
1.2	38°33'36.6"	16°5'5.8"	0.1744	0.2893		0.3497	0.1885	0.2853
1.3	38°33'40.2"	16°5'9.9"	0.1724	0.3177		0.4209	0.2894	0.2737
2.1	38°33'29.8"	16°5'5.1"	0.2376	0.2863		0.3685	0.2651	0.2997
2.2	38°33'32.3"	16°5'8.7"	0.2175	0.2917		0.3882	0.2642	0.3240
2.3	38°33'36.2"	16°5'13.3"	0.2276	0.3573		0.4034	0.2625	0.3913
3.1	38°33'26.3"	16°5'10"	0.1712	0.2700		0.2889	0.2590	0.3187
3.2	38°33'29.1"	16°5'12.1"	0.2189	0.3257		0.3829	0.2454	0.3293
3.3	38°33'32.2"	16°5'16.9"	0.2087	0.2850		0.3921	0.2642	0.3387

Site 2G

ID	Latitude	Longitude	23/09/2009		01/10/2009		08/10/2009	
			g/g	cm <sup>3</sup> /cm <sup>3</sup>	g/g	cm <sup>3</sup> /cm <sup>3</sup>	g/g	cm <sup>3</sup> /cm <sup>3</sup>
1.1	38°29'42"	16°14'23"	0.3482	0.2517		0.2537	0.2320	0.3834
1.2	38°29'37.3"	16°14'21"	0.6592	0.2510		0.2160	0.5995	0.4055
1.3	38°29'32.8"	16°14'18.7"	0.6474	0.2100		0.2343	0.2574	0.3045
2.1	38°29'43.2"	16°14'17"	0.4860	0.2153		0.2917	0.3684	0.3986
2.2	38°29'40.1"	16°14'12.3"	0.4338	0.1810		0.1690	0.9634	0.3668
2.3	38°29'35"	16°14'13.1"	0.3676	0.2047		0.1913	0.2960	0.3393
3.1	38°29'45.7"	16°14'11.5"	0.3605	0.2530		0.2127	0.6407	0.3904
3.2	38°29'40.9"	16°14'9.7"	0.4232	0.2470		0.2297	0.8089	0.6693
3.3	38°29'36.6"	16°14'7.3"	0.5639	0.2543		0.4007	0.2414	0.3455

Site 2H

ID	Latitude	Longitude	23/09/2009		01/10/2009		08/10/2009	
			g/g	cm <sup>3</sup> /cm <sup>3</sup>	g/g	cm <sup>3</sup> /cm <sup>3</sup>	g/g	cm <sup>3</sup> /cm <sup>3</sup>
1.1	38°29'39.7"	16°10'54.6"	0.3392	0.2207		0.2317	0.3275	0.3169
1.2	38°29'35.1"	16°10'56.7"	0.5204	0.2383		0.2767	0.5014	0.3647
1.3	38°29'30.3"	16°10'58.2"	0.5552	0.3337		0.2950	0.6013	0.4092
2.1	38°29'37.9"	16°10'48.7"	0.4931	0.2780		0.2623	0.4123	0.3537
2.2	38°29'34.1"	16°10'50.8"	0.4661	0.2753		0.3223	0.5313	0.3190
2.3	38°29'29"	16°10'52.3"	0.4939	0.2683		0.2900	0.4888	0.2152
3.1	38°29'36.8"	16°10'42.8"	0.4298	0.2487		0.2677	0.5340	0.2784
3.2	38°29'32.5"	16°10'46.5"	0.5730	0.2313		0.2457	0.4483	0.2773
3.3	38°29'27.6"	16°10'46.3"	0.3415	0.1827		0.2003	0.3115	0.2371

Site 2I

ID	Latitude	Longitude	23/09/2009		02/10/2009		08/10/2009	
			g/g	cm <sup>3</sup> /cm <sup>3</sup>	g/g	cm <sup>3</sup> /cm <sup>3</sup>	g/g	cm <sup>3</sup> /cm <sup>3</sup>
1.1	38°31'35.1"	16°2'41.3"	0.3385	0.2250		0.2639	0.3278	0.2675
1.2	38°31'37"	16°2'35.6"	0.3349	0.2593		0.2415	0.2893	0.1895
1.3	38°31'38.9"	16°2'29.9"	0.2124	0.3023		0.2918	0.2073	0.2774
2.1	38°31'30.5"	16°2'39.1"	0.2942	0.2597		0.3816	0.2425	0.2775
2.2	38°31'32.4"	16°2'33.3"	0.2324	0.2703		0.3040	0.1903	0.2243
2.3	38°31'34.4"	16°2'27.7"	0.2066	0.1640		0.2495	0.1743	0.2017
3.1	38°31'25.1"	16°2'36.5"	0.2477	0.3167		0.3087	0.2309	0.3210
3.2	38°31'27.9"	16°2'31.2"	0.2406	0.2673		0.3714	0.2440	0.3434
3.3	38°31'29.8"	16°2'25.5"	0.1674	0.2797		0.2485		0.3021

Site 2J

ID	Latitude	Longitude	25/09/2009		03/10/2009		08/10/2009	
			g/g	cm <sup>3</sup> /cm <sup>3</sup>	g/g	cm <sup>3</sup> /cm <sup>3</sup>	g/g	cm <sup>3</sup> /cm <sup>3</sup>
1.1	38°37'32.3"	15°59'29.8"	0.2697	0.2927		0.3437	0.2500	0.3227
1.2	38°37'33.9"	15°59'23.9"	0.3713	0.3087		0.3760	0.3800	0.3620
1.3	38°37'35.6"	15°59'18.1"	0.2495	0.3500		0.4460	0.3076	0.3540
2.1	38°37'36.4"	15°59'32.8"	0.3431	0.3640		0.4990	0.2634	
2.2	38°37'38.5"	15°59'25.6"	0.3400	0.3337		0.3940	0.3794	
2.3	38°37'40.3"	15°59'19.8"	0.3634	0.3160		0.3997	0.3315	0.3180
3.1	38°37'41.5"	15°59'33.9"	0.2922	0.3290		0.4723	0.3529	
3.2	38°37'43.2"	15°59'27.7"	0.2545	0.3593		0.3350	0.1981	
3.3	38°37'44.9"	15°59'21.9"	0.1972	0.3193		0.3977	0.1942	

Site 2K

ID	Latitude	Longitude	25/09/2009		03/10/2009		08/10/2009	
			g/g	cm <sup>3</sup> /cm <sup>3</sup>	g/g	cm <sup>3</sup> /cm <sup>3</sup>	g/g	cm <sup>3</sup> /cm <sup>3</sup>
1.1	38°40'8"	15°57'22.5"	0.3212	0.3063		0.2630	0.4067	
1.2	38°40'13"	15°57'22.2"	0.3341	0.3033		0.3050	0.2661	
1.3	38°40'17.7"	15°57'21.6"	0.3994	0.2620		0.2730	0.3824	
2.1	38°40'8.2"	15°57'16.3"	0.4349	0.2333		0.2297	0.2888	
2.2	38°40'13.2"	15°57'16"	0.3673	0.2410		0.2453	0.3428	
2.3	38°40'18.1"	15°57'15.5"	0.3750	0.3003		0.2993	0.3850	
3.1	38°40'8.3"	15°57'10.1"	0.4164	0.2913		0.2013	0.3617	
3.2	38°40'13.1"	15°57'9.8"	0.2366			0.3163	0.1934	
3.3	38°40'18"	15°57'9.3"	0.2407	0.2797		0.2953	0.1784	

Site 2L

ID	Latitude	Longitude	25/09/2009		02/10/2009		08/10/2009	
			g/g	cm <sup>3</sup> /cm <sup>3</sup>	g/g	cm <sup>3</sup> /cm <sup>3</sup>	g/g	cm <sup>3</sup> /cm <sup>3</sup>
1.1	38°31'47.9"	16°0'53.2"	0.2476	0.3187		0.3786	0.1881	0.3060
1.2	38°31'50.4"	16°0'47.9"	0.2552	0.3653		0.3947	0.2281	0.3547
1.3	38°31'52.3"	16°0'42.1"	0.2634	0.3923		0.3874	0.2806	0.3980
2.1	38°31'44.1"	16°0'49.4"	0.2396	0.3207		0.3453		
2.2	38°31'46.8"	16°0'43.9"	0.2640	0.3563		0.4225		
2.3	38°31'48.5"	16°0'38.2"	0.1867	0.3000		0.3260	0.2189	0.2943
3.1	38°31'40.3"	16°0'45.6"	0.2743	0.3027		0.3993		
3.2	38°31'43.2"	16°0'39.6"	0.2085	0.3287		0.3543		
3.3	38°31'45.1"	16°0'33.8"	0.2347	0.2473		0.3603	0.2831	0.3757

Site 2M

ID	Latitude	Longitude	28/09/2009		03/10/2009		08/10/2009	
			g/g	cm <sup>3</sup> /cm <sup>3</sup>	g/g	cm <sup>3</sup> /cm <sup>3</sup>	g/g	cm <sup>3</sup> /cm <sup>3</sup>
1.1	38°39'16.9"	16°12'25.9"	0.2395	0.1587	0.1730	0.0404	0.0543	
1.2	38°39'14"	16°12'20.9"	0.2529	0.3237	0.3267	0.1634	0.2813	
1.3	38°39'11.1"	16°12'15.9"	0.3363	0.3537	0.4140	0.4346	0.4577	
2.1	38°39'20.8"	16°12'22.3"	0.2386	0.3140	0.3490	0.2071	0.2867	
2.2	38°39'17.8"	16°12'17.1"	0.1688	0.2273	0.2117	0.0816	0.1197	
2.3	38°39'15"	16°12'12.2"	0.2382	0.3280	0.3533	0.2000	0.2953	
3.1	38°39'25.3"	16°12'19.8"	0.1907	0.3123	0.3080	0.1553	0.2757	
3.2	38°39'22.4"	16°12'14.9"	0.2357	0.2963	0.3247	0.1885	0.2157	
3.3	38°39'19.1"	16°12'9"	0.1883	0.2413	0.2477	0.1667	0.2690	

Site 2N

ID	Latitude	Longitude	28/09/2009		03/10/2009		08/10/2009	
			g/g	cm <sup>3</sup> /cm <sup>3</sup>	g/g	cm <sup>3</sup> /cm <sup>3</sup>	g/g	cm <sup>3</sup> /cm <sup>3</sup>
1.1	38°41'8"	16°10'39.6"	0.2281	0.3450	0.4127	0.2061	0.3210	
1.2	38°41'3.4"	16°10'37.6"	0.2719	0.3853	0.3830	0.2426	0.3430	
1.3	38°40'58.8"	16°10'36.1"	0.2700	0.3873	0.4093	0.1990	0.2960	
2.1	38°41'5.8"	16°10'44"	0.2837	0.3637	0.4477	0.2388	0.3677	
2.2	38°41'1.6"	16°10'43"	0.2281	0.3220	0.3873	0.2519	0.3870	
2.3	38°40'57.5"	16°10'42"	0.2959	0.3547	0.3847	0.2247	0.3167	
3.1	38°41'5.5"	16°10'50.5"	0.3123	0.3207	0.4113	0.2509	0.3150	
3.2	38°41'0.6"	16°10'49.6"	0.2937	0.3760	0.3257	0.2251	0.0920	
3.3	38°40'56"	16°10'47.9"	0.2477	0.3370	0.4007	0.1792	0.3380	

Site 2O

ID	Latitude	Longitude	28/09/2009		02/10/2009		08/10/2009	
			g/g	cm <sup>3</sup> /cm <sup>3</sup>	g/g	cm <sup>3</sup> /cm <sup>3</sup>	g/g	cm <sup>3</sup> /cm <sup>3</sup>
1.1	38°28'2.7"	16°0'40.6"	0.1362	0.1887	0.2500	0.1270	0.2147	
1.2	38°28'4.4"	16°0'43.5"	0.2098	0.2900	0.3460	0.2312	0.3350	
1.3	38°28'6.7"	16°0'46.5"	0.2664	0.3467	0.3868	0.2729	0.4104	
2.1	38°28'5.6"	16°0'38.3"	0.1308	0.1923	0.2716	0.1331	0.2462	
2.2	38°28'7.1"	16°0'41.2"	0.2545	0.3153	0.3101	0.2369	0.3393	
2.3	38°28'9.6"	16°0'44.8"	0.2222	0.2837	0.3075	0.2195	0.2989	
3.2	38°28'10.2"	16°0'39.4"	0.1490	0.2557	0.2961	0.1875	0.3297	
3.3	38°28'11.8"	16°0'41.5"	0.2071	0.2753	0.3107	0.1930	0.2953	









# Jasper Van doninck

## *Curriculum vitae*

**Contact** Groenstraat 67  
1800 Vilvoorde  
Belgium  
Tel.: +32/(0)477.42.31.62  
Jasper.Vandoninck@UGent.be  
jasper\_van\_doninck@hotmail.com

**Education** *Licentiaat in de Geografie*, September 2002  
Vrije Universiteit Brussel, Belgium

Thesis: *Sub-pixel classificatie van Landsat ETM+ data in stedelijke gebieden*  
Promotor: dr. Frank Canters

*Advanced Studies Master of Science in Earth Observation*,  
July 2008  
Katholieke Universiteit Leuven, Belgium  
Purdue University, IN, USA

Thesis: *Assessment of cropped areas in Ethiopia using soft classification of medium resolution imagery: Influence and integration of elevation data.*  
Promotor: Prof. dr. Jos Van Orshoven

## **Employment**

04/2004–06/2006,  
09/2008–12/2008 Beleidsmedewerker ruimtelijke ordening  
Dienst Leefmilieu en Ruimtelijke Ordening  
Gemeentebestuur Grimbergen  
Grimbergen, Belgium  
04/2009–03/2013 Research assistant  
Laboratory of Hydrology and Water Management  
Department of Forest and Water Management  
Faculty of Bioscience Engineering  
Ghent University  
Ghent, Belgium

## Scientific curriculum

### International publications with peer review (ISI - Web of Science)

Peters, J., De Baets, B., **Van doninck, J.**, Calvete, C., Lucientes, J., De Clercq, E., Ducheyne, E., Verhoest, N. (2011). Absence reduction in entomological surveillance data to improve niche-based distribution models for *Culicoides imicola*. *Preventive Veterinary Medicine*, **100**(1), 15-28.

**Van doninck, J.**, Peters, J., De Baets, B., De Clercq, E., Ducheyne, E., Verhoest, N. (2011). The potential of multitemporal Aqua and Terra MODIS apparent thermal inertia as a soil moisture indicator. *International Journal of Applied Earth Observation and Geoinformation*, **13**(6), 934-941.

**Van doninck J.**, Peters, J., Lievens, H., De Baets, B., Verhoest, N. (2012). Accounting for seasonality in a soil moisture change detection algorithm for ASAR Wide Swath time series. *Hydrology and Earth System Sciences*, **16**(3), 773-786.

**Van doninck, J.**, Peters, J., De Baets, B., De Clercq, E., Ducheyne, E., Verhoest, N. (2012). Influence of topographic normalization on the vegetation index-surface temperature relationship. *Journal of Applied Remote Sensing*, **6**, 063518.

Peters, J., Conte, A., **Van doninck, J.**, Verhoest, N., De Clercq, E., Goffredo, M., De Baets, B., Hendrickx, G., Ducheyne, E. (2013). On the relation between spatio-temporal soil moisture dynamics and the geographical distribution of *Culicoides imicola*. *Ecohydrology*, early view.

**Van doninck, J.**, Wagner, W., Melzer, T., De Baets, B., Verhoest, N. Seasonality in the angular dependence of ASAR Wide Swath backscatter. *IEEE Geoscience and Remote Sensing Letters*, submitted.

**Van doninck, J.**, De Baets, B., Peters, J., Hendrickx, G., Ducheyne, E., Verhoest, N. Modelling the spatial distribution of *Culicoides imicola*: climatic versus remote sensing data. *International Journal of Applied Earth Observation and Geoinformation*, submitted.

Peters, J., Waegeman, W., **Van doninck, J.**, Ducheyne, E., Calvete, C., Lucientes, J., Verhoest, N., De Baets, B. Predicting spatio-temporal *Culicoides imicola* distributions based on environmental habitat characteristics and species dispersal. *Ecological Modelling*, submitted.

### Contributions to international conferences and workshops

**Van doninck, J.**, Delrue, J., Gilliams, S., Bossyns, B., Van Orshoven, J. (2008). Hard and soft classification of remotely-sensed imagery using artificial neural networks in Ethiopia. *7th International Conference of the African Association of Remote Sensing of the Environment*, Accra, Ghana, oral presentation.

**Van doninck, J.**, Verhoest, N., Peters, J., De Baets, B., De Clercq, E., Ducheyne, E. (2010). Soil moisture proxies from MODIS-derived apparent thermal inertia time series. *EGU General Assembly 2010*, Vienna, Austria, poster presentation.

Peters, J., **Van doninck, J.**, Ducheyne, E., De Clercq, E., De Baets, B., Verhoest, N. (2010). Remote sensing for niche-based epidemiological modelling. *7th International Conference on Ecological Informatics*, Ghent, Belgium, oral presentation.

Peters, J., De Baets, B., **Van doninck, J.**, De Clercq, E., Ducheyne, E., Verhoest, N. (2011). Presence-absence modelling of *Culicoides imicola* through data reduction and machine learning. *1st Conference on Spatial Statistics*, Enschede, The Netherlands, poster presentation.

**Van doninck, J.**, Peters, J., De Baets, B., De Clercq, E., Ducheyne, E., Verhoest, N. (2011). Topographic normalization of thermal infrared data. *EGU General Assembly 2011*, Vienna, Austria, oral presentation.

**Van doninck, J.**, Peters, J., De Baets, B., De Clercq, E., Ducheyne, E., Verhoest, N. (2011). Soil moisture estimation from multitemporal ENVISAT ASAR Wide Swath images in mountainous terrain. *EGU General Assembly 2011*, Vienna, Austria, poster presentation.

**Van doninck, J.**, Peters, J., De Baets, B., Ducheyne, E., Verhoest, N. (2012). Using remote sensing and machine learning for the spatial modelling of a bluetongue virus vector. *EGU General Assembly 2012*, Vienna, Austria, poster presentation.

**Van doninck, J.**, Verhoest, N. (2012). Multi-temporal angular correction of ASAR Wide Swath data and the influence of vegetation phenology. *EGU General Assembly 2012*, Vienna, Austria, poster presentation.

**Van doninck, J.**, Verhoest, N., Peters, J., De Baets, B., Ducheyne, E. (2012). Identifying relevant remote sensing products for the spatial modelling of a bluetongue vector using Random Forests. *Belgian-Dutch Conference on Machine Learning & Workshop on Predictive Modeling for the Life Sciences 2012*, Ghent, Belgium, oral presentation.

April 16, 2013



